Design and development of devices for robotized needle insertion procedures

Nitish Kumar

UNIVERSITÉ DE STRASBOURG

ÉCOLE DOCTORALE :

269 Mathématiques, Sciences de l'Information et de l'Ingénieur (MSII)

AVR, ICube

THÈSE présentée par :

Nitish Kumar

soutenue le : **26 Novembre 2014**

pour obtenir le grade de : **Docteur de l'Université de Strasbourg**

Discipline/ Spécialité : **Signal, Image, Automatique et Robotique**

Design and development of devices for robotized needle insertion procedures

THÈSE dirigée par :

M. Bernard Bayle	Professeur, Université de Strasbourg

RAPPORTEURS :

M. Vigen Arakelyan	Professeur, INSA de Rennes
M. Just Herder	Professeur, TU Delft, Pays-Bas

EXAMINATEURS :

M. François Pierrot	Directeur de Recherche au CNRS, LIRMM
M. Olivier Piccin	Maître de Conférences, INSA de Strasbourg

To my family...

Acknowledgements

I would like to begin by thanking thesis committee members for having accepted to read and examine my work.

- Vigen Arakelyan, Professor at INSA Rennes
- Just Herder, Professor at TU Delft, Netherlands
- François Pierrot, Research Director at CNRS, LIRMM
- Olivier Piccin, Associate Professor at INSA Strasbourg
- Bernard Bayle, Professor at University of Strasbourg

Their valuable suggestions and critiques have helped me to improve this thesis report and its presentation.

I would like to give my sincere thanks to my thesis supervisor, Professor Bayle, who gave me the opportunity to do this thesis work under the framework of ProteCT project. I am deeply indebted to him for his valuable guidance and directions at each step which helped me to complete this work in a timely manner.

I would like to express my gratitude towards co-supervisor of my thesis, Professor Piccin, for countless hours of discussion on different topics of my research work. His invaluable insights have helped me provide solutions to several scientific and technological problems. Apart from the academic help, I am also grateful for his assistance in settling into a new city and handling the administrative procedures at beginning of my thesis work.

I would like to thank the following organisations for the financial assistance which have helped me to focus only on my research work without worrying about the monetary concerns.

- Image guided hybrid surgery institute (IHU), Strasbourg
- Foundation ARC for research on cancer
- Investissements d'Avenir through the Robotex Equipment of Excellence
- Labex CAMI(ANR-10-EQPX-44 and ANR-11-LABX-0004)
- Association des Instituts Carnot

I would also like to thank IRCAD, Strasbourg for providing me a wonderful workplace to carry out my daily work and research activities.

I would like to thank INSA, Strasbourg for giving me an opportunity to acquire valuable teaching experience and making me available the traction machine where I did most of the testing and validation of the prototypes. I would like to thank Professor Meylheuc for guiding me through these tests and preparing the initial set-ups. She has also provided me with her expertise on testing and characterisation of polymer based prototypes.

I would like to thank the AVR team of ICUBE laboratory for providing me a hospitable and stimulating environment for three years. I would like to thank Laurent Barbé in particular for his support for the test bench for the experiments at IRCAD. In particular, thanks goes to François Schmitt with whom I collaborated a lot within the ProteCT project and for his help with prototyping. I would like to thank as well all the PhD students with whom I have spent a wonderful and unforgettable time.

Finally, I would like to conclude by thanking my father and mother for their unwavering mental support throughout these years and believing in me. I want to remember here my brother Sunny who passed away couple of years back due to Leukemia. He has given me strength and motivation to carry out this research work. I would like to thank my girlfriend Kasia who has been with me through the difficulties and successes I have had these past years. Without their encouragement and constant appreciation, this work would not have been possible.

Strasbourg, 26 Nov. 2014 N. K.

Nitish KUMAR

Design and development of devices for robotized needle insertion procedures

Abstract

This thesis focuses on finding solutions for the design and the technological bottlenecks involving development of a slave robotic assistant for needle insertion procedures. The needed functionalities for the slave device were sought to be achieved by adopting a modular approach. This required the design and the development of different devices which satisfy targeted functionalities. A study of needle positioning devices was carried out which led to the synthesis of novel mechanisms for the task of needle axis translation and the needle axis orientation. A novel dimensional synthesis algorithm was developed to calculate the structural parameters of these mechanism while studying their singularities and considering the antagonistic constraints of system compactness, actuation torques and workspace size. The modular decomposition also allowed to offer solutions for an insertion tool dedicated to needle insertion with force feedback. This insertion tool consists of a device for inserting the needle, a device for grasping the needle and a force sensor for force feedback.

Résumé

Ces travaux de thèse apportent plusieurs contributions à la conception de dispositifs d'assistance robotisés pour la réalisation de procédures d'insertion d'aiguille sous imageur à rayons X. Partant de la tâche de positionnement et d'orientation d'une aiguille, plusieurs architectures mécaniques inédites à quatre degrés de liberté ont été proposées. Un algorithme de synthèse dimensionnelle a été conçu pour calculer les paramètres structuraux de ces mécanismes en étudiant leurs singularités, tout en tenant compte des contraintes antagonistes de compacité du système, de capacité d'actionnement et de taille d'espace de travail. Une décomposition modulaire du dispositif d'assistance a permis de proposer des solutions pour un outil dédié à l'insertion d'aiguille avec retour d'effort. Cet outil comporte un dispositif d'insertion, un système de préhension d'aiguille et un capteur d'effort spécifique pour le retour d'effort.

Contents

1 Introduction

Contents

1.1 Minimally invasive surgery and Interventional Radiology

Minimally invasive surgery or MIS, aims at minimizing the invasiveness of the medical procedures as compared to open surgery procedures. Open surgery often involves trauma due to blood loss, pain, scarring and leads to long recovery periods for the patient. MIS procedures tend to utilize single or multiple incisions on the patient's body wherein a tube like structure, a catheter or a needle is inserted. When possible, if open surgery can be replaced by a MIS procedure, it is recommended as it requires much shorter hospital stay and less expenses. Though MIS is promising in terms of its effectiveness and benefits to the patient, nonetheless it is not trivial in terms of the planning and application of the medical procedure. In an open surgery, the practitioner has a direct view and access to the organs and tissues of the patient's body. In comparison, during MIS procedures, practitioners have to rely on an imaging modality to visualize the instruments and their relative placement inside the body. For example, during laparoscopic surgery small cameras or a fibre optic system is utilized to transmit the inside picture to the surgeon. In this case, surgeons also lack the direct feel of tissues and interaction

forces which makes these procedures less intuitive for them. As a result, special training is necessary for MIS procedures as well.

Interventional radiology (IR) is a medical speciality where radiologists make use of several imaging modalities including ultrasound imaging, computed tomography (CT) and magnetic resonance imaging (MRI) to diagnose and treat the patients utilizing minimally invasive techniques. These procedures have been developed for various diseases and disorders including vascular, cancerous, hepatic, renal etc. Though traditionally these procedures have been carried out manually by the radiologist, efforts are being made for the robotization of these procedures. The prime reason behind these robotic initiatives is to improve upon the manual gestures of the radiologist which would otherwise be difficult owing to the constraints introduced by the utilized imaging modality.

The above mentioned imaging modalities differ in the physical principle used for tissue imaging. A brief description of the imaging modalities utilized in interventional radiology and the constraints imposed by them are as follows:

a) **Ultrasound imaging [Carovac et al., 2011]** (US) is based on the reflection of high frequency sound waves. Tissues of different density attenuate the sound signals differently and return them at separate time intervals. The robotic assistance employed for ultrasound imaging is primarily for improving the precision of the needle insertion. This modality does not introduce major material related constraints for the fabrication of the robotic device. As a result, the robotic assistants dedicated to ultrasound imaging are generally fabricated without much regard to the nature of materials.

b) **X-ray imaging [Yu et al., 2009]** (CT, fluoroscopy) uses ionizing radiations (X-rays) for imaging the patient organs. Different radiation absorption rates of the tissues and organs leads to varying contrasts. Fluoroscopy can allow for real time imaging of the tissues as compared to CT. But fluoroscopy provides much lower contrasts whereas high contrast images leading to better tissue differentiation is achievable by CT. The need for the robotization of the needle insertion procedure comes from the need to protect the medical staff from the harmful nature of X-rays. One important possible advantage of the robotized solution is therefore teleoperation, which lets the practitioner perform the procedures at a distance, away from the radiations. With this image modality, the metallic materials tend to have very high radiation absorption rates which creates artefacts within the images, and, as a result, robotic assistants should minimize the use of such elements and avoid any metallic parts in the imaging plane.

c) **MRI imaging [Goh et al., 1999]** imposes strong magnetic static field and magnetic gradients within the tunnel where the patient is located. Sharp contrast images can be produced leading to much better tissue differentiation than US and even than CT. But MRI does not show air and hard bones where CT has much better results. The tunnel of the MRI after introduction of the patient severely restricts the space allowed for the manoeuvres of the practitioner. In MRI, a robotic assistant typically helps the radiologist to perform his movements more efficiently and accurately, with better ergonomics. The strong magnetic field does not allow

any ferromagnetic material to be present within its vicinity. Hence, technological solutions targeted for MRI imaging need to utilize only non ferromagnetic materials, which is the most difficult challenge for robotic assistants, not only from a technical point of view, but also because of the extra costs it causes for each technological component.

In this thesis, prime focus is on the percutaneous procedures involving the insertion of needles under CT imaging guidance. The hepatic biopsy and hepatic tumor radiofrequency ablation (RFA) are two pertinent examples of procedures being targeted in the present work. Liver biopsy [Ovchinsky et al., 2012] is a typical example of a diagnostic procedure which involves sampling of liver tissues with hollow needles for medical diagnosis. In liver RFA procedures [Passera et al., 2013], radiologist destroys small tumors with thin needle like electrodes using high frequency currents which heat and destroy the cancerous cells.

The manual clinical workflow for a typical percutaneous interventional procedure can be described in three major steps:

1) **Preparatory phase (figure 1.1(a))**:

Planning of the needle path: The location of the target organ/tumor is determined on the images obtained from the imaging modality and registration of the patient's anatomy is done. Thereafter a safe path for the needle is planned so as to avoid harming delicate and sensitive tissues.

Localisation of the point of entry: Finally, the entry point on the skin is chosen, marked and prepared for the incision. This point also serves as a center of rotation, as the needle is constrained to rotate about this point.

2) **Needle positioning (figure 1.1(b))**:

Translation and orientation of the needle: This act of the radiologist corresponds to translating the needle axis to the entry point and aligning the needle axis with the pre-determined line of insertion. Thereafter needle is slightly inserted through the skin at the marked entry point.

3) **Needle insertion (figure 1.1(c))**:

Verification with the image modality: Needle orientation and its alignment with the insertion axis is verified with the help of imaging modality.

Insertion of the needle in several steps: The needle insertion is divided into several strokes. Grasp and release of the needle is performed by the radiologist after and before each stroke. Between these strokes the needle is left to rotate freely around the entry point to limit the tissue lacerations which would result if the needle were firmly held. The radiologist may also perform image acquisitions between each insertion step to verify the needle position.

(a) Preparatory phase. (b) Needle positioning. (c) Needle insertion.

Figure 1.1 – Manual work flow for percutaneous procedures.

1.2 Robotic needle insertion devices

This section is aimed at classifying the existing needle insertion devices (NID) and giving a broad overview of key functionalities which are expected of a NID, especially for CT guided needle insertion procedures. This would make it easier to compare the different NID within the defined framework and discuss what they are missing. It would become evident later that focus of this work is to provide a compact integration of existing and some very important missing functionalities in existing NID.

1.2.1 Classification

The classification of the needle insertion devices can be either based on the selected architecture or based on the fixation of robotic device in the operating room. NID can either have a serial, parallel or hybrid architecture. Where manual needle insertion is required, NID consists only of the needle positioning device without possibility of robotic needle insertion. Such NID have a serial or parallel architecture. For NID incorporating robotic needle insertion, the insertion mechanism is most often serially connected to the positioning device for security reasons making it an hybrid architecture. On the other hand, NID can be classified on the basis of whether they are attached to the table of the imaging device (table mounted systems TMS) or are mounted on the body of the patient (patient mounted systems PMS). Representative examples of TMS and PMS systems are shown in figure 1.2(a) and figure 1.3(a), respectively. TMS are generally of serial architecture, as shown in figure 1.2(b), and therefore can have large orientation and translational workspace, extra degrees of freedom (DOF) without much regard for compactness. On the downside they are generally with higher inertia, weight and without compensation for movement of the patient body surface. Hence, they can pose safety issues in case of sudden involuntary motion by the patient. On the other hand PMS are compact, portable, allow to partially compensate for the patient motion and have a parallel architecture, as shown in figure 1.3(b). Hence PMS are intrinsically safer. Owing to the primarily parallel structure, PMS have relatively smaller workspace and have to deal with the problem of singularity free workspace. With higher DOF and actuators on-board, size and weight of

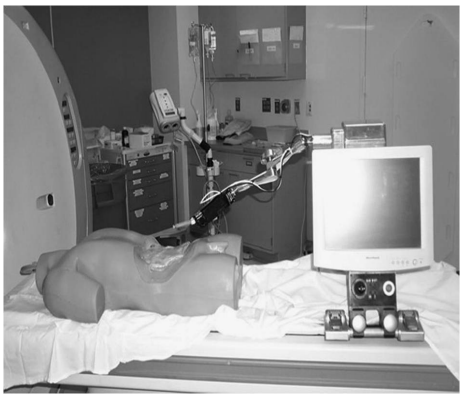

(a) Acubot, a table mounted NID with serial architecture [Stoianovici et al., 2003].

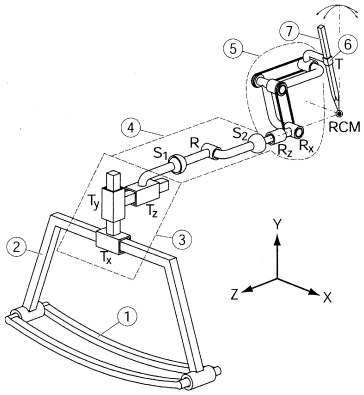

(b) Acubot : schematics [Stoianovici et al., 2003].

Figure 1.2 – Representative table mounted device.

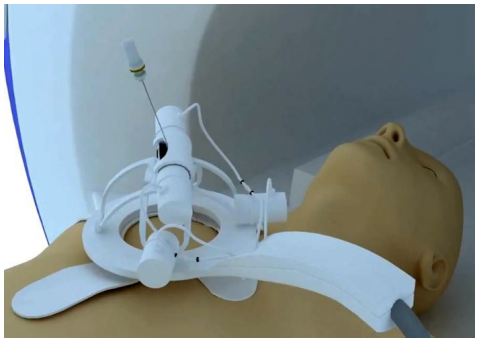

(a) Robopsy, a patient mounted NID with parallel architecture [Walsh et al., 2008].

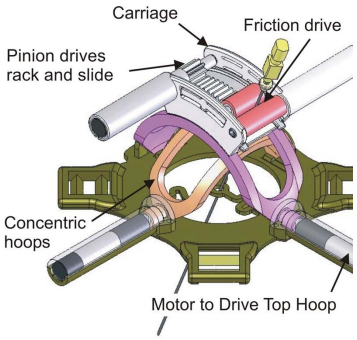

(b) Robopsy : schematics [Walsh et al., 2008].

Figure 1.3 – Representative patient mounted device.

the NID increases considerably. The other reason for selecting the Acubot and Robopsy, as representative NID, here is that they incorporate the essential functionality of the remote center of motion (RCM). The presence of this RCM point allows the NID to rotate about a fixed point which coincides with the insertion point on the patient skin. This assumes special significance, in the particular case where the needle is slightly inserted inside the patient body and the radiologist tries to change the orientation of the needle. Even though the tissue stiffness may constrain the NID to rotate about the insertion point without need for RCM, it will lead to the tissue damage. Moreover, after the cut has been made on the patient skin, the opened area doesn't really correspond to a point. The presence of the RCM point allows the radiologist to choose a fixed point on the patient skin without depending on the tissue stiffness.

The manual workflow described in the previous section listed the common acts and movements of the radiologist. The idea behind the robotization of the percutaneous procedures is

not to replace the radiologist but to modify the workflow, with certain acts performed by a robotic assistant which could be either automatic or teleoperated. The modification in the manual workflow results from the introduction of the robotic assistant as an intermediate interface between the radiologist and the patient. Most importantly *the preparatory phase* in the overall workflow has to be adapted to account for the robotic assistant. For example the additional steps such as, preparation of the robot including its sterilization, placement of the robot relative to the patient and the registration of the robot along with patient anatomy has to be carried out. The robotic assistants therefore aim at replicating two important acts, namely needle positioning and needle insertion. Not every robotic assistant tries to replicate the needle insertion act and it remains manual and performed by the radiologist. For such NID, only needle positioning act is mimicked.

1.2.2 Key functionalities

As outlined in the previous sub-section, the constraints for the robotic assistant vary for each imaging modality, with MRI imposing the most severe constraints. A robotic assistant compatible with MRI would in most cases satisfy the main constraints of the CT and ultrasound but may not necessarily be adapted for the other imaging modalities, in particular because registration may differ from an imaging device to another. Requirements for CT compatible robotic assistant and the needed typical functionality integration are as follows:

1) *Needle positioning*: An integrated CT compatible robotic assistant should be capable of needle positioning, in order to protect the radiologist during the intervention. This includes needle axis orientation and translation to mimic the movements of the radiologist. The dedicated mechanism must have $2-3$-DOF for the translation of the needle axis and $2-3$-DOF for the orientation of the needle axis.

2) *Needle grasp/release*: The robotic assistant should be able to grasp and release the needle during the insertion procedures, which is required, in particular, to prevent tissue lacerations due to physiological motions. This highlights the need for a dedicated needle grasping device (NGD) which has been quite neglected in the development of recent NID.

3) *Robotic needle insertion*: A robotic assistant developed for CT should be capable of inserting the needles at a distance, so as to keep the radiologist away from the ionizing radiations. A minimum 1-DOF is needed for the insertion mechanism. It may have another 1-DOF for the needle steering as it has been shown to improve the accuracy of needle insertion [Meltsner et al., 2007; Badaan et al., 2011]. For other imaging modalities, the needle insertion part may be kept manual as the radiologist can be present close to the patient.

4) *Teleoperation*: The act of needle insertion is a critical part of the overall insertion procedure. Therefore for reasons of safety, it is preferable that the radiologist performs it either manually or through telemanipulation using a haptic device. In such a scenario the radiologist has full control over the needle insertion part. However, the act of needle positioning can be fully automated, given the less critical nature of the operation. The choice of either manual or

teleoperated needle insertion depends mainly on the imaging modality. For example, in case of MRI or ultrasound, the radiologist can be present near the patient and manually insert the needle. But in case of CT, the needle positioning and insertion should be teleoperated to provide optimum protection against the overexposure of the X-rays. Also, through teleoperation radiologist has an added benefit of getting a feedback of insertion forces through the haptic device.

5) *Force feedback*: During teleoperation, the radiologist benefits from force feedback to augment the visual perception which is not real-time in case of CT. As in manual practice, haptic feedback allows to detect the key characteristics of the needle insertion, such as tissues stiffness or membranes ruptures. The use of force measurements, and therefore the presence of a force sensor is preferable to implement safe force feedback or at least force monitoring. It allows higher accuracy and better restitution of the haptic cues.

6) *Size/weight*: Constraints arise from the size of the tunnel of the CT scanner, which demands the patient mounted robotic assistants to be light and small in size. The typical diameter of a CT scanner bore is about 700 – 800mm and the remaining space after the introduction of the patient is typically about 200 – 300mm.

7) *Needle orientation*: The needle insertion may require in extreme cases an inclination of the needle by 60 deg, relative to the normal to the patient surface. Robotized needle insertion with capability of large orientation range offers a significant amount of flexibility to the radiologist for carrying out his natural movements.

8) *Patient movement compensation*: As the patient breathes and the anaesthesia may be local, the errors due to patient body surface movement or accidental/sudden body movement must be compensated to not cause injuries.

9) *Sterilization*: NID and all of its components must be sterilized before they can be used in the operating room in contact with the patient and the medical staff. In such a case, modular design of the NID helps to make some components disposable and some components reusable after sterilization.

1.2.3 Typical examples

Several NID have been described in the literature which perform a subset of the functionalities listed above. This subset depends on the type of medical intervention and constraints of the imaging modality. For the needle positioning and needle insertion requirements, the number of DOF can also vary a lot depending on the architecture and the compromise in functionality. Few typical NID are discussed below in detail and compared against each other.

AcuBOT (figure 1.2(a)): is a TMS developed by [Stoianovici et al., 2003] at the URobotics laboratory, Johns Hopkins University, USA. This system was developed for fluoroscopy and/or CT guided needle insertion interventions like needle biopsy and RFA procedures targeting the kidney. It has a gross pre-positioning unit which accounts for 3-DOF in translation. The decoupled 2-DOF in orientation is achieved by a RCM module allowing for orientation of

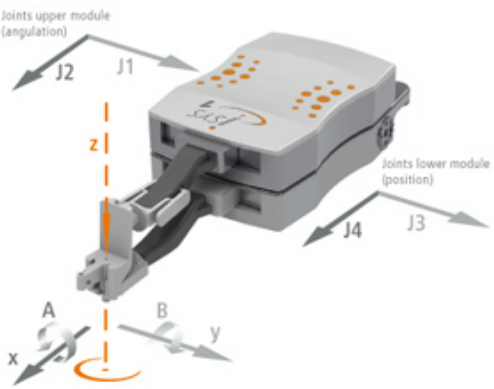

(a) iSYS [iSYS Medizintechnik, 2013].

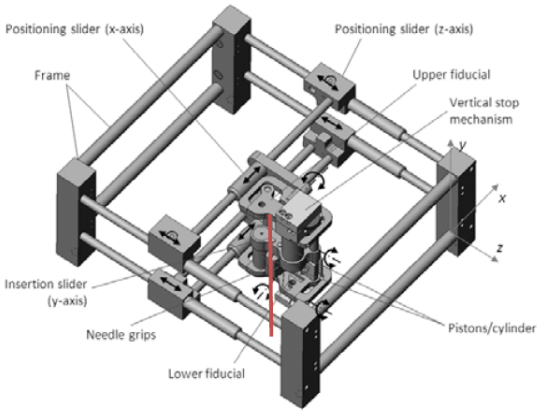

(b) New LPR [Hungr et al., 2011].

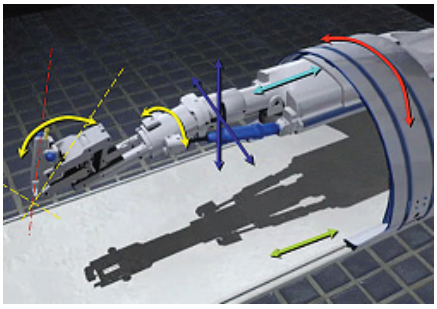

(c) Innomotion [Melzer et al., 2008].

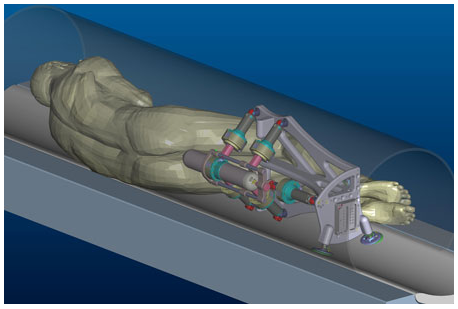

(d) MRBot [Cunha et al., 2010].

Figure 1.4 – More Needle insertion devices.

the needle about two perpendicular axes. It has another DOF for the robotized insertion of the needle. Even though providing a very large orientation range for the needle positioning, major requirements of needle grasp/release, teleoperation and haptic force feedback were not incorporated in this device.

Robopsy (figure 1.3(a)): is a PMS developed by [Walsh et al., 2008] at Massachusetts Institute of Technology, USA. This system is developed for CT guided percutaneous procedures targeting lung biopsies. It does not include the translational mobility for the needle positioning. Instead a compact structure with 2-DOF for the orientation and 1-DOF for the robotized needle insertion has been developed. This device does provide an extra DOF for the controlled teleoperated needle grasp/release. However, it has limited orientation capability (around 30 deg) and no haptic force feedback to the radiologist is provided.

iSYS (figure 1.4(a)): is a TMS which has been commercialized by iSYS Medizintechnik GmbH [iSYS Medizintechnik, 2013] for CT guided percutaneous procedures. It utilizes relative movement between two parallel plates to achieve 2-DOF for translation and 2-DOF in orientation, in a very compact device. It lacks in the needle grasp/release functionality. Though it allows for the teleoperated control of needle positioning, the needle insertion itself remains manual. Furthermore, it can not provide the haptic force feedback which would give the

radiologist feel of interaction forces between the needle and the tissues.

New LPR (figure 1.4(b)): is the second generation of the device developed by [Hungr et al., 2011] at the TIMC laboratory, Grenoble, France. It is a device compatible with both MRI and CT. Parallel motion between two planes, as for iSYS, has been utilized to obtain 2-DOF for translation and 2-DOF in orientation. But it too lacks the key functionalities of needle grasp/release, haptic force feedback and the telemanipulated control of the needle positioning and insertion. Furthermore it has limited angulation range (24 deg) in orientation.

CT-Bot (figure 1.5): is a PMS developed by [Maurin et al., 2008] in our lab during past work for CT compatibility. The CT-Bot shown in figure 1.5(a) has 3-DOF in translation and 2-DOF in orientation. During this project a first version of a grasping device, shown in figure 1.5(b), was developed by [Piccin et al., 2009] and integrated with the insertion tool. The insertion tool, shown in figure 1.5(c), allowed for robotized needle insertion with force feedback through teleoperation with a 1-DOF master haptic interface. Though several functionalities were achieved with two separate subsystems, integration of them in a compact, small and light weight device however proved to be a difficult challenge.

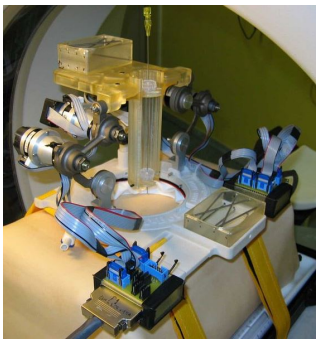

(a) CT-Bot : Slave NID [Maurin et al., 2008].

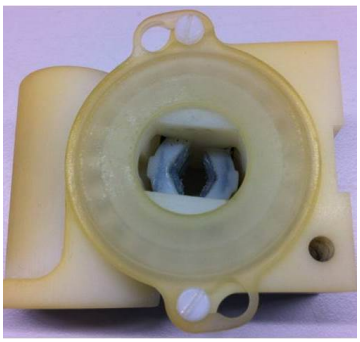

(b) Rigid version of NGD [Piccin et al., 2009].

(c) Robotized needle insertion [Piccin et al., 2009].

Figure 1.5 – CT-Bot Solution for teleoperated perctuaneous procedures.

1.2.4 Comparison of functionality integration

The functionality integration in the NID found in the literature is summarized in table 1.1. Two orientation ranges are given for NID in this table as the orientation workspace is not axi-symmetric for all of them. This table makes it easier to compare the existing robotic assistants, with CT compatibility and specific requirements in mind. None to few systems actually fulfil all of these key requirements. Most of them are rather focused on achieving one or other specific functionalities. The idea of *teleoperation with haptic force feedback* is central to the goal of providing robotic assistance in the interventional radiology procedures under CT imaging because it provides protection of the radiologist against X-rays and improved safety of the patient. The functionality of *needle grasp and release* during the intervention, as

[**Author, year**]	**Imaging Modality**	**Intervention**	**Needle positioning**	**Needle grasp/ release**	**Robotic Needle Insertion**	**Tele-operation**	**Force feedback**	**Orientation Range** (deg)	**Mobility** (**Needle positioning**)
[De Lorenzo et al., 2013]	Without Imaging	Neuro Surgery	Manual	No	No	No	Yes	N.A.	N.A.
[Hungr et al., 2012]	Ultrasound	Prostate	Yes	No	Yes	No	No	$(-30,30),(-30,30)$	3T2R
[Cole et al., 2009]	MRI	Neuro Surgery	Yes	No	No	No	No	$(-60,0),(-30,30)$	3T2R
[Seifabadi et al., 2012]	MRI	Prostate	No	No	Yes	Yes	No	Needle steering	N.A.
[Song et al., 2013b]	MRI	Abdominal	Manual	No	No	No	No	$(-80,80),(-80,80)$	2R
[Krieger et al., 2013]	MRI	Prostate	Yes	No	No	No	No	$(17.5,40),(-,-)$	2R
[Shang et al., 2013]	MRI	Prostate	No	No	Yes	Yes	Yes	Needle steering	N.A.
[Song et al., 2013a]	CT	Abdominal	No	Yes	Yes	No	No	Needle steering	N.A.
[Stoianovici et al., 2003]	CT	Abdominal	Yes	No	Yes	No	No	$(-180,180)$, $(-180,-180)$	3T2R
[Walsh et al., 2008]	CT	Abdominal	Yes	Yes	Yes	Yes	No	$(-30,30),(-30,30)$	2R
[Melzer et al., 2008]	MRI/CT	Abdominal	Yes	No	Yes	Yes	Yes	$(-40,40),(-23,70)$	3T2R
[Hungr et al., 2011]	MRI/CT	Abdominal	Yes	No	Yes	No	No	$(-32,24),(-20,10)$	2T2R
[iSYS Medizintechnik, 2013]	CT	Abdominal	Yes	No	No	Yes	No	$(-30,30),(-30,30)$	2T2R
[Piccin et al., 2009]	CT	Abdominal	Yes	Yes	Yes	Yes	Yes	$(0,60),(-25,25)$	3T2R
(Current project: ProteCT)	CT	Abdominal	Yes	Yes	Yes	Yes	Yes	$(-60,60),(-60,60)$	2R

Table 1.1 – Comparison of NID.

proposed in the CT-Bot, is also very important with regard to patient's health and recovery. None of the existing systems fulfil both these requirements. Moreover, for the systems that come close to satisfying these requisites, the orientation range of the needle axis remains quite limited (less than 30 deg.), even though large orientation capability represents a real improvement. The current project in our lab, presented in the next section, aims to provide an integrated system, which would cover these key functionalities and is adapted specifically to the necessities arising from non-vascular interventional radiology procedures utilizing the CT modality.

1.3 ProteCT Project

This thesis work was performed within the context of the ProteCT project funded by Image guided hybrid surgery institute (IHU), Strasbourg. IHU Strasbourg is a center created under the "*Programme Investissements d'Avenir*" for the medical and surgical diagnosis and treatment of the pathologies of the digestive system. It not only provides healthcare for the patients with minimally invasive techniques but also acts as a research center while bringing people from different backgrounds including clinicians, researchers and engineers to develop novel instruments and medical procedures.

1.3.1 Objectives

The need for the ProteCT project arose from the fact that the radiologists and medical support staff come under repeated exposure to the X-Rays when performing minimally invasive procedures under CT. This situation is aggravated by the lack of trained radiologists and the increase in number of such procedures. Hence, protection or shielding of the radiologist from these X-rays becomes important so as to allow him/her to perform a number of interventions for long durations. Current practice of wearing heavy and cumbersome lead aprons for protection not only restricts the natural movements of the radiologist but also leads to fatigue. Moreover, it does not shield the whole body from these radiations. Therefore, robotization of interventional radiology procedures under CT is taken as an alternative solution for protecting the radiologist.

A complete robotized solution may be envisaged under the teleoperation scheme as shown in figure 1.6. This figure and the representation will be invoked at the beginning of next chapters to put the discussion of each element in the perspective of this broad layout.

From figure 1.6, the project work can be identified to have three broad areas namely, telemanipulation, development of master device and development of slave device. The telemanipulation and the design and development of the master device is not part of this thesis work. This thesis work covers design and development aspects of the slave device shown in red in figure 1.6.

Telemanipulation : as the effect of X-Rays decreases with the distance from the scanner,

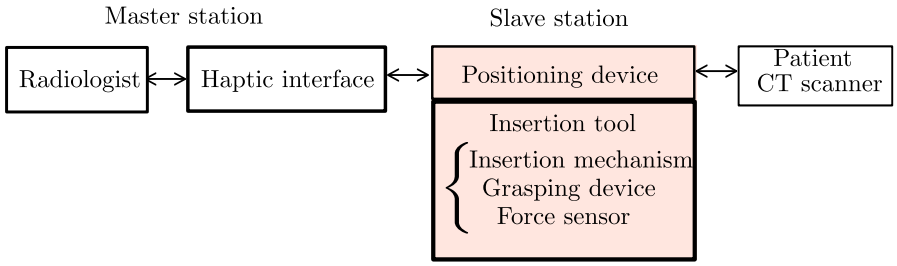

Figure 1.6 – Schematics : Telerobotic interventional procedures under CT scanner.

one way of protection is to enable the radiologist to perform his gestures from a distance. This can be fulfilled by utilizing a master device which the radiologist can operate to transfer his gestures, through teleoperation, to a slave robot. This slave robot is actually in contact with the patient and performs the acts of needle positioning and insertion. This capability of telemanipulation control was developed in our lab during the thesis work of [Barbé, 2007]. The functionality of inserting the needles through telemanipulation was demonstrated successfully in the work of [Piccin et al., 2009], where *in vivo* needle insertion procedures were carried out on an anaesthetized swine.

Master device : there exist commercial products like Omega from Force Dimension with varying DOF which can be directly utilized as master haptic device. Due to redundancy in these haptic devices, the design of a dedicated haptic interface with adequate DOF may be better suited and adapted to the acts of interventional radiology. Two linear 1-DOF master interfaces were developed in our lab during work of [Barbé et al., 2007] and [Joinie-Maurin et al., 2010] for controlling the insertion DOF through teleoperation. Overall a minimum of 4-DOF is required for needle positioning and 1-DOF for needle insertion. The design and development of this master device is not part of this thesis work.

1.3.2 Thesis objectives and organization

Thesis objectives: The slave device is certainly the most complex component in the whole teleoperated robotized solution given its proximity with the patient and the CT scanner resulting in the issues of sterilization, compatibility with the imaging device and safety. The work of this thesis is primarily focused on the design and development of this slave device and its components, as emphasized in figure 1.6. A slave device equipped to replicate the radiologist acts, transferred through kinematic mapping, must satisfy certain basic functionalities. To integrate these functionalities into the slave device, a modular approach is employed in the ProteCT project to arrive at a subsystem corresponding to each particular functionality. The first subsystem is the positioning device which is needed for the orientation and translation of the needle axis. This positioning mechanism can have either 2-DOF or 4-DOF depending on whether or not translational mobility is considered. The CT-Bot was developed for needle positioning but it has 5-DOF including one redundant DOF. Due to higher DOF and difficulty of placement of actuators near the base of CT-Bot, a compact positioning device was not

obtained. Therefore, in this thesis work efforts have been made to avoid the redundancy in the DOF of the positioning device, by synthesizing mechanisms with minimal required DOF, and to place the actuators near its base. The concept of needle grasping device for mimicking the needle grasp/release act was also developed during the CT-Bot project. In this thesis, building on the previous work with NGD, a new version of the NGD is proposed and experimentally validated. A different approach to the needle insertion mechanism is employed in this thesis work, as compared to CT-Bot, for compact integration and easy accessibility of the needle by the radiologist. Moreover, as the radiologist can not directly feel the interaction forces between the needle and tissues, a force sensor has to be integrated in the slave NID to feed the force information back to the radiologist. A commercial force sensor was employed during the CT-Bot project, which is not compatible with the CT imaging. Therefore for the ProteCT project, design and validation of a CT compatible and custom designed force sensor is taken up during this thesis work.

Thesis organization: This thesis is focused on the design and development of the different subsystems constituting the slave device. The design and technological solutions to the bottlenecks, for fulfilment of targeted functionalities of the slave device, are presented. The thesis is organized into two main parts.

Part-I details the synthesis and design of the two positioning devices, one with 4-DOF and another with 2-DOF. The first chapter of this part (chapter 2) discusses the task of needle positioning. A minimalist task description and corresponding mobility is derived for this task. A generic task-based approach for the type synthesis of parallel mechanisms is described and applied for the synthesis and enumeration of different parallel mechanism candidates for the task of needle positioning. This synthesis considers both needle translation and orientation aspects of the needle positioning. As needle orientation capability is more important than the needle translation, candidate mechanisms with fewer DOF satisfying only the orientation capability can also be considered for the reduced task of needle positioning. Hence different candidates with fewer DOF satisfying only the orientation requirement and RCM capability are discussed. A novel dimensional synthesis algorithm is proposed in chapter 3 to take into account the constraints of compactness, workspace size, singularity free workspace right in the initial stages of the overall design process. The level of actuation torques and base reactions are calculated for the two selected candidate mechanisms which satisfy the full and reduced positioning requirements. A comparative analysis of these two candidates is carried out on the basis of workspace size, level of actuation torques and practical considerations. Finally the solution for the positioning device along with its CAD implementation in the ProteCT project is presented. The CAD implementation of this positioning device was developed by Benoit Wach during his master thesis [Wach, 2014].

Part-II focuses on the design of the insertion tool which consists of a needle insertion mechanism, a needle grasping device and a force sensor for haptic force feedback. The first chapter of this part (chapter 4) details the design and development of an adapted insertion mechanism. The designed insertion mechanism has an adapted conical form which makes use of the Sarrus

mechanism for the insertion DOF and linear piezoelectric motors for the actuation. Thereafter, the design, development and experimental assessment of two variants of the needle grasping devices are presented. The needle grasping devices are fabricated out of the polymer material for the CT compatibility and make use of either compliant or rigid parts for grasping the needle. Chapter 5 describes the design, development and experimental assessment of a custom built force sensor adapted to CT scanner requirements and suited specifically for the interventional radiology needle insertion procedures. To alleviate the force sensor from the viscoelastic effects due to utilization of the polymer material, a novel identification procedure is proposed for the modeling of the force sensor. Furthermore, a novel compensation algorithm is derived from the identified model and utilized to compensate for the hysteresis and other time-dependent behaviour found in the force sensor signal. Finally the solution for the insertion tool along with its CAD implementation in the ProteCT project is presented. The CAD implementation of the insertion tool were developed with François Schmitt who is a research engineer in the ProteCT project.

Needle positioning device Part I

2 Synthesis of needle positioning mechanisms

Contents

2.1 Task definition and existing solutions

One of the key gestures of the radiologist is the needle positioning for targeting a specific part of the patient's body. Needle positioning can be seen as the placement of a line $\mathscr{L}$, supporting

the needle axis in 3D space, using the mechanism to be synthesized. Let $\mathscr{R}_b = (O_b, \mathbf{x_b}, \mathbf{y_b}, \mathbf{z_b})$ be a fixed reference frame and $\mathscr{R}_f = (O_f, \mathbf{x_f}, \mathbf{y_f}, \mathbf{z_f})$ be the frame affixed to the moving platform of the mechanism. In this specific context, two practical points can serve to define $\mathscr{L}$, namely an entry point E on the patient's skin and the point O_f attached to the moving platform such that the direction of $\mathscr{L}$ coincides with $\mathbf{z_f}$. The entry point E is specified by the radiologist in the images acquired in a pre-operative stage, but it is sometimes necessary to readjust its position. Assuming that the point O_b is the initial targeted entry point, a zone of operation around O_b is defined by a plane Π tangent to the skin at point O_b with a normal vector $\mathbf{z_b}$, as depicted in figure 2.1. After fixing the point E in Π, the needle is rotated around this point to obtain the required orientation for reaching the target zone.

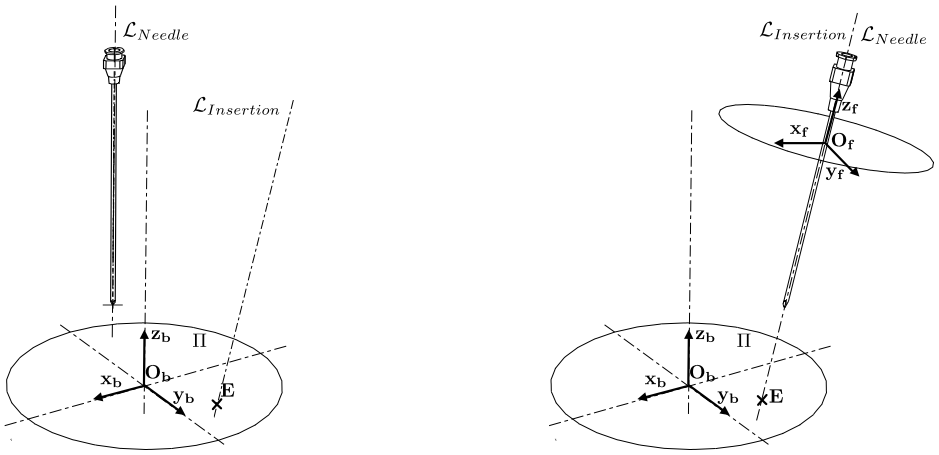

(a) Initial State. (b) Final State.

Figure 2.1 – Task definition for needle positioning.

From the above task definition a complete task definition Task-I and a reduced task definition Task-II can be deduced. The Task-I is defined as having the requirement for needle axis translation and needle axis orientation, whereas Task-II requires only orientation of the needle axis. The mechanisms with reduced mobility require fewer actuators and are much easier to implement and realize practically. The kinematic structure of the mechanism for Task-I has at least 4-DOF or more precisely the mechanism may have a 2T2R (T-Translational and R-Rotational) mobility. Whereas for Task-II, the mechanism has at least 2-DOF and a 2R mobility. At the start of the procedure, the radiologist may wish to tilt the needle axis around the entry point while the needle has just been slightly inserted. Then, a key requirement is the presence of a RCM point which coincides with the entry point on the patient's skin. This facilitates the orientation of the mechanism without causing any tissue lacerations.

A number of dedicated robotic systems have been developed during the last decade but there is still a need for improvements in the compactness and the functionality integration. While the TMS [Stoianovici et al., 2003; iSYS Medizintechnik, 2013] usually satisfy all the requirements

of the needle positioning, they require additional passive or active gross pre-positioning units, which makes the overall system less compact. The PMS [Mazor Robotics, 2013; Walsh et al., 2008] generally satisfy the reduced Task-II definition. The CT-Bot presented in the work of [Maurin et al., 2008] has a 3T2R mobility and satisfies the Task-I requirement but it has one extra DOF than required. The new LPR [Hungr et al., 2011] is a PMS which has a minimal 2T2R mobility satisfying Task-I requirements. Not every such system is designed to ensure the entry point on the patient's skin as the RCM point. The work in [Li et al., 2013] discusses a family of RCM mechanisms based on the intersecting motion planes. However, the RCM point in these mechanisms does not ensure spherical motion of the end-effector carrying the needle axis. Instead, a translational *parasitic* motion along the needle axis is present for most of these mechanisms which can not be decoupled from the needle positioning. It is not desirable to couple the needle positioning mechanism with the mechanism of needle insertion, as it does not allow for direct measurement of axial needle insertion forces. Few parallel mechanisms with 2T2R mobility have been reported in the literature and even less work has gone into mechanisms with this mobility for needle positioning requirements. For example, the mechanisms presented in [Zhang and Ting, 2012; Fan et al., 2011; Li and Huang, 2003; Wang, 2011] are developed for applications other than the needle positioning and hence, their mobility does not satisfy the requirements of the targeted procedure.

A task-based methodology utilizing the screw theory and motion patterns is presented for synthesis of adapted mechanisms. Starting from this minimal task definition Task-I and the reduced task definition Task-II, a constraint wrench system is determined for each task. Based on decomposition of the constraint wrench systems, the synthesis of serial legs is presented. Several novel candidate 2T2R mechanisms are obtained by combination of these serial legs and tested for full-cycle mobility and validity of selection of their actuated joints. This work has been published in the Elsevier journal of mechanism and machine theory and can be found here [Kumar et al., 2014a]. Finally, mechanisms corresponding to reduced mobility 2R and Task-II are considered and discussed for the task of needle axis orientation. Throughout the synthesis it is ensured that the resulting mechanisms have a RCM point.

2.2 Task-based synthesis methodology for parallel mechanisms

Generally, parallel mechanisms are synthesized beforehand and the applications to which they might be suited, are discovered later. An approach based on the application motivated task-based synthesis has however the potential to synthesize novel parallel mechanisms which are better suited to the needs of the application. A general parallel mechanism consists of at least two kinematic chains or legs connected from the base of the mechanism to the platform [Merlet, 2006]. The mobility of each kinematic chain is a superset of the mobility of the parallel mechanism. Therefore, the synthesis of parallel mechanisms has to start with the enumeration of these kinematic chains which includes both the serial and closed-loop types.

There are several methods available for the synthesis of parallel mechanisms which may fall

into two large categories. The first one is based on the study of the motion of the moving platform, resulting from the intersection of motions provided by each leg. Depending on the representation chosen to describe the motion, powerful synthesis methods have been proposed based on the group theory [Hervé, 1999; Angeles, 2004; Li et al., 2004; Fan et al., 2013] or based on the theory of linear transformations [Gogu, 2008, 2006]. The second category uses a dual approach, since the focus is rather set on the constraints applied to the moving platform, which are formed by the union of the constraints imposed by each leg. Screw theory is often used for this approach since it can describe in a unified manner both motions and constraints acting on the rigid bodies. Several reference works have recently appeared on the subject of the type synthesis of the parallel mechanisms based on the screw theory [Wolf and Shoham, 2006; Kong and Gosselin, 2007; Huang et al., 2013]. The synthesis of mechanisms using screw theory is based on the principle of reciprocity which implies finding the reciprocity conditions between screw systems, namely wrench and twist systems. This approach can be conducted algebraically [Dai and Jones, 2003] and involves calculating the null bases of a given set of wrenches to derive the reciprocal twist systems. However, there also exists more geometric deductive reasoning leading to similar results which are widely used in research works focused on type synthesis of parallel mechanisms [Kong and Gosselin, 2006, 2007].

The synthesis of mechanisms often starts with a mobility requirement pertaining to a given task. However, the concept of mobility [Gogu, 2005], stated as the number of independent coordinates to define the configuration of a mechanism, is not sufficient to characterize fully and accurately the motion capability of the mechanism. A more comprehensive description can be gained by considering the DOF partitioning into their rotational and translational components [Srivatsan et al., 2013; Altuzarra et al., 2013]. The above approach is quite generic. It is also applicable to mechanisms with variable mobility over the workspace and in singular configurations. Still, these methods are applied at instantaneous configurations and are not feasible to apply for each point of the workspace. In the present work, only mechanisms with invariable mobility are considered and this eliminates the need for calculating instantaneous mobilities over the whole workspace. Since screw theory produces mechanisms with instantaneous mobility only, some criterion has to be utilized to ascertain the invariability of the mobility. In this context, the concept of full-cycle mobility [Gogu, 2008; Huang et al., 2013] is used as a criterion and can be verified using geometric properties via the screw theory instead of algebraic or numeric calculations. Without full-cycle mobility the mechanisms might exhibit different output motions and constraints in different configurations. This means that the mechanism will not exhibit the required mobility for finite configurations and will be rendered useless for the particular task it was synthesized.

Even with DOF partitioning of the mobility into rotational and translational components and the validation of the full-cycle mobility criterion, there could still exist an ambiguity in the description of the mobility of a mechanism. This is specially the case in the context of the mechanism synthesis presented later on, where two different motion patterns are identified corresponding to the same DOF partitioning and same mobility. This problem of mobility specification can be disambiguated using the tools of screw theory which provide a deeper

insight into the motion of the end-effector and the constraints applied to it. The concept of motion pattern along with the virtual chain approach introduced by Kong and Gosselin [Kong and Gosselin, 2006] helps to solve this issue of mobility specification. Though the concept of motion pattern is utilized in the present work, the synthesis method using virtual chains is not employed since it is not always possible to find a virtual chain for every motion pattern.

The synthesis of parallel mechanisms is not complete until the choice of the actuated joints has been validated. For satisfying the constraints as well as the mobility of the parallel mechanism, a minimum number of legs is required. Exceeding this number of legs imposes additional constraints on the mechanism but often it becomes necessary for locating the actuated joints near the base and enhancing the rigidity of the mechanism. These over-constraints introduce additional geometrical conditions on the placement of the joints axes in the mechanism. The effect of having these geometric conditions not met need to be investigated for ascertaining the mobility of the mechanism. As pointed out in [Huang et al., 2011b], the construction of certain parallel mechanisms turns out to be a challenging task because the required geometric conditions are very difficult to meet and consequently the fabricated mechanism may not exhibit the expected mobility. Therefore, a set of preference rules will be proposed based on the feasibility and practical considerations, in order to obtain parallel mechanism candidates with reduced geometrical complexity.

Since the objective of a task-based synthesis procedure is to obtain mechanisms in the context of a practical application, one does not need to enumerate all possible candidates but to find the best candidate with the least architectural complexity.

2.2.1 Preference rules for leg composition

During the synthesis process, the following *preference rules* will be followed for the selection of serial legs :

1) **Types of joints**: the generated legs should avoid prismatic joints if possible.

2) **Redundancy**: the generated legs will be non-redundant to avoid extra actuators.

3) **Overconstraints**: the number of overconstraints for the parallel mechanism should be minimized.

4) **Geometric conditions within a leg** (decreasing order of preference):
(a) Two revolute joints parallel to each other $(RR)_p$.

(b) Three revolute joints parallel to each other $(RRR)_p$.

(c) Two revolute joints intersecting each other at one point $(RR)_i$.

(d) Three revolute joints intersecting each other at one point $(RRR)_i$.

5) **Geometric conditions between legs** (decreasing order of preference):
(a) Parallelism between sets of $(RR)_p$.

(b) Parallelism between sets of $(RRR)_p$.

(c) Sets of $(RR)_i$ intersect at one common point.

(d) Sets of $(RRR)_i$ intersect at one common point.

2.2.2 Synthesis procedure

Though type synthesis with the screw theory and motion pattern is a well established method, it has to be adapted for task specific synthesis problems. The task-based synthesis formulation presented below derives the motion patterns directly from the task-description rather than starting from an arbitrary constraint description. It also differs from establish approaches [Kong and Gosselin, 2006] in utilizing the set of preference rules defined in previous subsection to synthesize mechanisms with least architectural complexity rather than total enumeration of mechanisms. This method is quite generic in the sense that it can be applied to any task description which can be formulated in terms of constraints and allowed reciprocal motion.

Step 1: **Identification of the mobility requirements from the task definition**
(a) Identification of all possible motion patterns

Step 2: **Corresponding to each motion pattern, identification and decomposition of its wrench system**

Step 3: **Generation of legs, serial or closed loops, conforming to the possible combination of the wrench systems**
(a) Identification of the legs with least architecture complexity based on the rules expressed in section 2.2.1

Step 4: **Generation of candidate parallel mechanisms by possible combination of legs**
(a) Check for the full-cycle mobility criterion

(b) Check for the validity of the choice of actuated joints

Step 5: **If steps** $4a$ **and** $4b$ **are not satisfied go to step** 3.

Though the steps $3-4$ are common in the synthesis process using screw theory, a task-based synthesis process requires steps 1 and 2 before proceeding with next steps.

2.3 Synthesis of legs

As a first step, the wrench system based on the motion pattern needs to be identified. Twists and wrenches of pitch h are denoted as $\$^h$ and $\hat{\$}^h$ respectively. Accordingly, wrench systems of order n formed by zero and infinite pitch wrenches are denoted as n-$\hat{\$}^0$ and n-$\hat{\$}^\infty$. A wrench generator corresponding to the desired motion pattern will be referred to as $\hat{\$}^h_{mp}$.

Serial legs with the expected properties will be composed of serial kinematic subchains, which

include only revolute and prismatic joints. The principle of reciprocity imposes the following geometric conditions on the placement of the revolute and the prismatic joints within the subchains depending on the wrench system to be generated :

***Condition* 1** Each prismatic joint needs to be perpendicular to the direction of $\hat{\$}^0_{mp}$.

***Condition* 2** Each revolute joint axis should be coplanar with the axis of $\hat{\$}^0_{mp}$. This condition can be further refined into (a) Each revolute joint should either intersect the axis of the $\hat{\$}^0_{mp}$ or/and (b) Each revolute joint should be parallel to the axis of $\hat{\$}^0_{mp}$.

***Condition* 3** Each revolute joint should be perpendicular to the direction of the $\hat{\$}^\infty_{mp}$.

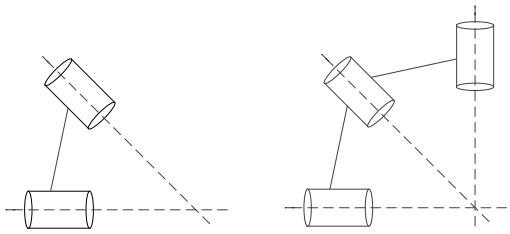

(a) $(RR)_i$. (b) $(RRR)_i$.

Figure 2.2 – Subchains with intersecting axes.

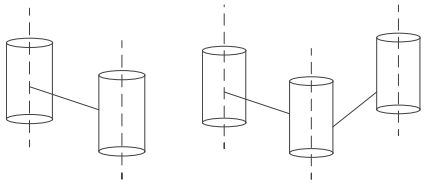

(a) $(RR)_p$. (b) $(RRR)_p$.

Figure 2.3 – Subchains with parallel axes.

As it can be noticed, ***Condition* 1** applies only for prismatic joints whereas ***Condition* 2** and ***Condition* 3** apply for the revolute joints. From ***Condition* 1** , there can be one or at most two prismatic joints which are perpendicular to the axis of $\hat{\$}^0_{mp}$. From ***Condition* 2** (a), two subchains as shown in figure 2.2(a) and 2.2(b), can be identified where either two or three revolute joints are intersecting the axis of $\hat{\$}^0_{mp}$. From ***Condition* 2** (b), two groups as shown in figure 2.3(a) and 2.3(b) can be identified, where either two or three revolute joints are parallel to the axis of $\hat{\$}^0_{mp}$. In figure 2.2(b) and 2.3(b), the three revolute axes are not coplanar.

2.3.1 Wrench system/motion pattern for Task-I

Based on the 2T2R mobility described before, the required twist system for the mechanism is derived to be 2-$\$^0$–2-$\$^\infty$. Hence, the reciprocal wrench system of the mechanism turns out to be 1-$\hat{\$}^0$–1-$\hat{\$}^\infty$ and is generated by two wrenches: i) a zero-pitch wrench $\hat{\$}^0_{mp}$ whose axis coincides with the line $(E, \mathbf{z_b})$ and ii) an infinite-pitch wrench $\hat{\$}^\infty_{mp}$. These two constraint wrenches describe the required motion pattern for the task.

The direction of $\hat{\$}^\infty_{mp}$ need not remain fixed and it can vary with the platform configuration. Two cases can be identified, as shown in figure 2.4(a) and 2.4(b), on the basis of two different motion patterns mp_1 and mp_2 respectively. In Case-1, the wrench $\hat{\$}^\infty_{mp_1}$ is configuration dependent but neither fixed relative to the base nor to the platform. In Case-2, the wrench $\hat{\$}^\infty_{mp_2}$ is also configuration dependent but has a direction always parallel to $\mathbf{z_f}$. In this Case-2, the mechanism prohibits rotation around the needle's axis $\mathbf{z_f}$ in all configurations.

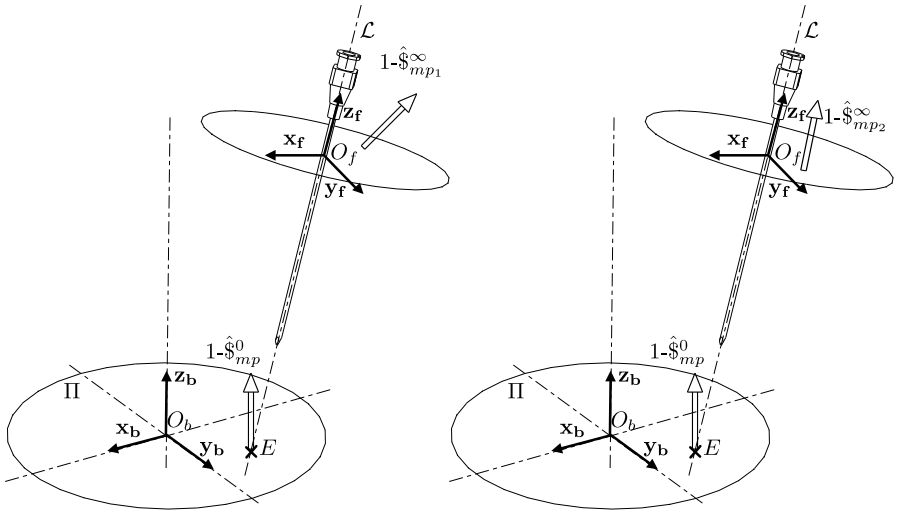

(a) Case-1. (b) Case-2.

Figure 2.4 – Identified wrench systems for Task-I.

As it can be noticed from the above results, two cases have the same mobility with the same DOF partitioning. But still, a clear distinction can be arrived between the two cases by using the concept of motion patterns. As it will be shown in later sections, different mechanism architectures will be synthesized from these two cases.

The generation of the wrench system 1-$\hat{\$}^{0}$–1-$\hat{\$}^{\infty}$ may be either done directly or using the combinations of elementary wrench systems 1-$\hat{\$}^{0}$ and 1-$\hat{\$}^{\infty}$. In the following discussion, the reciprocity of twist and wrench systems is used to synthesize legs providing a desired wrench system taking into account the aforementioned preference rules expressed in section 2.2.1.

2.3.2 Wrench system/motion pattern for Task-II

Based on the 2R mobility required for this reduced task definition, the required twist system for the mechanism is derived to be 2-$\$^{0}$. Hence, the reciprocal wrench system of the mechanism turns out to be 3-$\hat{\$}^{0}$–1-$\hat{\$}^{\infty}$ and is generated by four wrenches: i) three zero-pitch wrench $\hat{\$}^{0}_{mp_3}$ whose axes are coplanar with the line $(E, \mathbf{z_b})$ and ii) an infinite-pitch wrench $\hat{\$}^{\infty}_{mp_3}$. The presence of the RCM point dictates that three constraint wrenches in the system 3-$\hat{\$}^{0}_{mp_3}$ intersect at the entry point E which also serves as the RCM point. These four constraint wrenches, as shown in figure 2.5, describe the required motion pattern for this task. It should be noted that since the two translational DOF are not considered here, the entry point coincides with the origin O_b of the base frame.

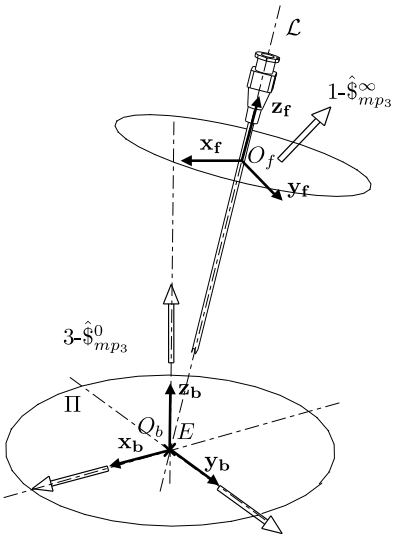

Figure 2.5 – Identified wrench system for Task-II.

2.3.3 Synthesis of legs corresponding to wrench system $1\text{-}\hat{\$}^0$–$1\text{-}\hat{\$}^\infty$

For a non-redundant serial chain with wrench system $1\text{-}\hat{\$}^0$–$1\text{-}\hat{\$}^\infty$, the order of the wrench system is two. Hence, the number of joints amounts to $n_{\text{joints}} = 6-2 = 4$.

Unfortunately, there does not exist a serial chain with four revolute joints, which satisfies simultaneously the ***Condition* 2** and ***Condition* 3** . The only serial chain with wrench system $1\text{-}\hat{\$}^0$–$1\text{-}\hat{\$}^\infty$, corresponding to figure 2.4(a) has two prismatic joints (P-prismatic joint) conforming to ***Condition* 1** , attached to the base and a $(RR)_i$ subchain attached to the platform, as shown in figure 2.6. There does not exist a serial chain with wrench system $1\text{-}\hat{\$}^0$–$1\text{-}\hat{\$}^\infty$ corresponding to figure 2.4(b). Exhaustive enumeration of serial chains with wrench system $1\text{-}\hat{\$}^0$ and $1\text{-}\hat{\$}^\infty$ is not done here as it can be readily found in literature by several authors [Huang et al., 2013; Kong and Gosselin, 2007; Fang and Tsai, 2002]. In the following two sections, serial chains with only revolute joints are considered.

2.3.4 Synthesis of legs corresponding to wrench system $1\text{-}\hat{\$}^0$

Any non-redundant serial chain with this wrench system must have five joints. For a leg with only revolute joints which must satisfy ***Condition* 2** , there exists the following two possibilities, by combining the subchains listed in figure 2.2 and 2.3:

1. $(RRR)_p(RR)_i$
2. $(RR)_p(RRR)_i$

The above mentioned combinations need to satisfy the requirement of the wrench system as well as that of the required mobility. Serial chain number 1 was selected, since it has the simplest geometric conditions on the placement of its joints based on the preference rules set

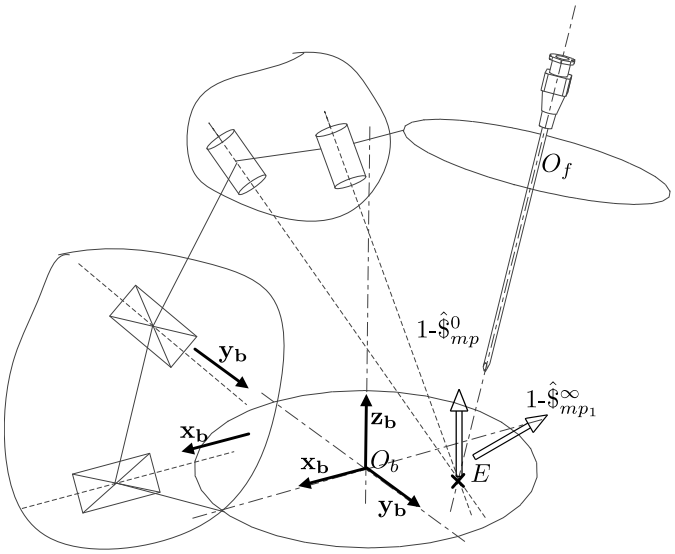

Figure 2.6 – Selected 2P2R chain with wrench system 1-$\hat{\mathbf{\$}}^0$–1-$\hat{\mathbf{\$}}^\infty$.

in section 2.2.1. The resulting serial leg is formed by a $(RRR)_p(RR)_i$ chain.

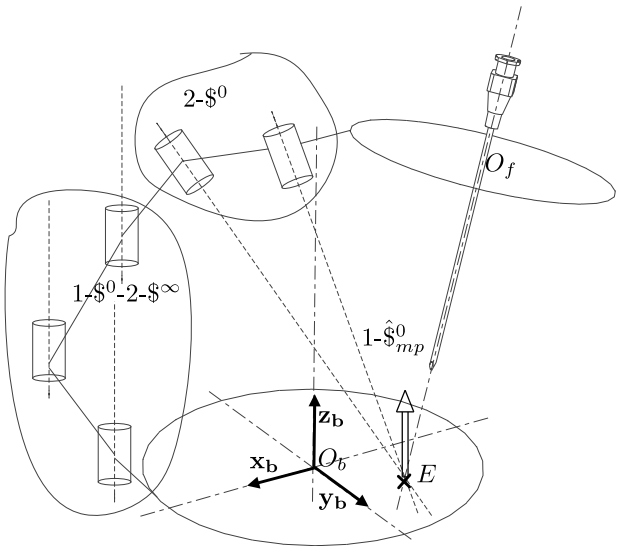

Figure 2.7 – Selected $(RRR)_p(RR)_i$ chain with wrench system 1-$\hat{\mathbf{\$}}^0$.

At this step, it needs to be verified that the selected serial leg also has the correct twist system or the required mobility. When the twist systems 1-$\mathbf{\$}^0$–2-$\mathbf{\$}^\infty$ and 2-$\mathbf{\$}^0$ for the two subchains are combined, as shown in figure 2.7, the desired 3-$\mathbf{\$}^0$–2-$\mathbf{\$}^\infty$ twist system for the serial chain is obtained, provided that the adjacent axes of the two subchains are set skew. Additionally, the order of composition of these revolute joints in the subchains is important for the correct motion pattern and the condition of full-cycle mobility. Hence, the subchains $(RRR)_p$ and $(RR)_i$ need to be attached to the base and to the platform respectively. These subchains respectively ensure that ***Condition* 2** (b) and ***Condition* 2** (a) are met. The resulting chain

prohibits one translational DOF along $\mathbf{z_b}$ and allows for rotations in all three directions.

2.3.5 Synthesis of legs corresponding to wrench system 1-$\hat{\$}^{\infty}$

The synthesis of legs with wrench system 1-$\hat{\$}^{\infty}$ is done to comply with the desired wrench systems $\hat{\$}^{\infty}_{mp_1}$ and $\hat{\$}^{\infty}_{mp_2}$, as depicted in figure 2.4(a) and 2.4(b).

Case-1 – Wrench $\hat{\$}^{\infty}_{mp_1}$

A serial chain with this wrench system has five joints. From ***Condition* 3** , it is known that all the revolute joints need to be perpendicular to the direction of $\hat{\$}^{\infty}_{mp_1}$. There exists only one serial chain with only revolute joints, which satisfies this geometric condition. It consists of two subchains $(RRR)_p$ and $(RR)_p$. Again, the arbitrary permutation of individual revolute joints within the leg is not allowed and only the permutation of the two subchains is permitted. Hence, we can have either $(RRR)_p(RR)_p$ or $(RR)_p(RRR)_p$ as possible placement of revolute joints from base to platform. The former arrangement is shown in figure 2.8.

When the twist systems 1-$\$^0$–2-$\$^{\infty}$ and 1-$\$^0$–1-$\$^{\infty}$ for the two subchains are combined, the desired 2-$\$^0$–3-$\$^{\infty}$ twist system for the serial chain is obtained, provided that the adjacent axes of the two subchains are set skew. The resulting chain prohibits 1-DOF of rotation and allows for translations in three directions.

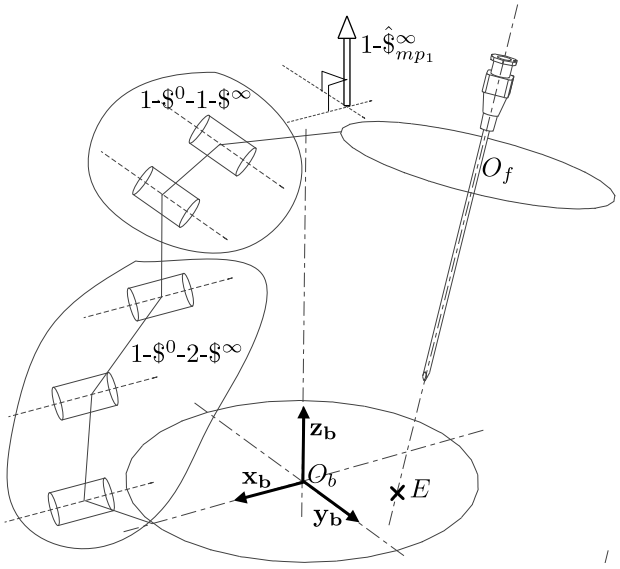

Figure 2.8 – Selected chain with wrench system 1-$\hat{\$}^{\infty}_{mp_1}$.

Case-2 – Wrench $\hat{\$}^{\infty}_{mp_2}$

Generally, mobility specifications are formulated with respect to the fixed reference frame $\mathscr{R}_b$ rather than a moving reference frame. But in Case-2, as shown in figure 2.4(b), the direction

of $\hat{\$}^{\infty}_{mp_2}$ is coincident with vector $\mathbf{z_f}$ which is associated with the frame $\mathscr{R}_f$ attached to the platform. One can note that the type synthesis of parallel mechanisms implicitly assumes that the constraints or motion patterns are defined with respect to a fixed reference frame. For taking into account the fact that the wrench system needs to be defined with respect to the platform frame $\mathscr{R}_f$, the kinematic inversion principle can be utilized during the synthesis process. After performing leg synthesis with respect to a fixed reference $\mathscr{R}_b$, the order of the joints within the leg is reversed from the base to the platform. The resulting leg obtained through kinematic inversion then features the desired wrench system expressed with respect to $\mathscr{R}_f$.

Hence, one has to start with the synthesis of legs with the wrench system 1-$\hat{\$}^{\infty}$ along the direction of $\mathbf{z_b}$ as shown in figure 2.9(b).

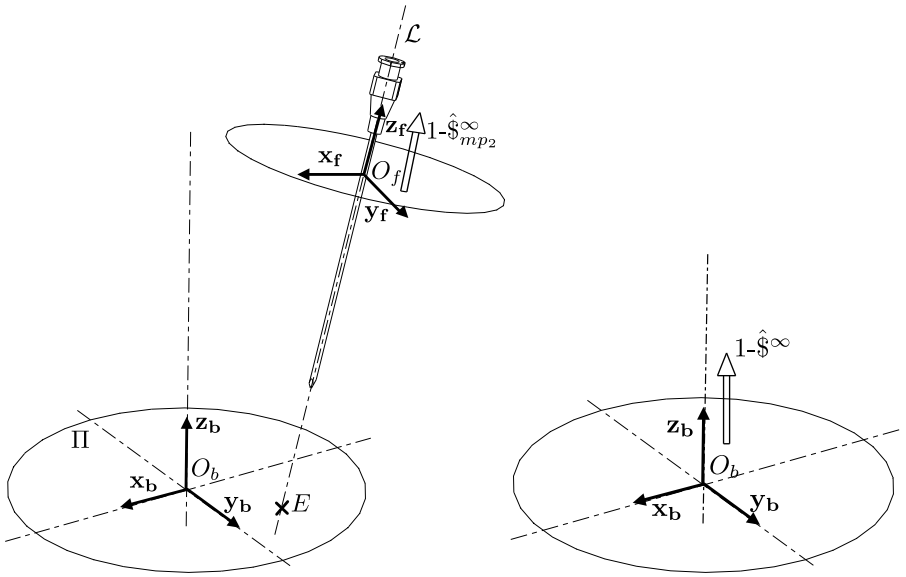

(a) Original–1-$\hat{\$}^{\infty}$. (b) Modified–1-$\hat{\$}^{\infty}$.

Figure 2.9 – Modification of the wrench system 1-$\hat{\$}^{\infty}$.

Considering only revolute and prismatic joints, there exists no open loop serial chain with five joints, which corresponds to the wrench system 1-$\hat{\$}^{\infty}$ with a fixed direction relative to $\mathscr{R}_b$. The legs obtained in Case-1 have the wrench system 1-$\hat{\$}^{\infty}_{mp_1}$ but their direction is fixed neither relative to $\mathscr{R}_b$ nor $\mathscr{R}_f$.

For the synthesis of this leg, the synthesis of serial chains with the wrench system 1-$\hat{\$}^{0}$–1-$\hat{\$}^{\infty}$, as shown in figure 2.10(b), is first described. Such a 4-DOF leg has the desired component 1-$\hat{\$}^{\infty}$ as part of its wrench system. The wrench system 1-$\hat{\$}^{0}$–1-$\hat{\$}^{\infty}$ is equivalent to the linear combination of two wrench systems 1-$\hat{\$}^{0}_{1}$ and 1-$\hat{\$}^{0}_{2}$ with parallel directions, as shown in figure 2.10. The direction of the resulting 1-$\hat{\$}^{\infty}$ wrench system is then perpendicular to the plane formed by the axes of 1-$\hat{\$}^{0}_{1}$ and 1-$\hat{\$}^{0}_{2}$. The synthesis of the serial chain with wrench system 1-$\hat{\$}^{0}$ was earlier done in section 2.3.4, with the only difference that the axis of 1-$\hat{\$}^{0}$ is now parallel to

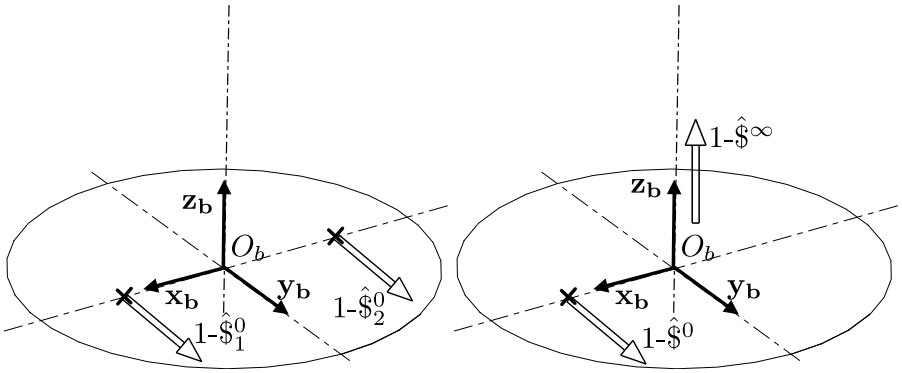

(a) 1-$\hat{\mathbf{\$}}_1^0$–1-$\hat{\mathbf{\$}}_2^0$. (b) 1-$\hat{\mathbf{\$}}^0$–1-$\hat{\mathbf{\$}}^\infty$.

Figure 2.10 – Two equivalent wrench systems 1-$\hat{\mathbf{\$}}_1^0$–1-$\hat{\mathbf{\$}}_2^0$ and 1-$\hat{\mathbf{\$}}^0$–1-$\hat{\mathbf{\$}}^\infty$.

the plane $(O_b, \mathbf{x_b}, \mathbf{y_b})$, as demonstrated in figure 2.10(a).

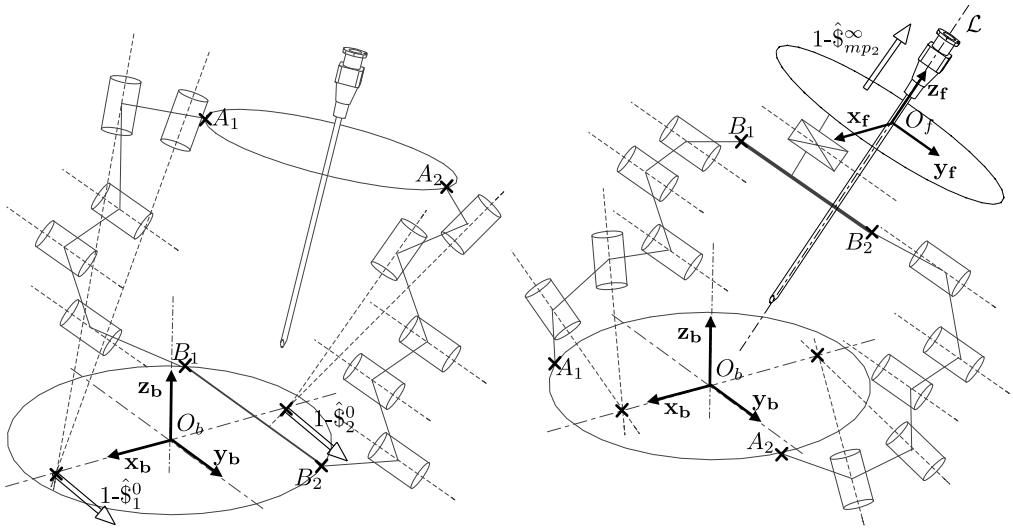

(a) closed kinematic chain. (b) Inverted closed kinematic chain.

Figure 2.11 – Kinematic Inversion.

Thus, a kinematic loop $B_1B_2A_2A_1$ generating a wrench system 1-$\hat{\mathbf{\$}}^0$–1-$\hat{\mathbf{\$}}^\infty$ is obtained, as shown in figure 2.11(a). Finally, the objective is to obtain a leg with a wrench system 1-$\hat{\mathbf{\$}}^\infty$, as shown in figure 2.9(b). In the kinematic loop $B_1B_2A_2A_1$, to remove the constraint wrench 1-$\hat{\mathbf{\$}}^0$, it suffices to add a prismatic joint to the line B_1B_2 with a direction parallel to the axes of 1-$\hat{\mathbf{\$}}_1^0$ and 1-$\hat{\mathbf{\$}}_2^0$. Thus, after the addition of one prismatic joint to the kinematic loop $B_1B_2A_2A_1$, only one constraint wrench remains (that of 1-$\hat{\mathbf{\$}}^\infty$) with a direction parallel to $\mathbf{z_b}$ and defined with respect to $\mathscr{R}_b$.

Thus, a closed loop kinematic chain 2-$(RR)_i(RRR)_p$-P with a wrench system 1-$\hat{\mathbf{\$}}_{mp_2}^\infty$ is ob-

tained, as shown in figure 2.11(b). The wrench system 1-$\hat{\$}^{\infty}_{mp_2}$ has a direction parallel to $\mathbf{z_f}$ and is defined with respect to $\mathscr{R}_f$, as required. To obtain another possibility for the closed loop kinematic chain, it suffices to replace the $(RR)_i(RRR)_p$ chain with $(RRR)_i(RR)_p$, which imposes more stringent geometrical relationships than the former.

2.3.6 Synthesis of legs corresponding to wrench system 3-$\hat{\$}^0$–1-$\hat{\$}^{\infty}$

For a non-redundant serial chain with wrench system 3-$\hat{\$}^0$–1-$\hat{\$}^{\infty}$, the order of the wrench system is four. Hence, the number of joints amounts to $n_{\text{joints}} = 6-4 = 2$. The unique and the simplest serial chain with two revolute joints which satisfies simultaneously the ***Condition* 2** and ***Condition* 3** is the subchain $(RR)_i$ as shown in figure 2.12.

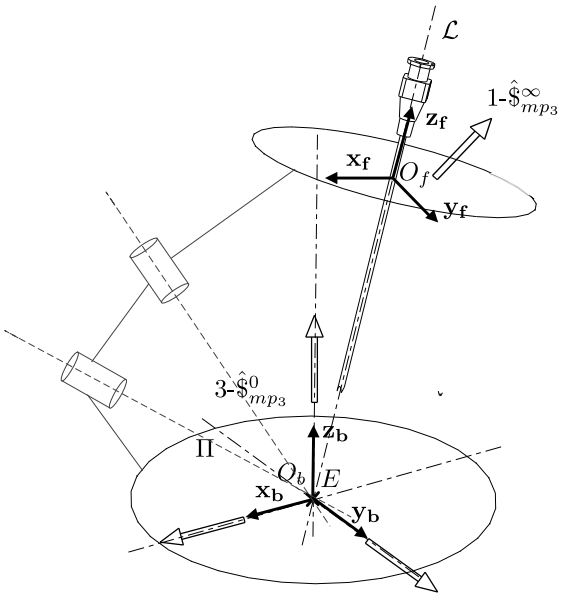

Figure 2.12 – Selected chain with wrench system 3-$\hat{\$}^0_{mp_3}$–1-$\hat{\$}^{\infty}_{mp_3}$.

2.4 Novel 2T2R mechanisms for Task-I

In the previous sections 2.3.3 to 2.3.5, the legs with reduced complexity were obtained for a given constraint wrench taking into account the preference rules set in section 2.2.1. In this section, several candidates are now successively examined with respect to the geometric conditions between legs, the condition of full-cycle mobility and the validity of the selection of the actuated joints.

2.4.1 Architecture candidate I

For a fully parallel and symmetrical mechanism with identical legs, this 2T2R parallel mechanism would consist of four 2P2R legs with wrench system 1-$\hat{\$}^0$–1-$\hat{\$}^\infty$, as depicted in figure 2.6. In this case, the 4-legged 2P2R parallel mechanism has overconstraints owing to the additional three legs.

Geometric conditions between and within the legs

Without loss of generality, within the leg j with $j = 1\ldots4$, one can assume that prismatic joints are parallel to a plane Π. The axes of the two revolute joints of the subchain $(RR)_i$ of leg j intersect each other in E and form the plane Π_j.

Between the legs, group of prismatic joints are parallel to plane Π. This condition ensures that the axes of $\hat{\$}^0_{mp}$ are parallel for all legs. The revolute joints of the subchain $(RR)_i$ in each leg intersect in E, which is common to all legs. This condition ensures that each axis of $\hat{\$}^0_{mp}$ has a common point of origin. To make certain that each leg generates the same $\hat{\$}^\infty_{mp_1}$ wrench system, the planes Π_j need to be parallel in every configuration. As each plane Π_j passes through the point of entry E, they have to be coincident.

Mobility check

A parallel mechanism synthesis conducted using screw theory does not necessarily produce mechanisms with full-cycle mobility, hence this has to be investigated. If all the conditions within and between legs, listed in section 2.4.1 are satisfied in all the configurations, then the parallel mechanism is said to have full-cycle mobility. Unfortunately, the last condition which requires that the planes Π_j be coincident can only be satisfied in one configuration. Hence this 4-2P2R mechanism does not have full-cycle mobility and is not a valid candidate. As the 2P2R chain is the only possible leg choice with the 1-$\hat{\$}^0$–1-$\hat{\$}^\infty$ wrench system, a fully parallel mechanism with identical legs can not be obtained.

2.4.2 Architecture candidate II

As it could be concluded that the synthesis of 2T2R parallel mechanisms with identical legs is not possible, legs derived from elementary wrench systems are used to synthesize the 2T2R parallel mechanisms with different legs. In the above scenario, as a compromise between the rigidity and workspace, the number of overconstraints n_{oc} is chosen to be equal to one.

For a non-overconstrained mechanism, there would be only two legs, each corresponding to the elementary wrench systems 1-$\hat{\$}^0$ and 1-$\hat{\$}^\infty$. With one overconstraint, the number of legs rises to three and the supplementary leg has to be chosen with a 1-$\hat{\$}^0$ or 1-$\hat{\$}^\infty$ wrench system. The wrench system of this second candidate corresponds to the one depicted in figure 2.4(a).

As it can be observed from figure 2.13, the chain A_1B_1 is a $(RRR)_p(RR)_i$ leg which has the wrench system 1-$\hat{\$}^0$. The chains A_2B_2 and A_3B_3 are the $(RRR)_p(RR)_p$ legs which have the wrench system 1-$\hat{\$}^\infty$ corresponding to figure 2.4(a). With regard to the geometric analyses to come, the successive axes in the legs 1,2 and 3 will be referred to as e_{ik}, where $k = 1\ldots3$ indicates the leg number and $i = 1\ldots5$ is for the five revolute joints from the base to the platform. If the axes e_{ik} and e_{jk} form a plane, it would be referred by Π_{ijk}. The same nomenclature will be applied as well for the next mechanism candidates.

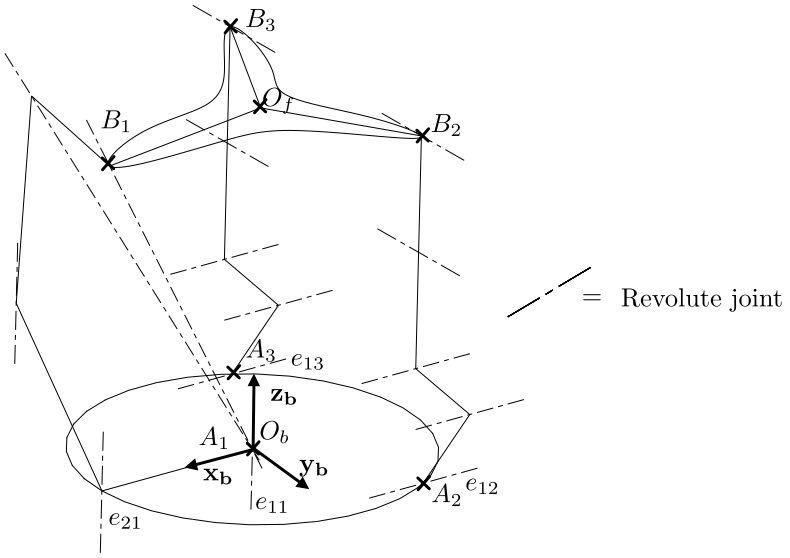

Figure 2.13 – 2T2R–Candidate II.

Geometric conditions between and within the legs

This mechanism candidate has one leg with the wrench system 1-$\hat{\$}^0$ and two legs with the wrench system 1-$\hat{\$}^\infty$. Hence the overconstraint is that of the supplementary wrench system 1-$\hat{\$}^\infty$.

For the leg $(RRR)_p(RR)_i$, the axes of the revolute joints within the subchain $(RRR)_p$ are parallel to the vector $\mathbf{z_b}$ whereas those within the subchain $(RR)_i$ intersect in E.

For the legs $(RRR)_p(RR)_p$, the axes of the revolute joints within the subchain $(RRR)_p$ are parallel to vector $\mathbf{x_b}$ whereas those within the subchain $(RR)_p$ are parallel to each other. Between the two $(RRR)_p(RR)_p$ legs, the subchains $(RRR)_p$ have axes parallel to each other and similarly, the subchains $(RR)_p$ of the two legs have axes parallel to each other.

Mobility check

All the above conditions within and between legs are satisfied in all configurations, hence the parallel mechanism with a 1-$(RRR)_p(RR)_i$–2-$(RRR)_p(RR)_p$ architecture has a full-cycle 2T2R

mobility.

Choice of the inputs

As four inputs are needed to control this 2T2R parallel mechanism and this candidate has three legs, one of the legs needs to be assigned two inputs. One input is assigned to each $(RRR)_p(RR)_p$ leg and is located at the first revolute joint, namely e_{12}, e_{13} connected to the base whereas the other two inputs are assigned to the $(RRR)_p(RR)_i$ leg and are located at the first two joints starting from the base, namely e_{11}, e_{21}. This choice of the inputs needs to be validated to ascertain whether the applied actuation wrenches lock every DOF in a general configuration.

A formulation of unique form of screw based Jacobian for lower mobility parallel manipulators is given in [Hong and Choi, 2010] but the proposed form of the Jacobian matrix includes only the actuation wrenches and not the constraint wrenches. Hence, the alternate form of direct Jacobian matrix described in [Huang et al., 2011a] is utilized, which includes the constraint wrenches. The validation of the actuated joints is conducted by analyzing the full direct Jacobian $\mathbf{J}_{\mathbf{x}\mathrm{II}}$ of the mechanism candidate II, which can be obtained by stacking the four actuation wrenches $\hat{\$}_{i,a}$ and the two constraint wrenches $\hat{\$}_{j,c}$ of the parallel mechanism. The four actuation wrenches can be expressed as $\hat{\$}_{i,a} = \begin{bmatrix} \mathbf{s_i} & \mathbf{s_i} \times \mathbf{r_i} \end{bmatrix}^T$ where, $\mathbf{s_i}$ denotes the direction of the actuation wrench and $\mathbf{r_i}$ is the position vector directed from a point of the wrench axis to the origin O_b. The two constraint wrenches $\hat{\$}_{j,c}$ produced by the mechanism have the form $\hat{\$}_{1,c} = \begin{bmatrix} \mathbf{z_b} & \mathbf{z_b} \times \mathbf{EO_b} \end{bmatrix}^T$ and $\hat{\$}_{2,c} = \begin{bmatrix} \mathbf{0} & \mathbf{m_1} \end{bmatrix}^T$ where $\mathbf{m_1}$ is the direction of the wrench system 1-$\hat{\$}^{\infty}_{mp_1}$. Therefore the vectorial Jacobian of the parallel mechanism can be displayed as :

$$\mathbf{J}_{\mathbf{x}\mathrm{II}} = \begin{bmatrix} \mathbf{s_1} \times \mathbf{r_1} & \mathbf{s_1} \\ \mathbf{s_2} \times \mathbf{r_2} & \mathbf{s_2} \\ \mathbf{s_3} \times \mathbf{r_3} & \mathbf{s_3} \\ \mathbf{s_4} \times \mathbf{r_4} & \mathbf{s_4} \\ \mathbf{z_b} \times \mathbf{EO_b} & \mathbf{z_b} \\ \mathbf{m_1} & \mathbf{0} \end{bmatrix}.$$

It can be noticed that each row of this Jacobian is the transpose of the actuation and constraint wrenches written in axis coordinates. The choice of the selected inputs is invalid if the matrix $\mathbf{J}_{\mathbf{x}\mathrm{II}}$ is singular in all configurations. Actuated joints e_{11}, e_{21}, e_{12}, e_{13} are shown in figure 2.13.

With the notations defined before section 2.4.2, a geometric interpretation of the actuation wrench system 4-$\hat{\$}_a$ can be obtained. The actuation wrenches $\hat{\$}_{1,a}$ and $\hat{\$}_{2,a}$ are each defined by the intersection of the planes taken in the pairs (Π_{231}, Π_{451}) and (Π_{131}, Π_{451}). Thus, it can be concluded that $\hat{\$}_{1,a}$ and $\hat{\$}_{2,a}$ both lie on the plane Π_{451} and hence must intersect each other if not parallel to each other. Thus $\hat{\$}_{1,a}$–$\hat{\$}_{2,a}$ forms a planar pencil of lines. Similarly,

actuation wrenches $\hat{\$}_{3,a}$ and $\hat{\$}_{4,a}$ are defined respectively by the intersection of the planes in the pairs (Π_{232}, Π_{452}) and (Π_{233}, Π_{453}). For simplicity it is assumed that each axes pair (e_{41}, e_{42}) and (e_{51}, e_{52}) contains coincident axes. This assumption makes Π_{452} and Π_{453} coincident. Following this, it can be concluded that $\hat{\$}_{3,a}$–$\hat{\$}_{4,a}$ lies on the same plane and hence form a planar pencil of lines. The constraint wrench $\hat{\$}_{1,c}$ is a line passing through E and parallel to $\mathbf{z_b}$. The constraint wrench $\hat{\$}_{2,c}$ is a line orthogonal to the axes quintuple $(e_{12}, e_{22}, e_{32}, e_{42}, e_{52})$.

From the above discussion, the following three geometric conditions can be derived when the variety formed by 4–$\hat{\$}_a$ and 2–$\hat{\$}_c$ degenerates :

1. The wrenches $\hat{\$}_{1,a}$ and $\hat{\$}_{2,a}$ become coincident. This condition occurs, whenever planes (Π_{131}, Π_{231}) become coincident. This condition occurs at the boundary of the workspace.

2. The wrenches $\hat{\$}_{3,a}$ and $\hat{\$}_{4,a}$ become coincident. This condition occurs, whenever planes (Π_{232}, Π_{233}) become coincident. This condition occurs inside the workspace of the mechanism.

As the matrix $\mathbf{J}_{\mathbf{x}\mathrm{II}}$ is not singular for every possible configuration of the platform, the choice of the inputs is valid.

2.4.3 Architecture candidate III

For the synthesis of parallel mechanism with mobility corresponding to figure 2.4(b), the number of overconstraints n_{oc} is chosen to be zero. Hence, $n_{\mathrm{legs}} = 2 + n_{\mathrm{oc}}$ equals two. The first leg corresponding to the wrench system 1-$\hat{\$}^0$ is the same as the one chosen for candidate II. For the second leg with 1-$\hat{\$}^\infty$ Case–2, a closed loop kinematic chain with two points of attachment at the base, as shown in figure 2.11(b), is chosen. To comply with the nomenclature defined before section 2.4.2, this closed loop kinematic chain can be considered as consisting of two legs connecting the platform at the prismatic joint. Thus, the architecture 1-$(RRR)_p(RR)_i$–2-$(RR)_i(RRR)_p$-P is obtained as a parallel mechanism candidate with a wrench system corresponding to figure 2.4(b). A wire model of this candidate III is shown in figure 2.14.

Geometric conditions between and within the legs

For the first leg $(RRR)_p(RR)_i$, the axes of the revolute joints within the subchain $(RRR)_p$ are parallel to vector $\mathbf{z_b}$, whereas the axes of the revolute joints within the subchain $(RR)_i$ intersect in E, which in the reference configuration shown in figure 2.14, coincides with O_b.

Within the second 2-$(RR)_i(RRR)_p$-P leg, which consists of the closed kinematic chain $A_2A_3B_3B_2$, the axes of the revolute joints within the subchains $(RRR)_p$ are parallel to each other and to $\mathbf{y_f}$. The axes of the revolute joints within the subchains $(RR)_i$ intersect at points P_2 and P_3, which lie on the axis $(O_b, \mathbf{x_b})$. The direction of the prismatic joint is parallel to the axes of the revolute joints in the subchains $(RRR)_p$ and to $\mathbf{y_f}$.

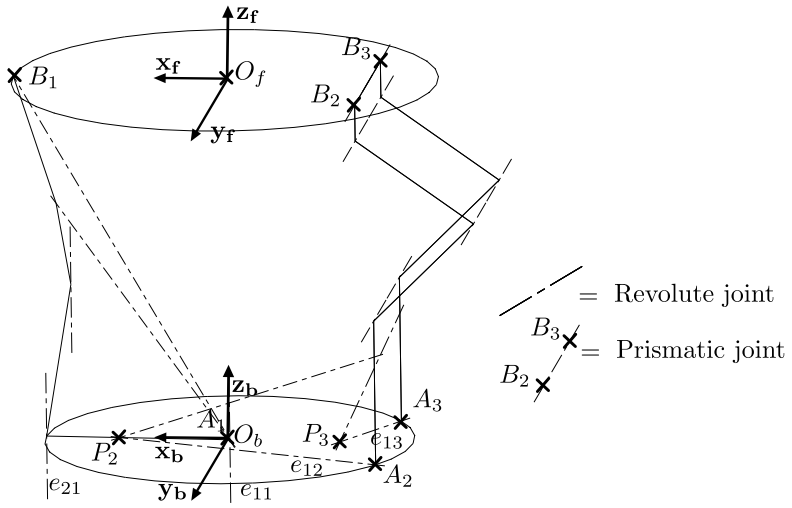

Figure 2.14 – 2T2R–Candidate III.

Mobility check

All the above conditions within and between legs are satisfied in all configurations, hence the architecture 1-$(RRR)_p(RR)_i$–2-$(RR)_i(RRR)_p$-P as 2T2R parallel mechanism has a full-cycle mobility.

Choice of the inputs

As with candidate II, four inputs are needed to control this 2T2R parallel mechanism. This candidate has two legs, with two inputs assigned to each. The $(RRR)_p(RR)_i$ leg is assigned two inputs to the first two revolute joints from the base. The chain 2-$(RR)_i(RRR)_p$-P is assigned two inputs to the two revolute joints attached to the base. The actuated joints e_{11}, e_{21},e_{12} and e_{13} are shown in figure 2.14. The full direct Jacobian matrix $\mathbf{J}_{\mathbf{x}\mathrm{III}}$ for this candidate is displayed below :

$$\mathbf{J}_{\mathbf{x}\mathrm{III}} = \begin{bmatrix} \mathbf{s_1} \times \mathbf{r_1} & \mathbf{s_1} \\ \mathbf{s_2} \times \mathbf{r_2} & \mathbf{s_2} \\ \mathbf{m_1} & \mathbf{0} \\ \mathbf{m_2} & \mathbf{0} \\ \mathbf{z_b} \times \mathbf{EO_b} & \mathbf{z_b} \\ \mathbf{z_f} & \mathbf{0} \end{bmatrix}$$

As before, the first four rows of $\mathbf{J}_{\mathbf{x}\mathrm{III}}$ correspond to the four actuation wrenches $\hat{\mathbf{\$}}_{i,a}$ with $i = 1\ldots4$ and the last two rows correspond to the two constraint wrenches $\hat{\mathbf{\$}}_{i,c}$ with $i = 1\ldots2$.

Let the axis of the prismatic joint be denoted by e_6. In addition, let the planes orthogonal to the axes e_{22} and e_{23} be denoted by π_1 and π_2 respectively and the planes orthogonal to the

axes sets $\{e_{32}, e_{42}, e_{52}\}$ and $\{e_{33}, e_{43}, e_{53}\}$ be denoted by π_3 and π_4 respectively. The planes π_3 and π_4 are perpendicular to $\mathbf{y_f}$ and hence also parallel to each other.

With this notation, a geometric interpretation of the actuation wrench system 4-$\hat{\mathbf{\$}}_a$ can be obtained. The description of the actuation wrenches $\hat{\mathbf{\$}}_{1,a}$ and $\hat{\mathbf{\$}}_{2,a}$ is same as for the candidate II, as one leg is common to all the candidates. The axes of the actuation wrenches $\hat{\mathbf{\$}}_{3,a}$ and $\hat{\mathbf{\$}}_{4,a}$ are the intersection of the plane couples (π_1, π_3) and (π_2, π_4), respectively. As the sets of axes $\{e_{32}, e_{42}, e_{52}\}$ and $\{e_{33}, e_{43}, e_{53}\}$ are parallel to each other, the planes π_3 and π_4 are also parallel to each other.

The axis of the constraint $\hat{\mathbf{\$}}_{1,c}$ is a line passing through E and parallel to $\mathbf{z_b}$, whereas the axis of $\hat{\mathbf{\$}}_{2,c}$ is a line parallel to $\mathbf{z_f}$ and hence also parallel to π_3 and π_4. Finally, the axes of $\hat{\mathbf{\$}}_{3,a}$, $\hat{\mathbf{\$}}_{4,a}$ and $\hat{\mathbf{\$}}_{2,c}$ are all parallel to the planes π_3 and π_4, hence are linearly dependent in all configurations. Thus, the matrix $\mathbf{J}_{\mathbf{x}\mathrm{III}}$ is singular in all configurations. Hence, the choice of inputs for the actuated joints is not valid for this architecture candidate.

2.4.4 Architecture candidate IV

As the choice of the inputs for the candidate III could not be validated, a second variant architecture candidate corresponding to the constraint wrench system shown in figure 2.4(b) is now proposed. This architecture is derived from candidate III in which the two subchains $(RR)_i(RRR)_p$ in the loop $A_2A_3B_3B_2$ have been replaced by two subchains $(RRR)_i(RR)_p$ of higher complexity. These two subchains $(RR)_i(RRR)_p$ and $(RRR)_i(RR)_p$ are interchangeable as mentioned at the end of the section 2.3.5, since both have the same 1-$\hat{\mathbf{\$}}^0$ wrench system. The number of overconstraints n_{oc} is zero which is same as for candidate III. A similar nomenclature applies as for the candidate III and a wire model of this candidate IV is shown in figure 2.15.

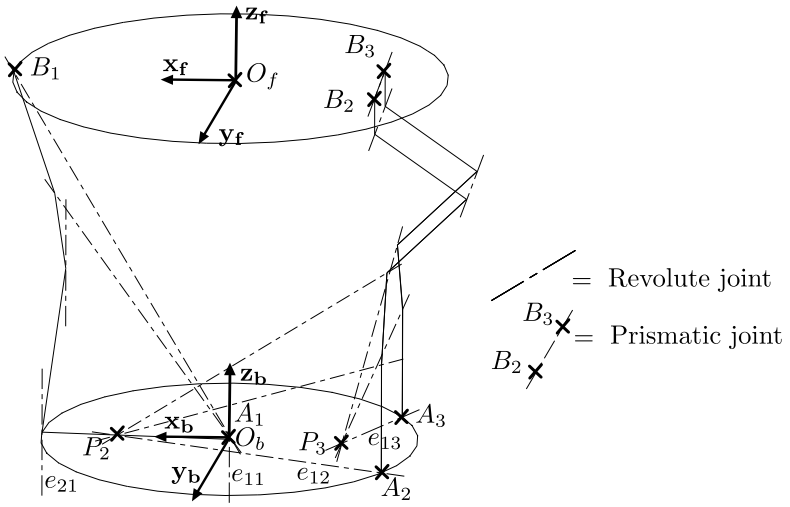

Figure 2.15 – 2T2R–Candidate IV.

Geometric conditions between and within the legs

The geometric conditions for the leg $(RRR)_p(RR)_i$ are similar to those of candidate III. Within the second 2-$(RRR)_i(RR)_p$-P leg which consists of the closed kinematic chain $A_2A_3B_3B_2$, the axes of the revolute joints within the subchains $(RR)_p$ are parallel to $\mathbf{y_f}$, whereas the axes of the revolute joints within the subchains $(RRR)_i$ intersect at P_2 and P_3. These latter points lie on the axis $(O_b, \mathbf{x_b})$. The direction of the prismatic joint is parallel to the axis of the revolute joints in the subchains $(RR)_p$ and to the vector $\mathbf{y_f}$.

Mobility check

All the above conditions within and between legs are satisfied in all configurations. Hence, the architecture candidate 1-$(RRR)_p(RR)_i$–2-$(RRR)_i(RR)_p - P$ as a 2T2R parallel mechanism has a full-cycle mobility.

Choice of the inputs

As with previous candidates, four inputs are needed to control this 2T2R parallel mechanism. The inputs assignment is similar to that of the candidate III leading to the four actuated joints e_{11}, e_{21}, e_{12} and e_{13}, as displayed in figure 2.15. The full direct Jacobian matrix $\mathbf{J}_{\mathbf{x}\mathrm{IV}}$ for this candidate is given below :

$$\mathbf{J}_{\mathbf{x}\mathrm{IV}} = \begin{bmatrix} \mathbf{s_1} \times \mathbf{r_1} & \mathbf{s_1} \\ \mathbf{s_2} \times \mathbf{r_2} & \mathbf{s_2} \\ \mathbf{s_3} \times \mathbf{r_3} & \mathbf{s_3} \\ \mathbf{s_4} \times \mathbf{r_4} & \mathbf{s_4} \\ \mathbf{z_b} \times \mathbf{EO_b} & \mathbf{z_b} \\ \mathbf{z_f} & \mathbf{0} \end{bmatrix}$$

where the actuation wrenches $\hat{\mathbf{\$}}_{1,a}$ and $\hat{\mathbf{\$}}_{2,a}$ are defined similarly to candidate II. However, the derivation of the actuation wrenches $\hat{\mathbf{\$}}_{3,a}$ and $\hat{\mathbf{\$}}_{4,a}$ is not straightforward as in previous cases.

Let us define two intermediate wrenches $\hat{\mathbf{\$}}^*_{3,a}$ and $\hat{\mathbf{\$}}^*_{4,a}$ whose axes are respectively the intersection of the plane couples (Π_{232}, Π_{452}) and (Π_{233}, Π_{453}). As it can be readily seen, the wrenches $\hat{\mathbf{\$}}^*_{3,a}$ and $\hat{\mathbf{\$}}^*_{4,a}$ are not reciprocal to the twist $\mathbf{\$}^\infty_6$ associated with the prismatic joint which has a direction parallel to $\mathbf{y_f}$.

Below, the expressions for $\hat{\mathbf{\$}}_{3,a}$ and $\hat{\mathbf{\$}}_{4,a}$ are given without any developed proof but it is easy to verify that these two actuation wrenches are reciprocal to $\mathbf{\$}^\infty_6$:

$$\hat{\mathbf{\$}}_{3,a} = \hat{\mathbf{\$}}^*_{3,a} - (\hat{\mathbf{\$}}^*_{3,a} \cdot \mathbf{\$}^\infty_6)\, \hat{\mathbf{\$}}^*_{1,c}$$
$$\hat{\mathbf{\$}}_{4,a} = \hat{\mathbf{\$}}^*_{4,a} - (\hat{\mathbf{\$}}^*_{4,a} \cdot \mathbf{\$}^\infty_6)\, \hat{\mathbf{\$}}^*_{2,c}$$

where $\hat{\$}^*_{1,c}$ and $\hat{\$}^*_{2,c}$ are the lines passing through P_2 and P_3 respectively and parallel to the vector $\mathbf{y_f}$. The axes of $\hat{\$}_{3,a}$ and $\hat{\$}_{4,a}$ are both orthogonal to $\mathbf{y_f}$ and parallel to the planes Π_{452} and Π_{453}, respectively. From the above discussion, the following geometric conditions leading to the degeneracy of the variety formed by the wrench systems 4–$\hat{\$}_a$ and 2–$\hat{\$}_c$ can be formulated :

1. The planes (Π_{131}, Π_{231}) become coincident. In such a case, wrenches $\hat{\$}_{1,a}$ and $\hat{\$}_{2,a}$ become coincident. This condition is same as for the candidate II.

2. The planes Π_{452} and Π_{453} are coincident and parallel to the plane formed by $\mathbf{x_f}$ and $\mathbf{y_f}$. In this case, $\hat{\$}_{3,a}$ and $\hat{\$}_{4,a}$ constitute a 2-system which includes a moment with a direction parallel to $\mathbf{z_f}$. Hence, the variety formed by $\hat{\$}_{3,a}$, $\hat{\$}_{4,a}$ and $\hat{\$}_{2,c}$ degenerates to a 2-system.

As the matrix $\mathbf{J}_{\mathbf{x}\mathrm{IV}}$ is not singular for every possible configuration of the platform, the choice of the inputs is valid for 1-$(RRR)_p(RR)_i$–2-$(RRR)_i(RR)_p$-P as 2T2R parallel mechanism.

Candidate	I	II	III	IV
Motion Pattern	mp_1	mp_1	mp_2	mp_2
Full-cycle mobility	No	Yes	Yes	Yes
Choice of actuation valid	–	Yes	No	Yes

Table 2.1 – Summary of candidate mechanisms.

From the above discussion on the four architecture candidates and from table 2.1, it could be inferred that the candidates II and IV are feasible candidates as they satisfy the essential criteria of full-cycle mobility and validity of the selection of the actuated joints. This concludes the part on synthesis of the 2T2R mechanisms for the task of needle positioning.

2.5 2R mechanisms for Task-II

The interest of the 2R mechanisms for the needle orientation is due to its simplicity especially if a serial architecture is considered. They potentially can be much lighter, occupy less volume and have less demanding constraints in terms of number of actuators and input actuation torques. However, the serial architecture can be modified to include different realizations of the revolute joint in 2R serial chain, in order to address issues of placement of actuators and the RCM point. If the entry point on the skin can be decided and targeted using external features from the imaging device and is not altered after the robot mounting, the requirement for 2-DOF in translation for the needle positioning can be removed.

2.5.1 Different realizations of the 2R mechanism candidate

Even though there is a unique leg shown in figure 2.12 corresponding to the 2R mobility, still different realizations of this leg can be discussed. A 2-DOF mechanism for the orientation of the needle axis must include a RCM point so as to kinematically constrain the mechanism

rotation around the entry point on the skin. Such a mechanism with two revolute joints has only one geometric condition that the axes must intersect in the RCM point. A revolute joint can also be implemented by two hollow discs rotating against each other about their common axis. This realization of the revolute joint does not require a physical revolute joint at the center thus allowing empty space for the needle to pass through. Two such realizations of the revolute joint can be combined serially to produce the required spherical motion if their axes are made to intersect at one point. The double ring RCM mechanism for robotic needle guidance [Song et al., 2013b] makes use of such realization for needle orientation in MRI-guided liver interventions.

There also exist 1-DOF parallelogram based RCM mechanisms combined in series with a revolute joint to realize the desired 2-DOF RCM mechanisms for the Task-II. The implementation of this type of mechanisms for needle positioning procedures can be found in the literature. In the work of [Waspe et al., 2006], a 1-DOF RCM parallelogram based mechanism in series with an intersecting revolute joint (figure 2.16(a)) is used for constructing a robotic needle positioning system for small animal imaging applications. Similar kinematics and mechanism can be found in the work of [Cole et al., 2009]. In this work the mechanism (figure 2.16(b)) was designed for MRI-guided deep brain stimulation electrode placement. The interest for such realizations is to address the issue of placement of actuators, as will be described in detail in the next section. Moreover, with such realizations it is still possible to achieve large orientation ranges for needle axis orientation.

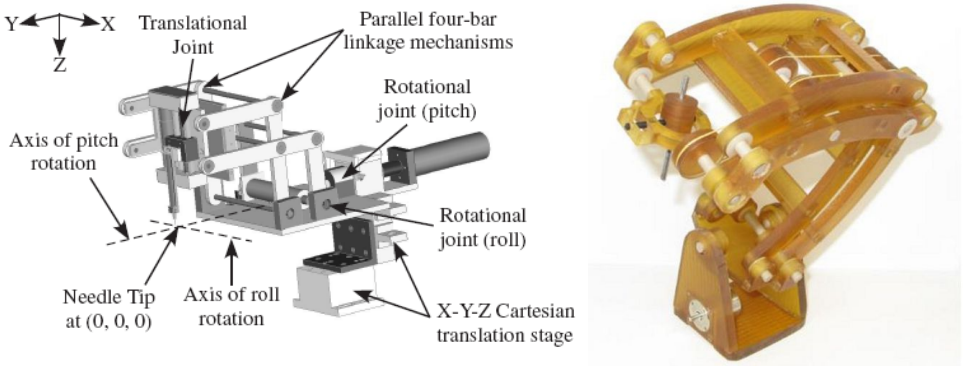

(a) [Waspe et al., 2006]. (b) [Cole et al., 2009].

Figure 2.16 – Implementation of the 2R RCM with parallelogram based 1-DOF RCM mechanism.

In our laboratory, there has been previous work of two master students in the past [Roch, 2009; Hoffman, 2010] which focussed on a compliant adaptation of the above parallelogram based RCM mechanism (figure 2.17) for the task of needle axis orientation. The first revolute joint was realized using two hollow circular discs rotating against each other about their common axis. This realization is beneficial with respect to stiffness and stability as the ground support is a circular disc. Compliant version was then preferred to ease the assembly and provide more accurate needle positioning by removing the joint backlash. However due to compliant revolute joints, the orientation range was quite limited.

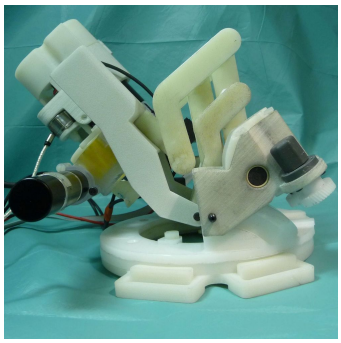

Figure 2.17 – 2R RCM with compliant joints.

2.5.2 Synthesis of 1-DOF parallelogram based RCM mechanism

The 2R RCM mechanisms in general can be constructed out of two 1-DOF RCM mechanisms. As the two revolute joints in these 2R mechanisms need to be actuated, it could be beneficial for placement of actuators to have the RCM point situated at a distance from the actuated revolute joint axes. This deferred placement of the RCM point can be achieved by a simple four bar parallelogram mechanism. Though with such a simple mechanism one can obtain a deferred placement of RCM point and actuator placement, there is still a need for a physical revolute joint to be present at the RCM point. Ideally one would avoid a physical revolute joint at RCM point, as the needle has to pass through this point. This calls for the synthesis of 1-DOF RCM mechanisms where one can obtain a RCM point for the mechanism without a physical revolute joint passing through it.

A systematic synthesis approach for such 1-DOF RCM mechanisms was formulated in the work of [Zong et al., 2008]. We will utilize the proposed concept and the results presented in this paper to arrive at such a mechanism for our application. Zong defines the concept of virtual center (VC) mechanisms, virtual center of motion (VCM) and remote center of motion (RCM) mechanisms. The VC mechanisms possess at least a point which can rotate about a fixed point whereas for a VCM mechanism there is at least a link or collection of points which rotate about a fixed point. The RCM mechanisms are defined as having a fixed center of rotation which is distant from the mechanism. The RCM mechanisms are a subset of VCM mechanisms, where the center of rotation can be anywhere, inside or outside of the mechanism. The figure 2.18 shows a parallelogram VC mechanism which is perhaps the simplest VC mechanism, an extension of the simple four bar parallelogram mechanism. Here it can be seen that there is one point J on the mechanism which undergoes circular motion around the point E.

A theorem is proposed in the work of Zong for combining two or more VC mechanisms in order to obtain VCM or RCM mechanisms. The theorem states that:

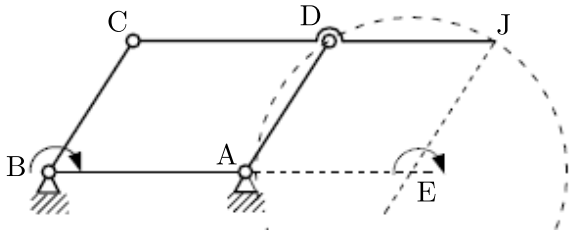

Figure 2.18 – Parallelogram VC mechanism, adapted from [Zong et al., 2008].

"*If any two distinct points in a rigid body can move along the concentric circles, and the two points are not collinear with the center, then the rigid body must accomplish a circular motion whose center is coincident with that of the concentric circle.*".

The application of this theorem is shown in figure 2.19, where a 1-DOF RCM mechanism is synthesized by combining two VC mechanisms. An arrangement of two VC mechanisms which is referred to as *serial-parallel* by Zong has been employed to arrive at parallelogram based RCM mechanisms. In the *serial-parallel* arrangement, the driving links and other parts of the two VC mechanisms need to coincide apart from the usual condition of center of rotation of two VC mechanisms being coincident. Thereafter a link is established between the points H and J of the two VC mechanisms which are undergoing circular motion around the common center of rotation E. The obtained mechanism is equivalent to the single four bar

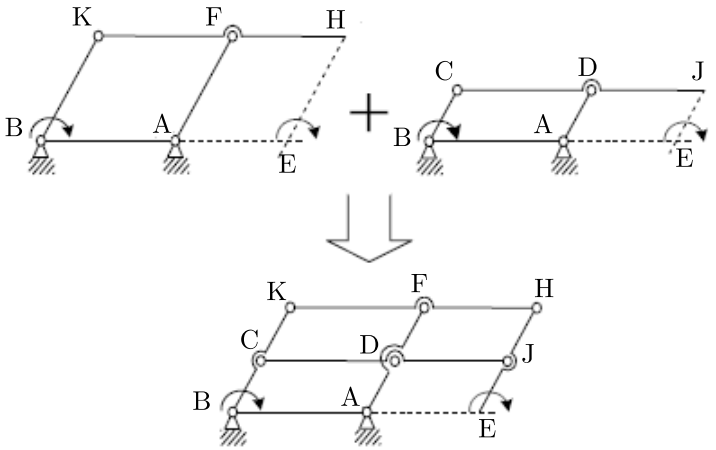

Figure 2.19 – Synthesis of 1-DOF RCM mechanisms by combination of two VC mechanisms, adapted from [Zong et al., 2008].

EADJ mechanism with a virtual revolute join at the point E. Thus a deferred placement of the RCM point without having a physical revolute joint at E is achieved. Also this mechanism can have much larger ranges of circular motion which is only hindered by the link interferences and the parallel singularity of the parallelogram mechanism EADJ. The mechanism synthesized

is over-constrained owing to the extra links. Other variants of this mechanism are shown in

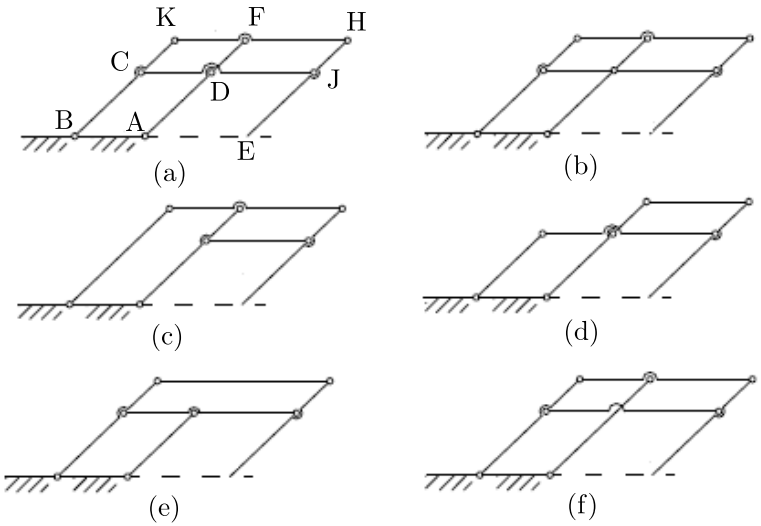

Figure 2.20 – 1-DOF parallelogram based RCM mechanisms, adapted from [Zong et al., 2008].

figure 2.20 (b)-(f) which are obtained by removing these over-constraints. All of these variants also allow for actuated revolute joint here A or B near the base to be at an finite distance from the RCM point E.

2.5.3 2R mechanism candidate

For the current ProteCT project, the candidate mechanism for the Task-II is chosen as consisting of two hollow circular discs rotating against each other about their common axis as the implementation of the first R joint and a 1-DOF parallelogram based RCM mechanism with regular revolute joints as the second R joint. For the parallelogram based 1-DOF RCM mechanism, the variant shown in figure 2.20(d) has been chosen due to its compactness compared to other variants. The schematics of the candidate mechanism for Task-II can be seen in figure 2.21. The continuous red and blue lines represent a link. It should be clarified here that the links FD, DA do not rotate about the point D as they are part of the single link FDA. Similarly, the links CD and DJ do not rotate about the point D as they are part of the single link CDJ. The first revolute joint is shown in blue at the center which has axis along $\mathbf{z_1}$ coincident with $\mathbf{z_b}$. Let e_i with $i = 1 \cdots 7$ represent the axes of the revolute joints of the parallelogram mechanism. This 1-DOF parallelogram based RCM mechanism is equivalent to the virtual revolute joint in red whose axis is along $\mathbf{z_2}$ passing through the center O_b.

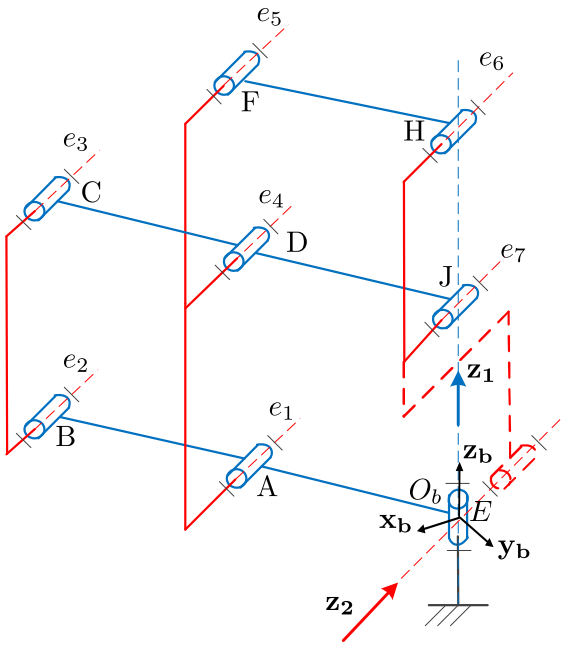

Figure 2.21 – 2R mechanism candidate for Task-II.

Geometric conditions within the leg

This is a hybrid architecture with a revolute joint in series with the parallelogram based 1-DOF RCM mechanism. So geometric conditions within this leg are more complex than that of a pure serial 2R chain. Axis of the virtual revolute joint, which is along $\mathbf{z_2}$, is determined by the intersection of planes formed by the axes couple (e_1, e_2) and (e_6, e_7). Axis of the first revolute joint and the second virtual joint of the 2R mechanism candidate must intersect in the point O_b which is the desired RCM point for the mechanism. $ABCD$, $JDFH$ and O_bADJ must form three parallelograms. The parallelogram based RCM mechanism is equivalent to the single four bar O_bADJ mechanism.

Choice of the inputs

As this mechanism has 2-DOF, two actuators must be placed to control it. The first actuator is placed at the first revolute joint. As the placement of actuator is preferred near the base of the mechanism for minimizing the inertia of moving parts, there are two choices for the placement of the second actuator. It can be placed either at the revolute joint A or at the revolute joint B. As the revolute joint at point B is further away from the insertion point E, it is selected for placement of the second actuator.

2.6 Summary

This chapter was devoted to the synthesis of candidate mechanisms and obtaining feasible candidates for the task of needle positioning and the task of needle orientation. A generic task-based procedure for the synthesis of parallel mechanisms was presented and illustrated with the task of needle positioning. While stressing on the importance of the architecture kinematic complexity, a systematic methodology based on screw theory was demonstrated for the inclusion of preference rules at an early stage of the design process. Two different novel motion patterns, corresponding to 2T2R mobility, were derived for the first time and consequently, two entirely different parallel mechanisms having the same mobility were synthesized. As the 2T2R candidate II has lower complexity for geometrical conditions than the 2T2R candidate IV, it is retained for further study and analysis. Also the mechanisms with 2R mobility having RCM point were detailed for the task of needle orientation. Different realizations of the 2R serial chain were discussed and a suitable candidate for the task of needle orientation was selected.

These candidate mechanisms have simpler architecture in terms of geometric complexity but following the same synthesis procedure, it is possible to derive more complex variants that would fit the same task. The validity of the selection of actuated joints and the conditions of full-cycle mobility have been verified. This work also reinforces the understanding that the concept of mobility is not sufficient for mechanism synthesis purposes and should be complemented with motion patterns that convey more accurately the motions and constraints expected for the desired mechanism. During the synthesis process, the application of the principle of kinematic inversion was demonstrated for the synthesis of parallel mechanisms in special cases where the motion pattern is specified with respect to the end-effector reference frame. This method could be applied to other syntheses where motion or constraint description are given with respect to a moving reference frame instead of a base frame.

3 Dimensional synthesis of the positioning device

Contents

Two positioning mechanisms, the 2T2R candidate II and the 2R candidate were proposed in the previous chapter as result of the architectural synthesis for the Task-I and Task-II definition. In the context of our application, these candidate mechanisms will be placed in the tunnel of the CT scanner for the image-guided needle positioning. After the introduction of a patient in the tunnel of a CT scanner, the available height is less than 300 mm [Walsh et al., 2008]. The space inside the scanner becomes even less when we consider overall needle insertion device with its needle positioning device and its insertion tool. This requires such robotic devices to

be very small in size and compact in form. In addition to such constraints, a large orientation workspace is required for the positioning of the needle, which is a difficult design challenge.

Mechanisms whether serial, parallel (as in the case of 2T2R mechanism candidate II) or hybrid (as in case of 2R mechanism candidate) admit singularities in their workspace. The workspace and the singularities are closely linked and both very sensitive to the structural parameters of the mechanism. Hence, a proper dimensional synthesis algorithm is very important, which involves finding dimensions of its structural parameters subject to design constraints and objectives. Most of these algorithms for dimensional synthesis are based on the evaluation of performance indices like isotropy, transmission or manipulability index [San Martin et al., 2007] or condition number [Li et al., 2006].The major drawback with these algorithms is that their complexity increases rapidly with the number of structural parameters, as the effect of each structural parameter has to be analyzed by numerical computation of the Jacobian matrices while discretizing the parameter space. In the work of [Arakelian et al., 2008], singularity-free zones in the workspace of parallel manipulators are sought to be increased by using mechanisms of the variable structure. The variable structure of the legs helps to change the structural parameters and hence avoid the singularities. The mechanism behaves like a redundant manipulator with extra joints and links which can be locked by the use of electromagnetic clutches. This solution though effective for enlarging the workspace of parallel manipulators comes with disadvantages of increase in the number of actuators and a more complex mechanism.

Algorithms based on the kinematic mapping [Ravani and Roth, 1983] and kinematic constraints [Hayes and Husty, 2003] of the mechanism provide an alternative. In the works [Purwar and Gupta, 2011; Wu et al., 2012], a visual approach using specific trajectory and motion planning as criteria has proven successful for the design of planar mechanisms where motion description is simpler. This approach relies on the kinematic mapping from Cartesian to planar quaternions to express the kinematic constraints as constraint manifolds. It is not yet adapted for spatial parallel mechanisms like the 2T2R mechanism candidate II which has complex spatial motion owing to its mobility. It has constraints on the workspace size as opposed to any trajectory specific constraints due to the nature of the targeted application. Moreover, the trajectory specification through specific points for the planar mechanism is equivalent to the set of points representing the workspace and its size for a spatial mechanism. Therefore in this work, the kinematic constraint analysis and the workspace size are considered for the dimensional synthesis algorithm. The kinematic constraints of a serial, parallel or hybrid mechanism, which constrain its motion can be described by its singularities. Using screw theory and a geometrical approach, it is possible to enumerate and describe these kinematic constraints in a vectorial form. This form is independent of the choice of the kinematic mapping and the parameterization used for representing intermediate reference frames of the mechanism. This leaves an open choice for use of either quaternions, Euler angles, Cartesian coordinates or a user-defined one, for kinematic mapping in order to represent the end-effector reference frame. Also, for parameterization of the intermediate reference frames, one has open choice of using either the Denavit-Hartenberg (DH) convention or using twists

with screw motion.

This chapter deals with the dimensional synthesis of the positioning mechanisms synthesized in the chapter 2. A novel dimensional synthesis algorithm is presented which is based on the mechanism singularities. This work has been presented at the ASME IDETC 2014 conference and can be found here [Kumar et al., 2014b]. The modeling and design constraints for the two mechanism candidates are described. This modeling expresses the vectorial form of these singularities into mathematical equations. These constraint equations along with the design constraints are then used for the workspace analysis of these mechanisms leading to the calculation of their structural parameters. Finally a static analysis of these mechanisms is performed to obtain the necessary actuation torques with the calculated structural parameters.

3.1 Dimensional synthesis based on mechanism singularities

The dimensional synthesis of these candidate mechanisms is based on the objective of achieving the required workspace size, while maintaining the system compactness within certain limits. The needle positioning in free space has already been defined as the alignment of the needle's axis with the axis of insertion such that it passes through the entry point on the patient's skin. This whole task can be decomposed in two sequential steps: first the translation of the needle axis to match the entry point and the subsequent orientation of the needle axis about this entry point. Hence, the workspace definition for needle positioning can be considered to be the union of the constant-orientation translation workspace and of the constant-position orientation workspace. One interesting aspect for parallel mechanisms is that such a workspace is the intersection of the workspace of its individual legs, which can be studied independently [Merlet, 2006]. This is not true of a general workspace, e.g. for the reachable workspace. This special property removes any coupling between the structural parameters of the different legs and thus it simplifies the dimensional synthesis of the 2T2R mechanism candidate II. As the legs of the 2T2R mechanism candidate II have only revolute joints, the workspace boundary of each leg is the locus of its singularities [Agrawal, 1991]. Thus the workspace of the 2T2R mechanism can be generated by plotting the loci of its singularity curves. The workspace size is limited by its external and internal boundaries. Where external boundaries need to be modified, the internal boundaries namely the voids need to be eliminated. Also, the additional curves due to the presence of parallel singularities need to be investigated.

3.1.1 Singularity analysis of the 2T2R mechanism candidate II

The figure 3.1, shows a simplified CAD model of the 2T2R mechanism candidate-II synthesized in section 2.4.2. This candidate mechanism has the least architectural complexity out of the two feasible candidates-II and IV. Hence, for further analysis and dimensional synthesis, this mechanism is studied and explored in more detail.

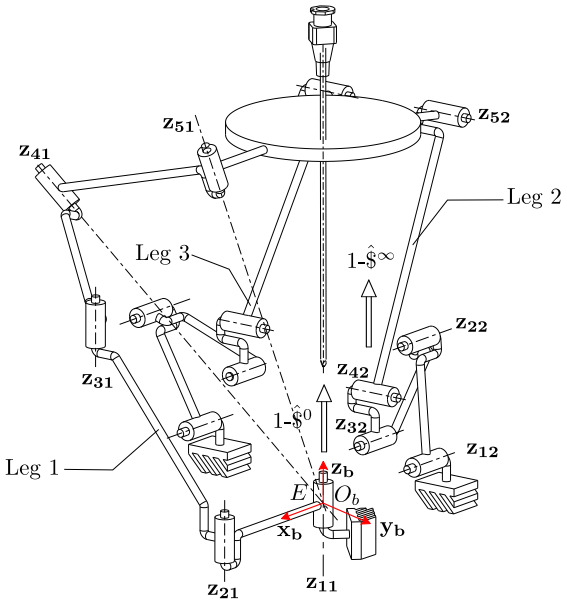

Figure 3.1 – Simplified CAD model of the 2T2R parallel mechanism candidate-II in its reference configuration.

Each of the three legs has five revolute joints. Considering a joint i in the leg k ($i = 1\ldots5, k = 1\ldots3$), let $\mathbf{z_{ik}}$ as shown in figure 3.1 and $\mathbf{t_{ik}}$ represent the direction of the joint axis and the position vector directed from O_b to any point on the joint axis, respectively. With this representation, the unit twist of the i^{th} joint of leg k is $\mathbf{\$}^0_{ik} = \begin{bmatrix} \mathbf{z_{ik}} & \mathbf{t_{ik}} \times \mathbf{z_{ik}} \end{bmatrix}^T$. If the axes of $\mathbf{\$}^0_{ik}$ and $\mathbf{\$}^0_{jk}$ form a plane, it would be referred to as Π_{ijk}.

Let the $\mathbf{X}$ and $\mathbf{q}$ be the column vector denoting the operational and joint coordinates. The velocity equation for the 2T2R parallel mechanism $\mathbf{J_X\dot{X}} = \mathbf{J_q\dot{q}}$ needs to be considered for discussion of its singularities. The full direct Jacobian $\mathbf{J_X}$ can be obtained by stacking the four actuation wrenches $\hat{\mathbf{\$}}_{i,a}$ and the two constraint wrenches $\hat{\mathbf{\$}}_{j,c}$ of the 2T2R parallel mechanism. The four actuation wrenches can be expressed as $\hat{\mathbf{\$}}_{i,a} = \begin{bmatrix} \mathbf{s_i} & \mathbf{r_i} \times \mathbf{s_i} \end{bmatrix}^T$ where $\mathbf{s_i}$ denotes the direction of the actuation wrench and $\mathbf{r_i}$ is the position vector directed from origin the O_b to a point of the wrench axis. The two constraint wrenches $\hat{\mathbf{\$}}_{j,c}$ produced by the mechanism have the form $\hat{\mathbf{\$}}_{1,c} = \begin{bmatrix} \mathbf{z_b} & \mathbf{O_bE} \times \mathbf{z_b} \end{bmatrix}^T$ and $\hat{\mathbf{\$}}_{2,c} = \begin{bmatrix} \mathbf{0} & \mathbf{m_1} \end{bmatrix}^T$ where $\mathbf{m_1}$ is the direction of the wrench system 1-$\hat{\mathbf{\$}}^{\infty}$. Therefore, the $\mathbf{J_X}$ and $\mathbf{J_q}$ matrices of the 2T2R parallel mechanism can be displayed as :

$$\mathbf{J_X} = \begin{bmatrix} \mathbf{s_1} & \mathbf{r_1} \times \mathbf{s_1} \\ \mathbf{s_2} & \mathbf{r_2} \times \mathbf{s_2} \\ \mathbf{s_3} & \mathbf{r_3} \times \mathbf{s_3} \\ \mathbf{s_4} & \mathbf{r_4} \times \mathbf{s_4} \\ \mathbf{z_b} & \mathbf{O_bE} \times \mathbf{z_b} \\ \mathbf{0} & \mathbf{m_1} \end{bmatrix} \qquad \mathbf{J_q} = \begin{bmatrix} \hat{\mathbf{\$}}_{1,a} \cdot \mathbf{\$}^0_{11} & 0 & 0 & 0 & 0 & 0 \\ 0 & \hat{\mathbf{\$}}_{2,a} \cdot \mathbf{\$}^0_{21} & 0 & 0 & 0 & 0 \\ 0 & 0 & \hat{\mathbf{\$}}_{3,a} \cdot \mathbf{\$}^0_{12} & 0 & 0 & 0 \\ 0 & 0 & 0 & \hat{\mathbf{\$}}_{4,a} \cdot \mathbf{\$}^0_{13} & 0 & 0 \\ 0 & 0 & 0 & 0 & 0 & 0 \\ 0 & 0 & 0 & 0 & 0 & 0 \end{bmatrix}$$

The parallel and serial singularities occur when the rank of $\mathbf{J_X}$ and $\mathbf{J_q}$ is less than six and four respectively but neither the symbolic form of $\mathbf{J_X}$, nor of $\mathbf{J_q}$, allow to derive the simplest representation of singularity conditions.

In the further subsections, a screw theory based inspection is used to obtain the geometrical form of the singularities, as this form is independent of the choice of the parametric representation and produces the simplest expression with the minimal number of structural parameters.

Serial singularity analysis of individual legs

As the legs 2 and 3 are kinematically identical, only serial singularities of legs 1 and 2 are discussed. The leg 1 is made up of two sub-units, $(RRR)_p$ and $(RR)_i$. The twist system of leg 1 is the union of the twist system of these two sub-units. The twist system of the $(RRR)_p$ and $(RR)_i$ units is 1-$\$^0$-2-$\$^\infty$ and 2-$\$^0$ respectively. Hence, the twist system of this leg is 3-$\$^0$-2-$\$^\infty$. Applying the principle of reciprocity, its wrench system is derived as 1-$\hat{\$}^\infty$. Aside from this constraint wrench, extra constraint wrenches develop when the leg 1 is in singularity. The following conditions characterize the singularity of the leg 1 :

Singularity-11 (figure 3.2(a)): occurs when the normal to the plane Π_{451} is perpendicular to $\mathbf{z_{31}}$ and is given by the following equation:

$$(\mathbf{z_{41}} \times \mathbf{z_{51}}) \cdot \mathbf{z_{31}} = \mathbf{0}. \tag{3.1}$$

In this case, the twist system of the leg degenerates to 2-$\$^0$-2-$\$^\infty$. The extra constraint moment, denoted as $\hat{\$}^\infty_{11,c}$, at singularity is shown in figure 3.2(a).

Singularity-21 (figure 3.2(b)) : occurs when the three joint axes $\mathbf{z_{11}}$, $\mathbf{z_{21}}$ and $\mathbf{z_{31}}$ are coplanar:

$$(\mathbf{t_{31}} - \mathbf{t_{21}}) \times (\mathbf{t_{21}} - \mathbf{t_{11}}) = \mathbf{0}. \tag{3.2}$$

This is the well-known elbow singularity occurring in serial mechanisms with revolute joints. In this case, the twist system of the leg degenerates to 3-$\$^0$-1-$\$^\infty$. The extra constraint force $\hat{\$}^0_{21,c}$ at singularity is shown in figure 3.2(b).

The leg 2 is made up of two sub-units, $(RRR)_p$ and $(RR)_p$. The twist system of the $(RRR)_p$ and $(RR)_p$ units is 1-$\$^0$-2-$\$^\infty$ and 1-$\$^0$-1-$\$^\infty$ respectively. The wrench system of the leg 2 is derived as 1-$\hat{\$}^\infty$. The following conditions characterize the singularity of leg 2 :

Singularity-12 (figure 3.2(c)): occurs when the normal to the plane Π_{452} is perpendicular to $\mathbf{z_{32}}$:

$$[(\mathbf{t_{52}} - \mathbf{t_{42}}) \times \mathbf{z_{42}}] \cdot \mathbf{z_{32}} = \mathbf{0}. \tag{3.3}$$

In this case, the twist system of the leg degenerates to 2-$\$^0$-2-$\$^\infty$. The extra constraint force

$\hat{\$}^0_{12,c}$ at singularity is shown in figure 3.2(c).

Singularity-22 (figure 3.2(d)): is the typical elbow singularity and it occurs when the $\mathbf{z_{12}}$, $\mathbf{z_{22}}$ and $\mathbf{z_{32}}$ are coplanar:

$$(\mathbf{t_{32}} - \mathbf{t_{22}}) \times (\mathbf{t_{22}} - \mathbf{t_{12}}) = 0. \tag{3.4}$$

In this case, the twist system of the leg degenerates to 2-$\$^0$-2-$\$^\infty$. The extra constraint force $\hat{\$}^0_{22,c}$ at singularity is shown in figure 3.2(d).

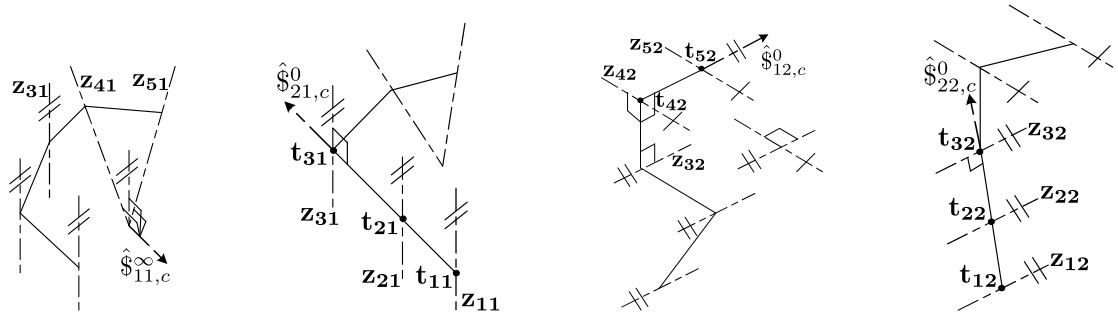

(a) Singularity-11. (b) Singularity-21. (c) Singularity-12. (d) Singularity-22.

Figure 3.2 – Singularities for legs 1 and 2.

Parallel singularity analysis

With the notations defined at the beginning of this section, a geometric interpretation of the actuation wrench system 4-$\hat{\$}_a$ can be obtained. The actuation wrenches $\hat{\$}_{1,a}$ and $\hat{\$}_{2,a}$ are each defined by the intersection of the planes taken in the pairs (Π_{231}, Π_{451}) and (Π_{131}, Π_{451}). Thus, it can be concluded that $\hat{\$}_{1,a}$ and $\hat{\$}_{2,a}$ both lie on the plane Π_{451} and hence must intersect each other if not parallel to each other. Thus $\hat{\$}_{1,a}$–$\hat{\$}_{2,a}$ forms a planar pencil of lines. Similarly, actuation wrenches $\hat{\$}_{3,a}$ and $\hat{\$}_{4,a}$ are defined respectively by the intersection of the planes in the pairs (Π_{232}, Π_{452}) and (Π_{233}, Π_{453}). The constraint wrench $\hat{\$}_{1,c}$ is a line passing through O_b and parallel to $\mathbf{z_b}$. The constraint wrench $\hat{\$}_{2,c}$ is a line orthogonal to the axes quintuple ($\mathbf{z_{12}}, \mathbf{z_{22}}, \mathbf{z_{32}}, \mathbf{z_{42}}, \mathbf{z_{52}}$). The conditions for the parallel singularity of 2T2R parallel mechanism are:

1. The wrenches $\hat{\$}_{1,a}$ and $\hat{\$}_{2,a}$ become coincident. This condition occurs whenever the planes (Π_{231},Π_{131}) become coincident. This condition is identical to the serial elbow singularity of leg 1 expressed in equation (3.2).

2. The wrenches $\hat{\$}_{3,a}$ and $\hat{\$}_{4,a}$ lie in the same plane when planes in pair (Π_{232},Π_{233}) are coincident. Two different parallel singularities can be identified when the following additional conditions are taken into account:
(a) The wrenches $\hat{\$}_{3,a}$ and $\hat{\$}_{4,a}$ become coincident when the planes in pair (Π_{452},Π_{453}) are

coincident.

$$\hat{\$}_{3,a} = \pm\hat{\$}_{4,a} \tag{3.5}$$

But if the planes in the pair (Π_{452},Π_{453}) are put non coincident in the reference assembly configuration, they remain non coincident for every platform configuration. Hence, this parallel singularity can be avoided by choosing different structural parameters defining the point of placement of legs 2 and 3 on the base, as expressed later in equation (3.11). Greater the difference in these structural parameters, better will be the distance from this parallel singularity.

(b) The wrenches $\hat{\$}_{3,a}$ and $\hat{\$}_{4,a}$ have parallel axis directions. Then the system of actuation wrenches $\hat{\$}_{3,a}$-$\hat{\$}_{4,a}$ becomes equivalent to a force $\hat{\$}_{3,a}$ and a pure moment $\hat{\$}^{\infty}_{4,a*}$. As the constraint wrench $\hat{\$}_{2,c}$ is a pure moment, a parallel singularity occurs when direction of the actuation wrench $\hat{\$}^{\infty}_{4,a*}$ is the same as $\hat{\$}_{2,c}$. The equation (3.6) states explicitly the components of $\hat{\$}^{\infty}_{4,a*}$ and $\hat{\$}_{2,c}$ in vectorial representation:

$$\hat{\$}_{2,c} = \begin{bmatrix} \mathbf{0} & \mathbf{m_1} \end{bmatrix}^T \quad \hat{\$}^{\infty}_{4,a*} = \begin{bmatrix} \mathbf{0} & \mathbf{m_{2*}} \end{bmatrix}^T \quad \text{where} \quad \mathbf{m_1} = \mathbf{z_{32}} \times \mathbf{z_{42}} \quad \mathbf{m_{2*}} = (\mathbf{t_{32}} - \mathbf{t_{22}}) \times \mathbf{z_{32}}. \tag{3.6}$$

Therefore, the equation for this parallel singularity can be derived as follows:

$$\mathbf{m_1} \times \mathbf{m_{2*}} = \mathbf{0} \quad \text{or} \quad (\mathbf{z_{32}} \times \mathbf{z_{42}}) \times [(\mathbf{t_{32}} - \mathbf{t_{22}}) \times \mathbf{z_{32}}] = \mathbf{0}. \tag{3.7}$$

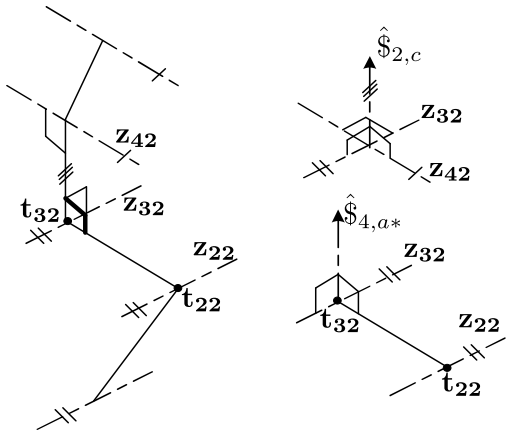

Figure 3.3 – Parallel singularity 2.

3. There is no constraint singularity as $\hat{\$}_{1,c}$ and $\hat{\$}_{2,c}$ are linearly independent in every configuration.

3.1.2 Singularity analysis of the 2R mechanism candidate

The 2R mechanism candidate has a hybrid structure as compared to a pure serial or a pure parallel architecture. There is no serial singularity as the twist system $2-\$^0$ of the mechanism does not degenerate throughout its configuration range. But there exists a parallel singularity for the parallelogram based 1-DOF RCM mechanism. It was stated in section 2.5.3 that this mechanism is equivalent to the parallelogram four bar O_bADJ mechanism with a virtual revolute joint at O_b. The condition for this parallel singularity is illustrated in figure 3.4, as the configuration where the parallelogram four bar O_bADJ is flattened (figure 3.4(b)):

$$(\mathbf{JO_b} \times \mathbf{AO_b} = \mathbf{0}). \tag{3.8}$$

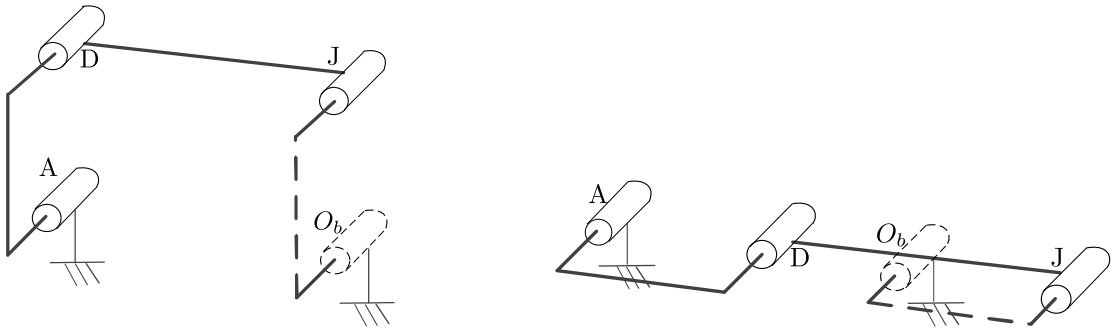

(a) Non-singular configuration. (b) Singular configuration.

Figure 3.4 – Parallel constraint singularity for the 2R mechanism candidate.

3.1.3 Dimensional synthesis algorithm

The dimensional synthesis algorithm to be described is based on the premise that serial singularities restrict the motion of the end-effector by producing extra constraint wrenches. This in turn limits the workspace of the mechanism. Hence the locii of the serial singularities also describe the boundaries of the workspace. By manipulating and modifying the singularities locii, one can obtain the required workspace size. Though the parallel singularities do not restrict the workspace, they have important consequences on the actuator torques in those configurations. Hence the locii of the parallel singularity curves should be made exterior to the required workspace boundaries.

The dimensional synthesis algorithm for the mechanisms with revolute joints, whether serial or parallel, can be described as follows:

Step 1: Derivation of both serial and parallel singularity conditions from a screw based inspection as opposed to derivation from the symbolic form of the matrix $\mathbf{J_X}$ or $\mathbf{J_q}$, as it will lead to the simplest form for the singularity conditions.

Step 2: Use of the DH parameters and resolution of the inverse kinematics to obtain the equations relating the operational coordinates and the structural parameters, corresponding to each singularity.

Step 3: Division of the singularity equations to separate curves corresponding to voids and curves corresponding to external boundaries.

Step 4: Modification of the singularity curves.
(a) Eliminate or minimize the void formation.

(b) Optimize or extend the external boundaries up to the required limits.

Step 5: Resolution of the equations corresponding to the singularity curves and design constraints, in order to find the set of DH parameters for the mechanism.

This dimensional synthesis algorithm provides an *a priori* formulation based on constraint analysis by including both the kinematic constraints introduced by serial singularities and constraints on the limits of actuation moments, reaction forces introduced by parallel singularities. It is in stark contrast with the *a posteriori* methods based on performance indices which are iterative and computationally very expensive. A framework for identification and elimination of the voids has also been provided in this algorithm which is absent from other algorithms. Different parametrizations for the mechanism and the end-effector can be chosen which suit the mechanism and the task description better. This algorithm can be more effectively applied for lower mobility mechanisms, as the complexity of this algorithm is dependent on the number of operational parameters. Though in the present work only the mechanisms with revolute joints are considered, it can be extended to mechanisms with prismatic joints and with joint limits as well. Moreover, more general workspaces like reachable workspace can be considered though with a higher complexity and possibly a strong coupling between structural parameters of different legs. It should be remarked here that this algorithm does not take into account link interferences.

Even with these singularity equations (3.1)-(3.7) for the 2T2R mechanism candidate II and equation (3.8) for the 2R mechanism candidate, the problem of dimensional synthesis is underconstrained and one needs to introduce some design constraints which in our case would correspond to the overall size of the positioning mechanism. The complexity of this algorithm does not increase with the increase in the number of structural parameters, as it amounts to solving the same number of equations. It will be evident in later sections, that each of singularity equation (3.1)- equation (3.8) could be reduced to cosine or sine of some angle θ obtained from the solution of the inverse kinematics. Hence, for this algorithm to work, a closed-form solution of the inverse kinematics is necessary to obtain the analytical expressions for the singularities. The above algorithm can be schematically presented in the form of the flow chart depicted in figure 3.5.

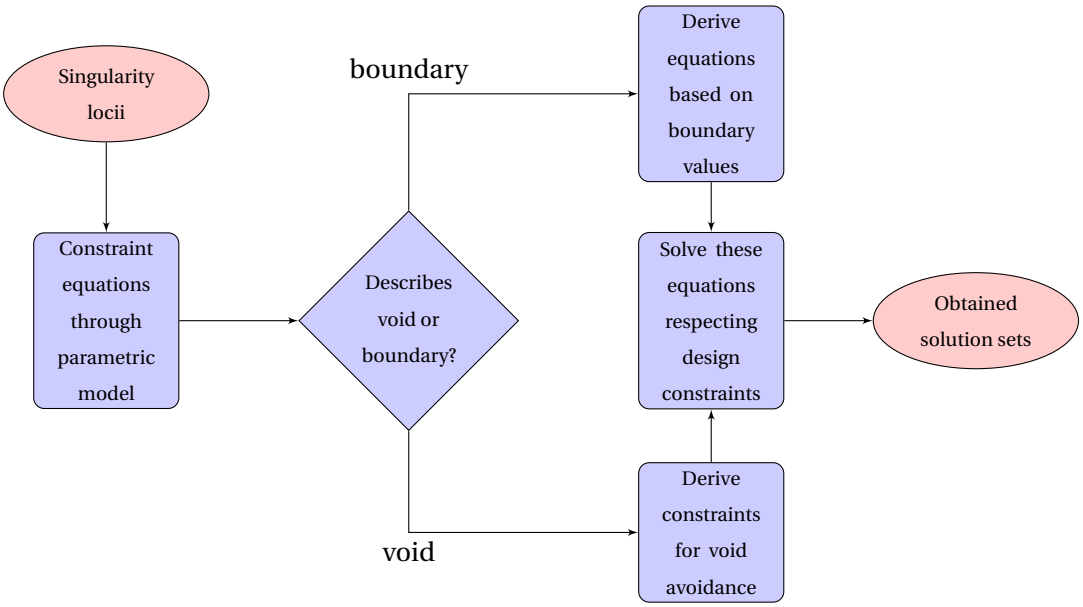

Figure 3.5 – Schematic representation of the dimensional synthesis algorithm.

3.2 Dimensional synthesis of the 2T2R mechanism candidate II

3.2.1 Modeling and design constraints

Mathematical modeling

As the legs 2 and 3 are identical, the models for only legs 1 and 2 are described. For the mathematical modeling of this 2T2R parallel mechanism, the modified Denavit-Hartenberg parameters [Khalil and Kleinfinger, 1986] are used, since it can readily take into account mechanisms with closed chains or parallel architecture. The DH parameters are given in table 3.1, where as the structural parameters for the legs 1 and 2 are given in figure 3.6. The red and blue lines in the figure represent the z and x axes of the DH convention, where as green lines represent the structural parameters. The reference frames $\mathscr{R}_{pk}$ are intermediate frames other than the base frame, shown in table 3.1, which help to position the point of attachment of each leg on the base. The $\mathscr{R}_{fk}$ are the frames attached to the end-effector of the 2T2R manipulator, shown in table 3.1, which help to derive the loop-closure relations. The angle θ_{ik} and θ_{rik} are the i^{th} angles, presented in table 3.1, between the successive x-axes of the DH model, in the general and reference configuration of the leg k (shown in figure 3.6), respectively. The notation for the parameters of the leg 3 would follow those of leg 2, with the subscript $k = 3$.

From table 3.1, the set of design parameters $\mathscr{D}_{P_1}$ for leg 1 is given in equation (3.9a). Some design constraints $\mathscr{D}_{C_1}$, given in equation (3.9b), are also imposed to take into account the size of the parallel mechanism and to avoid obtaining values practically difficult to realize. For

θ_{i1}	θ_{ri1}	α_{i1}	d_{i1}	r_{i1}
$\theta_{p1}=0$	$\theta_{rp1}=0$	0	0	0
θ_{11}	$\theta_{r11}=0$	0	0	0
θ_{21}	$\theta_{r21}=-\frac{\pi}{2}$	0	d_{21}	0
θ_{31}	θ_{r31}	0	d_{31}	r_{31}
θ_{41}	θ_{r41}	α_{41}	d_{41}	r_{41}
θ_{51}	θ_{r51}	α_{51}	0	0
$\theta_{f1}=\frac{\pi}{2}$	$\theta_{rf1}=\frac{\pi}{2}$	α_{f1}	0	0

(a) leg 1.

θ_{i2}	θ_{ri2}	α_{i2}	d_{i2}	r_{i2}
$\theta_{p2}=\frac{\pi}{2}$	$\theta_{rp2}=\frac{\pi}{2}$	0	0	r_{p2}
θ_{12}	θ_{r12}	$\pi/2$	d_{12}	r_{12}
θ_{22}	θ_{r22}	0	d_{22}	0
θ_{32}	θ_{r32}	0	d_{32}	0
θ_{42}	θ_{r42}	$\pi/2$	d_{42}	0
θ_{52}	θ_{r52}	0	d_{52}	r_{52}
$\theta_{f2}=0$	$\theta_{rf2}=0$	$\pi/2$	d_{f2}	r_{f2}

(b) leg 2.

Table 3.1 – DH parameters for the legs of the 2T2R mechanism.

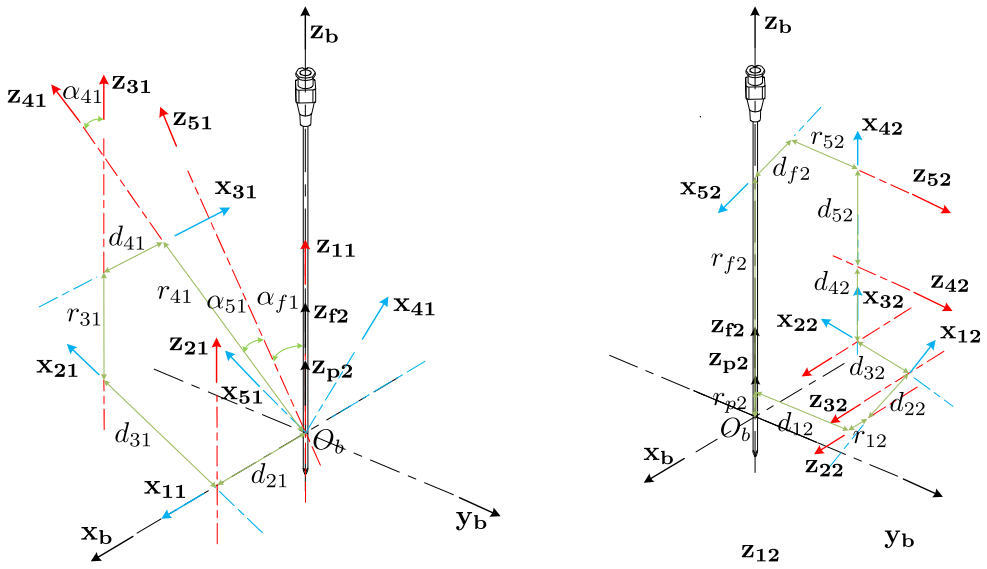

(a) leg 1 in reference configuration.

(b) leg 2 in reference configuration.

Figure 3.6 – Structural parameters for the legs of the 2T2R mechanism.

example, the value of d_{21} in $\mathscr{D}_{C_1}$ determines the size of the base of the mechanism.

$$\mathscr{D}_{P_1} = \{\theta_{r31}, \theta_{r41}, \theta_{r51}, \alpha_{41}, \alpha_{51}, \alpha_{f1}, d_{21}, d_{31}, d_{41}, r_{31}, r_{41}\} \tag{3.9a}$$

$$\mathscr{D}_{C_1} = \{d_{21} \leq 50 \text{ mm}, \quad \alpha_{i1} \leq \frac{\pi}{4}\} \tag{3.9b}$$

The design parameters $\mathscr{D}_{P_2}$ and the design constraints $\mathscr{D}_{C_2}$ for leg 2 are given in equation (3.10a) and equation (3.10b), respectively. Here the parameters r_{f2} and d_{12} in $\mathscr{D}_{C_2}$ determine the height and size of the base of the mechanism, respectively. The constraint on the sum of the angles in $\mathscr{D}_{C_2}$, ensures that the 2T2R mechanism in reference configuration has the constraint

wrench $\hat{\mathbf{\$}}_{2,c}$ along $\mathbf{z_b}$.

$$\mathscr{D}_{P_2} = \{\theta_{r12}, \theta_{r22}, \theta_{r32}, \theta_{r42}, \theta_{r52}, d_{12}, d_{22}, d_{32}, d_{42}, d_{52}, d_{f2}, r_{p2}, r_{12}, r_{52}, r_{f2}\} \tag{3.10a}$$

$$\mathscr{D}_{C_2} = \theta_{r12} + \theta_{r22} + \theta_{r32} = \frac{\pi}{2}, \theta_{r42} + \theta_{r52} = \frac{\pi}{2}, d_{12} < 50, r_{12} > -50 r_{f2} \geq -120 \text{ mm} \tag{3.10b}$$

To avoid the parallel singularity condition (3.5), the following design constraint needs to be satisfied where r_{13} for leg 3 is the corresponding parameter to r_{12} of leg 2:

$$r_{12} \neq r_{13}. \tag{3.11}$$

It should be kept in mind that out of the design parameters in $\mathscr{D}_{P_1}$ and $\mathscr{D}_{P_2}$, all the parameters are not independent. The assembly in the reference configuration, as shown in figure 3.6, imposes six independent constraints for each leg. But at the start, it is not possible to identify which parameters should be assumed independent. Hence, the entire set of design parameters is considered at the beginning of the algorithm.

Parameterization of the End-Effector of the 2T2R parallel mechanism

The homogeneous matrix representing the end-effector reference frame is :

$${}^0T_f = \begin{bmatrix} m_{11} & 0 & m_{13} & p_x \\ m_{21} & m_{22} & m_{23} & p_y \\ m_{31} & m_{32} & m_{33} & 0 \\ 0 & 0 & 0 & 1 \end{bmatrix} \tag{3.12}$$

where the terms m_{12} and p_z are zero. The condition $m_{12} = 0$ arises from the constraint 1-$\hat{\mathbf{\$}}^{\infty}$ provided by the legs 2 and 3, which restrict 1-DOF of rotation. The condition $p_z = 0$ arises from the constraint 1-$\hat{\mathbf{\$}}^{0}$ provided by the leg 1, which restricts the translation of the entry point E along the z-axis. Overall there are four independent parameters in the homogeneous matrix corresponding to 4-DOF of the 2T2R manipulator. The column vector $\mathbf{z_f} = \begin{bmatrix} m_{13} & m_{23} & m_{33} \end{bmatrix}^T$ represents the components of the vector $\mathbf{z_f}$ attached to the end-effector and coincident with the needle axis. The origin O_f is chosen at the entry point $E = (p_x, p_y)$ on the needle axis. The operational coordinates m_{13}, m_{23}, p_x, p_y are chosen as the four independent parameters which describe the configuration of the end-effector. These four operational parameters would be utilized to plot and discuss the workspace boundaries of the 2T2R parallel mechanism and its legs. In the reference configuration of the 2T2R parallel mechanism, as shown in figure 3.6, the values of operational coordinates are: $m_{13} = 0, m_{23} = 0, p_x = 0, p_y = 0$.

3.2.2 Inverse kinematics solution for the 2T2R mechanism candidate II

The inverse kinematics solution for the two legs of the 2T2R mechanism candidate II are developed and presented in appendix A.

3.2.3 Workspace analysis of the 2T2R parallel mechanism candidate-II

Design goal

A typical orientation range for percutaneous procedures lies within a cone of axis along $\mathbf{z_b}$ with a $\theta_m = 30$ deg half-angle, whereas a typical translational range is within a circular area of radius $r_m = 20$ mm centered at O_b. Within the ProteCT project, the aim was to increase this typical orientation range θ_m from 30 deg to 60 deg. With the design constraints imposed in section 3.2.1, especially with the limit on height of the mechanism, no feasible solutions existed for the dimensional synthesis of the 2T2R mechanism for $\theta_m = 60$ deg. Therefore, dimensional synthesis of the 2T2R mechanism candidate was carried out with the typical value of $\theta_m = 30$ deg. Let us denote these typical orientation and translation workspaces by W_O and W_t for further referencing. The prime objective of this dimensional synthesis is to achieve the required workspace size as shown in figure 3.7. This goal can also be defined in

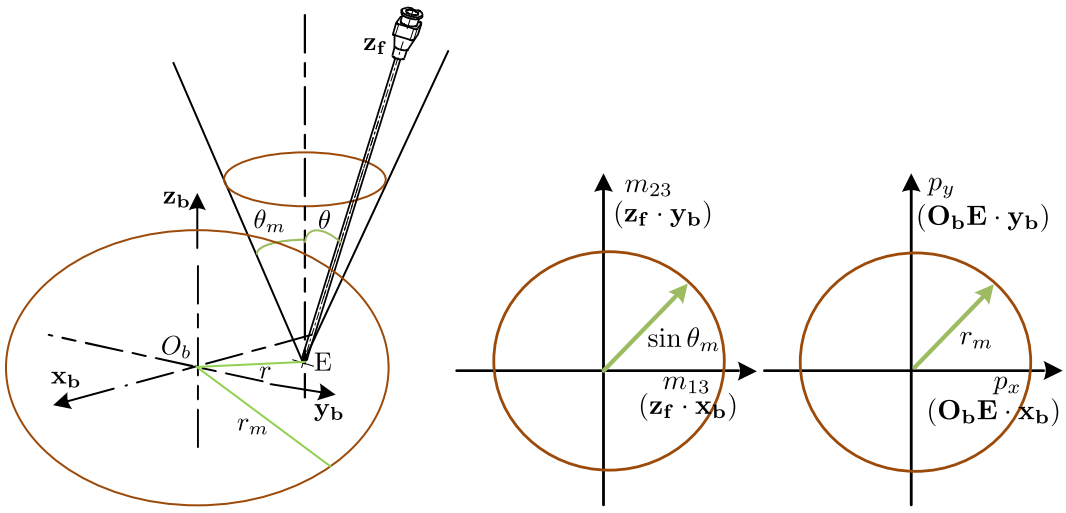

(a) Workspace requirement.

(b) Constant-position orientation workspace.

(c) Constant-orientation translational workspace.

Figure 3.7 – Desired workspace as design goal.

terms of the end-effector parameterization as described below:

$$m_{33} = \cos\theta \implies m_{13}^2 + m_{23}^2 = 1 - m_{33}^2 = \sin^2\theta_m \quad \text{and} \quad p_x^2 + p_y^2 = r^2. \tag{3.13}$$

The structural parameters of the 2T2R parallel mechanism are sought, which would lead to the design goal of the workspace mentioned earlier. For percutaneous procedures, the size of the orientation workspace is more important than the size of the translational workspace. Hence, for each leg, the orientation workspace is discussed first and then the resulting constraints are applied to obtain the translational workspace.

Workspace analysis of leg 1

In this and the next subsection, the expressions for the singularity equation (3.1) to equation (3.4) are reformulated to allow for the representation in terms of the DH parameterization. The developed expressions will be utilized to discuss the workspace boundaries and the elimination of voids. Reformulating the Singularity-11 described by equation (3.1) and considering the intermediate reference frames of leg 1 leads to:

$$\mathbf{x_{41}} \cdot \mathbf{z_{31}} = 0. \tag{3.14}$$

However the angle between $\mathbf{x_{41}}$ and $\mathbf{z_{31}}$ does not represent directly any angle from the DH parameters of the leg 1. The following equality for the intermediate reference frames of DH parameterization holds and can easily be proved :

$$\mathbf{x_{31}} \times \mathbf{x_{41}} = (\mathbf{x_{41}} \cdot \mathbf{z_{31}})\mathbf{z_{41}}. \tag{3.15}$$

Now substituting equation (3.14) into equation (3.15) yields equation (3.16a). Using equation (3.16b) rather than equation (3.16a) has two advantages. First, it allows to break the singularity locus into two separate curves at the equality. Second, it gives the inequality for avoiding the singularity.

$$\mathbf{x_{31}} \times \mathbf{x_{41}} = 0 \implies \sin\theta_{41} = 0 \tag{3.16a}$$

$$-1 \leq \cos\theta_{41} \leq +1 \tag{3.16b}$$

Also, a closed-form solution for θ_{41} is known from the solution of the inverse kinematics. Assuming that $\cos\alpha_{51} \neq 0$ the developed expressions for equation (3.16b), resulting from the solution of inverse kinematics for this leg, are presented below :

$$-m_{31}\sin\alpha_{f1} - m_{33}\cos\alpha_{f1} + \cos(\alpha_{41} - \alpha_{51}) \geq 0 \tag{3.17a}$$

$$-m_{31}\sin\alpha_{f1} - m_{33}\cos\alpha_{f1} + \cos(\alpha_{41} + \alpha_{51}) \leq 0. \tag{3.17b}$$

Equation (3.17) clearly identify the parameters affecting the orientation workspace of the leg 1 and is independent of the position of the end-effector. It is difficult to predict which expression represents the outer boundary and which expression represents the void. Plotting with the inverse kinematics model (IKM) is done to clarify that, with the following arbitrary chosen values of the parameters :

$$\alpha_{41} = \frac{\pi}{6} \quad \alpha_{51} = \frac{\pi}{4} \quad \alpha_{f1} = \frac{\pi}{3}. \tag{3.18}$$

The figure 3.8(a) shows the inverse kinematics plot where reachable and unreachable points are presented in blue and red colors respectively. In this figure, the formation of void can be clearly seen. figure 3.8(b) shows the plot of equation (3.17a) and equation (3.17b) at equality, where the void and the external workspace boundary are presented in black and green colors respectively. The same color convention will be applied for describing external boundaries,

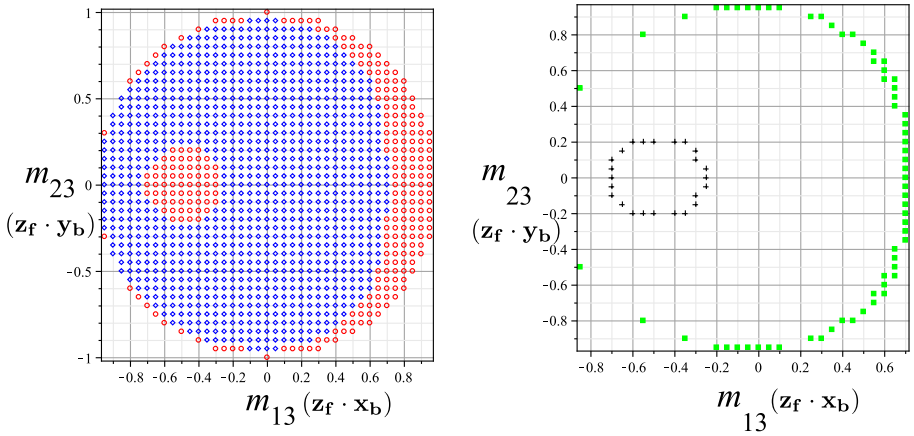

(a) IKM Plot.

(b) Boundary Plot.

Figure 3.8 – Typical orientation workspace of the leg 1.

voids and IKM plots later in this section. Thus, two separate equations are obtained for the leg 1, which control the behaviour of the outer workspace boundary and the void. Hence from equation (3.17a), the condition $\alpha_{41} = \alpha_{51}$ can be obtained for the void-avoidance. From equation (3.9b) and equation (3.17b), the condition $\alpha_{41} + \alpha_{51} = \frac{\pi}{2}$ can be obtained for the optimization of the external boundary. Thus it solves for two structural parameters of leg 1, which gives $\alpha_{41} = \alpha_{51} = \frac{\pi}{4}$.

After substituting the values of the α_{41} and α_{51} in equation (3.17a) and equation (3.17b) at equality, a point $[m_{13} = \sin\alpha_{f1}, m_{23} = 0]$ and a line $m_{13} = \cos\alpha_{f1}$ are obtained, respectively for the internal and the external singularities, as shown in figure 3.9(a). The inverse kinematics plots and the plots obtained from the analytical expressions are superimposed. The important thing to notice here is that, though the area of the void has been eliminated, there is still a singular point inside the workspace. The area inside the brown circle is the obtained orientation workspace W_O which keeps a distance of 15 deg from either singularity.

Upon reformulating Singularity-21 described by equation (3.2), equation (3.19a) is obtained.

$$\mathbf{x_{11}} \times \mathbf{x_{21}} = 0 \implies \sin\theta_{21} = 0 \tag{3.19a}$$

$$-1 \leq \cos\theta_{21} \leq +1 \tag{3.19b}$$

The inequalities in equation (3.19b) are presented below for the 2T2R parallel mechanism in a constant orientation chosen from the reference configuration :

$$(p_x - p_{xc})^2 + (p_y - p_{yc})^2 \geq (d_{31} - d_{21})^2 \tag{3.20a}$$

$$(p_x - p_{xc})^2 + (p_y - p_{yc})^2 \leq (d_{31} + d_{21})^2. \tag{3.20b}$$

This is the trivial case of an elbow singularity. From equation (3.20a), it is evident that the void is canceled for $d_{31} = d_{21}$. Equation (3.20) taken at equality is plotted for the following

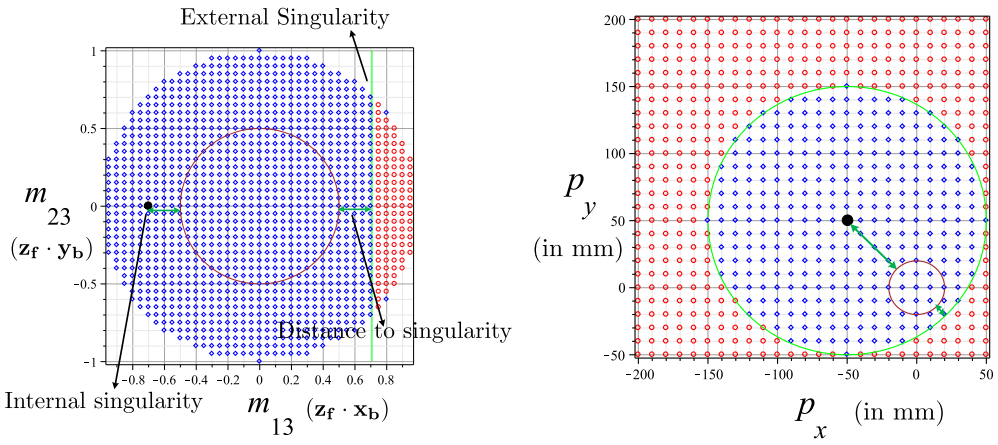

(a) Desired orientation workspace, $\alpha_{f1} = \frac{\pi}{4}$.

(b) Desired translational workspace.

Figure 3.9 – Desired workspace for the leg 1.

values of the parameters, in the figure 3.9(b), which include the constraints derived from the optimization of the orientation workspace :

$$\alpha_{41} = \alpha_{51} = \alpha_{f1} = \frac{\pi}{4} \qquad d_{21} = d_{31} = 50 \text{ mm}. \tag{3.21}$$

With the above values of the parameters, $p_{xc} = -50$ mm and $p_{yc} = 50$ mm is obtained. The achieved translational workspace is within the brown circle of diameter 40 mm, as shown in figure 3.9(b) and it keeps a minimum distance of approximately 10 mm from either singularity.

The dependent structural parameters obtained after solving the system of equations , arising from assembling the leg 1 in the reference configuration as shown in figure 3.6(a), are :

$$\theta_{31} = \theta_{41} = \theta_{51} = 1.99 \text{ rad} \tag{3.22a}$$

$$d_{41} = -24.80 \quad r_{31} = 66.22 \quad r_{41} = -93.65 \text{ mm}. \tag{3.22b}$$

Workspace analysis of legs 2 **and** 3

The analysis of leg 2 would be carried out in a different manner than the leg 1, as some of the obtained analytical expressions have a more complex form and the two singularities of leg 2 are coupled to each other.

Reformulating the Singularity-12, as described by equation (3.3) and considering the intermediate reference frames of leg 2, provides equation (3.23a):

$$\mathbf{x_{42}} \cdot (\mathbf{z_{42}} \times \mathbf{z_{32}}) = 0 \implies \cos\theta_{42} = 0 \tag{3.23a}$$

$$-1 \leq \sin\theta_{42} \leq +1. \tag{3.23b}$$

The developed expressions for equation (3.23b) can be written as:

$$d_{52} + r_{12} + d_{f2}\sqrt{1 - m_{13}^2} + m_{13} r_{f2} \geq p_x \tag{3.24a}$$

$$-d_{52} + r_{12} + d_{f2}\sqrt{1 - m_{13}^2} + m_{13} r_{f2} \leq p_x. \tag{3.24b}$$

To ensure equation (3.24) produces real values at equality for every point in the desired translational workspace W_t, following condition equation (3.25) must be fulfilled :

$$Discr = -p_x + r_{12} - d_{52} + \sqrt{d_{f2}^2 + r_{f2}^2} \geq 0. \tag{3.25}$$

where *Discr* is the discriminant of the quadratic equation in m_{13} obtained from equation (3.24b) at equality. To ensure that equation (3.25) is satisfied for the range, -20 mm $\leq p_x \leq 20$ mm, it is assumed that equation (3.25) is at equality for $p_x = 22$ mm. Hence, the following condition is obtained.

$$Discr = -22 + r_{12} - d_{52} + \sqrt{d_{f2}^2 + r_{f2}^2} = 0 \tag{3.26}$$

Reformulating Singularity-22, which is described by equation (3.4), leads to equation (3.27a).

$$\mathbf{x_{12}} \times \mathbf{x_{22}} = 0 \implies \sin\theta_{22} = 0 \tag{3.27a}$$

$$-1 \leq \cos\theta_{22} \leq +1 \tag{3.27b}$$

The full expression for equation (3.27b) is too complex to be detailed here and it is a function of all four operational parameters. This equation is obtained from inverse kinematics solution for the angle θ_{22}.

Reformulating the parallel singularity condition, which is described by equation (3.7), leads to equation (3.28a). The inequality for avoiding the parallel singularity is given by equation (3.28b).

$$\mathbf{x_{32}} \times (\mathbf{x_{22}} \times \mathbf{z_{32}}) = \mathbf{x_{22}}(\mathbf{x_{32}} \cdot \mathbf{z_{32}}) - \mathbf{z_{32}}(\mathbf{x_{32}} \cdot \mathbf{x_{22}}) = \mathbf{0} \implies \mathbf{x_{32}} \cdot \mathbf{x_{22}} = \mathbf{0} \implies \cos\theta_{32} = 0 \tag{3.28a}$$

$$-1 \leq \sin\theta_{32} \leq +1 \tag{3.28b}$$

The full expression for the equation (3.28) is too complex to be detailed here, but its derivation follows that of the inverse kinematics solution for joint angle θ_{32}.

The figure 3.10 shows the IKM plot of leg 2 for the orientation workspace with the following arbitrary chosen values of parameters :

$$r_{p2} = 0, r_{12} = -43.30, r_{52} = 1.05, r_{f2} = -120 \text{ mm}$$
$$d_{12} = 25, d_{22} = 35, d_{32} = 35, d_{42} = 10, d_{52} = 77.13 \text{ mm}, d_{f2} = 56.52 \text{ mm}. \tag{3.29}$$

In this figure, three separate singularity curves can be clearly seen, which in fact are plots of

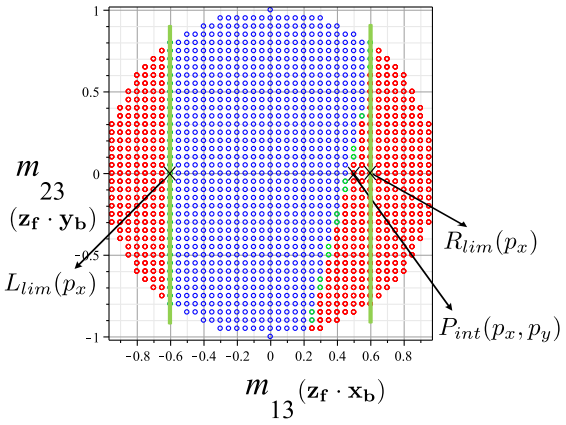

Figure 3.10 – Typical orientation workspace of the leg 2.

equation (3.24a), equation (3.24b) and equation (3.27b) at the equality. The term $\cos\theta_{22} = -1$ obtained from equation (3.27), which represents the collapsed position of the elbow singularity, is not present as the typical condition ($d_{22} = d_{32}$) in equation (3.29) removes any voids within the workspace. The boundary values (L_{lim}, R_{lim}, P_{int}), indicated in figure 3.10, are the values of m_{13}, which are the limiting factor for obtaining the W_O.

L_{lim} and R_{lim} are obtained from equation (3.24a) and (3.24b), respectively, at the equality and they are function of p_x only. P_{int} is obtained from the intersection of the term $\cos\theta_{22} = 1$ (equation (3.27)) with the line $m_{23} = 0$. It is function of both p_x and p_y. To solve for the desired orientation and translational workspaces W_O and W_t, equations are formed based on these boundary values and then solved for the DH parameters of leg 2, as discussed further in this subsection. Variation of the above boundary values with respect to p_x and p_y is :

$$\frac{\partial L_{lim}}{\partial p_x} < 0, \frac{\partial R_{lim}}{\partial p_x} < 0, \frac{\partial P_{int}}{\partial p_x} < 0, \frac{\partial P_{int}}{\partial p_y} > 0 \tag{3.30}$$

Hence, the worst case scenarios are given below at the boundary of the desired translational workspace W_t, where $m_{13lim} = 0.5$ corresponds to size of the desired orientation workspace W_O :

$$L_{lim}(-20 \text{ mm}) = -m_{13lim} \quad R_{lim}(+20 \text{ mm}) = m_{13lim},$$
$$P_{int}(+20 \text{ mm}, -20 \text{ mm}) = m_{13lim} \tag{3.31}$$

We consider the intersection of two lines $m_{13} = 0$ and $m_{23} = 0$ with the parallel singularity curve represented by equation (3.28). This gives two points each on the m_{23} and m_{13} axis which are assumed to lie on the boundary of the desired orientation and translational workspace. These

four points are given in the equation (3.32).

$$P1_{23}(-20\text{ mm}, +20\text{ mm}) = m_{13lim} \quad P2_{23}(-20\text{ mm}, -20\text{ mm}) = -m_{13lim}$$
$$P1_{13}(-20\text{ mm}, -20\text{ mm}) = +m_{13lim} \quad P2_{13}(-20\text{ mm}, -20\text{ mm}) = -m_{13lim} \tag{3.32}$$

The following independent parameters were chosen before solving the system of equations for legs 2 and 3:

$$d_{42} = d_{43} = 5, \quad r_{p2} = r_{p3} = 20, \quad r_{f2} = r_{f3} = -120\text{ mm} \tag{3.33}$$

Solving for the rest of the dependent parameters with equation (3.9b), equation (3.26), equation (3.31), equation (3.32), equation (3.33) and the equations derived from the assembly of the legs 2 and 3 in reference configuration, as shown in figure 3.6(b), the unknown parameters in equation (3.10a) are obtained:

$$\theta_{r_{12}} = 1.34, \theta_{r_{13}} = 1.40, \theta_{r_{22}} = 2.58, \theta_{r_{23}} = -2.40, \theta_{r_{32}} = -2.35, \theta_{r_{33}} = 2.57,$$
$$\theta_{r_{42}} = -0.04, \theta_{r_{43}} = .1, \theta_{r_{52}} = 1.61, \theta_{r_{53}} = 1.47\ rad \tag{3.34a}$$

$$d_{12} = 36.65, d_{13} = -39.25, d_{22} = 54.99, d_{23} = 43.05, d_{32} = 54.99, d_{33} = 43.05,$$
$$d_{52} = 80.26, d_{53} = 89.23, d_{f2} = 23.40, d_{f3} = 0,$$
$$r_{12} = -20.00, r_{13} = -8.78, r_{52} = -10.20, r_{53} = 8.89\text{ mm} \tag{3.34b}$$

The area inside the brown circle represents the desired common W_O obtained for the legs 2 and 3, as shown in figure 3.11, for different values of p_x and p_y. As it can be seen that even in worst scenarios depicted in figure 3.11(b) and 3.11(c), the desired orientation workspace W_O is obtained for every point in the translational workspace W_t.

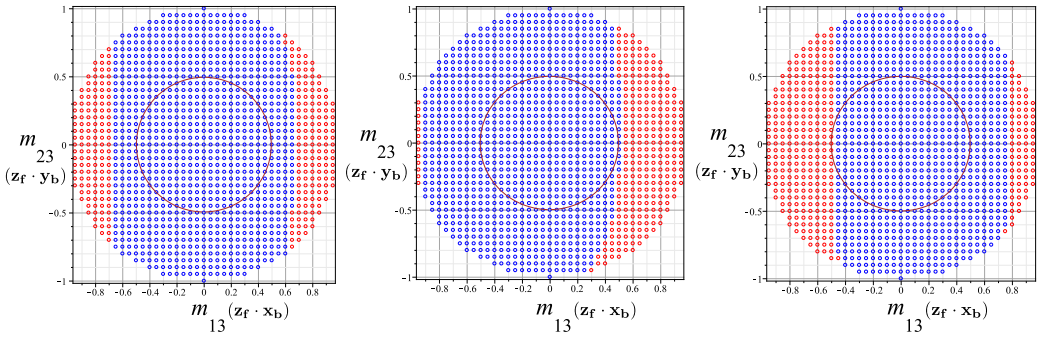

(a) $(p_x, p_y) = (0,0)$. (b) $p_x = 20, p_y = -20$ mm. (c) $p_x = -20, p_y = -20$ mm.

Figure 3.11 – Common orientation workspace W_O of the legs 2 and 3.

The important structural parameters which determine the size of the base and height of the

2T2R parallel mechanism in its reference configuration are:

$$d_{21} = 50, \quad d_{12} = 36.65, \quad d_{13} = -39.24 \text{ mm}, \tag{3.35a}$$

$$r_{12} = -20, \quad r_{13} = -10, \quad r_{f2} = r_{f3} = -120 \text{ mm} \tag{3.35b}$$

Here d_{12}, $|d_{13}|$ and $|r_{f2}|$ represent the size of the base and height of the mechanism, respectively. Hence, the height and base size of the mechanism are limited to a characteristic dimension of 120 mm which were put as the design constraints at the start of the dimensional synthesis.

The figure 3.12(a) and 3.12(b) show a preliminary prototype without actuators set in the reference and in an arbitrary configuration, respectively. The fabricated prototype of the 2T2R parallel mechanism holds a 16 G (approx. 1.7 mm diameter) 200mm long biopsy needle.

(a) Reference configuration. (b) In arbitrary configuration.

Figure 3.12 – Preliminary prototype.

3.2.4 Static analysis

Recalling the velocity equation for the 2T2R parallel mechanism from section 3.1.1 it can be written as $\mathbf{J_X}\dot{\mathbf{X}} = \mathbf{J_q}\dot{\mathbf{q}}$, where the two matrices $\mathbf{J_X}$ and $\mathbf{J_q}$ can be displayed as :

$$\mathbf{J_X} = \begin{bmatrix} \hat{\$}_{1,a} & \hat{\$}_{2,a} & \hat{\$}_{3,a} & \hat{\$}_{4,a} & \hat{\$}_{1,c} & \hat{\$}_{2,c} \end{bmatrix}^T \quad \mathbf{J_q} = \begin{bmatrix} \hat{\$}_{1,a} \cdot \$^0_{11} & 0 & 0 & 0 & 0 & 0 \\ 0 & \hat{\$}_{2,a} \cdot \$^0_{21} & 0 & 0 & 0 & 0 \\ 0 & 0 & \hat{\$}_{3,a} \cdot \$^0_{12} & 0 & 0 & 0 \\ 0 & 0 & 0 & \hat{\$}_{4,a} \cdot \$^0_{13} & 0 & 0 \\ 0 & 0 & 0 & 0 & 0 & 0 \\ 0 & 0 & 0 & 0 & 0 & 0 \end{bmatrix}$$

Static equilibrium of the 2T2R mechanism under action of the external wrench $\hat{\mathbf{\$}}_{ext}$ has to be achieved by the set of four actuation wrenches 4-$\hat{\mathbf{\$}}_a$ and two constraint wrenches 2-$\hat{\mathbf{\$}}_c$. The following equation gives the decomposition of the $\hat{\mathbf{\$}}_{\text{ext}}$ in the space spanned by the 4-$\hat{\mathbf{\$}}_a$ and 2-$\hat{\mathbf{\$}}_c$, where the components of $\mathbf{I}_{decom}$ corresponds to the norm of four actuation and two constraint wrenches, respectively:

$$\mathbf{I}_{decom} = {\mathbf{J_X}}^{-T} \hat{\mathbf{\$}}_{ext} \tag{3.36}$$

The equation (3.36) gives a relationship between the norm of the constraint wrenches, the actuation wrenches and the structural parameters of the mechanism. A closed form symbolic expression for the ${\mathbf{J_X}}^{-T}$ is very difficult to obtain for a spatial mechanism like the 2T2R mechanism. This difficulty does not allow the static analysis constraints such as limits on the norm of constraint wrenches and the actuations wrenches to be considered at the beginning of the dimensional synthesis procedure. However, for simple planar parallel manipulators it is possible to obtain a closed form solution for the ${\mathbf{J_X}}^{-T}$. In the work of [Briot et al., 2013], a closed form formulation for the ${\mathbf{J_X}}^{-T}$ is used to investigate the effort transmission in planar parallel mechanisms including the limits on the norms of the reaction forces.

The four actuation moments can be calculated by the following equation:

$$\begin{bmatrix} M_1 & M_2 & M_3 & M_4 & 0 & 0 \end{bmatrix}^T = {\mathbf{J_q}}^T \mathbf{I}_{decom} \tag{3.37}$$

Based on the modeling described before, in section 3.2.1, for the 2T2R mechanism and the values of the structural parameters obtained during dimensional synthesis procedure, it is possible to calculate numerically the actuation moments and the norm of the constraint and actuation wrenches for a given end-effector position. It is of special interest to see the evolution of the actuation moments through the workspace, especially for getting an idea of the maximum actuator torque required, which would dictate the choice of actuation technology. For calculation of the actuation torques, a combined effect of gravity and axial insertion forces along $\mathbf{z_f}$ is considered. The magnitude of the axial insertion forces is assumed to be 15N. The force due to gravity is assumed to be 5N. The center of gravity of the mechanism is assumed to lie on the insertion axis at a distance of 130mm from the origin O_b. Under the action of the this external wrench the torque feasible workspace was calculated and plotted for nine positions of the entry point in figure 3.13. The maximum of the four actuation moments $M_{max} = \max(M_1, M_2, M_3, M_4)$ was calculated. The set of red points represent the unreachable workspace. The set of blue points represent the reachable workspace where the $M_{max} < 2$N·m. The set of yellow points represent the reachable workspace where the $2 < M_{max} < 10$N·m. The set of black crosses represent the reachable points where the Jacobian matrix $\mathbf{J_X}$ is very ill-conditioned and the actuation moments are very high and $M_{max} > 10$N·m. The area inside the brown circle is the desired orientation workspace W_O. The incidence of these isolated black crosses and yellow points pose problems for the choice of a technological solution for the actuation, especially given the teleoperation scenario of the slave positioning device. The configurations corresponding to the black points within the workspace would have to be

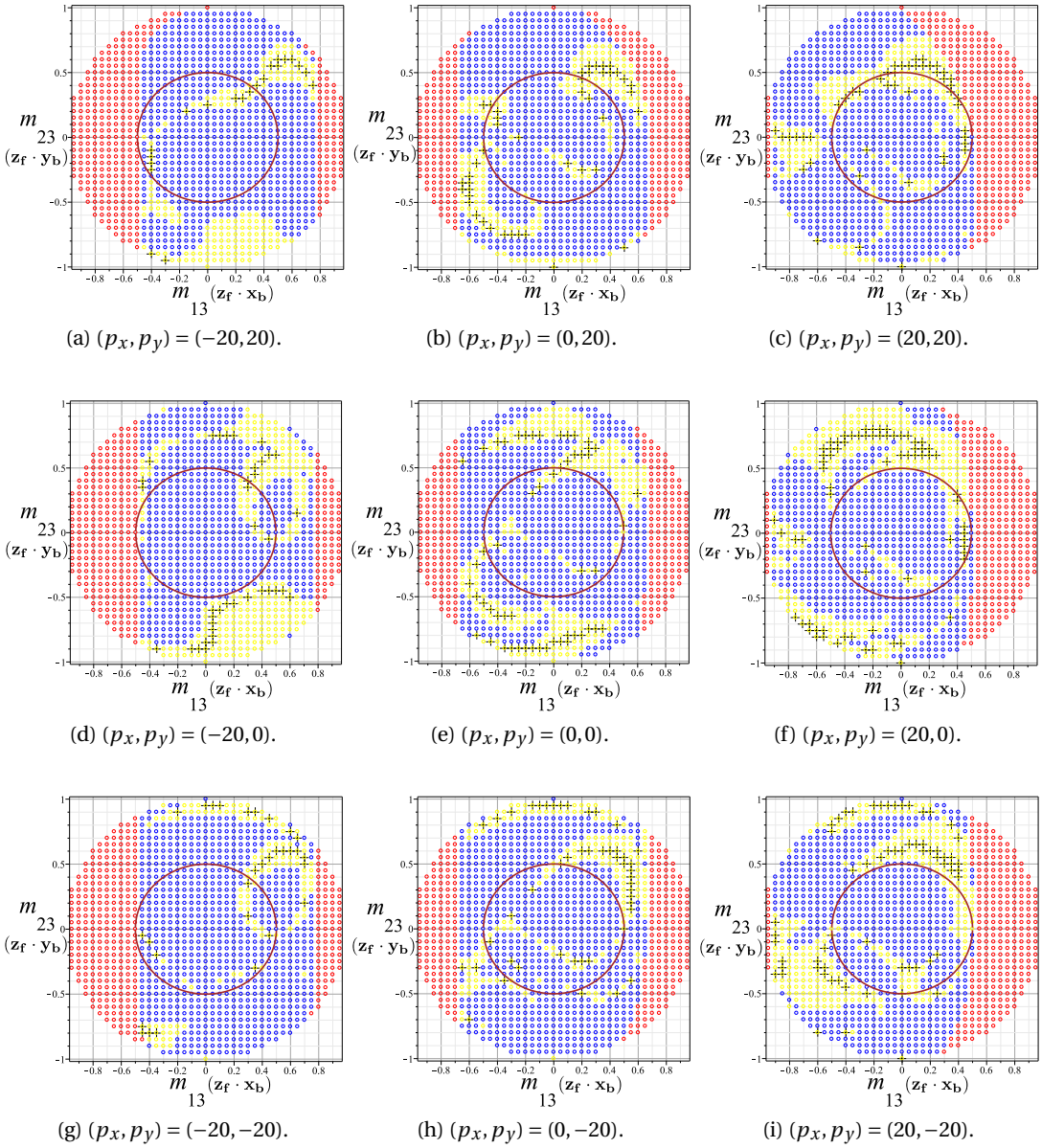

(a) $(p_x, p_y) = (-20, 20)$. (b) $(p_x, p_y) = (0, 20)$. (c) $(p_x, p_y) = (20, 20)$.

(d) $(p_x, p_y) = (-20, 0)$. (e) $(p_x, p_y) = (0, 0)$. (f) $(p_x, p_y) = (20, 0)$.

(g) $(p_x, p_y) = (-20, -20)$. (h) $(p_x, p_y) = (0, -20)$. (i) $(p_x, p_y) = (20, -20)$.

Figure 3.13 – Torque feasible workspace for the 2T2R mechanism candidate at boundaries of the translational workspace W_t.

restricted to the radiologist while he/she manipulates the master device which is very much unacceptable given the nature of the application.

The values of very high actuation moments are the configurations where the Jacobian matrix $\mathbf{J_X}$ degenerates. The degeneration of this matrix is also associated to the parallel singularity configurations. Though, the parallel singularity conditions derived by screw theory were presented and taken into account at the beginning of the dimension synthesis procedure, very high actuation moments indicate that not all parallel singularity conditions were enumerated.

This is due to the asymmetrical nature of the 2T2R parallel mechanism with two different leg types for which the system spanned by 4-$\hat{\$}_a$ and 2-$\hat{\$}_c$ wrenches does not degenerate in a regular and predictable manner. This leads to isolated singularity configurations which are very difficult to predict by application of screw theory. This limitation is however not present in symmetrical fully parallel mechanisms, where systematic enumeration of parallel singularity conditions by screw theory is possible.

3.3 Dimensional synthesis of the 2R mechanism

3.3.1 Modeling and design constraints

The 2R mechanism candidate consists of a revolute joint in series with a 1-DOF parallelogram based RCM mechanism. For purpose of workspace analysis, 2R mechanism candidate is modeled as consisting of the first revolute joint and and the virtual revolute joint shown in red in figure 2.21. Three reference frames $\mathscr{R}_1$, $\mathscr{R}_2$ and $\mathscr{R}_f$ are introduced and set according to the modified DH convention [Khalil and Kleinfinger, 1986]. The figure 3.14 shows the modeling of the 2R mechanism candidate along with its structural parameters. The axis of the first revolute joint is along $\mathbf{z_1}$ passing through O_b and is associated with the reference frame $\mathscr{R}_1$. The axis of the second virtual revolute joint is along $\mathbf{z_2}$ passing through O_b and is associated with the reference frame $\mathscr{R}_2$. The axis of the end-effector, coincident with the needle axis is along $\mathbf{z_f}$ passing through O_b and is associated with the reference frame $\mathscr{R}_f$. The modified DH

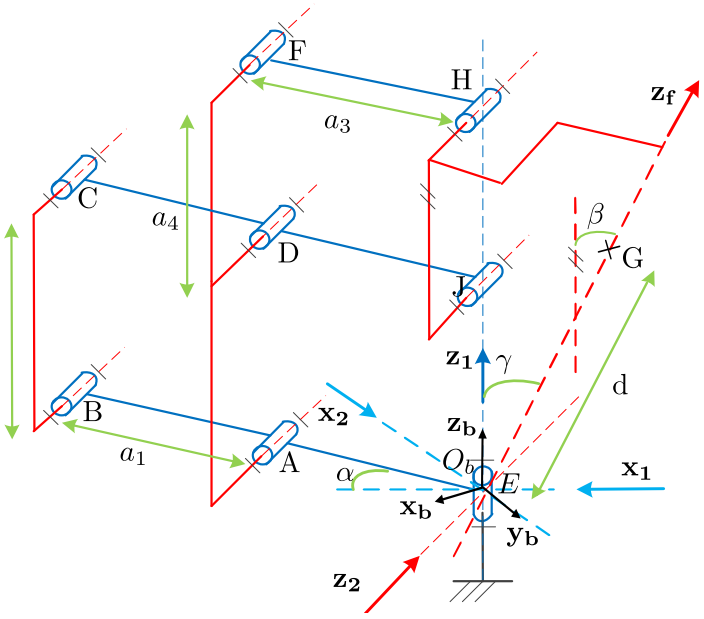

Figure 3.14 – Modeling of the 2R mechanism candidate.

parameters for the 2R mechanism candidate are given in table 3.2.

θ_i	α_i	d_i	r_i
θ_1	0	0	0
θ_2	$\pi/2$	0	0
$\theta_f = 0$	$\pi/2$	0	0

Table 3.2 – DH parameters for the 2R mechanism candidate.

The RCM point is defined by the origin O_b of the base frame coincident with point E. The plane perpendicular to $\mathbf{z_2}$ and passing through O_b determines the plane of the parallelogram mechanism. The line O_bAB makes an angle α with $\mathbf{x_1}$. This angle α is intended to help place the RCM point on the patient's skin surface which might not be at the same level as the base of the mechanism. The insertion tool which contains the needle axis makes up for most of the weight in the mechanism and its design has a symmetry around the needle axis as we will see later. Therefore the center of gravity G of the mechanism, is assumed to be lying on the insertion axis. The insertion axis does not necessary has to coincide with the line O_bJH. So another variable γ is defined, which describes the angle between the insertion axis and $\mathbf{z_b}$. The angle β between the line O_bJH and the insertion axis along $\mathbf{z_f}$ gives the freedom to place it at an offset angle from the line O_bJH.

Parameterization of the end-effector of the 2R mechanism

The homogeneous matrix representing the end-effector reference frame is :

$$ {}^0T_f = \begin{bmatrix} \cos\theta_1\cos\theta_2 & \sin\theta_1 & \cos\theta_1\sin\theta_2 & 0 \\ \sin\theta_1\cos\theta_2 & -\cos\theta_1 & \sin\theta_1\sin\theta_2 & 0 \\ \sin\theta_2 & 0 & -\cos\theta_2 & 0 \\ 0 & 0 & 0 & 1 \end{bmatrix} = \begin{bmatrix} m_{11} & m_{12} & m_{13} & p_x \\ m_{21} & m_{22} & m_{23} & p_y \\ m_{31} & m_{32} & m_{33} & p_z \\ 0 & 0 & 0 & 1 \end{bmatrix} \tag{3.38} $$

where the terms m_{32} and p_x, p_y and p_z can be seen to be zero. Overall there are two independent parameters in the homogeneous matrix corresponding to 2-DOF of the 2R mechanism. The column vector $\mathbf{z_f} = \begin{bmatrix} m_{13} & m_{23} & m_{33} \end{bmatrix}^T$ represents the components of the vector $\mathbf{z_f}$ attached to the end-effector and coincident with the needle axis. The operational coordinates m_{13}, m_{23} are chosen as the two independent parameters which describe the configuration of the end-effector. These two operational parameters would be utilized to discuss the workspace boundaries of the 2R mechanism.

3.3.2 Inverse kinematics solution for the 2R mechanism candidate

Inverse kinematics problem amounts to solving for θ_1 and θ_2 given the two operational coordinates m_{13}, m_{23}. From equation(3.38), the values of joint variables can be calculated as

function of the operational coordinates:

$$\theta_1 = \arctan2(m_{23}, m_{13}) \quad \theta_2 = \arccos(-m_{33}) \tag{3.39}$$

Thus there are two inverse kinematics solutions for the 2R mechanism with the assumption that $m_{33} > 0$, as we are only interested in positive values of angle which $\mathbf{z_f}$ makes with $\mathbf{z_b}$. As $m_{33} = \cos\gamma$, the equation $\theta_2 = \arccos(-m_{33})$ gives two solution for θ_2 as $\theta_2 = \pi \pm \gamma$. It can be verified that the solution corresponding to the schematics, as shown in figure 3.14, is $\theta_2 = \pi + \gamma$.

3.3.3 Workspace analysis of the 2R mechanism candidate

There are no serial singularities for this mechanism which would affect the workspace of this mechanism candidate. However, there is a parallel singularity which was described in section 3.1.2. The vectorial representation of this parallel singularity is given by equation (3.8). Restating equation (3.8) by utilizing the modeling adopted for the 2R mechanism and since $\theta_2 = \pi + \gamma$, we get the following equation (3.40):

$$\cos\left(\gamma - \alpha - \beta\right) = 0 \tag{3.40}$$

The mechanism singularities are met when $\gamma = \alpha + \beta \pm \frac{\pi}{2}$.

There is no theoretical limit to the value of the joint angle θ_1 by the parallel singularity condition. However, the limits of the angle θ_2 are determined by equation (3.40). The limits on the value of γ can be obtained as follows:

$$\alpha + \beta - \pi/2 \leq \gamma \leq \alpha + \beta + \pi/2 \tag{3.41}$$

Since we are interested only in limits to the positive value of γ, and as α and β are both positive, there is no parallel singularity for values of γ less than 90 deg. For the application of needle orientation, a value of $\gamma = 60$ deg is more than sufficient. In fact, this orientation range has not yet been achieved by the existing needle positioning mechanisms in the literature, where the typical value is 30 deg as was also chosen for the dimensional synthesis of the 2T2R parallel mechanism in earlier sections. Thus the achievable workspace for this candidate mechanism would rather be limited by practical challenges such as the interference and the collision between the links of the mechanism.

3.3.4 Static analysis

Apart from the workspace constraints, actuation requirements for the 2R mechanism candidate need to be investigated upon the action of the external forces. The axial needle insertion force $\mathbf{F_{in}}$ along the $\mathbf{z_f}$ and the force due to gravity m$\mathbf{g}$ along $-\mathbf{z_b}$ are the external forces considered for the static analysis of this mechanism. The assumption is made that the base of the mechanism is fixed to the ground. The vector of external forces is given by $\mathbf{F_{ext}} = \mathbf{F_{in}} + m\mathbf{g}$.

The first revolute joint of the 2R mechanism candidate which is along $\mathbf{z_1}$ is actuated. The second actuator is placed at the revolute joint, at point B, in the 1-DOF parallelogram based RCM mechanism. Let the vector of actuation moments for two joints be given by $[M_1 \quad M_2]^T$. The axis of the first revolute joint $\mathbf{z_1}$ is along $\mathbf{z_b}$. The center of gravity is assumed to lie on the insertion axis at a distance d from O_b, as shown in figure 3.14. The external wrench $\mathbf{F_{ext}}$ lie in a plane passing through O_b and containing the $\mathbf{z_1}$ axis. Thus the external wrench $\mathbf{F_{ext}}$ is reciprocal to the twist corresponding to the first revolute joint. Hence under static equilibrium $M_1 = 0$.

For calculation of the actuation moment M_2 we proceed with the static analysis of the planar parallelogram mechanism. First we break the mechanism into five bars namely, BC, CDJ, ADF, HF and HJ as shown in figure 3.15. Each revolute joint is assumed to be frictionless hence there

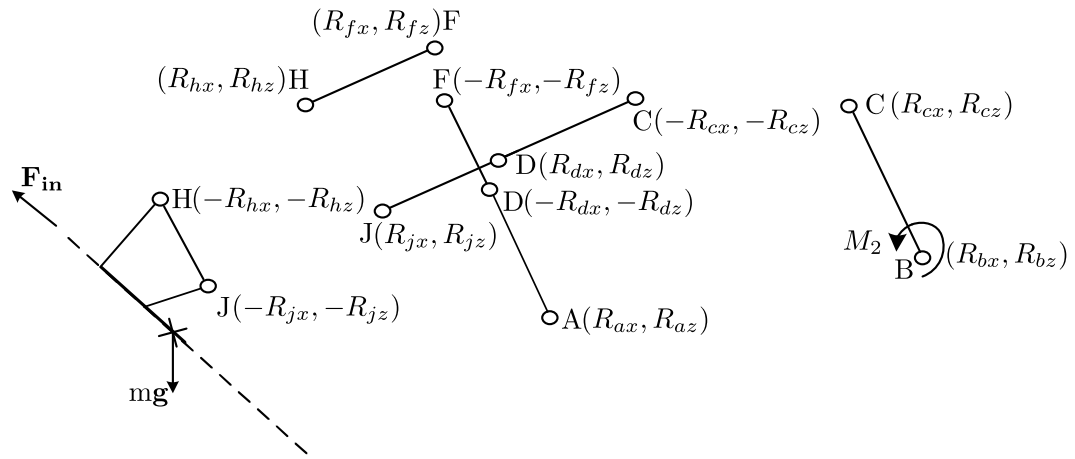

Figure 3.15 – Bar by bar analysis with their free body diagrams.

are only reaction forces which are projected along $\mathbf{z_1}$ and $\mathbf{x_1}$ in two orthogonal components. There are a total of 5 rigid bodies in a plane which leads to 15 independent equations. There are in total of 7 pivot points leading to 14 independent reaction forces. Together with the actuation torque M_2, there are 15 variables to be solved from a system of 15 equations. As the number of variables and the number of equations are same, a unique solution can be found for non-singular configurations.

The expression of the actuation torque M_2 is derived to be :

$$M_2 = -mgd\sin\gamma \tag{3.42}$$

Thus this actuation torque depends only on the force due to gravity, distance of the center of gravity from the origin and the angle insertion axis makes with $\mathbf{z_b}$. As it can be seen structural parameters of the mechanism have no effect on both actuation torques M_1 and M_2. The expression for the calculated reaction forces at the joints A, B, C, D, F, J, H can be found in the appendix B.

For obtaining a collision free orientation range of $\gamma = +60$ deg, the following structural parameters were chosen and arrived after several iterations from the CAD design of the prototype.

$$(a_1, a_2, a_3, a_4) = (45\text{ mm}, 100\text{ mm}, 18\text{ mm}, 40\text{ mm})$$
$$(\alpha, \beta) = (35\text{ deg}, 30\text{ deg}) \quad (3.43)$$

For calculation of the actuation torques, reaction forces and their evolution over the range of $\gamma = 0..60$ deg, a combined effect of gravity and axial insertion forces along $\mathbf{z_f}$ is considered. The magnitude of the axial insertion forces is assumed to be 15N. The force due to gravity is assumed to be 5N. The center of gravity of the mechanism is assumed to lie on the insertion axis at a distance of $d = 130$mm from the origin O_b. With these values of the structural parameters,

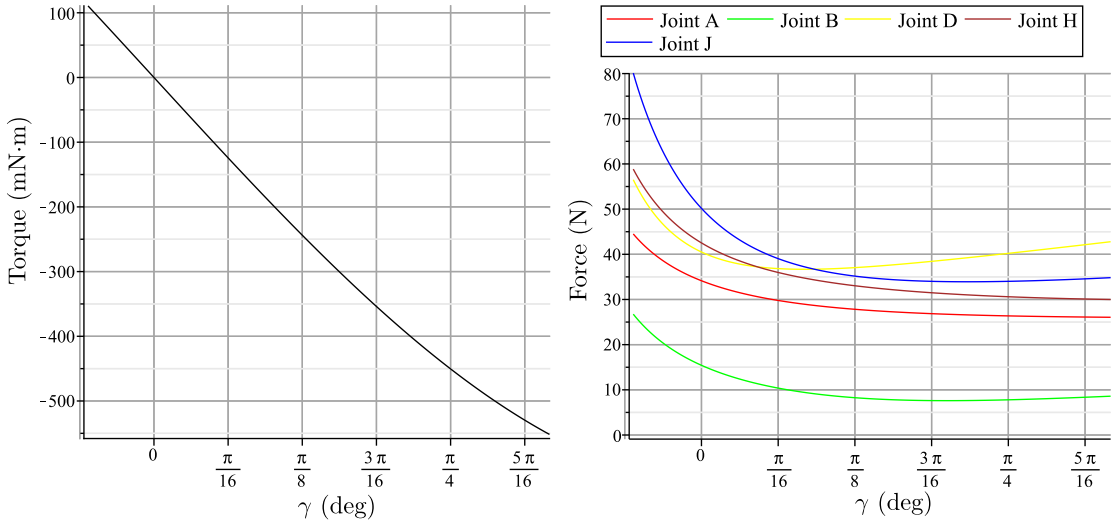

(a) Actuation torque M_2

(b) Norm of reaction forces at joints A, B, D, H, J.

Figure 3.16 – Variation of the actuation moment and the norm of joint reaction forces.

the actuation torque and the reaction forces in five revolute joints can be calculated and are plot in figure 3.16. The maximum values of the actuation torque and the maximum value of the norm of these reaction forces from these plots serve for selection of actuators and bearings for individual joints.

3.4 Solution for the ProteCT project

3.4.1 Comparison between the 2R and 2T2R mechanism candidate

The two positioning mechanism candidates 2T2R and 2R were discussed in this chapter along with their dimensional synthesis leading to workspace and static analysis. The interest of the

2T2R mechanism comes from the functionality to change the entry point on the surface of the patient's skin. However, serious drawbacks associated with ill-conditioned Jacobian matrices within the workspace were discovered. Suitability of the mechanism as the slave device during the teleoperation also came into question, as not all points in the reachable workspace can be reached without encountering very high actuation torques. Relatively higher level of actuation torques for the reachable points in the workspace reduced the feasibility of the selection of a suitable actuation technology, especially given the constraints of size and weight of the overall mechanism. Having a motor with higher actuation torque output means having bigger, heavier motor with bigger gearboxes. Moreover, the mechanism requires four such actuators accompanied by their gearboxes. Though the achieved workspace for the 2T2R mechanism candidate conformed to the typical requirements, it was difficult to achieve larger orientation ranges (> 30 deg) without increasing the overall height of the mechanism.

On the other hand 2R mechanism's workspace was found to be free from any singularities, serial or parallel within the desired workspace. Therefore, the utilization of the 2R mechanism candidate as the slave device would pose no problem for teleoperation. Also, the level of actuation torques were found to be much smaller for the 2R mechanism which enabled the choice of a suitable actuation and transmission technology while respecting the size and weight constraints. Also due to fewer DOF, the 2R mechanism needs only two actuators on-board which also facilitates their placement while avoiding intersection with the imaging plane of the CT scanner. A much larger workspace in orientation 60 deg, than the typical range 30 deg, can be achieved by the 2R mechanism candidate. Given the time constraints within the ProteCT project and the feasibility of practical implementation, the 2R mechanism candidate was retained for further analysis including the embodiment design.

3.4.2 CAD of the 2R positioning device

The CAD implementation of the 2R positioning device was developed by Benoit Wach during the course of his master thesis [Wach, 2014] carried out under the ProteCT project and the fabrication of the prototype is being outsourced. The figure 3.17(a) shows the base of the positioning device for strapping onto the patient body. The placement of two actuators on the base can be seen in figure 3.17(b). The first R joint would be realised by utilizing ball bearings on which a large spur gear with 250 teeth is attached rigidly. The transmission from the first rotary actuator is done through a coupling between a smaller spur gear with 28 teeth and the larger spur gear with a reduction factor of 8.9. The transmission from the second rotary actuator to the revolute joint is done through a worm drive. This makes it possible to use a small brushless servo actuator (31g, $\phi 13 \times 37$mm) with low actuation torque of 0.11mN·m whose output actuation torque was magnified by a reduction factor of 10, as a result of the worm drive coupling. For the actuation of the first revolute joint, the brushless servo motor with same specifications is used. The figure 3.18(a) shows the CAD of the parallelogram mechanism with the value of structural parameters given in equation (3.43). The overall CAD of the 2R positioning device is shown in figure 3.18(b). Parts shown in the CAD are either

commercial products in polymer materials like PEEK or would be prototyped/fabricated in polymer material. This ensures that apart from the two motors most of the positioning device remains transparent under the CT scanner.

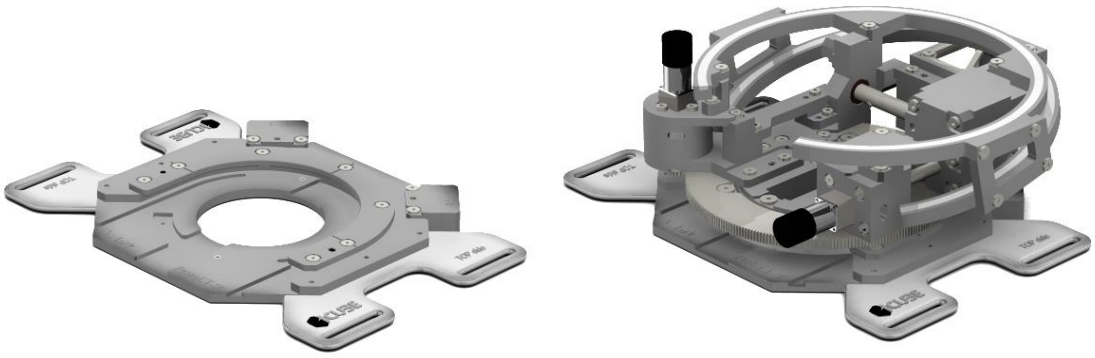

(a) Base for strapping the slave device on to the patient. (b) Base with two actuators.

Figure 3.17 – CAD of base of the positioning device [Wach, 2014].

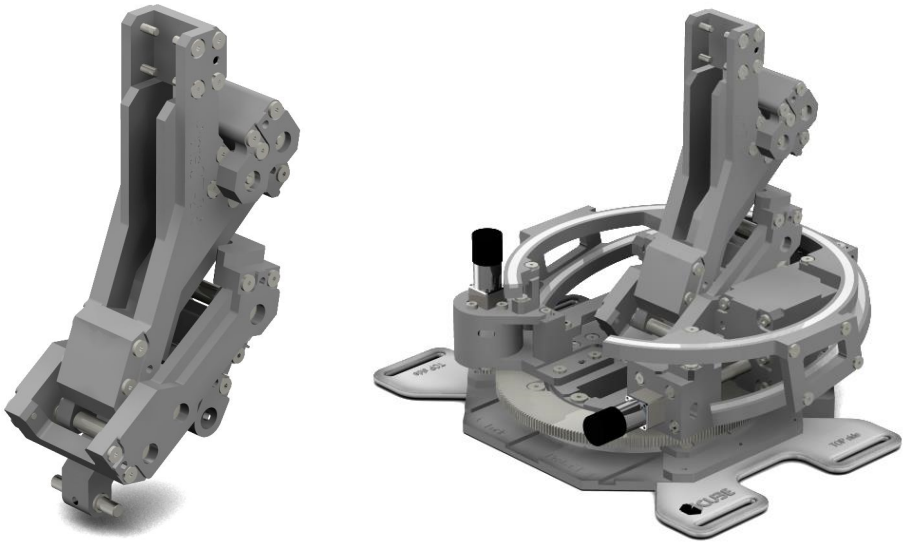

(a) Parallelogram mechanism. (b) CAD prototype of the 2R positioning device.

Figure 3.18 – CAD design of the positioning device [Wach, 2014].

3.5 Summary

As a result of the dimensional synthesis, the structural parameters of the 2T2R mechanism were calculated corresponding to the desired workspace requirements. Despite achieving the typical workspace size, the static analysis of the 2T2R mechanism candidate revealed limitations, specially for the choice of a suitable actuation and transmission technology for the application. Despite interest for such a 2T2R mechanism for the needle positioning, it could not be retained as solution for the needle positioning device for the ProteCT project. Modeling for the 2R mechanism candidate was also described. The workspace analysis revealed that despite a parallel singularity, a large orientation workspace is possible. Static analysis of the 2R mechanism was carried out taking into consideration its parallelogram structure. The values of the actuation moments and the reaction forces were found to be reasonable for choice of suitable actuation technologies and bearings for the joints. Therefore this 2R mechanism candidate was selected as the needle positioning device for the project despite the lack of needle positioning. A final CAD implementation of the prototype is presented with the integrated actuation and transmission technology.

An integrated dimensional synthesis algorithm which includes i) the generation of the workspace ii) the identification and the localization of the sensitive structural parameters to each singularity iii) the identification and the elimination of the voids was used for determining the structural parameters of 2T2R parallel mechanism candidate II. The systematic division of singularities into voids and external boundaries as well as the derivation of the inequality expressions for avoiding singularities is presented. As illustrated in this chapter, this method can be specially effective for the dimensional synthesis of lower mobility mechanisms, where the operational parameters are fewer in number. The static equilibrium conditions are closely linked to the degeneration of the Jacobian matrix which are also the parallel singularity conditions. Though the workspace requirements were successfully taken into account at the initial stages of the dimensional synthesis procedure, the requirements corresponding to the static equilibrium are still too complex to be considered, especially for asymmetric parallel mechanisms. This is partly due to difficulty in enumerating all possible parallel singularity conditions geometrically in vectorial form from the screw theory. For asymmetric parallel mechanisms, the degeneration of the Jacobian matrix is not regular and there can be isolated singularity configurations. In such cases, we can only evaluate the static equilibrium once the dimensional synthesis procedure has been completed. Better results are expected if this dimensional synthesis algorithm is employed for symmetric fully parallel mechanisms, where the systematic enumeration of parallel singularity configurations is possible via screw theory.

Insertion tool Part II

4 Design and development of the insertion tool

Contents

Insertion tool is perhaps the most important and critical part of the overall robotic needle insertion device. The functionalities of needle positioning and haptic force feedback discussed before have only the enabling effect on the final act of inserting the needle itself. The needle has to be grasped or fixed to the robotic device before insertion can take place. Conventionally, needle has been attached rigidly to the robotic device which is then inserted via a proper insertion mechanism. But the acts of the radiologists as observed during the manual workflow show that the insertion of the needle does not take place in a single step, but rather in a series of steps. Between these steps, needle is released and grasped again to allow it to move freely. This ensures that there are limited tissue lacerations due to a rigid needle placed inside the body trying to inhibit the movement of patient's organs during non-insertion phase. This necessitates the use of needle grasping devices which can mimic this functionality.

From literature survey several systems dedicated to needle insertion that consequently provide solutions for needle grasping, could be identified. The most frequent working principle involves opposing rollers to perform simultaneously the needle grasping as well as its insertion motion (e.g. Refs [Stoianovici et al., 2003; Walsh et al., 2008]). However, axial insertion force measurement turns out to be very difficult or even impossible with this principle since the

force measurement highly depends on the friction conditions with the needle barrel. To add this important functionality of axial insertion force measurement to a needle insertion device, it seems necessary to uncouple the needle displacement from its grasping. The schematic, in figure 4.1, shows the cycle of decoupled insertion and grasp/release of the needle. For

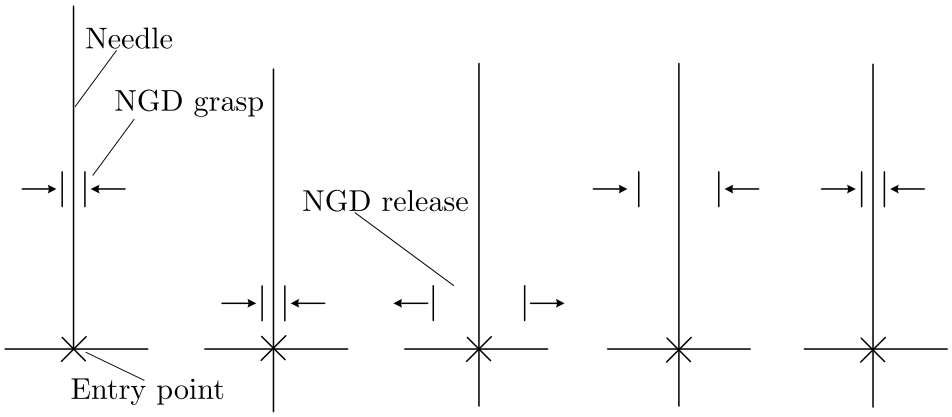

Figure 4.1 – Decoupled insertion followed by grasp/release.

instance, the axial force measurement issue is addressed in the system developed by [Badaan et al., 2011] with a custom built force sensor set on the transmission chain of the insertion motion. In this system, the grippers are snapped manually on the needle before the insertion starts and can be reopened on demand to release the needle. However, it does not provide a controlled feature for re-centering and gripping back the needle during insertion.

During the prior work in the lab, two versions of NGD were developed. The first miniature-chuck-based device which used a blocking part to avoid any movement of the needle was presented in [Piccin et al., 2005]. In this design, the functionality to release and re-grasp the needle during the insertion procedure was overlooked. In the second iteration presented in [Piccin et al., 2009], the needle grasping device design was taken up to include the previously missing functionality. During this thesis, a third variant of the NGD was designed and experimentally validated. This version improved upon the gripping force and the stiffness requirements by utilizing deformable parts. In this chapter, the task of needle insertion is separated into two separate functionalities of needle grasping and insertion. This allows to measure the axial needle insertion force, as mentioned earlier, which will be developed in the chapter 5. After a discussion on the possible mechanism candidates for the needle insertion, CAD implementation of the chosen insertion mechanism with choice of the actuation technology is presented. A general framework for the synthesis of the NGD is presented. The design of the rigid body NGD developed previously in the lab [Piccin et al., 2009] is briefly discussed. Thereafter, the new version of the NGD is presented in detail. An experimental assessment is carried out to compare the different versions of the NGD. The corresponding needle grasping device is mounted as part of the insertion tool on the robotic assistant as indicated in figure 4.2. The work presented on NGD in this chapter was done with Professor

Olivier Piccin and Professor Laurence Meylheuc of National Institute of Applied Sciences (INSA), Strasbourg and can be found in [Piccin et al., 2012]. The design and simulation of the NGD, including the FEA analysis, were developed by Professor Olivier Piccin and Professor Laurence Meylheuc.

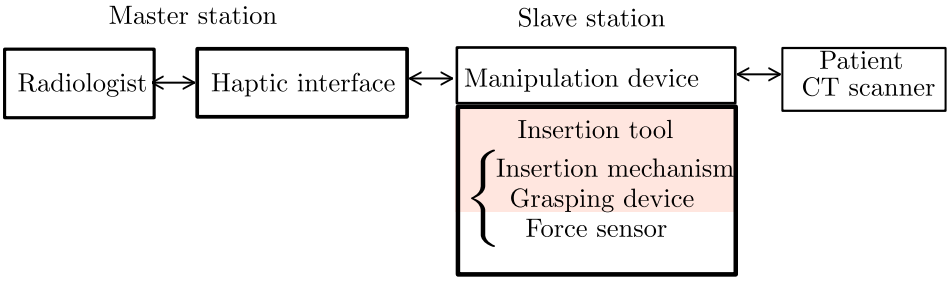

Figure 4.2 – The needle grasping device within the general layout of teleoperated percutaneous procedures.

4.1 Requirements for the insertion tool

The available space between a CT-scanner ring and a patient is a limiting factor as it was evoked during the design of the positioning device. Depending on the patient's build, the available space for the robotic assistant is at most of the order of 200mm. As this space is just enough to accommodate the length of most biopsy needles, the size of the insertion tool should be as small as possible. In addition, it is beneficial to comply with existing surgical needles, in terms of diameter and length, and thus avoid the use of a needle specific device. Another important feature for the insertion tool is the capacity to allow a wide opening around the needle. Given the space constraints mentioned before, the limit for the size of the insertion mechanism is set to 100mm. Moreover, the insertion mechanism should at least allow a stroke length of 25mm. The NGD should allow the centering of the needle during re-grasping. On the side of force transmission, the grasping device should sustain a maximum insertion action of 15N without letting the needle slip. Concerning the material requirement, the grasping device and insertion mechanism should not generate artefacts in CT scanner images so its construction needs to set a good level of radiolucency.

4.2 Insertion mechanism

As stated earlier, the most important functionality of the insertion tool is the ability to insert the needles inside body of the patient. The insertion DOF has to be achieved by a 1-DOF translation mechanism for guiding the needle along the insertion axis. This 1-DOF in translation can be achieved by a simple prismatic joint. A prismatic joint is most commonly realized by a simple linear guide. Metallic linear guides though very efficient in terms of friction between

the sliding surfaces, are heavy and not compatible with the CT imaging. A linear guide fabricated out of polymer would require lubrification which is not recommended due to possibility of contaminating the sterilized environment of the operating room. The transmission using helical gears and screw mechanism, as used in the work [Piccin et al., 2009], are not compact and can introduce inaccuracies due to the backlash in the gear coupling. In the work of [Hungr et al., 2012], rail and ball screw along with a rotary brushless DC servo motor are used for the insertion mechanism and its actuation. Usage of metallic DC servo motors with the insertion tool is not desirable due to artefacts produced by them with CT imaging. Mechanism with belt and pulley system actuated by piezomotors are used for the insertion mechanism in the work of [Seifabadi et al., 2012], which is not compact and can introduce inaccuracies due to flexibility and slippage of the belt on the pulley. In the work of [Walsh et al., 2008], rollers are used for combined action of gripping and insertion of the needle, which does not allow for direct measurement of axial insertion forces. A mechanism based on linkages with a prismatic and revolute joints is used in the work of [Badaan et al., 2011] for needle insertion, which produces an approximate straight line. This mechanism is asymmetric and consists of prismatic joints which introduces problems with the friction. Moreover, for our application we are interested in mechanisms which produce the exact straight line as compared to the approximate straight line mechanisms, as the guidance of the needle along the exact trajectory is very important for reasons of safety. Choosing a mechanism primarily with revolute joints for the transmission helps to avoid aforementioned drawbacks and be more accurate while maintaining a fixed needle axis orientation.

In the family of exact straight line mechanisms with revolute joints, there are many planar mechanisms based on linkages like the Peaucellier's linkage (figure 4.3a), Hart's A-frame (figure 4.3b). The Sarrus mechanism depicted in the (figure 4.3c) has a parallel 3-D structure and consists of two serial kinematic chains with three revolute joints each. Though the most common variant of the Sarrus mechanism produces a vertical straight line motion, other variants of the Sarrus mechanism producing tilted straight line motion can also be obtained, as described in the work [Li et al., 2013]. As stated in section 4.1, the insertion mechanism

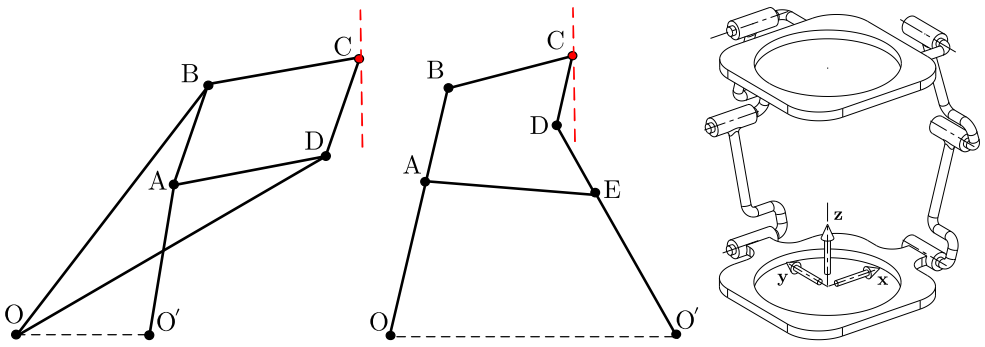

(a) Peaucellier–Lipkin linkage. (b) Hart's A-frame. (c) Sarrus mechanism.

Figure 4.3 – Examples of straight line mechanisms.

should allow a opening around the needle axis in order to let it pass through. Out of the three mechanisms, the Sarrus mechanism can satisfy this requirement. Due to the parallel 3-D structure, the Sarrus mechanism is preferred for the insertion mechanism in place of 2-D planar mechanisms. Also the symmetry of the legs in Sarrus mechanism around the needle axis allows for better rigidity as compared to asymmetrical planar mechanisms.

The Sarrus mechanism along with a cylindrical joint is chosen as the insertion mechanism for implementation of the electric actuation. The obvious solution is to actuate one of the revolute joints directly by placing an electric rotary motor. This solution would require heavier and bulkier motors along with transmission for the level of input motor torque which is not small for producing the insertion forces at the level of 15N. Therefore the base and the platform of the Sarrus mechanism are connected by the two linear piezoelectric motors for actuation of the one translational DOF. The linear piezoelectric motors from the PiezoMotor AB company can produce a nominal force output of 10N. These piezoelectric motors weight less than 30g

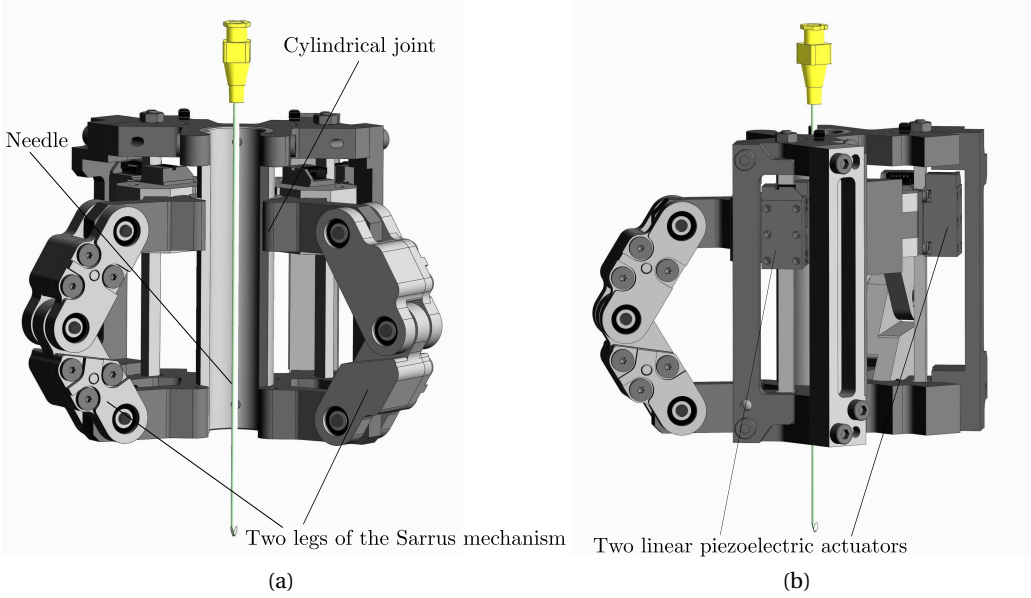

Figure 4.4 – CAD implementation of the insertion mechanism with two linear piezo motors (With François Schmitt).

and are very compact in form. Therefore these two piezoelectric motors are used to actuate the insertion mechanism. Here the Sarrus mechanism along with the cylindrical joint serves for the transmission of these forces to the needle. The CAD implementation of the insertion device with Sarrus mechanism in shown in figure 4.4(a). The length of the links of the Sarrus mechanism has been set to 29mm. With this link length, the Sarrus mechanism can easily achieve a stroke length of 25mm without any link interference. The overall height of the designed insertion mechanism is 80mm. It has been developed with François Schmitt who is a research engineer of the ProteCT project. The figure 4.4(b) shows the insertion mechanism

with two linear piezoelectric motors which are used for the actuation. As the insertion device has not been fabricated yet, the final prototype could not be shown.

4.3 Needle grasping device design

To establish the functional structure of a NGD, mainly four elementary subfunctions is considered, which can be formulated as (1) put obstacles around the needle, (2) move obstacles radially, (3) transmit motion to the obstacles and (4) actuate moving obstacles. This decomposition tends to formulate the essential problems at a higher level of abstraction in order to leave open possible solutions and make a systematic approach easier [Pahl et al., 2007]. The Table 4.1 presents several solution principles for the NGD subfunctions.

Subfunctions			Solution Principles 1	2	3	4	5
	1	SF_1	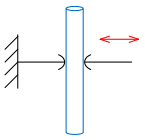	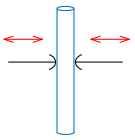	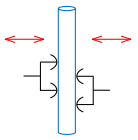	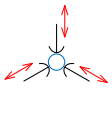	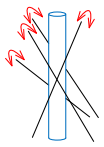
	2	SF_2	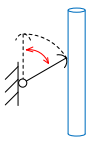	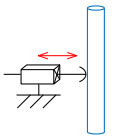	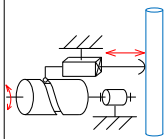	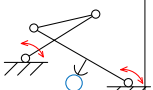	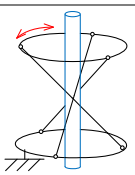
	3	SF_3	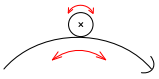	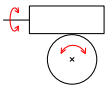	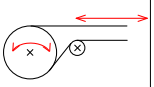		
	4	SF_4		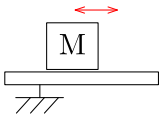	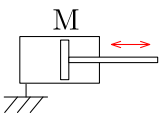		

Table 4.1 – Solution principles for the subfunctions of a NGD.

In the first row, the columns 1 to 5 describe several design principles to fulfill the subfunction SF_1. The simplest embodiment for this subfunction requires at least two opposing obstacles acting radially on the needle as described in the sketches 1 to 3. The solutions 4 and 5 suggest a higher number of obstacles in operation for gripping the needle barrel. Another important design option refers to how obstacles move with respect to the needle and how many contact points each obstacle does have with the needle.

In the second row of the table are presented some options to realize the motion of the obstacles. Basic ideas depicted in the first two columns correspond to a simple pivoting or translation of the obstacle. The solution principle 3 moves the obstacle using a radial slider driven by a slot-follower element. Columns 4 and 5 present two possible planar and spatial linkages that could serve for the obstacle motion. At this stage, the required motion to impart to the obstacles could be a rotation or a translation. Therefore, the last two rows of the table describe possible choices for actuation and transmission of the required motion to the obstacles.

In light of the proposed classification scheme, the gripping device of the Robopsy system [Walsh et al., 2008] corresponds to the solution variant of the first column, namely 1.1–2.1–3.1–4.1 whereas the two grasping devices developed in prior research work of the lab [Piccin et al., 2005, 2009] can be related to the variants 1.4–2.3–3.1–4.1 and 1.3–2.3–3.2–4.1. In section 4.3.1, construction details of the rigid-body NGD first presented in [Piccin et al., 2009] will be briefly given. A new design candidate based on the solution variant 1.5–2.5–3.2–4.1 will be discussed in more detail along with its design and experimental assessment. This solution variant is selected because the option 5 corresponding to SF_1 provides a line contact whereas point contact is obtained with other options. The transmission using worm gear is more compact than using spur gears for same reduction ratio, so the option 2 corresponding to SF_3 is selected. Also the transmission using belt and pulleys has disadvantages of slipping and therefore lacks in accuracy of transmitted motion. Rotary motor is better suited and is more compact than the linear motor, hence the option 1 corresponding to SF_4 is chosen.

4.3.1 Rigid-body NGD

The NGD presented in [Piccin et al., 2009] is used as a starting point to detail its construction issues. The proposed chuck comprises of a main body, two jaws, two pairs of rods and a gear as described in figure 4.5. During the tightening of the chuck, the displacement of each jaw is a translation along the direction followed by the rods 1 and 2 inside the slots 1 and 2 on the main body. Simultaneously, each chuck is driven by the slots 3 constructed within the bore of the gear and followed by the rods 1 (which are longer than the rods 2) when the gear is rotated about its axis.

The central problem for designing this type of NGD consists in constructing adequate slots on the gear to obtain the desired grasping function. The construction of the slots 3 within the gear must be compatible with the translation of the jaws within the main body. This problem can be reformulated geometrically using a kinematic inversion for the chuck mechanism. The gear is now considered as fixed to the ground and a jaw is moving with a combined motion of translation and rotation. During this displacement, the line Δ coincident with the axis of the rod 1 intersects the cylinder $\mathscr{C}$ formed by the bore of the gear and the resulting curves can be used to cut the appropriate slots 3 in the gear. To this end, it is required to determine the equations of these curves.

Let us denote $\mathscr{R} = (O, \mathbf{x}, \mathbf{y}, \mathbf{z})$ a reference frame, such that the cylinder $\mathscr{C}$ has $(O, \mathbf{z})$ as its axis

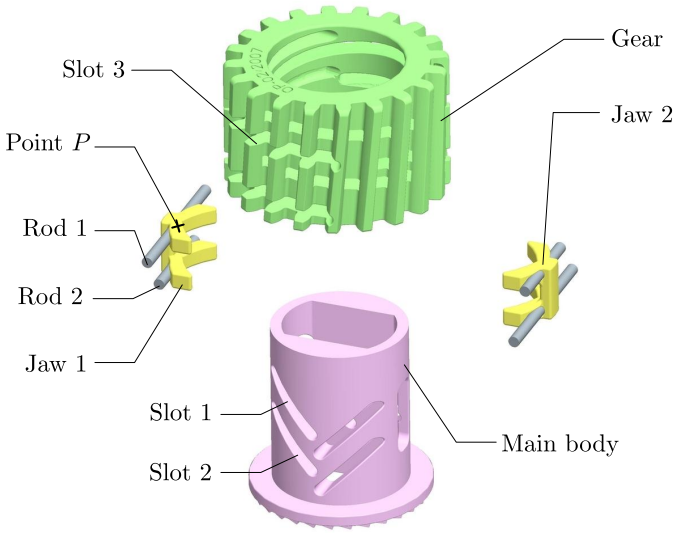

Figure 4.5 – Exploded CAD view of a rigid-body NGD [Piccin et al., 2009].

and radius R. The line Δ is undergoing a combined motion of rotation and translation in space and its intersecting curves with the cylinder $\mathscr{C}$ need to be determined. Additionally, the line Δ always lies in a moving plane which keeps orthogonal to the cylinder axis. The line Δ is defined by a point P and a unit vector $\mathbf{u}$ and an orthonormal basis $(\mathbf{u},\mathbf{z},\mathbf{n})$ is attached to Δ. The configuration of Δ with respect to $\mathscr{R}$ can be described using three parameters: θ defined by $\cos\theta = \mathbf{x}\cdot\mathbf{n}$, $r = \mathbf{OP}\cdot\mathbf{n}$, $z = \mathbf{OP}\cdot\mathbf{z}$ as indicated in figure 4.6.

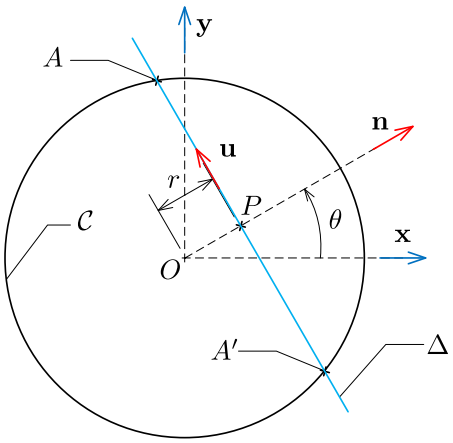

Figure 4.6 – Parameterization of the moving line Δ.

Depending on the value of r with respect to R, there may be no solution ($r > R$), one single point solution when $r = R$ or two solution points (A and A') when $r < R$. This last case is studied, since the other ones are of no practical interest. In this case, the moving line Δ

generates two spatial curves Γ and Γ' traced on $\mathscr{C}$ corresponding to the set of points A and A'. It should be noted that each of two points A and A' are symmetric with respect to the axis $(O, \mathbf{n})$.

The intersection curves Γ and Γ' can be described by the vector function

$$\Gamma_\varepsilon(\theta, r, z) = r\,\mathbf{n} + \varepsilon\sqrt{R^2 - r^2}\,\mathbf{u} + z\,\mathbf{z} \tag{4.1}$$

where r, θ and z are functions of a parameter t chosen in the interval $[0;1]$ and where the value ε, taken in set $\{-1;+1\}$, determines the curve Γ or Γ'. For sake of simplicity the functions were chosen linear with respect to t as following:

$$\begin{cases} r(t) = r_{max}\,t & (4.2) \\ \theta(t) = \theta_{max}\,t & (4.3) \\ z(t) = z_{max}\,t & (4.4) \end{cases}$$

where r_{max}, θ_{max} and z_{max} denote constant parameters describing the final position of Δ. figure 4.7 depicts the intersection curves Γ and Γ', defining the geometry of the slots 3 drawn for some values of the rotation angle θ_{max}.

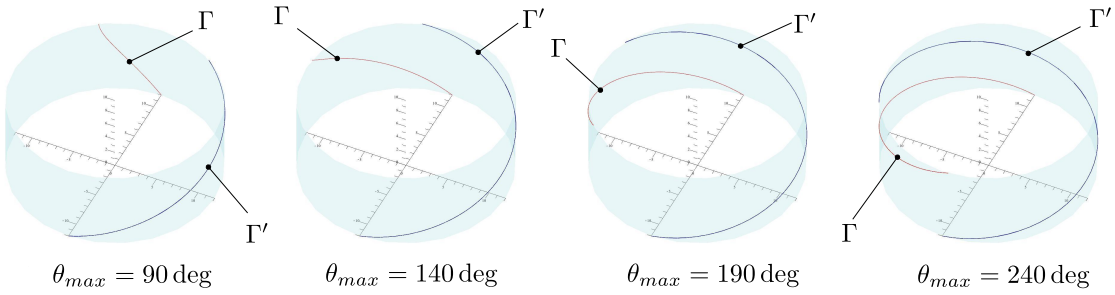

Figure 4.7 – Intersection curves Γ and Γ' for some values of θ_{max}.

To fulfill a slot-follower function for each jaw it is necessary to generate two couples of curves Γ and Γ' with sufficient axial offset along the cylinder axis to ensure a minimum wall thickness between the slots and to avoid any curve crossing. The influential parameter to validate this condition is the angle of rotation θ_{max} which was set to 140 deg.

The resulting NGD can provide a theoretical grasping force F exerted by each opposing jaw on the needle barrel which is related to the driving torque τ_m applied by the motor

$$F = \frac{n\theta_{max}}{n_j r_{max}}\tau_m \tag{4.5}$$

where n and n_j denote respectively the number of teeth of the gear and the number of jaws (here, $n_j = 2$).

4.3.2 Flexible-body NGD

The second NGD that is considered here uses thermoplastic flexible parts. In this design variant the number of moving obstacles is increased to three. Constituting parts of this NGD are shown in figure 4.8 and include a main body on which, three flexible jaws equipped with high grip neoprene pads, are hinged. Each jaw is then connected to the gear via a pin joint. Simultaneously, the gear is guided in rotation with respect to the main body part.

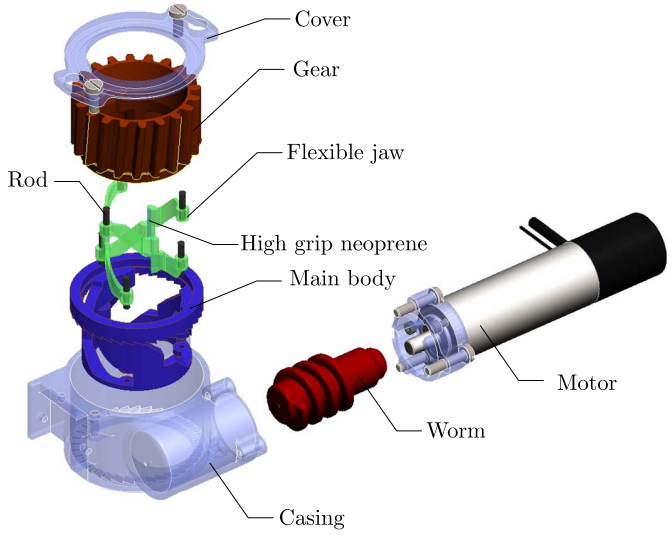

Figure 4.8 – Exploded CAD view of the flexible NGD with the servo actuator.

The geometry of the jaw has been iterated to provided two interrelated models, namely a pseudo-rigid-body model [Howell, 2001] and the corresponding flexible and monolithic form of the model as described in figure 4.9.

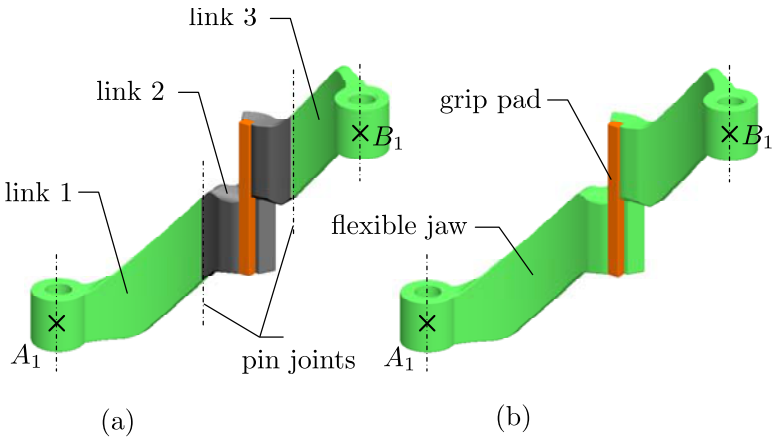

Figure 4.9 – CAD view of one flexible jaw in (a) pseudo-rigid-body form (b) and in monolithic form .

Pseudo-rigid-body modeling

To investigate the NGD behaviour and iterate its design, a pseudo-rigid-body model has been constructed in which each jaw was segmented into three rigid links connected by pin joints as indicated in figure 4.9 (a). During the NGD operation, the end point A_1 of a flexible jaw is hinged to the fixed main body part whereas the other end point B_1 is driven on a circle by the rotating gear as depicted in figure 4.10. The NGD closes with a 90 deg rotation of the gear and

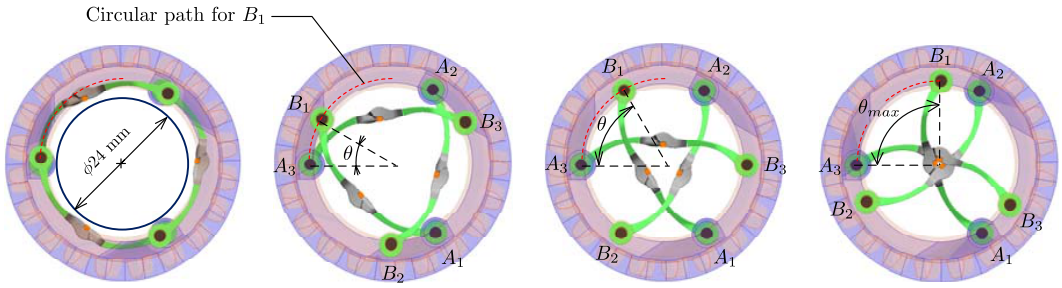

Figure 4.10 – CAD topview of the flexible NGD operation.

allows a maximum clearance included within a cylinder with diameter 24 mm. The theoretical grasping force of each jaw can be calculated using equation (4.5) with $\theta_{max} = 90$ deg, $r_{max} = 12$ mm and $n_j = 3$.

The pseudo-rigid-body modeling was not formulated to arrive at an approximate model for calculating the associated deformation as result of the movement of jaws, as a detailed numerical FEA model, described in next section, can give more accurate results. However, the pseudo-rigid modeling allowed to simulate the movement of jaws in Pro/Engineer, which otherwise would be not possible. The pseudo-rigid modeling was done as an intermediate step to verify the functioning of the NGD with the CAD design, before moving on to the detailed FEA calculations for obtaining the deformation and stress levels.

Flexible-body modeling

When considering the jaws as deformable bodies, the closing of the NGD causes a coordinated motion and deflection of the three jaws around the needle. In the case of thermoplastic parts such as those considered in this NGD, the low material stiffness and yield strength could create the conditions for nonlinear behaviours to occur [Trantina and Nimmer, 1994]. However, in the proposed NGD design, the dominant source of non-linearities comes from geometry and the occurrence of contact conditions between the jaws and the needle. Thus, it is assumed here that the problem includes mainly geometric and contact nonlinearities and can be consistently solved using linear material behaviour. As a result, the large displacement imposed to the jaws generates stresses and strains on the deformable parts which need to be calculated to check both the NGD functionality and the parts failure. For this purpose, two

operating phases for the modeling of the flexible NGD are considered which are following : i) the motion of the jaws in free space during the NGD closing and ii) the interaction with the needle barrel during the grasping itself. This loading scenario requires the modeling of large strains induced by the large displacement of the jaws rotated by the gear. This problem has been solved with a nonlinear FEA code allowing contact analysis.

Meshing The geometry of the parts were imported from CAD and included a segment of the needle and the three jaws equipped with high grip pads. The resulting mesh shown in figure 4.11 (a) uses 4-node tetrahedral elements for the jaws and the neoprene pads and 6-node wedge elements for the needle. Meshing of the jaws and the pads has been refined in regions where large stress gradients are expected such as in the contact area. The total number of nodes for the entire model is 36 270. Each part of the FEA model was assigned with the corresponding material namely polymer resin for the jaws (PX220, Axson Tech. Inc.), neoprene for the pads and stainless steel for the needle. The polymer resin was chosen to be compatible with the fabrication process described in subsection 4.3.2.

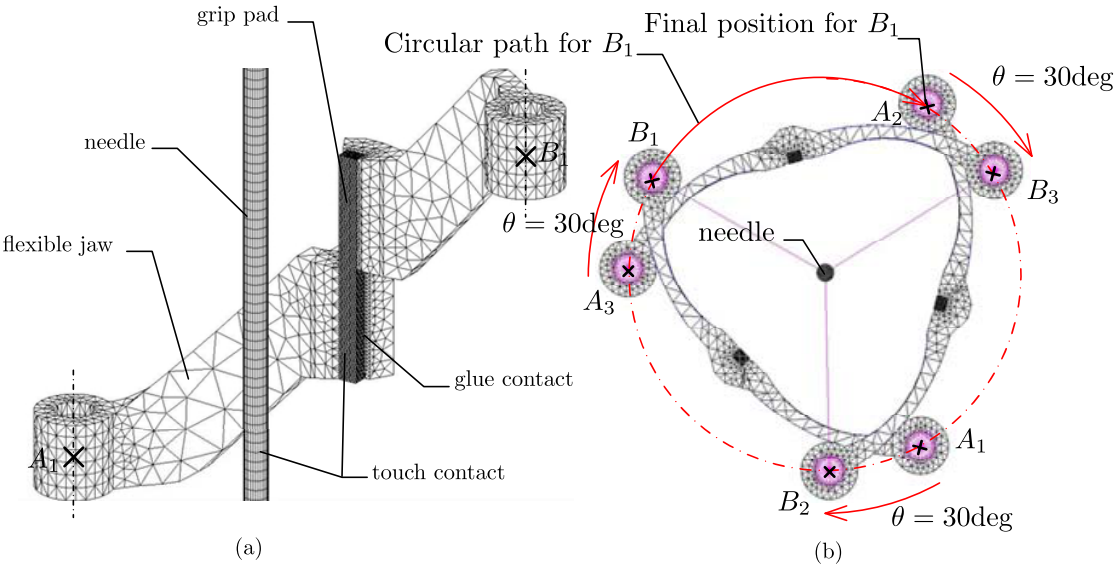

Figure 4.11 – (a) Mesh for one of the flexible jaw and a portion of the needle, (b) Boundary conditions and loads applied on the flexible NGD.

Boundary and loading conditions The modeling of the pin joints at both ends of each jaw is conducted using rigid body elements. A node at the hole center is rigidly connected to all the nodes on the hole circumference as indicated in figure 4.11 (b). This technique blocks the node motion in the radial direction but leaves them free to rotate about the hole center. The points A_i and B_i (i = 1..3) are respectively attached to the fixed main body part and the

rotating gear. Contacts are set between the jaws and the grip pads (indicated as glue contacts in figure 4.11 (a)) whereas contact areas between the grip pads and the needle barrel are specified in the model and denoted touch contact in figure 4.11 (a).

Loading conditions on the jaws are applied in the form of imposed displacements of the points B_i along a circular path centered with the needle axis.

Results The resolution of the problem with three moving jaws has been solved. firstly the displacements of the jaws during the closing of the NGD was understood. The figure 4.12 (a) and (b) present the displacements of the deformed shapes of the NGD with an indication of the starting configuration plotted in wireframe display style. As the first contact between the grip pads and the needle is gained at the configuration $\theta = 88$ deg, the analysis has been continued until $\theta = 120$ deg.

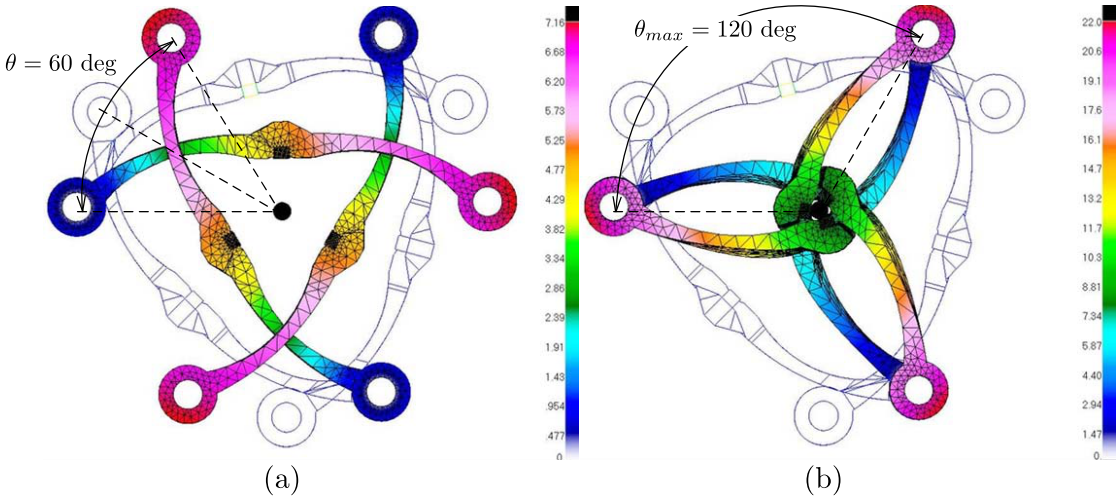

Figure 4.12 – Displacements distribution for the flexible NGD at (a) intermediate position $\theta = 60$ deg and (b) at final position $\theta_{max} = 120$ deg .

At this fully tighten position, the principal maximum strain for the jaw is located in the central area of the part as shown in figure 4.13 (a) and (b). Its value is in the order of 10 % which corresponds to the elongation at break for the chosen resin.

The Von Mises stresses in the configuration $\theta = 103$ deg are displayed in figure 4.14 (a) and (b) for a single jaw. The maximum VM stresses are also located in the central area of the part as shown in figure 4.13 (b). The location of stress concentration coincide with the highest level of strain. After reviewing the Von Mises stress results, one can note that the yield stress is reached for $\theta = 103$ deg. Consequently, a rotation of the gear by an angle in the range 103-120 deg may potentially deforms the jaws irreversibly.

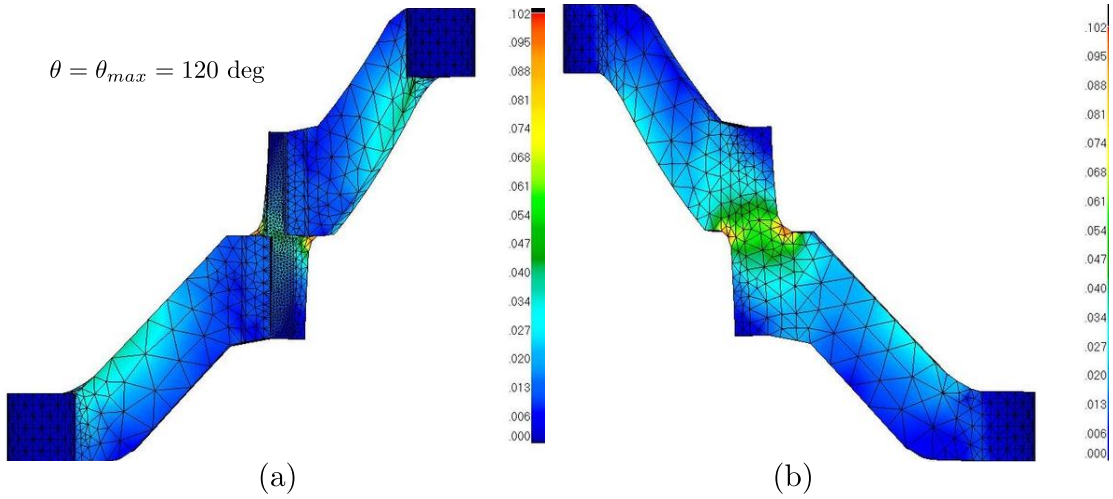

Figure 4.13 – Principal maximum strain for the flexible NGD at the fully tighten position θ = 120 deg: (a) front view and (b) back view .

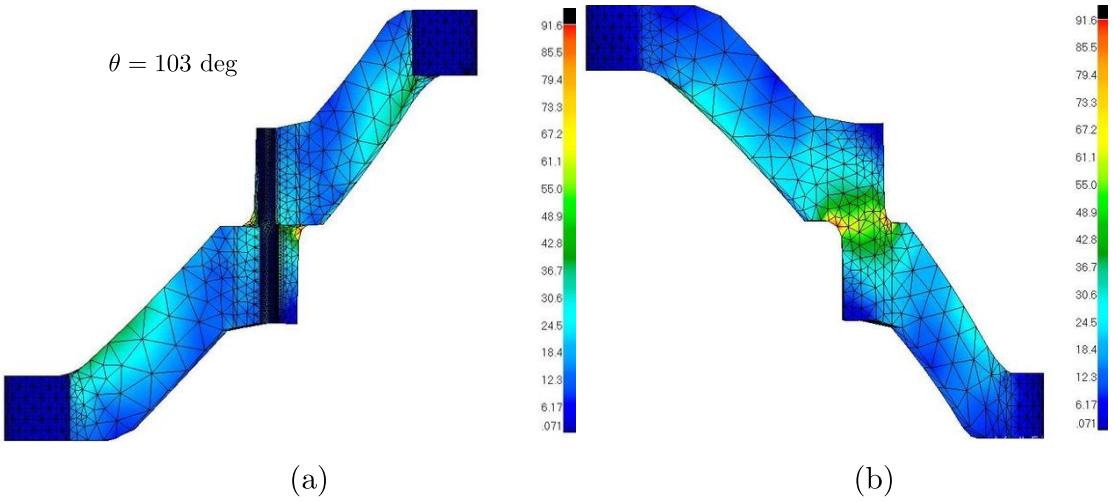

Figure 4.14 – Von Mises stresses calculated for the flexible NGD at the angular position θ = 103 deg: (a) front view and (b) back view .

Fabricated prototype

The flexible NGD has been fabricated using rapid prototyping techniques. The most critical parts in the NGD are the jaws due to the high level of strain and displacement applied on them. Consequently, the required mechanical properties for the yaws turned out to be difficult to obtain with classical 3D printing machines. Starting from a master part corresponding to the jaw fabricated with a conventional 3D printing machine, a silicon mold was constructed and a small series of parts could then be obtained using vacuum casting.

4.4 Experimental assessment of the NGD

The most important functional characteristics of the proposed NGD, is their ability to maintain the grip on the needle over the range of forces and the range of rate of force variation applied to it. The objective of the experiments is to characterize the grasping capability of both of the proposed NGD and assess the maximum force sustained by the NGD, without allowing the needle to slip. In real medical applications, the rate of change of force may vary depending upon the density of tissues encountered. For example, at the rupture of tissues there are sudden changes in force over very small periods of time.

4.4.1 Experimental setup

The experimental set-up consists of a traction machine from Zwick, GmbH (Z005 THN - Allround Line), capable of applying varying magnitudes of force and rates of change of force to the cross-head. An 18 gauge (1.3 mm), polished, stainless steel needle is held between the jaws which is attached to the cross-head. Both of the NGD are actuated by a Harmonic Drive DC servo motor (RH-5A-5502), which is controlled by another computer via I/O cards.

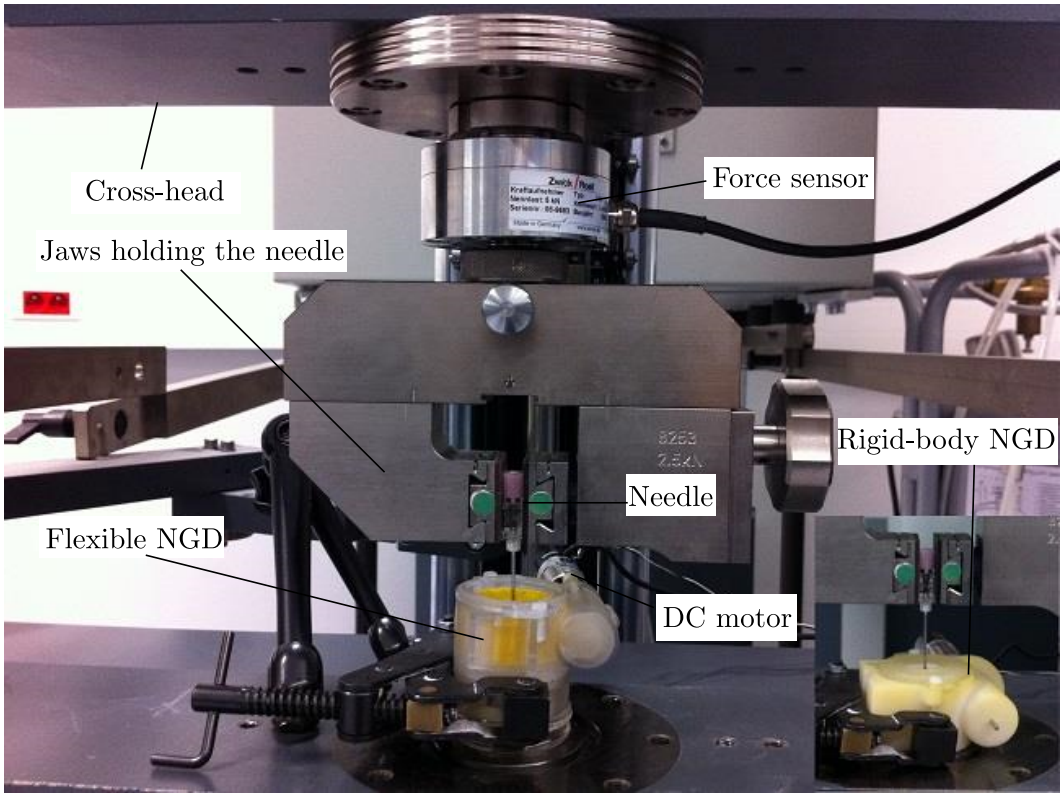

Figure 4.15 – Description of Experimental Setup.

In figure 4.15, the essential components of the experimental setup namely the cross-head,

a force sensor, the needle, two NGD and a passive manipulator for holding the NGD rigidly during experiment, can be seen. A force is applied to the cross-head by the traction machine, which in turn applies the force on the needle grasped tightly between the NGD. During the experiments, there is no slipping between the proximal end of the needle and the chuck jaws of the traction machine, so that the NGD experiences the same amount of force. The input current to the motor was maintained constant, so as to maintain a constant grasping force for each experiment. Also length of the needle, at which the NGD grasp it, is same for all experiments. This was done to maintain the same constant set of conditions at the beginning of each experiment.

4.4.2 Results

In this section, results of the traction experiments conducted on the proposed NGD and a qualitative and quantitative comparison of their respective performances, are presented. A total of 58 experiments were conducted on the rigid-body NGD and total of 46 experiments on the flexible NGD. For the rigid-body NGD, experiments were stopped after slipping of 4 mm, whereas for flexible NGD, experiments were stopped after slipping of 6 mm. Same can be observed in figure 4.16(*b*).

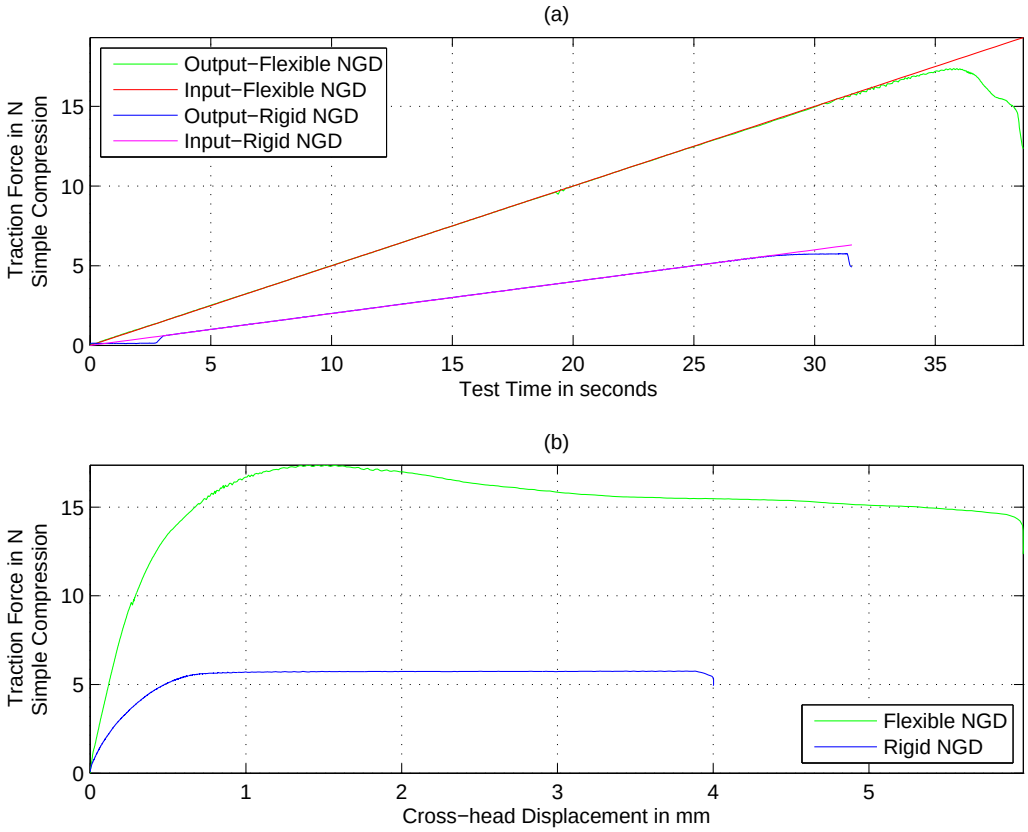

Figure 4.16 – Results of the Simple compression Loading.

During needle insertion two distinctive phases in the force profile could be observed i) a phase of constant rate of change of force when the needle is being inserted gradually through tissue of uniform density ii) a phase where force suddenly decreases over very small period of time, for example during tissue ruptures or sudden changes in tissue density. Therefore, experiments were designed in two parts: i) The input rate of change of force was kept constant, This part is named simple compression loading. ii)The different segments in the input force profile, each segment with a varying rate of change of force, were introduced. This part is named variable loading.

For the simple compression loading, the rate of change of force was kept constant, as shown in figure 4.16. The typical results for Rigid-NGD and for Flexible-NGD are presented. In figure 4.16(*a*), it can be observed that both of the NGD are capable to comply with the input force, as the curves for the input and the output fall on each other, until a certain threshold force, when the slipping occurs. Also it can be observed, that the value of the threshold force for flexible NGD is much higher than that for rigid body NGD.

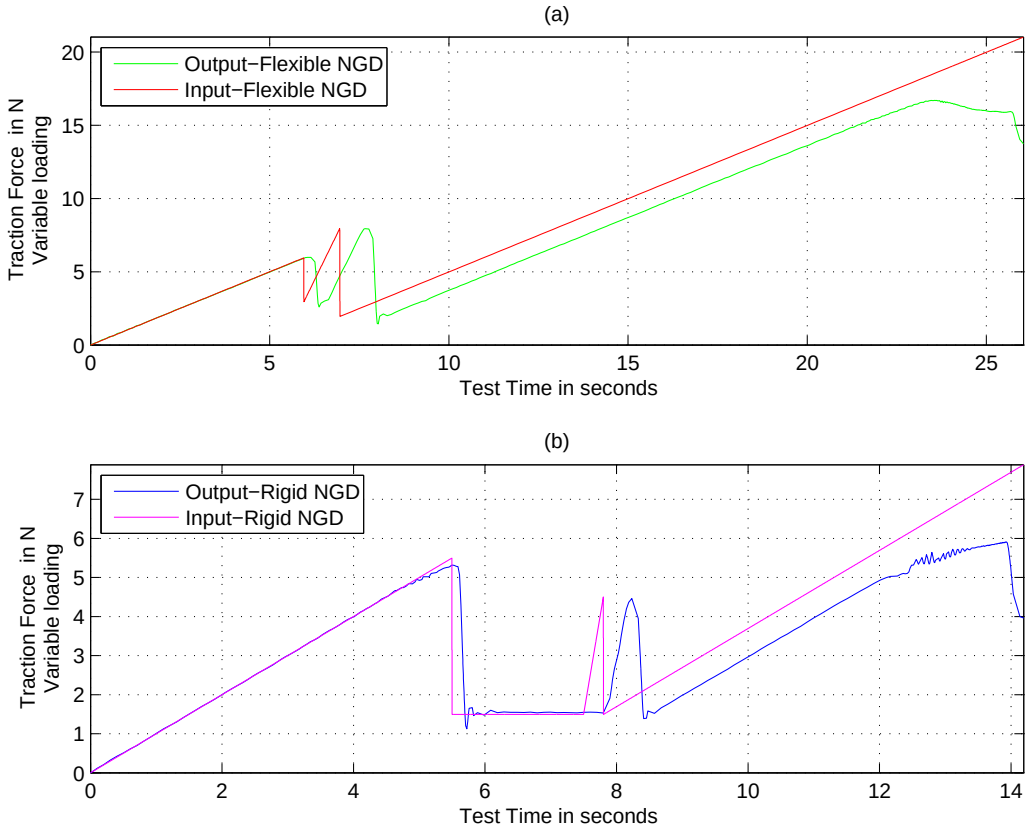

Figure 4.17 – Results of the Variable Loading.

For the variable loading, the force was allowed to decrease sharply, hence creating a rate of change of force of the order 1kN/s, the magnitude of which agrees with *in vivo* experimental

data presented in [Piccin et al., 2009].

In figure 4.17(a) and 4.17(b), two such instances of sharp decrease in forces were allowed. It can be observed that before this sharp change, compliance of the NGD with input force profile is very good. At the first decrease, It is observed that there is a short time delay between the input and the output. There is rough compliance with the upper and the lower levels of the force but time taken is evidently larger. This effect is more pronounced after second decrease of the force and It can be clearly noticed, that there is some time delay between the input force and output traction force, but again there is rough compliance with the upper and the lower levels of force. For the flexible NGD and the curve shown in figure 4.17(a) average of absolute difference for the upper and the lower levels of the force is less than 0.02 N and 0.5 N respectively. For the rigid NGD and the curve shown in figure 4.17(b) average of absolute difference for the upper and the lower levels of force is less than 0.1 N and 0.2 N respectively. Therefore, both of the NGD are capable of reproducing sudden change in input force as output, without letting the needle slip though with a time delay, importance of which grows with number of such sudden changes in force. In a way this points to a limit of the rate of change of force to which NGD can comply with. The experiments are allowed to continue after the sudden changes in input force, to test for threshold force at which slipping occurs.

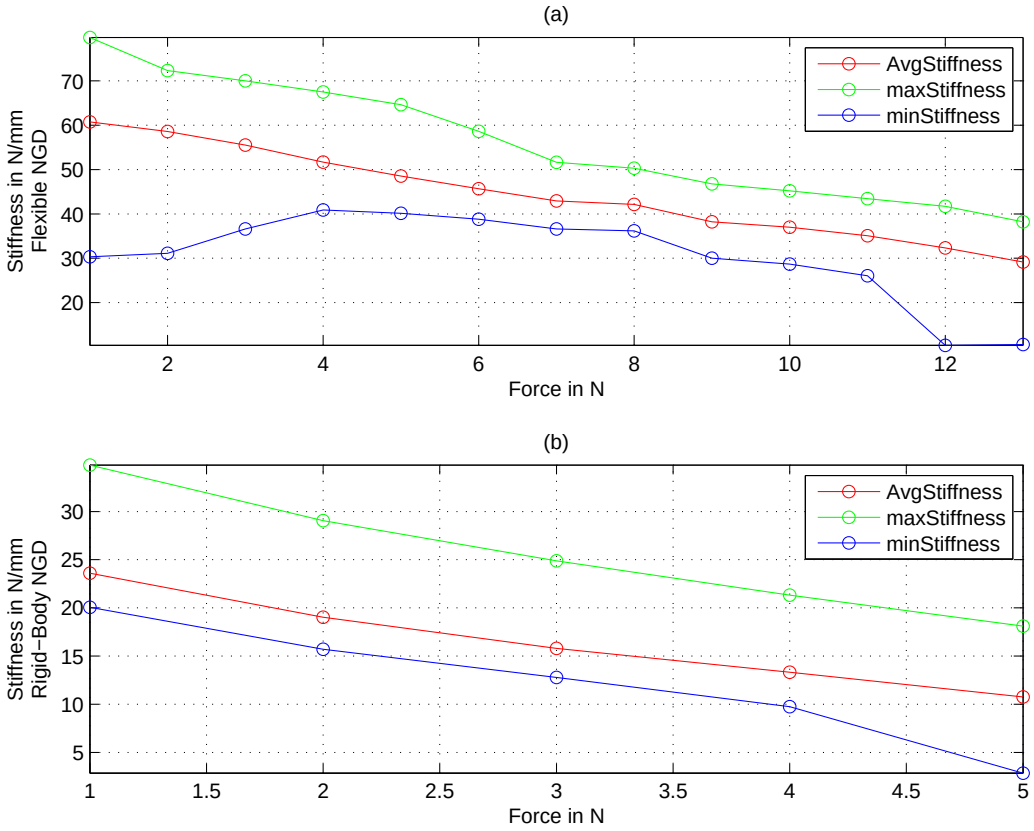

Figure 4.18 – Stiffness Characteristics of the NGD.

During needle insertion, stiffness plays an important role, for needle must not slip when there are sudden and big changes in the force. Stiffness here is defined as slope of the straight line passing from the point on curve in figure 4.16(b) through the origin. In figure 4.18(a) and figure 4.18(b), the quantitative measures of the stiffness at different levels of the input force are presented. This figure also describes the average value of slipping for both NGD at different force levels, which can be obtained by dividing the force level with average stiffness value. Threshold value of force, at which the needle starts slipping is not very well defined. Ideally it should be defined as the force at which instantaneous slope of the curve shown in figure 4.16(b) is nearing to zero. Here threshold value for slipping has been defined as the force at which the needle has slipped by 0.5 mm. This definition is more conservative than ideal one and required for safety considerations. The magnitude of the force for this threshold value is less than that of the ideal threshold value. In figure 4.18 the limit of the 13 N for the flexible NGD and the limit of the 5 N for the rigid-body NGD were chosen, because at these force limits, respective NGD have slipped on an average of less than 0.5 mm. As evident from this figure, the average stiffness of the sample decreases as force increases.
A comparative study of the above figures suggests that the flexible NGD outperforms the rigid-body NGD both in the value of the threshold force and the stiffness values. These results are of course influenced by several factors which might be improved by, for example, using a material of higher coefficient of friction between the NGD and the needle, to improve the traction force.

4.5 Summary

This chapter discussed the design and development of the insertion tool with the capability of needle insertion and needle grasp/release. However these two functionalities were achieved by two separate subsystems for allowing measurement of axial needle insertion forces. The needle insertion mechanisms used in the literature were discussed. Among linkage based mechanisms producing a straight line, with revolute joints, the Sarrus mechanism was chosen to serve as the insertion mechanism. The linear piezoelectric actuators were selected for actuation of the insertion mechanism. Finally the CAD implementation of the insertion mechanism was presented. The availability of the NGD appears to be a limiting factor to the development of robotized needle insertion assistants. The development of the NGD aims to incorporate the important act of needle grasp/release in the new robotized workflow. The work prior to thesis, relating to the design and development of NGD, was discussed briefly. The design and development of a new variant of the NGD based on flexible parts was presented. A comparative experimental assessment of this NGD and the prior version based on rigid parts was carried out. This study showed improved performance of the flexible NGD both with respect to the maximum level of force sustained and the overall stiffness characteristics. The flexible NGD also has a wider aperture to allow free motion of the needle when it is required by the medical procedure but remains compatible with needle re-grasping.

5 Force sensor for measurement of axial needle insertion forces

Contents

In the previous chapter 4, design and development of the insertion mechanism and the NGD as part of the insertion tool were covered. The insertion tool also comprises the force sensor for measurement of axial insertion forces and providing haptic force feedback to the radiologist. As the radiologist is not in direct contact with the patient, haptic force feedback [Okamura, 2004] is needed to help him in a bilateral teleoperation scenario. Apart from visual feedback from the CT imaging modality, the fine perception of interaction forces between the needle and tissues might help the radiologist in his/her gestures and decisions, as discussed in many contributions like [Gwilliam et al., 2009; Talasaz et al., 2012; Gerovich et al., 2004]. With this feedback, the radiologist can better detect the transitions between different organs or tissue layers of different density. The key events, such as tissue rupture where there is a sudden decrease in the level of interaction forces, can be immediately felt by the radiologist. Force sensors are recommended for providing this force feedback to the surgeon due to their higher accuracy leading to a better restitution of the haptic cues. Though forces sensors are not the only means to provide the force feedback. In the work of [Herder et al., 1997; Tolou and Herder, 2009] statically balanced compliant laparoscopic graspers are used to provide force feedback to the practitioner. This solution to provide the force feedback is not feasible in the teleoperation scenario where the insertion tool is not controlled manually but through a haptic master device.

The direct utilization of off-the-shelf commercial force sensors is not possible due to limitations imposed by the imaging modalities like CT or MRI on usable materials. Since MRI uses high magnetic fields, no ferromagnetic material can be present within its close surroundings. The imaging through X-rays produces artefacts in the image due to presence of predominantly metallic elements in the commercial force sensors. This distorts the image containing needle axis and may render it useless for extracting the needle axis position and orientation. The constraints of the MRI are more strict than those of CT which does not require total elimination of the electrical components. Several works [Gassert et al., 2006, 2008; Polygerinos et al., 2013] can be found on MRI compatible force sensors utilizing polymers as material and a sensing principle based on light to avoid any electrical components. The range of the measured forces and the DOF of these sensors vary depending on the medical intervention. Utilizing a polymer as a force sensor material introduces non-linearities, which can significantly affect its accuracy and performance if they are not properly modeled and accounted for. The above papers do report hysteresis but no modeling and compensation is proposed. In the work [Tan et al., 2011], the development and modeling of a triaxial force sensor for MRI compatibility is presented. To compensate for the hysteresis effects in particular, a nonlinear model using play operator of Prandtl–Ishlinskii [Al Janaideh and Krejci, 2013] has been used. The nonlinear models could potentially be less robust to noise, more complicated to model and sensitive to direction of loading. This approach models the hysteresis but may not model truly the nonlinearities of the system. A physical linear viscoelastic model involving springs and dashpots such as found in work of [Palli et al., 2012] can provide a good approximation of the inherent nonlinearities including hysteresis.

This chapter presents a new solution for a CT compatible force sensor with the ulterior motive of providing haptic force feedback to the radiologist, in the context of minimally invasive interventional radiology. This force sensor is part of the overall insertion tool which is mounted on the slave positioning device, as described in figure 5.1. The requirements

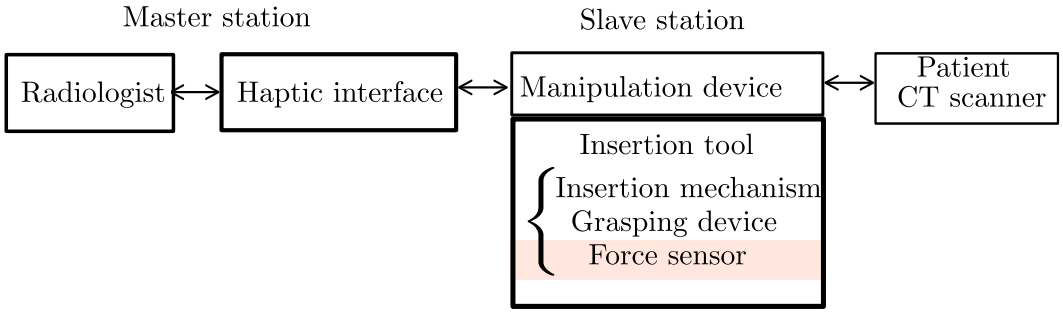

Figure 5.1 – The force sensor within the general layout of the teleoperated percutaneous procedures.

and the technical specifications of the required sensor are detailed and enumerated. Based on this information, the design of the force sensor and its flexure element is taken up and verified by a finite element simulation. First the static calibration and results for the quasi-static experiments are given which reveal the hysteresis and the time-dependent viscoelastic effects. Hence, a systematic identification procedure for the choice of a viscoelastic model has been proposed by considering the creep behaviour of the sensor and comparing it to the existing viscoelastic models. Thereafter, the parameters of the chosen viscoelastic model are obtained by curve fitting of the experimental creep response to its theoretical response. A novel compensation law has been proposed to correct the sensor signal from errors arising from these viscoelastic effects. This compensation law is robust to noise, computationally inexpensive and applicable to the sensor signal in real-time. Finally, this compensation law is applied to sensor signal arising from quasi-static to dynamic experiments including harmonic analysis. Upon comparison with simple elastic model with no compensation, the sensor signal with compensation shows much decreased levels of hysteresis and an improved dynamic response. A preliminary version of the work presented in this chapter has been presented at the IEEE/ASME AIM 2014 conference [Kumar et al., 2014c] and an extended version has been submitted to the IEEE journal of transactions on mechatronics for review.

5.1 Requirements for a CT compatible force sensor

Based on the literature review and the task of needle insertion, the following key requirements and technical specifications can be arrived:

a) **Size**: The designed force sensor is an integral part of the robotic assistant which may take the form of a table-mounted [Stoianovici et al., 2003] or patient-mounted [Maurin et al., 2008]

system. Mounting the robotic assistant on the patient leads to a more compact design with smaller footprint. After the introduction of a patient in the tunnel of a CT scanner, the available height is less than 300 mm [Walsh et al., 2008]. This constrains the size of the robotic assistant and all of its components. As a result, the force sensor has to be as compact as possible and a maximum volume of 25 × 25 × 25 mm has been put as the constraint on the size of the force sensor.

b) **Transparency of the insertion force transmission**: There could be scenarios, where the force sensor does not lie directly along the axis of insertion and involves intermediate mechanisms for transmission of the insertion forces. In such cases, the effect of friction in the transmission mechanism and the nature of the underlying mechanism itself changes the insertion force signal. This strategy does not ensure the transparency of transmission of the actual insertion force. It is preferable to have the force sensor lying along the insertion axis and to avoid the use of intermediate mechanisms. This would in turn require that the force sensor has a through hole at its center for allowing passage of the needle.

c) **Material - CT scanner compatibility**: CT scanner compatibility does not require a total elimination of the metallic parts. The appropriate CT image acquisition requires the imaging plane of the CT scanner to be free from interference of any artefacts. As the force sensor geometry needs to be defined so as to surround the needle barrel, its constitutive materials should be radiolucent. Hence, a polymer based material has to be chosen for fabrication of the prototype.

d) **DOF of the sensor**: The work of [Maurin et al., 2004] studied the *in vivo* evolution of forces during needle insertion in an anesthetized swine. The measure of forces and moments along the transverse directions were found to be in the order of 10^{-3}N and 10^{-3}Nmm, respectively, which is very small compared to the order of magnitude of the axial forces/moments. Hence, the component of the force in the axial direction is sufficient to give the radiologist the needed feedback for detecting the key events such as tissue rupture or traversing through tissue layers of different density. Hence, a 1-DOF sensor is sought to be designed, which can measure the axial forces while rejecting the moment disturbances along the same axis.

e) **Technical specifications**: The study in [Maurin et al., 2004] also showed that the magnitude of the axial forces during needle insertion can go up to 4N with skin puncture. Hence, the nominal rated force for the force sensor has been kept as 10N. A range of [0.1;25]N would be explored during experiments to provide a security factor. For the purpose of haptic feedback, high levels of precision and accuracy are not required though resolution and bandwidth of the force sensor should be enough to capture the haptic information. For a direct access to an organ, the axial force measurement can go up to 0.7N with a change of 0.1N during the event of capsule puncture. The work of [Graña et al., 2014] revealed after a frequency analysis that the power of insertion forces signal is concentrated in the frequency range of [0;3]Hz. Hence, a bandwidth up to 3Hz would ensure that relevant frequency content in the insertion force signal is not attenuated. Considering a typical insertion length of a single stroke 25 mm, the deflection of the force sensor in the axial direction has to be much lower (lower than 0.5mm). An axial stiffness of greater than 100N/mm would give a deformation of 0.25mm for

an applied force of 25N. A high rotational stiffness is required for rejecting the axial moment load disturbances. Hysteresis levels due to viscoelastic effects in the polymer based material has to be minimized.

f) **Choice of the sensing principle**: The sensing principles based on the reflection/refraction of light and optical fibres [Gassert et al., 2008; Su and Fischer, 2009] are widely utilized for the MRI compatible force sensors owing to its stringent requirements. A uniaxial force sensor using optical fibres compatible with ultrasound imaging was developed for minimally invasive beating heart surgery in the work [Yip et al., 2010]. However, optical fibres are difficult to route on the moving parts of the robotic assistant. In addition, they require an extra amplification mechanism as very small deformations can not be measured directly. This raises the difficulty of ensuring good transparency of the insertion force transmission, as discussed before in this section. On the other hand, the CT scanner compatibility is less constrained and allows the use of sensing principles other than based on optics. In the work [Shah et al., 2008], a three axis, CT compatible force sensor based on strain gages has been presented for integration with a robotic assistant. With this embodiment, the insertion force is not directly applied on the flexure member of the sensor and thus hinders the desired force transmission transparency due to utilization of the intermediate mechanisms, as discussed in paragraph *b*).
Because electric wires are easier to route on the moving parts than optical fibres and do not alter the CT image quality, the adopted measurement principle may be based on resistive sensing. Due to the working principle of strain gages, very small strains can be measured without the need for any amplification mechanism. Moreover, strain gages have the advantages of smaller size and easy integration to a flexible element. Hence, force sensing based on strain gages is selected for the measurement of insertion forces in this work.

5.2 Design of the force sensor

5.2.1 Choice of architecture

The classification of flexure elements for force sensing has been extensively studied in the field of force measurement [Stefanescu, 2011]. For the desired range of forces ([0.1;10] N), the best arrangement for flexure elements should preferably provide complementary tensile and compressive strains. The simplest embodiment for such deformations can be easily obtained using a beam submitted to flexion. The flexure elements should enable a small displacement of the force sensor platform along the direction of the needle axis in order to cause the insertion force to develop a work. This displacement needs to be minimized to keep the flexure elements within their elastic domain of operation as well as to maintain the accuracy of positioning of the distal tip of the needle. The displacements along transverse directions and the rotations along any directions must be as small as possible to reject unwanted contributions of the mechanical actions acting on the needle. The simplest mechanism obeying the aforementioned objectives would have only 1-DOF in translation.

The direct construction of such one translational kinematic function using sliding surfaces, eg.

with one or more P joints, is not desirable and would provide incompatible high friction and jamming. A classical constructive approach to limit these drawbacks consists in using linkages with revolute joints in the place of sliders. Within the family of straight-line mechanisms, the Sarrus linkage was found to be an appropriate candidate for the application, since it could allow enough space for the through passage of the needle. This type of mechanism has already been used for other purposes implying large translational motions. For instance, a fully compliant Sarrus mechanism was selected in [Hoover and Fearing, 2009] to design large displacement translational units for mobile robots. Our goal in this work will be to use the translational property of the Sarrus mechanism around a given static configuration with only small displacements.

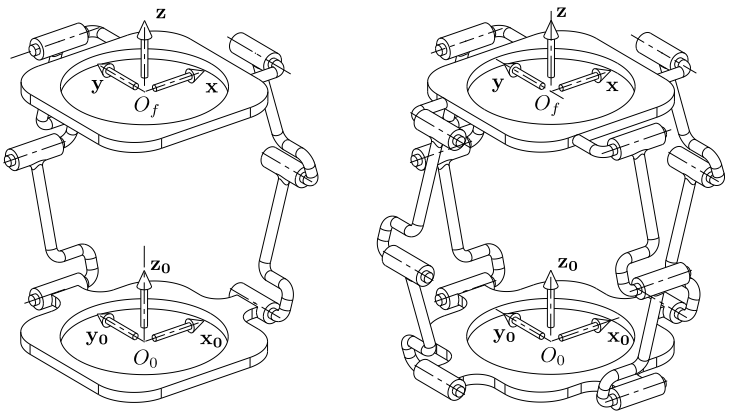

Figure 5.2 – (a) Sarrus mechanism (b) and its mirrored version with four legs.

The Sarrus linkage is an overconstrained parallel mechanism with a 2-3R architecture consisting of two legs. Each leg has a set of three parallel adjacent revolute joints. The directions of joints in each leg form a non-zero angle with each other generally fixed at $\frac{\pi}{2}$ as described in figure 5.2(a). The mobility of this mechanism is 1-DOF in translation and it's direction is parallel to the z-axis of the base. To improve the overall rigidity of the assembly, the number of legs can be augmented to three or more. In the present work, the study has been limited to the case of a 4-leg Sarrus mechanism in which two additional 3R legs can be mirrored with a plane of symmetry as shown in figure 5.2(b). As this duplication of legs augments the capacity of this one translational DOF mechanism to better sustain any mechanical actions but the forces along the axis $(O_f, \mathbf{z})$, this 4-3R architecture for the force sensor is retained.

5.2.2 Synthesis of the flexure element

The ideal rigid body model of the 4-leg Sarrus mechanism can be converted into a corresponding compliant model by replacing some of its revolute joints with equivalent deformable joints. This rigid-body replacement synthesis approach [Howell, 2001] for compliant mechanism

design takes advantage of a known rigid body mechanism and transforms some parts of the mechanism into flexible members. For sensing both tensile and compressive strains, the two links of each 3R chain are replaced by one single flexure element as depicted in figure 5.3.

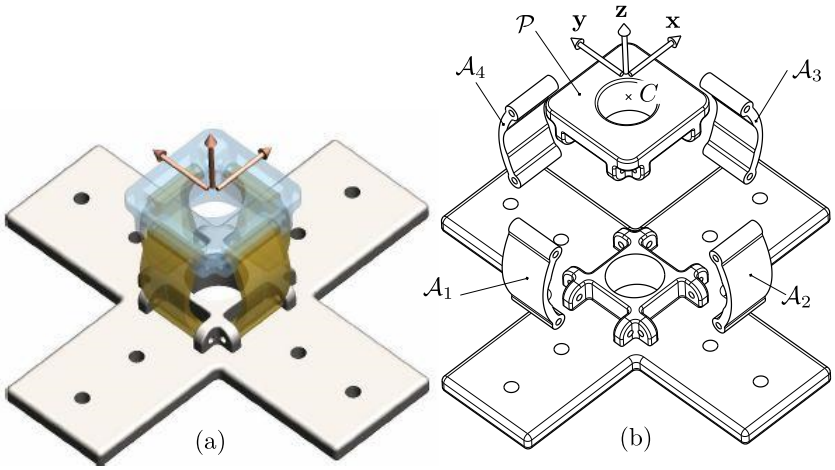

Figure 5.3 – Compliant Sarrus mechanism (a) CAD view (b) exploded view.

The attachment of each flexure element to the base and the platform is left unchanged with two revolute joints. Thus the resulting compliant Sarrus mechanism (CSM) can be considered as a deformable structure with a certain compliance along the direction **z** allowing the measurement of the desired axial force. Each flexure member or arm consists of a curved plate with the geometry described in figure 5.4. The width, height and global thickness of the plate

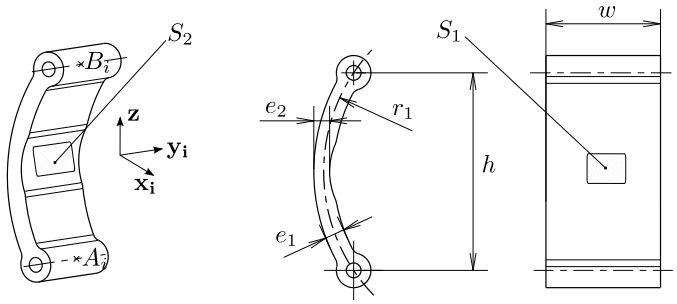

Figure 5.4 – Geometry of a flexure member.

are denoted by w, h and e_1, while its curved shape is given by a circular arc of radius r_1.

To account for the second revolute joint of the original Sarrus mechanism and favor the localized bending of the flexure members, the central part of each arm has a thinner thickness $e_2 = 0.8e_1$. The four arms $\mathscr{A}_i$ are connected at both ends to the base and the platform by pin joints with axes $(A_i, \mathbf{y_i})$ and $(B_i, \mathbf{y_i})$. Given the objective of smaller size required for the force sensor, the design variables h and w are considered as fixed parameters. When submitting the

force sensor platform to a force loading along $-\mathbf{z}$, the arms bend and the maximum tensile and compressive strains develop on the central thinner part of the outer and inner surfaces S_1 and S_2 of the flexible arms. Hence, the thinner central part of these surfaces will be selected for bonding the strain gages.

5.2.3 Material characterization

The material of the flexure element has to be radiolucent. Since the fabrication of the force sensor prototype was done using a rapid prototyping machine, the resulting properties of the fabricated material might differ from the material specification datasheet provided by the supplier. Part geometry and fabrication conditions such as part orientation on the tray are highly influencing factors on the resulting mechanical behaviour. Hence, material characterization pertaining to the Young's modulus and yield strength was carried out on samples using uniaxial tensile loadings in accordance with the `ISO 527-1` standard. The test samples were produced in the same material and a similar orientation than the one used for fabricating the flexure elements. The selected material was a `DM-8530-Grey60` polypropylene-like digital material used with a Connex 350 rapid prototyping machine. The test results have identified a tensile modulus of 750 MPa and a yield strength of 22.5 MPa.

5.2.4 CSM Force sensor simulation

A simulation setup has been constructed for checking the response of the CSM to various loading cases under different geometric configuration of the flexible arms driven by the structural parameters r_1 and e_1. Given the geometry of the CSM, the beam or plate theory can not be used to obtain a closed-form structural model. Based on the CAD model depicted in figure 5.3, a finite element model of the assembly has been prepared. The simulation model includes the four arms $\mathscr{A}_i$, the platform $\mathscr{P}$ and also describes the axes of the pin joints connecting the arms to the base and the platform.

Boundary and loading conditions

The simulated actions on the CSM platform are represented by a wrench $\hat{\mathbf{\$}}$ composed of a force $\mathbf{F}$ passing through the point O_f and a moment $\mathbf{M}$. The pin joints located at A_i and B_i on each arm have been modeled using beam elements describing the joint axes for which the rotation freedom about their axis has been released. The stiffness of these beam elements was set to fulfill the rigidity assumption for the axes of the pin joints. Lastly, the rigid modes of the base part have been blocked.

Model setup

As the CSM is assumed to undergo small displacements around its initial configuration, it can be studied using linear elasticity and the effects of the most general action $\hat{\$}$ can be obtained by linear superposition of the effects of unit forces and moments projected along the $\mathbf{x}, \mathbf{y}$ and $\mathbf{z}$ axes. As it will be detailed later, stress and strain levels are expected to stay largely under the yield point of the material and thus, the material properties are assumed to be linear and elastic.

Simulation results

The effects of an axial force applied to the CSM platform at point O_f and along $-\mathbf{z}$ have been studied.

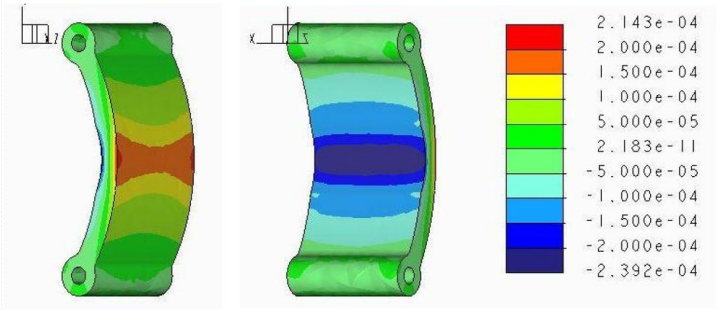

Figure 5.5 – Strain (ϵ_{zz}) of the flexible arm under unit load along $-\mathbf{z}$.

General behaviour of the CSM Several simulations have been conducted for different variants of the arms using variable values of the thickness e_1 and the radius r_1 and show that the strains of the CSM are always concentrated in the central part of each arm as depicted in figure 5.5. As expected, the outer and inner surfaces of the arms are respectively submitted to tension and compression. Furthermore, the compressive strain level is always higher by a 1.5 factor than that of the tensile strain whatever the tested parameters e_1 and r_1. Lastly, the strains remain nearly unchanged along the $\mathbf{y_i}$ direction.

Influence of the design parameters e_1 and r_1 The figure 5.6 shows both tensile and compressive strains of the arm when the CSM is submitted to an axial force $\mathbf{F_z} = -25\mathbf{z}$ N with the values of the design parameters (e_1, r_1) taken in $\{1.8; 2.0; 2.2\} \times \{14; 16; 18; 25; 28\}$. The variations of e_1 and r_1 affect the resulting stiffness of the CSM in a nonlinear manner despite the assumption of small displacements. Logically, it can be noted that the increase of the arm thickness e_1 raises the stiffness of the CSM and in turn reduces the strain level $|\epsilon_{zz}|$. In the same line, augmenting the radius r_1 also leads to a stiffer CSM since the arms would experience more

compression than bending. As bending rigidity is generally lower than compression rigidity, the design parameters should be chosen so as to favor the bending behaviour in order to gain a wider range of strain variation. Hence, the radius can be chosen such as $r_1 \leq 18$ mm.

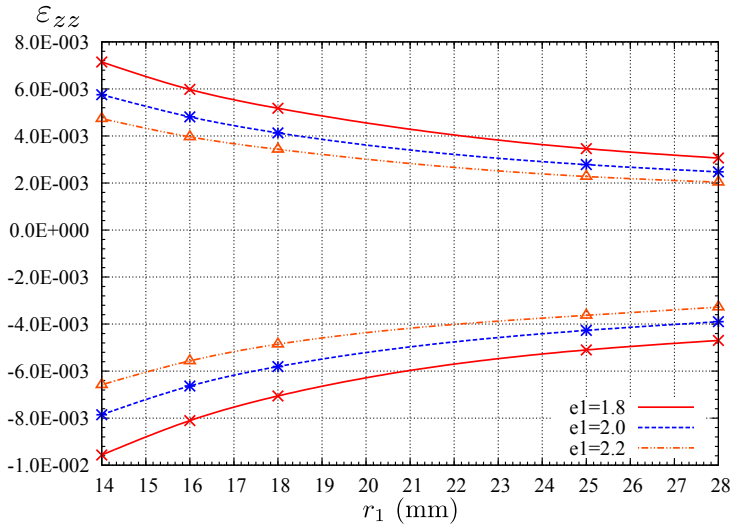

Figure 5.6 – Variation of the strain (ϵ_{zz}) in function of r_1 and e_1, for a 25N force applied along $-\mathbf{z}$.

Selection of r_1 and e_1 The simulations show that the maximum strains for the worst case ($F = 25$N, $e_1 = 1.8$, $r_1 = 14$) rise to $|\varepsilon_{zz}|_{max} = 10^{-2}$ which is compatible with the $5 \cdot 10^{-2}$ strain limit of most standard strain gages. However, to sustain occasional overloads without a risk of failure, we decided to set the maximum strain to $|\varepsilon_{zz}|_{max} = 6 \cdot 10^{-3}$. This restricts the possible parameter sets to ($e_1 = 2.0, r_1 = 18$), ($e_1 = 2.2, r_1 = 16$) and ($e_1 = 2.2, r_1 = 18$). To improve the strain sensitivity at low force loadings, the set ($e_1 = 2.0, r_1 = 18$) was finally selected since the other two design sets with $e_1 = 2.2$ have lower strains.

CSM stiffness The table 5.1 presents The calculated translational and torsional stiffness of the CSM along and about **z** as well as the platform displacement and rotation when submitted to a 25N axial force and a 25mN·m moment along and about the same direction. The calculated stiffness and the platform displacement along **z** when submitted to 25N axial force turns out to be 156N/mm and 0.16mm, respectively. This displacement along **z** is less than 0.5mm. The calculated torsional stiffness and the rotation of the CSM about **z** when submitted to a 25mN·m moment turns out be 6.7 10^5mN·m/rad and 3.7 10^{-4}rad, respectively. Under this load, the maximum strain at the place where the gages will be located is $|\varepsilon_{zz}|_{max} = 1.1\ 10^{-7}$. The platform rotation as well as the corresponding strains in the arms remain negligible, thus this torsional load does not disturb the axial force measurement. When submitted to an axial

Axial displacement along **z**	0.16 mm
Axial stiffness	156 N/mm
Platform rotation about $(O_f, \mathbf{z})$	$3.7\ 10^{-4}$ rad
Torsional stiffness	$6.7\ 10^{5}$mN·m/rad

Table 5.1 – Simulation results under loading conditions: axial force $-25\mathbf{z}$ N, axial moment $-25\mathbf{z}$ mN · m.

moment M_z, the platform rotation about $(O_f, \mathbf{z})$ as well as the strains in the arms remain negligible and thus does not disturb the axial force measurement.

5.2.5 Fabricated prototype

The parts composing the CSM with ($e_1 = 2.0, r_1 = 18$) have been fabricated in rapid prototyping with a Connex 350 machine and assembled using carbon axles (figure 5.7) To facilitate the gage setup, dual-pattern gages were chosen and glued onto the outer surface S_1 of the arm $\mathscr{A}_1$ and the inner surface S_2 of the arm $\mathscr{A}_3$ to form the four branches of a Wheatstone bridge. Dual-pattern gages were preferred over single element gages owing to less inaccuracies and errors while sticking the gages to the bonding surfaces of the CSM. The dimension of each gage is 7.4 × 5.8mm.

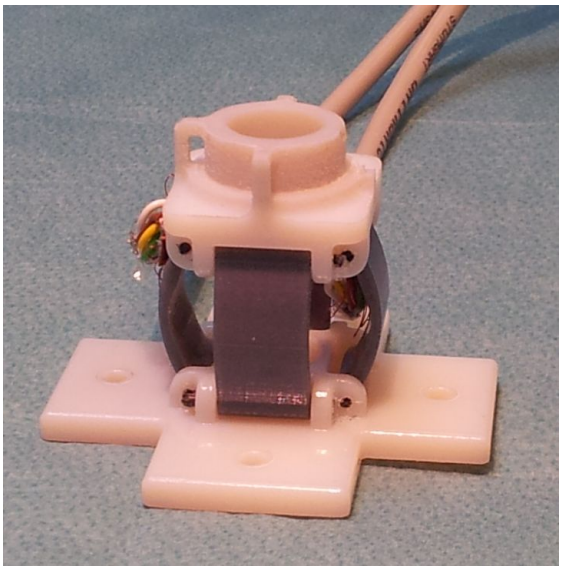

Figure 5.7 – Fabricated prototype.

5.3 Quasi-static characterization of the sensor

In this section, an experimental setup for quasi-static analysis of the force sensor is described. The initial results for the quasi-static characterization are first given, which brought to light the hysteresis effect in the force-deformation curve leading to the conclusion that a more elaborate model than the simple elastic one need to be used for the validation of the CSM force sensor.

5.3.1 Experimental setup

The first experimental setup utilized in quasi-static loading conditions is shown in figure 5.8. The essential components of the experimental setup, namely the cross-head, the calibrated force sensor (XForce HP 50N with an accuracy class 0.5 to ISO 5893 and NF ISO 7500-1) and the prototype CSM force sensor, can be seen in figure 5.8. It consists of a testing machine from

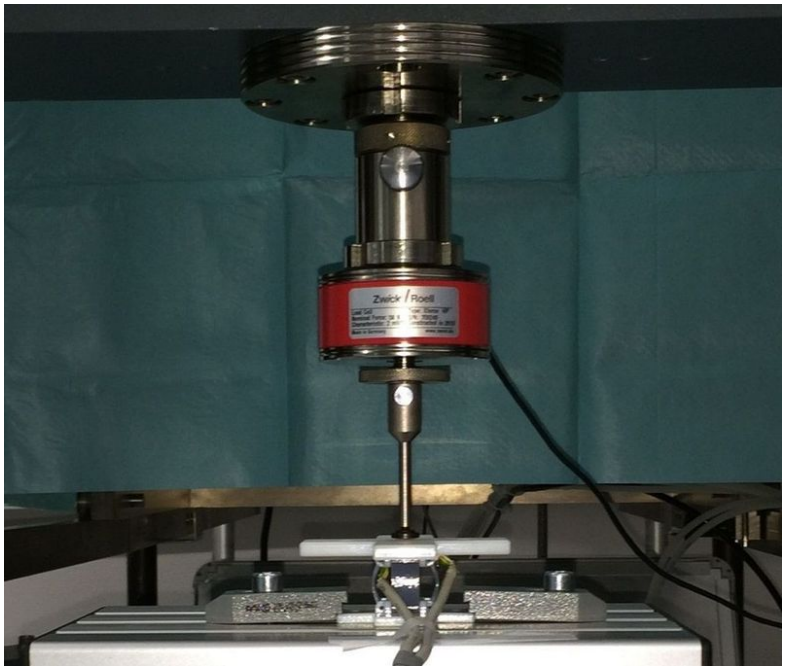

Figure 5.8 – Experimental setup for quasi-static loadings.

Zwick, GmbH (Z005 THN - Allround Line). The cross-head of the testing machine applies unidirectional force on the platform of the CSM along $-\mathbf{z}$. Though extremely accurate, this setup can not provide arbitrary input force profile such as harmonic excitations. A second experimental setup for assessing dynamic response of the CSM force sensor will be described in section 5.5. In both experimental setups, the voltage signal from the full Wheatstone bridge of the prototype is sent to a CPJ/CPJ2S analog signal conditioner from Scaime, which amplifies the signal. This amplified signal is in turn acquired by a computer.

5.3.2 Static experiment

This first experiment corresponds to what is generally called the sensor calibration. Different loads within the range $0.5, 1, 1.5, 2, 3, 4 \cdots 10$ N are applied to the prototype and each load gives one point of the static characteristics. Between two different loads, the time delay is far sufficient for the sensor signal to be stable. Each value gives one point of the static characteristics, that is pictured in figure 5.9. A least square fit is applied to obtain the gain

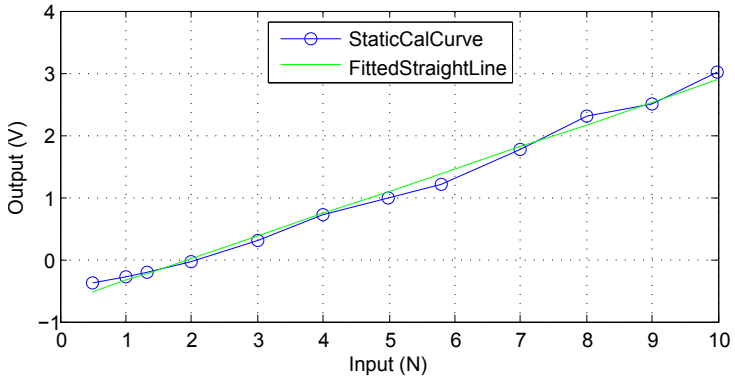

Figure 5.9 – Static calibration.

and offset required to derive the force value from the electrical measurement. The coefficient of determination for this fit is 0.993. The obtained gain is 0.37V/N. The linearity error of the force sensor is calculated to be 4.6%. With this fitting, the maximum deviation of the designed sensor output value remained within ±0.5N with respect to the ideal sensor value. The sensor has lower accuracy when measuring smaller values. Accuracy of the sensor might improve if a non-linear fitting is used to compensate for the non-linearities.

5.3.3 Constant force rate input experiment

In this second experiment, a sequence of linear force profiles is applied to the force sensor by the traction machine. The applied force increases linearly up to 25N at a rate of 1N/s. Then it decreases linearly to 0N (slightly more, so as to maintain contact) at −1N/s. The applied force is measured by the traction machine force sensor, while the electrical signal of the prototype force sensor is acquired separately and synchronized. The force and electrical measurement curves are respectively presented in figure 5.10(a) and (b). The rate of increase/decrease of the two measurements are compared. This is performed in the most linear part of the response, so as to characterize the sensor gain value. A total of 32 calibration curves were used which resulted in the 64 slope values. The slopes in the output curves were calculated. A mean slope value of 0.33V/s was calculated corresponding to the rate of change of 1N/s. This gives finally a mean gain value of 0.33V/N. The calibrated curve with this mean gain value is shown in figure 5.10(c).

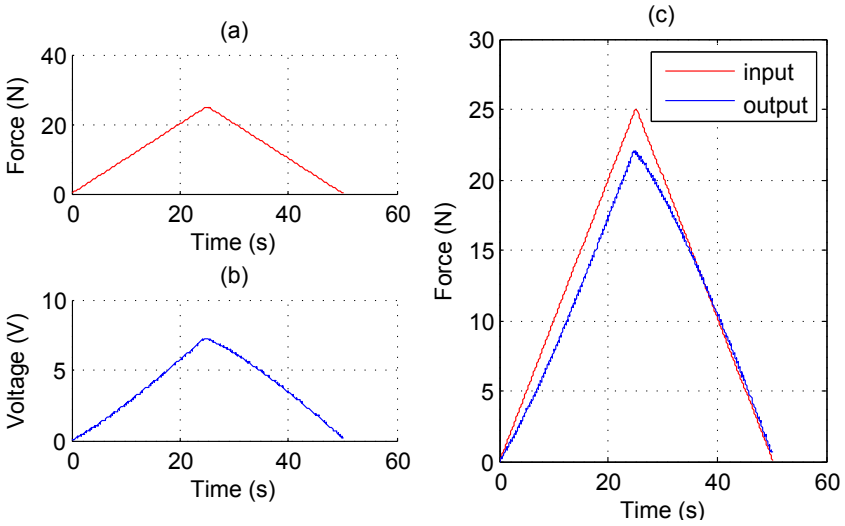

Figure 5.10 – (a) Calibration curve (b) output curve (c) calibrated curve.

The force applied by the testing machine *vs* the CSM force sensor voltage which coresponds to the prototype deformation is plot in figure 5.11 and shows an hysteresis. It can be observed that the CSM force sensor deformation is lagged with respect to the applied force during the reverse loading and that the initial deformation is not totally recovered at the end of the test. This effect is typical of the viscoelastic behaviour [Krishnamachari, 1993] found in the polymer materials. This emphasizes the fact that an approximation of the sensor model to a pure spring does not account for the error due to non-linearities. Therefore a more comprehensive viscoelastic model needs to be used for modeling of the prototype to minimize the error due to hysteresis and compensate for nonlinearities before proceeding to dynamic characterization and final validation of the CSM force sensor. It could however be refined by estimating the viscoelasticity of the system.

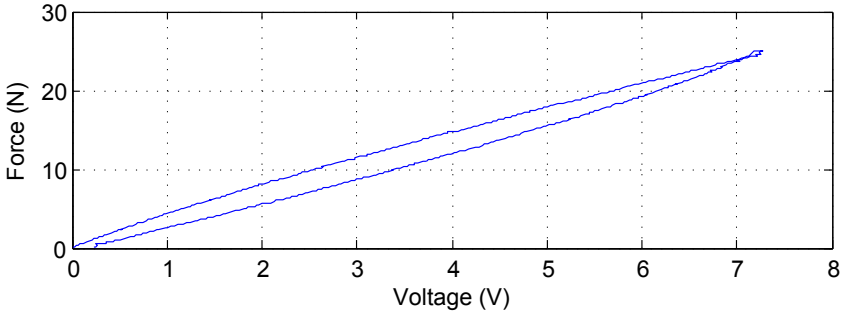

Figure 5.11 – Force/Voltage plot showing hysteresis.

5.4 Viscoelastic modeling

An adapted viscoelastic model would lead to a better understanding of the sensor behaviour, as compared to a simple elastic model. This will also give a compensation method to account for the hysteresis and the time-dependent effects such as drift in the sensor signal value during cyclic loadings, as discussed in section 5.4.3.

5.4.1 Viscoelastic model selection

A linear viscoelastic model can be described by an ordinary linear differential equation χ expressed as

$$\chi(F, \dot{F}, \cdots, \gamma, \dot{\gamma}, \cdots) = 0 \tag{5.1}$$

where F and γ denote the applied force and resulting deformation respectively. There are two main tests one can perform for the identification of the viscoelastic model χ:

1. Relaxation experiment: In this test the deformation is kept constant while the force levels are measured as a function of time.

$$\chi(F, \dot{F}, \cdots, \gamma = \gamma_0) = 0 \tag{5.2}$$

2. Creep experiment: In this test the force levels are kept constant while the deformation levels are measured as a function of time.

$$\chi(F = F_0, \gamma, \dot{\gamma}, \cdots) = 0 \tag{5.3}$$

Since the output of the force sensor is a tension corresponding to the deformation γ, the creep experiment must be used to identify the model χ. This test also allows to investigate the response of the CSM force sensor to a step force input.

Different linear viscoelastic models and their respective time response to a creep test [Krishnamachari, 1993] are shown in figure 5.12. The symbols k_i and η_i represent the stiffness and damping coefficients of the models. Even though the basic 2-parameter Maxwell and Kelvin models can describe the time-dependent behaviour, their combination with additional dashpots or springs provides overall better results for modeling viscoelastic behaviour. For instance, the Zener model also called the standard viscoelastic model enriches the Kelvin model with instantaneous elasticity. However, the deformation in the creep response of the Zener model becomes constant as time increases. To account for the fact that for certain viscoelastic materials, the deformation keeps increasing slowly as time increases, the Burgers model has been introduced. By matching the creep response of the actual prototype with one of these models or some other model, one could obtain an approximate viscoelastic model for the compensation of the output signal of the CSM force sensor. It should be noted here that the deformation γ corresponds to the sensor output, which is measured in voltage.

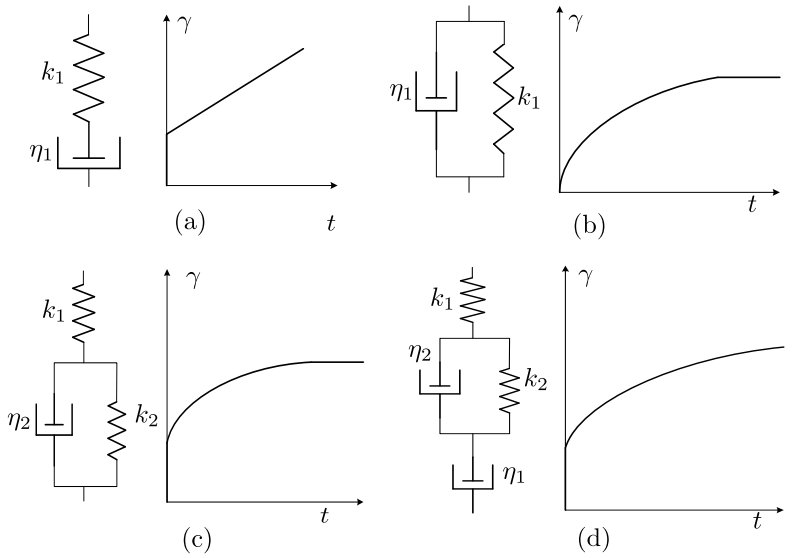

Figure 5.12 – Linear viscoelastic models and their creep response (a) Maxwell (b) Kelvin (c) Zener (d) Burgers.

Figure 5.13 shows the output of the CSM force sensor as response to the creep test with a constant force input of $F_c = 5N$. A careful observation shows a slow increase in the deformation

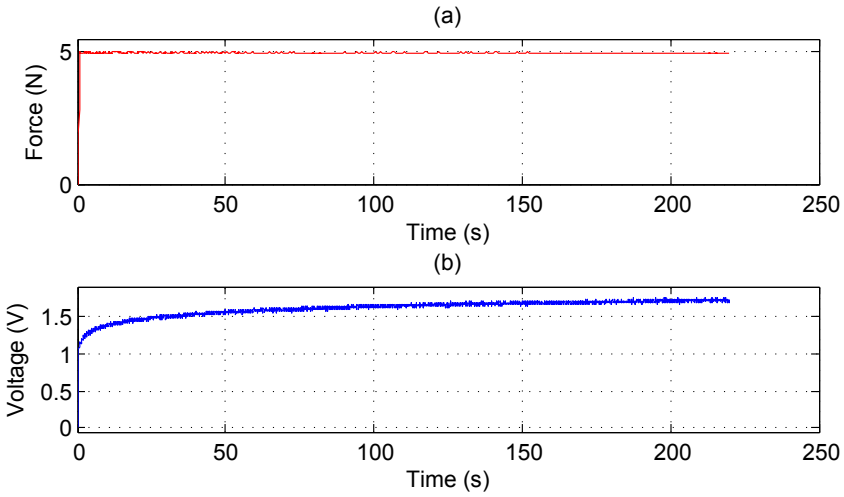

Figure 5.13 – Creep experiment on the CSM force sensor (a) Input load (b) Output response.

value as the time increases. Hence, figure 5.13(b) matches best with the creep response of the Burgers model with two springs and two dashpots as shown in figure5.12(d). Thus the identified model for describing the behaviour of the CSM force sensor is that of the Burgers.

5.4.2 Identification of the Burgers model parameters

The equation representing the Burgers model χ_{burgers} is given by

$$F\frac{k_2}{\eta_1} + \dot{F}\left(1 + \frac{k_2}{k_1} + \frac{\eta_2}{\eta_1}\right) + \ddot{F}\frac{\eta_2}{k_1} = k_2\dot{\gamma} + \eta_2\ddot{\gamma}. \tag{5.4}$$

Before formulating the compensation law, the four constant parameters k_1, k_2, η_1 and η_2 in equation (5.4) need to be identified using the creep response. For an input $F = F_c$, equation (5.4) reduces to

$$F_c\frac{k_2}{\eta_1} = k_2\dot{\gamma} + \eta_2\ddot{\gamma} \tag{5.5}$$

which can be solved analytically for γ with the initial conditions $\gamma(0) = \frac{F_c}{k_1}$ and $\dot{\gamma}(0) = F_c\left(\frac{1}{\eta_1} + \frac{1}{\eta_2}\right)$. The resulting solution to equation (5.5) is given by

$$\gamma(t) = F_c\left[\frac{1}{k_1} + \frac{1}{k_2}\left(1 - e^{\frac{-k_2 t}{\eta_2}}\right) + \frac{t}{\eta_1}\right] \tag{5.6}$$

where the three terms in the bracket correspond to i) the instantaneous elasticity due to the k_1 spring, ii) the lagged elasticity due to the k_2 spring and η_2 dashpot of the Kelvin model, iii) the viscous effect of the η_1 dashpot.

The four coefficients in equation (5.6) can be obtained through fitting this equation with the output creep profile in figure 5.13(b). The function `fittype` of Matlab has been used for the fitted curve plot in red in figure 5.14. The coefficient of determination for this curve fitting is

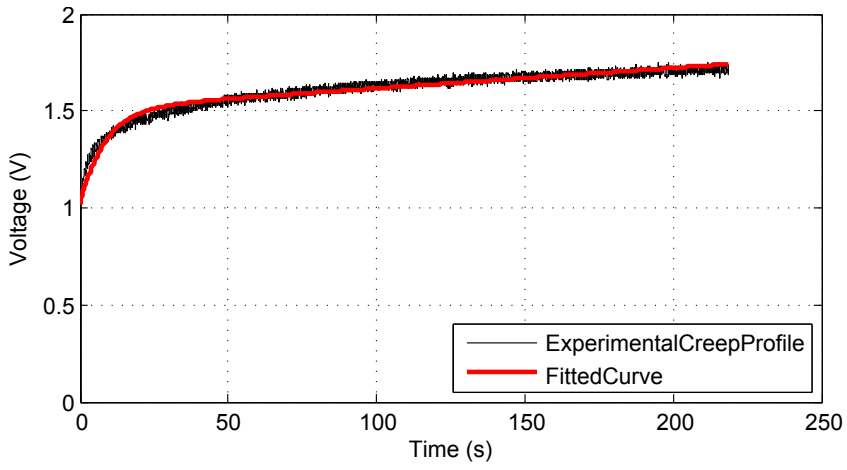

Figure 5.14 – Fitting of the experimental creep profile with the Burgers model.

0.902.

As a result, the fitting model parameters k_1, k_2, η_1, η_2 are calculated to be:

$$k_1 = 4.8 \text{ N/V} \qquad k_2 = 10.0 \text{ N/V} \qquad \eta_1 = 4627.94 \text{ Ns/V} \qquad \eta_2 = 85.12 \text{ Ns/V}. \tag{5.7}$$

This gives us a retardation time $\lambda = \frac{\eta_2}{k_2}$ equal to 8.51 s. The static stiffness coefficient can be calculated as follows :

$$k_s = \frac{k_1 k_2}{k_1 + k_2} \tag{5.8}$$

where the inverse of the k_s represents the static gain which is calculated to be 0.31 V/N. Hereafter, all the comparison between the uncompensated signal and the compensated sensor signal will be done using this value of the static gain. It should be noted that this value of the static gain is close to the gain values of 0.33 V/N and 0.36 V/N obtained experimentally from the quasi-static experiments described in section 5.3.

5.4.3 Compensation law for the CSM force sensor

To take into account the viscoelastic behaviour, a compensation law needs to be derived from the Burgers model. From equation (5.4), it is not possible to derive an analytical solution for F given an arbitrary input γ, Thus a numerical solution needs to be developed to compute F in real time.

The applied force corresponding to an arbitrary deformation history can be obtained using the Boltzmann superposition principle which reflects the assumed linearity of the viscoelastic behaviour. The corresponding equation writes:

$$F(t) = \int_0^t G(t-\tau)\dot{\gamma}(\tau)d\tau \tag{5.9}$$

where $G(t) = \frac{F_r(t)}{\gamma_c}$ is the relaxation modulus of the respective viscoelastic model. The equation for deriving the relaxation response $F_r(t)$ is obtained from Eqn (5.4) for the input $\gamma = \gamma_c$:

$$F_r \frac{k_2}{\eta_1} + \dot{F}_r \left(1 + \frac{k_2}{k_1} + \frac{\eta_2}{\eta_{\ 1}}\right) + \ddot{F}_r \frac{\eta_2}{k_1} = 0. \tag{5.10}$$

The relaxation modulus is derived to be of the form:

$$G(t) = a_1 e^{-r_1 t} + a_2 e^{-r_2 t} \tag{5.11}$$

where i) r_1 and r_2 are the roots of the polynomial $\frac{\eta_2}{k_1} r^2 - \left(1 + \frac{k_2}{k_1} + \frac{\eta_2}{\eta_1}\right) r + \frac{k_2}{\eta_1} = 0$, ii) a_1 and a_2 are constant coefficients defined using the initial conditions, namely $G(0) = k_1$ and $\dot{G}(0) = -k_1^2\left(\frac{1}{\eta_1} + \frac{1}{\eta_2}\right)$. The obtained numerical values are:

$$a_1 = 3.23 \text{ N/V} \qquad a_2 = 1.57 \text{ N/V} \qquad r_1 = 0.699 \cdot 10^{-3} \text{ s}^{-1} \qquad r_2 = 0.173 \text{ s}^{-1}. \tag{5.12}$$

The equation (5.9) in its original form requires the derivative of the input signal which might make it sensitive to noise. Hence, the alternative relation is obtained by using integration by parts:

$$F(t) = \gamma(t)G(0) - \int_0^t \dot{G}(t-\tau)\gamma(\tau)d\tau. \tag{5.13}$$

After substituting the equation (5.11) into equation (5.13) and after discretizing, the compensation law is obtained to process the sensor signal:

$$F_i = \gamma_i G(0) - a_1 r_1 e^{-r_1 t_i} \sum_{j=1}^{i} e^{r_1 t_j} \gamma_j T_s - a_2 r_2 e^{-r_2 t_i} \sum_{j=1}^{i} e^{r_2 t_j} \gamma_j T_s \tag{5.14}$$

where T_s is the sampling period. This form is free from the derivative term, so it would be robust against the noise and higher frequency terms. To validate the above compensation law, it was applied to the output signal resulting from cyclic constant force rate experiments. The input triangle sawtooth force profile is given in red in figure 5.15. The output of the CSM

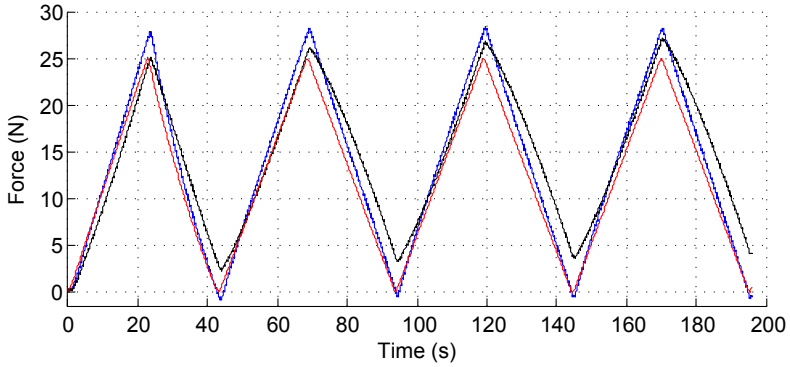

Figure 5.15 – CSM submitted to a triangle sawtooth force (red): output with (blue) and without compensation (black).

force sensor (in black), obtained without compensation, shows a drift of the minimum and maximum values, which is increasing with each cycle. At the end of the fourth cycle, the minimum has increased from 0 to 4 N. The compensated output force profile is shown in blue, where the level of the minimum for each of the four cycles has been brought near to zero values. Also the drift in the maxima of the sensor response has been corrected in the compensated force profile.

In figure 5.16, a comparison of the hysteresis levels is done between the signals with and without compensation. Both signals have been normalized for relative comparison of the hysteresis levels. The level of hysteresis is calculated to be approximately 20% and 4.5% for the uncompensated and the compensated signal, respectively. As a result, there is significant improvement in the hysteresis levels when using this viscoelastic model.

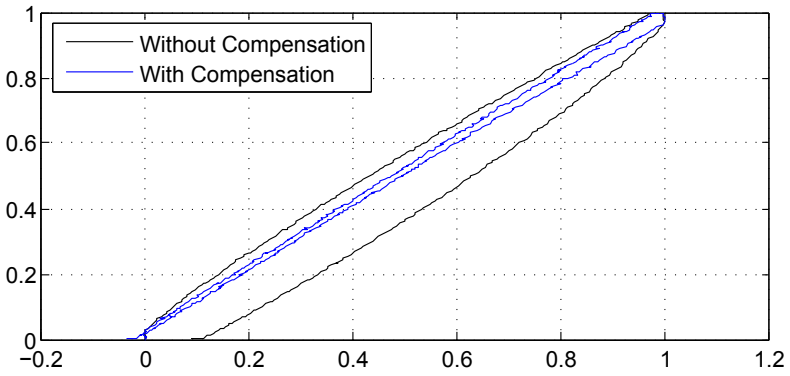

Figure 5.16 – Hysteresis comparison.

5.4.4 Sensor resolution

A resolution of 0.1N was stated in the specification to be achieved by the sensor. A rectangular wave signal of 0.1N was applied as an input to determine the prototype resolution. To avoid the issue of loss of contact between the testing machine and the CSM force sensor, a constant preload of 3.75N was applied in addition to the cyclic loading.

In response to the input of 0.1N maintained for 40s for every cycle, the sensor response was recorded along with compensation for four cycles with a sampling period of 0.1s. Average and standard deviation of the sensor values were calculated be 0.08N and 0.013N, respectively.

5.5 Dynamic characterization of the force sensor

In this section, a second experimental setup is used to complement the quasi-static analysis of the force sensor. The results are given using the compensation model and compared against the results without compensation.

Figure 5.17 – Experimental setup for dynamic loadings.

5.5.1 Experimental setup

To determine the sensor sensor reponse under arbitrary loadings, the setup shown in figure 5.17 has been utilized. It consists of a 2-DOF system (X-Y table from Nanomotion) with a calibrated force sensor (Scaime-K1107-20N). Only 1-DOF of the X-Y table is used, so as to apply axial forces to the prototype sensor as an input.

5.5.2 Step response

The CSM force is submitted to a 5N step input and the output is studied. figure 5.18 shows how the compensation improves the dynamic response of the sensor. The rise time of the step response for the compensated signal and uncompensated signal is 0.3s and 11.5s, respectively. It can also be observed that the slow increase with time is corrected after compensation and the resulting force measurement remains constant later on.

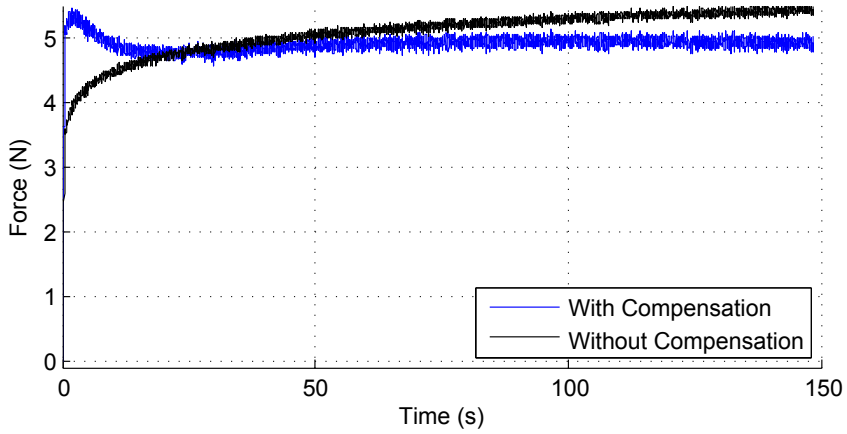

Figure 5.18 – Response to a step input of 5N.

5.5.3 Harmonic response

An harmonic analysis was performed over the frequency range [0.01;10] Hz. The vibrations in the setup increased notably at higher frequencies, hence the study was limited to frequency of 10 Hz. Figure 5.19 shows the Bode magnitude plot with and without compensation. There is a definite improvement in the frequency response at lower frequencies. At higher frequencies, the response seems to be comparable for both as effects due to dashpots are negligible. The offset between the two curves at higher frequencies is due to lower value of the static gain. The bandwidth (measured at -3dB point) for the uncompensated signal is roughly around 2Hz, whereas the bandwidth of the compensated signal is more than 8Hz. The resulting increase in the bandwidth is due to the upward shift in the response at lower frequencies.

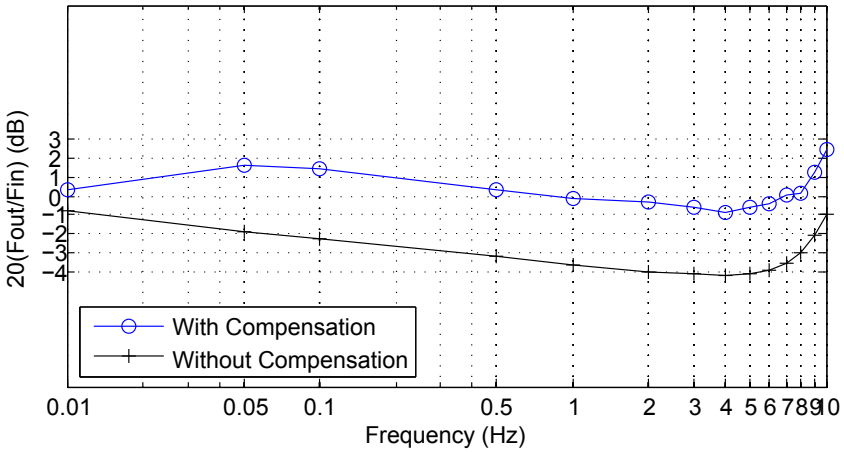

Figure 5.19 – Bode magnitude plot.

5.5.4 Validation

A final validation of the prototype force sensor was performed using an input force profile obtained from an actual *in vivo* needle insertion procedure carried out on an anesthetized swine (figure 5.20). This force profile was earlier presented and used in [Piccin et al., 2009]. The fit between the applied force and the measured force signal is much better with viscoelastic compensation than without compensation. This is reflected in the coefficient of the determi-

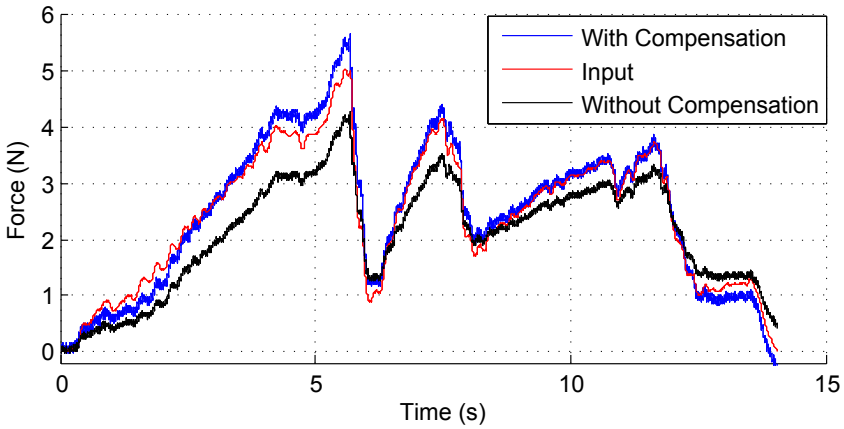

Figure 5.20 – Response to the experimental force profile as input.

nation for this fit, which is calculated to be 0.966 and 0.835 with and without compensation, respectively. In figure 5.20, most of the haptic information including the transients which are very important to feel key events such as ruptures of tissues are present, with very limited attenuation. Hence, the developed CSM force sensor can be effectively used for haptic force feedback in a bilateral teleoperation scenario.

5.6 Solution for the ProteCT project

This chapter concluded the design and development of the CSM force sensor for measurement of the axial insertion forces. In the preceding chapter 4 of the part-II, the design and development of the NGD and insertion mechanism was discussed. However, the integration of these three components constituting the insertion tool were not discussed yet. This section briefly describes the integration of the three elements of the insertion tool namely NGD, insertion mechanism and the CSM force sensor. The three devices need to be connected so as to ensure the three functionalities namely needle grasping, measurement of axial insertion forces and the insertion of the needle. The three devices are connected in series to give it an approximate conical form which is beneficial for avoiding collisions, in case large orientation of the needle is needed. The insertion mechanism is placed first followed by CSM force sensor and then the NGD. The NGD is placed at the bottom with the force sensor on its top. The CAD implementation of the assembly is shown in figure 5.21(a). This arrangement ensures that the axial needle insertion forces are transmitted directly to the CSM force sensor without need for any intermediate mechanisms. The insertion mechanism which is the top most part ensures the translation of the assembly, including CSM force sensor and the NGD holding the needle, along the insertion axis. The CAD implementation of the insertion tool is shown in figure 5.21(b) and it has been developed with François Schmitt who is a research engineer of the ProteCT project. The overall height of the insertion tool is limited to 137mm.

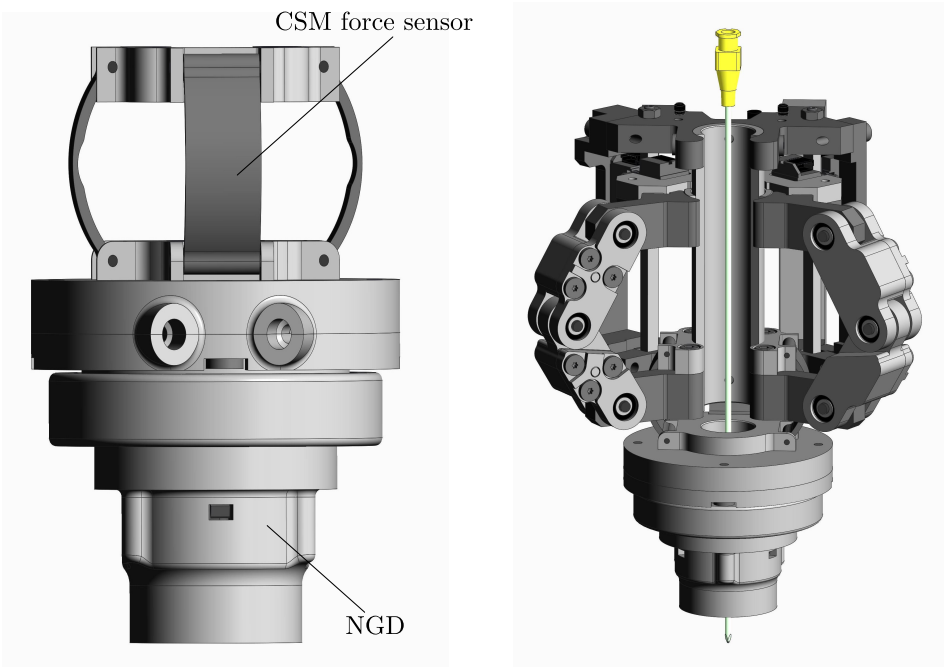

(a) Series assembly of the CSM force sensor and the NGD

(b) Series assembly of the insertion mechanism, CSM force sensor and the NGD

Figure 5.21 – CAD implementation of the insertion tool(with François Schmitt).

5.7 Summary

The requirements for the design of a force sensor compatible with CT scanner were clearly laid out. The design of a new flexible element for uniaxial force sensing has been proposed starting from a rigid body model of a Sarrus mechanism. The design of the force sensor ensured that many stringent constraints such as through hole for the passage of the needle, radiolucency, compactness, high stiffness were satisfied. The numerical model of the force sensor verified its theoretical working in the elastic range. It also helped choose the structural design parameters for the fabrication of the prototype. A complete characterization of the force sensor was done through quasi-static and dynamic analysis. A systematic viscoelastic model identification was done to model the time-dependent effects due to the polymer based material of the force sensor. A novel robust, computationally effective compensation law was derived from a linear viscoelastic model to improve the CSM force sensor response. The compensated CSM force sensor signal has much lower levels of the hysteresis and a much improved dynamic response. Through experimental evaluation, the requirements arising from the needle insertion procedures in interventional radiology set out in the beginning of the chapter have been shown to be met.

Though the CSM force sensor was developed for CT compatibility and for specific medical procedures, it could be adapted and utilized for wide variety of applications where uni-axial force sensing is a requirement. The viscoelastic model identification through representative creep response presented in this chapter can be used to model and compensate for the time-dependent response in sensors utilizing a wide variety of polymer based materials. This seems to be a promising alternative to using non-linear models for modeling the viscoelastic effects including hysteresis of the sensors fabricated out of polymer materials. For signals with varying frequency content, compensated signal corrects automatically for the gain of the sensor as compared to using single static or harmonic gain for all type of signals. Concluding the part on the design and development of the insertion tool, the integration of the three devices namely, NGD, insertion mechanism and the CSM force sensor and its CAD implementation was presented. This integration ensures a conical form of the insertion tool for achieving large orientation ranges and the basic functionalities of needle release/grasp, needle insertion and measurement of the axial insertion forces.

6 Conclusion

Contents

6.1 Thesis summary

The work of this thesis was carried out under the broad framework of the ProteCT project which aims at protecting the radiologist from overexposure of the X-rays during percutaneous procedures under CT scanner. This framework aims to put in place a teleoperated robotized procedure in which a master device is controlled at a distance by the radiologist and the procedure performed by a slave robotic device mounted on the patient. During this thesis, the work focused upon the design and the development of the slave robotic assistant. The slave robotic assistant was designed to ensure different functionalities which mimic the movements of the radiologist in a manual procedure. These functionalities are namely, needle positioning, needle insertion, needle release/grasp and the axial needle insertion forces measurement. Each functionality is achieved by the development of a dedicated device which caters to certain specific requirements keeping in perspective the integration of these devices into the slave robotic assistant. The design and technologies issues pertaining the size of the slave robotic assistant, the choice of actuators and the level of input actuation torques were raised throughout the manuscript.

For the design and development of the needle positioning device, the task was formulated based on the definition of the mechanism motion constraints. This enabled to perform a systematic synthesis of mechanisms dedicated for the task of needle positioning. The synthesized mechanisms ensured the inclusion of the RCM point which is an essential feature for the robotized percutaneous procedures. A systematic dimensional synthesis of the chosen

candidate mechanisms was carried out to limit the size of the mechanism and to determine the level of input actuation torques and reaction forces for the technological solution to the choice of actuators and other standard components such as bearings. A CAD embodiment of the designed positioning device chosen as solution for the ProteCT project was described.

A list of requirements for the design of the insertion tool composed of a insertion mechanism, a force sensor and a NGD was laid out. Based on these specifications, the design of a new variant of the NGD using flexible parts was carried out. A prototype of this NGD, fabricated using polymer parts, was subjected to the experimental assessment to validate its functioning. The flexible variant of the NGD outperformed the prior rigid version of the NGD with respect to the level of axial force sustained and the stiffness characteristics. The force sensor design using plastic parts was carried out to improve upon the transparency of the insertion tool under the CT scanner. A viscoelastic model for the force sensor was developed using a systematic model identification procedure to reduce the hysteresis and other time-dependent effects due to the plastic material used for its fabrication. Experimental assessment of the force sensor under quasi-static and dynamic conditions validated its functioning with respect to the desired technical specifications. A CAD embodiment of the integrated insertion tool along with the insertion mechanism, the CSM force sensor and the new variant of the NGD was presented.

6.2 Contributions

The different devices proposed in this thesis which constitute the slave robotic assistant provided various design and technical contributions to the robotized solution developed for the teleoperated percutaneous procedures under the ProteCT project. Apart from the contributions to needs in the medical context, the work in this thesis also contributed to the area of synthesis and design of the lower mobility parallel mechanisms.

For design of the needle positioning device, a generic task-based synthesis methodology was proposed. The novelty of this synthesis method lies in the utilization of the constraint wrench description derived from the task definition as a starting point for the mechanism synthesis. A set of preference rules were defined to characterize the mechanism architectural complexity with an end point of synthesizing practically realizable mechanisms. The combined usage of screw theory and concept of motion patterns illustrated how the limitations of the concept of mobility can be overcome and could be used to disambiguate between two mechanisms with the same mobility but very different end-effector motion descriptions. Moreover, the principle of kinematic inversion was applied to formulate motion patterns relative to a moving frame. Utilizing this synthesis methodology a new family of 2T2R parallel mechanisms, targeted for the robotized percutaneous needle insertion procedures, were synthesized for the first time.

A novel dimensional synthesis algorithm for calculating the structural parameters of the lower mobility parallel mechanisms was developed. This dimensional synthesis algorithm took a different approach by manipulating the boundaries of the singularities, obtained through screw theory-based inspection, to achieve the desired workspace size. For limiting the level of

input actuation torques and the reaction forces, the parallel singularities were also included in the algorithm along with the serial singularities. Based on the modeling and analysis of the mechanisms presented in this work, technological solution for the actuators and bearings for joints were chosen for the embodiment design of the needle positioning device for the ProteCT project.

The work in this thesis built on the prior work and versions of the NGD already developed in our lab. A new variant of the NGD based on the flexible parts was designed according to the requirements for the percutaneous procedures. The novelty of this NGD arises from the combined functionalities of needle grasp/release and and re-centering of the needle while re-grasping. Also the design of the NGD decoupled the needle grasping with the needle insertion itself. The experimental assessment of the fabricated prototype validated the functioning of the NGD. The design and development of the NGD fills an important functionality gap which is present in the current robotic assistants designed for percutaneous procedures.

As a result of decoupling between the needle insertion and needle grasping, measurement of axial needle insertion forces became feasible. A custom-built force sensor based on the Sarrus mechanism was designed and experimentally validated under quasi-static and dynamic loading conditions. Novelty of the work lies in the design of a flexible element which was fabricated out of prototyped plastic parts to enhance the transparency in the CT scanner. The systematic viscoelastic model identification procedure using the creep response led to the selection of a linear viscoelastic model as compared to complex non-linear models, which was used to model the hysteresis and time-dependent effects. A novel compensation law was proposed based on this modeling which improved the dynamic response and the hysteresis levels of the force sensor by a factor of 4.

6.3 Perspectives

The work in this thesis lays foundation for the development of clinical prototype of the complete robotic assistant for providing robotized solutions to the percutaneous procedures within the context of interventional radiology.

Though a particular mechanism candidate was selected for the positioning device, several mechanisms dedicated to the robotized needle positioning were synthesized. The task-based synthesis methodology along with its set of preference rules can be applied for synthesis of mechanisms adapted for other task descriptions as well. Though mostly legs with serial types were considered for synthesis of the parallel mechanisms, closed-loop mechanisms can also be considered which would enlarge the scope of the synthesis procedure.

The dimensional synthesis algorithm can be easily applied to other lower-mobility parallel mechanisms especially for special types of workspaces like constant-orientation or constant-position workspace. The extension to the more general workspace like the reachable workspace are also possible but would result in the coupling of structural parameters of different legs. Though the dimensional synthesis algorithm considered only the mechanisms

with revolute joints, the analysis can be extended to the mechanisms with prismatic joints by considering the joints limits. The static analysis of the 2T2R parallel mechanism showed very ill-conditioned Jacobian matrices suggesting configurations close to the parallel singularity. This shows that not all the parallel singularity conditions were accounted for using the screw theory. However, this should not be seen as the limitation of the method, rather the irregular behaviour of the system spanned by actuation and constraint wrenches for the asymmetrical 2T2R parallel mechanism. For fully parallel mechanism with identical leg types, systematic enumeration of all parallel singularity conditions is possible via screw theory. Therefore, the dimensional synthesis method is expected to achieve much better results for the levels of actuation moments and constraint wrenches. It should be remarked here that the approach using indices like isotropy, manipulability which depend upon the explicit numerical calculation of the Jacobian matrix is inherently linked to the parallel singularity analysis. This is evident from the fact that indices values worsen close to the parallel singularity due to degeneration of the Jacobian matrices. However the index based methods become computationally too expensive as the number of structural parameters increases. A combination of this index based approach and the geometrical approach using singularities, presented in this thesis, perhaps could lead to better results for dimensional synthesis of asymmetrical parallel mechanisms.

Though a new variant of the NGD based on the flexible parts was developed, there exists possibility to obtain several other variants with different actuation principles by combining different solution principles proposed in this work. The use of the dedicated NGD for percutaneous procedures is expected to minimize the tissue lacerations and achieve faster recovery times for the patient. It also takes the robotic assistants a step closer to mimicking the actual movements of the radiologist in a clinical setting. Despite the fact that the CSM force sensor was designed for interventional radiology procedures under CT scanner, the designed flexible element can be used for wide variety of applications where uni-axial force sensing is needed. The viscoelastic modeling of the flexible element presented in this work can be used to model force sensors made from a wide variety of polymer materials. This is especially relevant for the force sensors designed for MRI, where similar problems with the viscoelastic effects are encountered. This approach of using linear viscoelastic models seems as a promising alternative to using non-linear models for compensation of the hysteresis.

Even though the prototypes of the NGD and the force sensor were validated through experiments separately, the experiments with the overall insertion tool still needs to be done. In this work, the implementation of the positioning device and insertion tool as an integrated slave robotic assistant were not covered. This thesis also did not discuss the registration issues related to the slave robotic assistant. However, details of the CAD implementation of the slave robotic assistant along with the markers for registration can be found in the master's thesis work of [Wach, 2014]. The fabrication of the complete slave robotic assistant could not be completed during the thesis work due to the time constraints. A dedicated master console was designed with two rotational DOF and one insertion DOF which was not part of this thesis work. The experimental validation of the slave robotic assistant along with the haptic master device in clinical settings will further validate the design concepts developed in this thesis.

6.4 Publications

The following works were published during this thesis or have been submitted for review:

Peer-reviewed journal papers:

-**N. Kumar**, O. Piccin, and B. Bayle, “A task-based type synthesis of novel 2T2R parallel mechanisms,” Mechanism and Machine Theory, vol. 77, pp. 59–72, Jul. 2014.

-**N. Kumar**, O. Piccin, L. Meylheuc, L. Barbe, and B. Bayle, "Design, Modeling and Compensation of Viscoelastic Effects for a Polymer Force Sensor", IEEE/ASME Transactions on Mechatronics, (***under review***).

Peer-reviewed conference articles:

-**N. Kumar**, O. Piccin, and B. Bayle, "Dimensional synthesis of a novel 2T2R parallel manipulator for medical applications", In ASME 2014 International Design Engineering Technical Conferences and Computers and Information in Engineering (IDETC/CIE) conference, Aug 17–20, Buffalo, New York. (***in press***).

-**N. Kumar**, O. Piccin, L. Meylheuc, L. Barbe, and B. Bayle, “Design, development and preliminary assessment of a force sensor for robotized medical applications,” in 2014 IEEE/ASME International Conference on Advanced Intelligent Mechatronics (AIM), 2014, pp. 1368–1374.

-**N. Kumar**, O. Piccin, L. Meylheuc, L. Barbe, and B. Bayle, "Compliant grasping device for robotized medical applications", 21éme Congrés Français de Mécanique, Bordeaux, 26 au 30 aout 2013.

-O. Piccin, **N. Kumar**, L. Meylheuc, L. Barbe, and B. Bayle, "Design, development and preliminary assessment of grasping devices for robotized medical applications", In ASME 2011 International Design Engineering Technical Conferences and Computers and Information in Engineering (IDETC/CIE) Conference, American Society of Mechanical Engineers, pp. 65–73, Aug. 2012.

Patent:

-O. Piccin, **N. Kumar**, L. Meylheuc, L. Barbe, B. Bayle, F. Schmitt, Device for grasping an elongated body, such as a needle, and robotized device comprising the same, CIB: A61B17/00; A61B17/34; A61B19/00; B23B31/12; B25J15/08; B25J15/10; B25J15/12 (Feb. 2014).

A Inverse kinematics solution for the 2T2R mechanism candidate II

This appendix presents the inverse kinematics solution for the two legs of the 2T2R mechanism candidate II discussed in section 3.2.2. The symbolic calculation of the inverse kinematics solution for the 2T2R mechanism candidate II was developed in Maple software.

A.1 Inverse kinematics solution for leg 1

Let the matrix ${}^{i1}T_{j1}$ refer to the transformation matrix from the frame i to the frame j, where i, j range from $0, p, 1, 2, \cdots, 5, f$ where the indices p and f are associated with the base and end-effector reference frames as indicated in table 3.1(a).

The inverse kinematics solution for leg 1 amounts to solving for the set of joint angles $\theta_{11}, \theta_{21}, \cdots, \theta_{51}$ given the transformation matrix M (equation (A.1)) representing the end-effector configuration. Let $\theta_{p1} = 0$ and $\theta_{f1} = \pi/2$ which are free to be defined by the user.

$$ {}^{01}T_{p1}\,{}^{p1}T_{11}\,{}^{11}T_{21}\,{}^{21}T_{31}\,{}^{31}T_{41}\,{}^{41}T_{51}\,{}^{51}T_{f1} \quad = \quad M \quad = \quad \begin{bmatrix} m_{11} & 0 & m_{13} & p_x \\ m_{21} & m_{22} & m_{23} & p_y \\ m_{31} & m_{32} & m_{33} & 0 \\ 0 & 0 & 0 & 1 \end{bmatrix} \tag{A.1} $$

From the equality ${}^{01}T_{41}(3,3) - M^{f1}T_{41}(3,3) = 0$, the following equation can be obtained which gives two values for θ_{51}:

$$ \begin{aligned} m_{32}\sin\alpha_{51}\sin\theta_{51} - \left(m_{31}\cos\alpha_{fl} - m_{33}\sin\alpha_{fl}\right)\sin\alpha_{51}\cos\theta_{51} \\ - \left(m_{31}\sin\alpha_{fl} + m_{33}\cos\alpha_{fl}\right)\cos\alpha_{51} + \cos\alpha_{41} = 0 \end{aligned} \tag{A.2} $$

From the equalities ${}^{01}T_{41}(3,1) - M^{f1}T_{41}(3,1) = 0$ and ${}^{01}T_{41}(3,2) - M^{f1}T_{41}(3,2) = 0$, the following equations can be obtained which determine uniquely θ_{41} given a value of θ_{51} obtained

previously:

$$\sin\alpha_{41}\cos\theta_{41} + m_{32}\cos\alpha_{51}\sin\theta_{51} - \left(m_{31}\cos\alpha_{f1} - m_{33}\sin\alpha_{f1}\right)\cos\alpha_{51}\cos\theta_{51} + \left(m_{31}\sin\alpha_{f1} + m_{33}\cos\alpha_{f1}\right)\sin\alpha_{51} = 0 \quad \text{(A.3a)}$$

$$\sin\alpha_{41}\sin\theta_{41} + m_{32}\cos\theta_{51} + \left(m_{31}\cos\alpha_{f1} - m_{33}\sin\alpha_{f1}\right)\sin\theta_{51} = 0 \quad \text{(A.3b)}$$

From the equalities ${}^{p1}T_{31}(1,4) - {}^{p1}T_{01}M^{f1}T_{31}(1,4) = 0$ and ${}^{p1}T_{31}(2,4) - {}^{p1}T_{01}M^{f1}T_{31}(2,4) = 0$, the following equations can be obtained which determine θ_{11} and θ_{21} given the values of θ_{41} and θ_{51} obtained previously:

$$\begin{aligned} &d_{31}\cos(\theta_{11}+\theta_{21}) + d_{21}\cos\theta_{11} - m_{12}d_{41}\cos\theta_{41}\cos\theta_{51} - m_{11}d_{41}\cos\theta_{41}\sin\theta_{51}\cos\alpha_{f1} \\ &+ m_{13}d_{41}\cos\theta_{41}\sin\theta_{51}\sin\alpha_{f1} + m_{12}d_{41}\sin\theta_{41}\cos\alpha_{51}\sin\theta_{51} \\ &- m_{11}d_{41}\sin\theta_{41}\cos\alpha_{51}\cos\theta_{51}\cos\alpha_{f1} + m_{13}d_{41}\sin\theta_{41}\cos\alpha_{51}\cos\theta_{51}\sin\alpha_{f1} \\ &+ m_{11}d_{41}\sin\theta_{41}\sin\alpha_{51}\sin\alpha_{f1} + m_{13}d_{41}\sin\theta_{41}\sin\alpha_{51}\cos\alpha_{f1} - m_{12}r_{41}\sin\alpha_{51}\sin\theta_{51} \\ &+ m_{11}r_{41}\sin\alpha_{51}\cos\theta_{51}\cos\alpha_{f1} - m_{13}r_{41}\sin\alpha_{51}\cos\theta_{51}\sin\alpha_{f1} \\ &+ m_{11}r_{41}\cos\alpha_{51}\sin\alpha_{f1} + m_{13}r_{41}\cos\alpha_{51}\cos\alpha_{f1} - p_x = 0 \end{aligned} \quad \text{(A.4a)}$$

$$\begin{aligned} &d_{31}\sin(\theta_{11}+\theta_{21}) + d_{21}\sin\theta_{11} - m_{22}d_{41}\cos\theta_{41}\cos\theta_{51} - m_{21}d_{41}\cos\theta_{41}\sin\theta_{51}\cos\alpha_{f1} \\ &+ m_{23}d_{41}\cos\theta_{41}\sin\theta_{51}\sin\alpha_{f1} + m_{22}d_{41}\sin\theta_{41}\cos\alpha_{51}\sin\theta_{51} \\ &- m_{21}d_{41}\sin\theta_{41}\cos\alpha_{51}\cos\theta_{51}\cos\alpha_{f1} + m_{23}d_{41}\sin\theta_{41}\cos\alpha_{51}\cos\theta_{51}\sin\alpha_{f1} \\ &+ m_{21}d_{41}\sin\theta_{41}\sin\alpha_{51}\sin\alpha_{f1} + m_{23}d_{41}\sin\theta_{41}\sin\alpha_{51}\cos\alpha_{f1} - m_{22}r_{41}\sin\alpha_{51}\sin\theta_{51} \\ &+ m_{21}r_{41}\sin\alpha_{51}\cos\theta_{51}\cos\alpha_{f1} - m_{23}r_{41}\sin\alpha_{51}\cos\theta_{51}\sin\alpha_{f1} \\ &+ m_{21}r_{41}\cos\alpha_{51}\sin\alpha_{f1} + m_{23}r_{41}\cos\alpha_{51}\cos\alpha_{f1} - p_y = 0 \end{aligned} \quad \text{(A.4b)}$$

From the equalities ${}^{01}T_{41}(1,3) - M^{f1}T_{41}(1,3) = 0$ and ${}^{01}T_{41}(2,3) - M^{f1}T_{41}(2,3) = 0$, the following equations can be obtained which determine uniquely $\theta_{11}+\theta_{21}+\theta_{31}$ given a value of θ_{41} and θ_{51} obtained previously:

$$\sin(\theta_{11}+\theta_{21}+\theta_{31})\sin\alpha_{41} + m_{12}\sin\alpha_{51}\sin\theta_{51} - m_{11}\cos\alpha_{f1}\sin\alpha_{51}\cos\theta_{51} + m_{13}\sin\alpha_{f1}\sin\alpha_{51}\cos\theta_{51} - \left(m_{11}\sin\alpha_{f1} + m_{13}\cos\alpha_{f1}\right)\cos\alpha_{51} = 0 \quad \text{(A.5a)}$$

$$-\cos(\theta_{11}+\theta_{21}+\theta_{31})\sin\alpha_{41} + m_{22}\sin\alpha_{51}\sin\theta_{51} - m_{21}\cos\alpha_{f1}\sin\alpha_{51}\cos\theta_{51} + m_{23}\sin\alpha_{f1}\sin\alpha_{51}\cos\theta_{51} - \left(m_{21}\sin\alpha_{f1} + m_{23}\cos\alpha_{f1}\right)\cos\alpha_{51} = 0 \quad \text{(A.5b)}$$

From the sum of $\theta_{11}+\theta_{21}+\theta_{31}$, the angle θ_{31} can be calculated as the values of θ_{11}, θ_{21} are determined from equation (A.4).

There are two solutions each corresponding to equation (A.2) and equation (A.4), so leg 1 admits a total of four solutions to the inverse kinematics problem, given an end-effector configuration.

A.2 Inverse kinematics solution for leg 2

Let the ${}^{i2}T_{j2}$ refer to the transformation matrix from the frame i to the frame j, where i, j range from $0, p, 1, 2, \cdots, 5, f$ where p and f refer to the base and end-effector reference frames as indicated in table 3.1(b).

The inverse kinematics solution for Leg 2 amounts to solving for set of joint angles $\theta_{12}, \theta_{22}, \cdots, \theta_{52}$ given the transformation matrix M (equation (A.6)) representing the end-effector configuration. Let $\theta_{p2} = \pi/2$ and $\theta_{f2} = 0$ which are free to be defined by the user.

$$ {}^{02}T_{p2}\,{}^{p2}T_{12}\,{}^{12}T_{22}\,{}^{22}T_{32}\,{}^{32}T_{42}\,{}^{42}T_{52}\,{}^{52}T_{f2} \quad = \quad M \quad = \quad \begin{bmatrix} m_{11} & 0 & m_{13} & p_x \\ m_{21} & m_{22} & m_{23} & p_y \\ m_{31} & m_{32} & m_{33} & 0 \\ 0 & 0 & 0 & 1 \end{bmatrix} \tag{A.6} $$

From the equalities ${}^{02}T_{32}(1,3) - M^{f2}T_{32}(1,3) = 0$ and ${}^{02}T_{32}(2,3) - M^{f2}T_{32}(2,3) = 0$, the following equations can be obtained which determine uniquely the sum of two angles $\theta_{42} + \theta_{52}$:

$$ -m_{11}\sin(\theta_{42}+\theta_{52}) + m_{13}\cos(\theta_{42}+\theta_{52}) = -1 \tag{A.7a} $$

$$ -m_{21}\sin(\theta_{42}+\theta_{52}) + m_{23}\cos(\theta_{42}+\theta_{52}) = 0 \tag{A.7b} $$

From the equalities ${}^{02}T_{32}(2,2) - M^{f2}T_{32}(2,2) = 0$ and ${}^{02}T_{32}(3,2) - M^{f2}T_{32}(3,2) = 0$, the following equations can be obtained which determine uniquely the sum of three angles $\theta_{12}+\theta_{22}+\theta_{33}$:

$$ -\sin(\theta_{12}+\theta_{22}+\theta_{32}) + m_{22} = 0 \tag{A.8a} $$

$$ \cos(\theta_{12}+\theta_{22}+\theta_{32}) + m_{32} = 0 \tag{A.8b} $$

From the equality ${}^{02}T_{32}(1,4) - M^{f2}T_{32}(1,4) = 0$, the following equation can be obtained which determine θ_{52} given the value of $\theta_{42} + \theta_{52}$ obtained earlier:

$$ m_{13}d_{52}\sin\theta_{52} + m_{11}d_{52}\cos\theta_{52} + r_{12} - m_{11}\left(-d_{42}\cos(\theta_{42}+\theta_{52}) - d_{f2}\right) + m_{12}r_{52} - m_{13}\left(-d_{42}\sin(\theta_{42}+\theta_{52}) - r_{f2}\right) - p_x = 0 \tag{A.9} $$

The angle θ_{42} can be obtained from the sum $\theta_{42}+\theta_{52}$ and the value of θ_{52} obtained earlier. From the equalities ${}^{02}T_{32}(2,4) - M^{f2}T_{32}(2,4) = 0$ and ${}^{02}T_{32}(3,4) - M^{f2}T_{32}(3,4) = 0$, the following equations can be obtained which determine θ_{12} and θ_{22} given the values of θ_{42} and θ_{52} obtained previously:

$$ d_{32}\cos(\theta_{12}+\theta_{22}) + d_{22}\cos\theta_{12} + d_{12} - m_{21}\left(-d_{42}\cos(\theta_{42}+\theta_{52}) - d_{52}\cos\theta_{52} - d_{f2}\right) + m_{22}r_{52} - m_{23}\left(-d_{42}\sin(\theta_{42}+\theta_{52}) - d_{52}\sin\theta_{52} - r_{f2}\right) - p_y = 0 \tag{A.10a} $$

$$d_{32}\sin(\theta_{12}+\theta_{22})+d_{22}\sin\theta_{12}+r_{p2}-m_{31}\left(-d_{42}\cos(\theta_{42}+\theta_{52})-d_{52}\cos\theta_{52}-d_{f2}\right)$$
$$+m_{32}r_{52}-m_{33}\left(-d_{42}\sin(\theta_{42}+\theta_{52})-d_{52}\sin\theta_{52}-r_{f2}\right)-p_z=0 \quad \text{(A.10b)}$$

From the sum of $\theta_{12}+\theta_{22}+\theta_{32}$, the angle θ_{32} can be calculated as the values of θ_{12},θ_{22} are determined from equation (A.10).

There are two solutions each correponding to equation (A.9) and equation (A.10), so leg 2 also admits a total of four solutions like leg 1 to the inverse kinematics problem, given an end-effector configuration.

B Reaction forces for the parallelogram mechanism of the 2R mechanism candidate

This appendix presents the expression for the calculated reaction forces at the joints A, B, C, D, F, J, H of the parallelogram mechanism of the 2R mechanism candidate discussed in section 3.3.4. The symbolic calculation presented in this appendix was developed in Maple software.

The reaction forces at the joint A are derived to be:

$$R_{ax} = \frac{-1}{2a_1a_2\cos(\alpha+\beta-\gamma)}\Big(a_1mgd\sin(\alpha+\gamma) - a_1mgd\sin(\alpha-\gamma) + a_1a_2F_{in}\sin(\alpha+\beta) - a_1a_2F_{in}\sin(\alpha+\beta-2\gamma) - a_2a_3mg\sin(\alpha+\beta-\gamma) + a_2a_3mg\sin(\alpha-\beta+\gamma) - a_2a_3F_{in}\sin(\alpha+\beta-2\gamma) + a_2a_3F_{in}\sin(\alpha-\beta)\Big) \quad \text{(B.1a)}$$

$$R_{az} = \frac{1}{2a_1a_2\cos(\alpha+\beta-\gamma)}\Big(a_1a_2F_{in}\cos(\alpha+\beta-2\gamma) + a_1a_2F_{in}\cos(\alpha+\beta) + 2a_1a_2mg\cos(\alpha-\gamma+\beta) - a_1mgd\cos(\alpha-\gamma) + a_1mgd\cos(\alpha+\gamma) + a_2a_3F_{in}\cos(\alpha-\beta) + a_2a_3F_{in}\cos(\alpha+\beta-2\gamma) + a_2a_3mg\cos(\alpha-\beta+\gamma) + a_2a_3mg\cos(\alpha+\beta-\gamma)\Big) \quad \text{(B.1b)}$$

The reaction forces at joint B are derived to be:

$$R_{bx} = -\frac{1}{a_1a_2\cos(\alpha+\beta-\gamma)}\Big(-a_1mgd\cos\alpha\sin\gamma + a_2a_3mg\cos\alpha\sin(\beta-\gamma) + a_2a_3F_{in}\cos\alpha\cos\gamma\sin(\beta-\gamma) + a_2a_3F_{in}\sin\alpha\sin\gamma\sin(\beta-\gamma)\Big) \quad \text{(B.2a)}$$

$$R_{bz} = -\frac{1}{a_1a_2\cos(\alpha+\beta-\gamma)}\Big(-a_1mgd\sin\alpha\sin\gamma + a_2a_3F_{in}\sin\alpha\sin\gamma\cos(\beta-\gamma) + a_2a_3mg\cos(\beta-\gamma)\cos\alpha + a_2a_3F_{in}\cos\alpha\cos\gamma\cos(\beta-\gamma)\Big) \quad \text{(B.2b)}$$

Appendix B. Reaction forces for the parallelogram mechanism of the 2R mechanism candidate

The reaction forces at joint D are derived to be:

$$R_{dx} = \frac{1}{a_1 a_2 a_4 \cos(\alpha+\beta-\gamma)}\Big(-a_1 {a_2}^2 F_{in}\cos\alpha\cos\gamma\sin(\beta-\gamma) - a_1 {a_2}^2 mg\cos\alpha\sin(\beta-\gamma)$$
$$- a_1 a_2 mgd\cos\alpha\sin\gamma - a_1 a_4 mgd\cos\alpha\sin\gamma - a_1 {a_2}^2 F_{in}\cos\alpha\sin\gamma\cos(\beta-\gamma)$$
$$- a_1 a_2 a_4 F_{in}\cos\alpha\sin\gamma\cos(\beta-\gamma) + a_1 a_2 a_4 F_{in}\sin\alpha\sin\gamma\sin(\beta-\gamma)$$
$$+ a_2 a_3 a_4 mg\cos\alpha\sin(\beta-\gamma) + a_2 a_3 a_4 F_{in}\cos\alpha\cos\gamma\sin(\beta-\gamma)$$
$$+ a_2 a_3 a_4 F_{in}\sin\alpha\sin\gamma\sin(\beta-\gamma)\Big) \quad \text{(B.3a)}$$

$$R_{dz} = \frac{-1}{a_1 a_2 a_4 \cos(\alpha+\beta-\gamma)}\Big(a_1 a_2 a_4 F_{in}\sin\alpha\cos\gamma\sin(\beta-\gamma) + a_1 a_2 a_4 mg\sin\alpha\sin(\beta-\gamma)$$
$$+ a_1 {a_2}^2 F_{in}\sin\alpha\cos\gamma\sin(\beta-\gamma) + a_1 {a_2}^2 mg\sin\alpha\sin(\beta-\gamma) + a_1 a_2 mgd\sin\alpha\sin\gamma$$
$$+ a_1 a_4 mgd\sin\alpha\sin\gamma + a_1 {a_2}^2 F_{in}\sin\alpha\sin\gamma\cos(\beta-\gamma) - a_2 a_3 a_4 F_{in}\cos(\beta-\gamma)\sin\gamma\sin\alpha$$
$$- a_2 a_3 a_4 mg\cos\alpha\cos(\beta-\gamma) - a_2 a_3 a_4 F_{in}\cos\alpha\cos\gamma\cos(\beta-\gamma)$$
$$- a_1 a_2 a_4 mg\cos\alpha\cos(\beta-\gamma) - a_1 a_2 a_4 F_{in}\cos\alpha\cos\gamma\cos(\beta-\gamma)\Big) \quad \text{(B.3b)}$$

The reaction forces at joint H are derived to be:

$$R_{hx} = \frac{\cos\alpha R_{hz}}{\sin\alpha} \quad \text{(B.4a)}$$

$$R_{hz} = \frac{-\sin\alpha}{a_4\cos(\alpha+\beta-\gamma)}\Big(a_2 F_{in}\cos\gamma\sin(\beta-\gamma) + a_2 mg\sin(\beta-\gamma)$$
$$+ a_2 F_{in}\sin\gamma\cos(\beta-\gamma) + mgd\sin\gamma\Big) \quad \text{(B.4b)}$$

The reaction forces at joint J are derived to be:

$$R_{jx} = \frac{-1}{a_4\cos(\alpha+\beta-\gamma)}\Big(-a_2 F_{in}\cos\alpha\cos\gamma\sin(\beta-\gamma) - a_2 mg\cos(\alpha)\sin(-\gamma+\beta)$$
$$- a_2 F_{in}\cos\alpha\sin\gamma\cos(\beta-\gamma) - mgd\cos\alpha\sin\gamma - a_4 F_{in}\cos\alpha\sin\gamma\cos(\beta-\gamma)$$
$$+ a_4 F_{in}\sin\alpha\sin\gamma\sin(\beta-\gamma)\Big) \quad \text{(B.5a)}$$

$$R_{jz} = \frac{1}{a_4\cos(\alpha+\beta-\gamma)}\Big(a_4 mg\sin\alpha\sin(\beta-\gamma) - a_4 mg\cos\alpha\cos(\beta-\gamma)$$
$$- a_4 F_{in}\cos\alpha\cos\gamma\cos(\beta-\gamma) + a_2 F_{in}\sin\alpha\cos\gamma\sin(\beta-\gamma) + a_2 mg\sin\alpha\sin(\beta-\gamma)$$
$$+ a_2 F_{in}\sin\gamma\sin\alpha\cos(\beta-\gamma) + mgd\sin\gamma\sin\alpha + a_4 F_{in}\sin\alpha\cos\gamma\sin(\beta-\gamma)\Big) \quad \text{(B.5b)}$$

The reaction forces at joint C can be obtained from the reaction forces at joint B by the relation $R_{cx} = -R_{bx}$ and $R_{cz} = -R_{bz}$. Similarly, the reaction forces at joint F can be obtained from the reaction forces at joint H by the relation $R_{fx} = -R_{hx}$ and $R_{fz} = -R_{hz}$.

C Résumé en français

C.1 Introduction

La radiologie interventionnelle (IR) est une spécialité médicale où les radiologues font usage de plusieurs modalités d'imagerie, y compris l'imagerie par ultrasons, la tomodensitométrie (TDM ou scanner CT) et l'imagerie par résonance magnétique (IRM) pour diagnostiquer et traiter les patients utilisant des techniques mini-invasives. Le développement d'une assistance robotique dans ce contexte médical est motivé par le souhait d'améliorer simultanément la réalisation des gestes et limiter certaines contraintes supportées par le praticien qui sont introduites par les dispositifs d'imagerie. Dans cette thèse, l'accent principal est porté sur les procédures percutanées impliquant l'insertion d'aiguilles sous TDM. La biopsie hépatique et l'ablation de tumeurs hépatiques par radiofréquence (RFA) sont deux exemples pertinents de procédures ciblés par cette thèse. Le flux de travail clinique manuel pour une procédure interventionnelle percutanée typique peut être décrit en trois grandes étapes: (1) une **phase préparatoire (figure C.1(a))** qui se compose de la planification de trajectoire de l'aiguille et et la localisation du point d'entrée de l'aiguille sur le corps du patient; (2) le **positionnement de l'aiguille (figure C.1(b))** dans l'espace libre qui consiste à faire coïncider l'axe de l'aiguille avec la direction d'insertion déterminée précédemment; (3) l'**insertion de l'aiguille (figure C.1(c))** réalisée sous contrôle du retour d'imagerie.

(a) Phase préparatoire. (b) Positionnement de l'aiguille. (c) Insertion de l'aiguille.

Figure C.1 – Étape principales pour les procédures percutanées.

C.1.1 Dispositifs d'insertion d'aiguilles robotique

Le classement des dispositifs d'insertion d'aiguille (needle insertion device: NID) peut être basé soit sur l'architecture mécanique choisie ou basé sur la fixation du dispositif robotique dans la salle d'opération. Un NID peut soit avoir une architecture parallèle ou série hybride. Lorsque l'insertion manuelle de l'aiguille est nécessaire, le NID se compose uniquement du dispositif de positionnement de l'aiguille sans possibilité d'insertion de l'aiguille robotisé. Ces NID ont une architecture série ou parallèle. Pour les NID incorporant la fonction d'insertion de l'aiguille robotisée, le mécanisme d'insertion est le plus souvent relié en série au dispositif de positionnement pour des raisons de sécurité ce qui en fait une architecture hybride. D'autre part, les NID peuvent être classifiés selon leur modalité d'installation selon qu'ils soient attachés à la table de l'imageur (Table Mounted System: TMS) ou bien directement installés sur le corps du patient (patient mounted systems: PMS) Des exemples représentatifs de systèmes de TMS et PMS sont présentés dans la figure C.2(a) et la figure C.2(b), respectivement.

(a) Acubot, un NID monté sur une table à architecture série [Stoianovici et al., 2003].

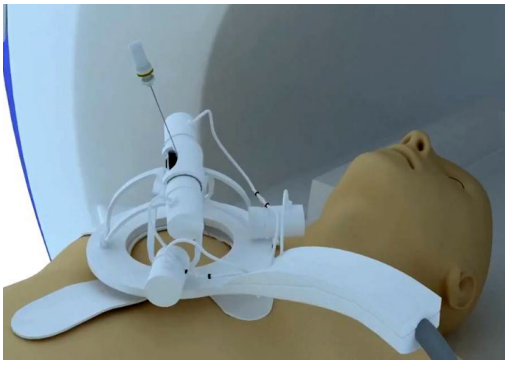

(b) Robopsy, un NID monté sur patient à architecture parallèle [Walsh et al., 2008].

Figure C.2 – Exemples de dispositifs d'insertion d'aiguilles (NID).

C.1.2 Projet ProteCT

Ce travail de thèse a été réalisé dans le cadre du projet ProteCT financé par l'IHU (Institut Hospitalo-Universitaire) de Strasbourg et la fondation ARC (fondation pour la recherche sur le cancer). L'institut de chirurgie guidée par l'image de Strasbourg développe une chirurgie innovante pour une prise en charge personnalisée des patients pour le diagnostic et le traitement des pathologies du système digestif, qui combine les technologies mini-invasives aux dernières avancées de l'imagerie médicale.

La nécessité de protéger le projet provenait du fait que les radiologues et du personnel de soutien médical relèvent exposition répétée aux rayons X lors de l'exécution des procédures minimalement invasives dans CT. Cette situation est aggravée par le manque de radiologues formés et l'augmentation du nombre de ces procédures. Par conséquent, la protection ou

blindage du radiologue de ces rayons X devient important afin de permettre lui / elle d'effectuer un certain nombre d'interventions pour de longues durées. La pratique actuelle de porter lourds et encombrants tabliers de plomb pour la protection non seulement limite les mouvements naturels du radiologiste, mais conduit également à la fatigue. Une solution robotisée complète peut être envisagée dans le cadre du système de téléopération comme le montre la figure C.3 qui permet d'identifier trois principaux thèmes à savoir la télémanipulation, le développement du dispositif maître et le développement du dispositif esclave. La télémanipulation et le développement du dispositif maître ne font pas partie de ce travail de thèse qui s'est focalisé sur le développement des éléments constitutifs du dispositif esclave indiqués en rouge sur la figure C.3.

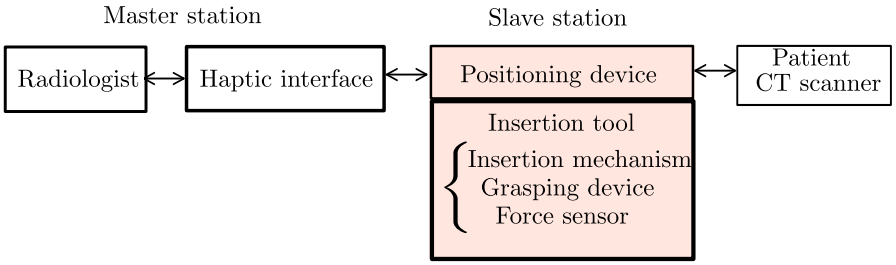

Figure C.3 – Schéma d'organisation pour des procédures interventionnelles télérobotiques sous scanner CT.

Objectifs de la thèse: Le dispositif esclave est certainement l'élément le plus complexe de l'ensemble de la solution robotisée étant donnée sa proximité avec le patient et le scanner CT. Il en résulte de nombreuses contraintes telles que la sécurité, la compatibilité avec le dispositif d'imagerie ou encore l'asepsie. Un dispositif esclave pour l'assistance aux gestes de radiologie interventionnelle doit satisfaire à certaines fonctionnalités de base. Pour intégrer ces fonctionnalités au dispositif, une approche modulaire a été employée dans le projet ProteCT pour arriver à plusieurs sous-systèmes remplissant chaque fonction particulière. Le premier sous-système est le dispositif de positionnement qui est nécessaire pour positionner et orienter l'axe de l'aiguille. Ce mécanisme de positionnement peut avoir soit quatre degrés de liberté (DDL), soit deux, selon que la mobilité en translation est prise en compte ou non. Dans cette thèse, une nouvelle version d'un dispositif de préhension d'aiguille (needle grasping device: NGD) est proposée et validée expérimentalement. Le mécanisme d'insertion de l'aiguille est quant à lui conçu pour une intégration compacte et pour procurer au radiologue un accès facile à l'aiguille. En outre, comme le praticien agissant à distance ne peut pas directement ressentir les forces d'interaction entre l'aiguille et les tissus, un capteur d'effort compatible avec l'imagerie par TDM a dû être intégré au dispositif esclave pour lui fournir ce retour d'information haptique.

C.2 Dispositif pour la positionnement d'aiguille

L'un des gestes essentiels du radiologue est la manipulation d'aiguilles dans l'espace libre. Cette manipulation d'aiguille peut être considérée comme la mise en place d'une ligne $\mathscr{L}$, coïncidente avec l'axe de l'aiguille dans l'espace 3D, à l'aide du mécanisme devant être synthétisé comme indiqué sur la Fig. C.4 dans laquelle $\mathscr{F}_b = (O_b, \mathbf{x_b}, \mathbf{y_b}, \mathbf{z_b})$ et $\mathscr{F}_f = (O_f, \mathbf{x_f}, \mathbf{y_f}, \mathbf{z_f})$ représentent les repères attachés respectivement à la base fixe et à la plate-forme mobile du mécanisme. Le point d'entrée E est spécifié par le radiologue grâce aux images acquises dans une étape pré-opératoire, mais il est parfois nécessaire de réajuster la position de E. Après avoir fixé le point E dans le plan Π, l'aiguille doit ensuite être pivotée autour de ce point pour obtenir l'orientation requise pour atteindre l'organe cible. Partant de la description de la tâche

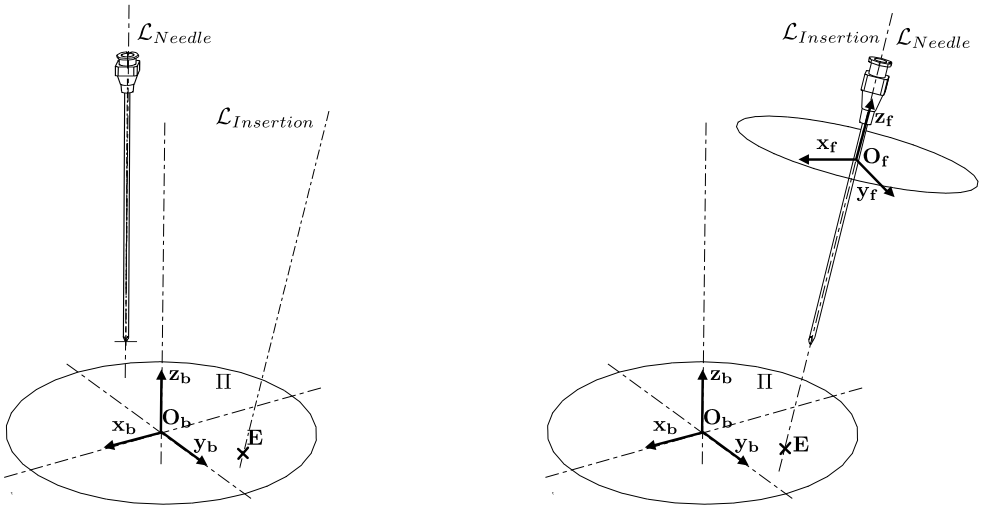

(a) Etat initial.

(b) Etat final.

Figure C.4 – Définition de tâche pour la manipulation de l'aiguille.

ci-dessus, deux tâches T_1 et T_2 peuvent être déduites. La tâche T_1 correspond à la mise en configuration complète de l'aiguille à la fois en position et en orientation alors que la tâche réduite T_2 ne concerne que l'orientation de l'axe de l'aiguille. La structure cinématique d'un mécanisme pour la tâche T_1 a au moins quatre DDL ou plus précisément, le mécanisme doit avoir une mobilité 2T2R (T-translationnelle et R-rotation). En revanche, pour accomplir la tâche T_2, un mécanisme nécessite au moins deux DDL et une mobilité du type 2R. Bien que ne répondant qu'à une version réduite de la tâche, les mécanismes à mobilité réduite nécessitent moins d'actionneurs et sont donc beaucoup plus faciles à mettre en œuvre et réaliser pratiquement. Au début de la procédure, le radiologue peut souhaiter corriger l'inclinaison de l'axe de l'aiguille autour du point d'entrée alors que l'aiguille vient d'être légèrement insérée. Une exigence clé est donc la présence d'un centre de rotation déporté (remote center of motion: RCM) qui coïncide avec le point d'entrée sur la peau du patient. Cette disposition facilite l'orientation du mécanisme sans causer de lacérations des tissus.

C.2.1 Procédure de synthèse des mécanismes basée sur la tâche

Bien que la synthèse de mécanismes par la théorie des torseurs soit une méthode bien établie, elle nécessite toutefois des adaptations pour permettre la synthèse d'architectures basée sur une description de tâche. La formulation proposée pour résoudre le problème de synthèse s'appuie sur l'identification d'un système de torseurs d'effort directement déduit de la tâche. Cette méthode est complétée par un ensemble de règles permettant la sélection des architectures les moins complexes tout en évitant les énumérations exhaustives d'architectures candidates. Cette méthode est très générique dans le sens où elle peut être appliquée à toute description de tâche formulée en termes de système de torseurs dual au système de torseurs cinématiques désiré pour la tâche. La procédure de synthèse proposée se décompose comme suit:

Étape 1: Identification de la mobilité requise à partir de la définition de tâche
(a) Identification de tous les types de mouvements possibles

Étape 2: Pour chaque type de mouvement, identification et décomposition de son système de torseurs d'effort associé

Étape 3: Génération de jambes, à chaînes cinématiques ouvertes ou fermées, conformes au système de torseurs d'effort souhaité
(a) Identification des jambes présentant la moindre complexité d'architecture

Étape 4: Génération de mécanismes parallèles par combinaison de jambes
(a) Vérification du critère de mobilité générale

(b) Vérification de la validité du choix des articulations motorisées

Étape 5: Si les étapes 4a et 4b ne sont pas satisfaites revenir à l'étape 3

Types de mouvements pour les tâches $\mathbf{T_1}$ et $\mathbf{T_2}$

Dans un premier temps, le système de torseurs d'effort correspondant au type de mouvement désiré doit être identifié. Les torseurs cinématique et d'effort de pas h sont respectivement désignés par $\$^h$ et $\hat{\$}^h$. En conséquence, les systèmes de torseurs d'effort d'ordre n de pas nul et infini seront notés n-$\hat{\$}^0$ et n-$\hat{\$}^\infty$. Un générateur du torseur d'effort correspondant au motif de mouvement mp sera désigné par $\hat{\$}^h_{mp}$. En conséquence, les systèmes de clés d'ordre n formés par zéro et l'infini clés de hauteur sont appelés n-$\hat{\$}^0$ et n-$\hat{\$}^\infty$. Un générateur de clé correspondant au motif de mouvement désiré être dénommée $\hat{\$}^h_{mp}$. Sur la base de la définition de tâches T_1 et T_2, trois différents types de mouvements peuvent être obtenus. La figure C.5 montre les trois systèmes de torseurs d'effort déduits de la description des tâches T_1 et T_2.

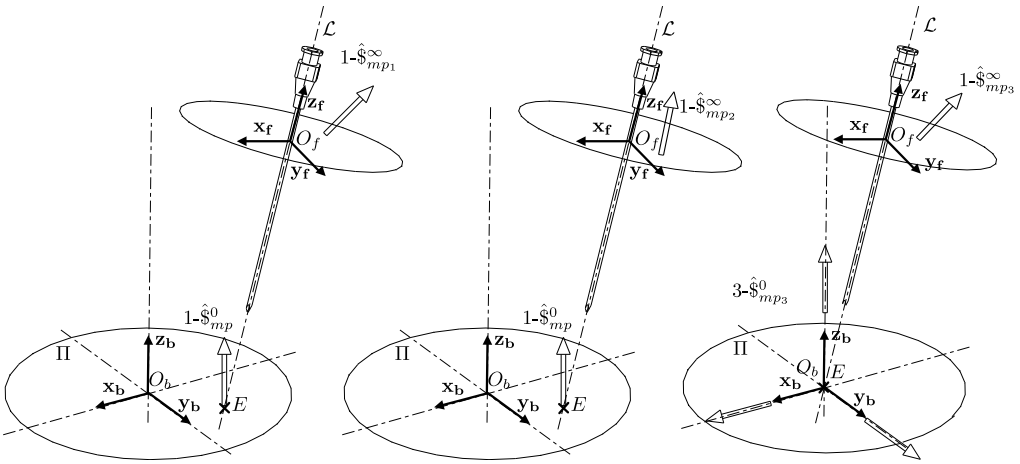

Figure C.5 – Types des mouvements.

Mécanismes synthétisés pour les tâches T_1 et T_2

En utilisant la théorie de torseurs, avec comme objectif de mobilité 2T2R et 2R et les types de mouvements pour les tâches T_1 et T_2, une synthèse d'architectures candidates viables a été proposée en tenant compte du critère de mobilité générale et de la validation des liaisons actionnées. Le résultat obtenu correspond à la synthèse de trois mécanismes tels que décrits sur la figure C.6, spécifiquement adaptés aux besoins de manipulation d'une aiguille et intégrant un centre de rotation déporté.

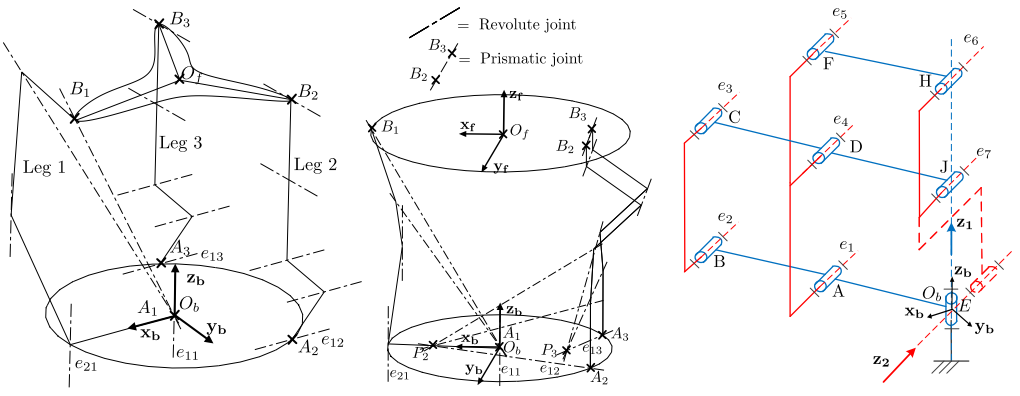

Candidat 2T2R-II pour la tâche T_1. Candidat 2T2R-IV pour la tâche T_1. Candidat 2R pour la tâche T_2.

Figure C.6 – Mécanismes synthétisés.

C.2.2 Algorithme de synthèse dimensionnelle

Cet algorithme de synthèse dimensionnelle fournit une formulation *a priori* basée sur l'analyse des contraintes provenant aussi bien des singularités série du mécanisme, des limites imposées par l'actionnement que des forces de réaction introduites par les singularités parallèles. Son principe se distingue nettement des méthodes d'analyse *a posteriori* basées sur des indices de performance qui sont itératifs et très coûteux en temps de calcul. Un cadre pour l'identification et l'élimination des vides dans l'espace de travail fait également partie de l'algorithme ce qui le distingue encore des autres approches. Différents paramétrages pour le mécanisme et l'effecteur peuvent être choisis afin de s'adapter au mieux à la description de la tâche. Cet algorithme peut être appliqué de manière plus efficace aux mécanismes de mobilité inférieure à six étant donné que sa complexité est fonction du nombre de paramètres structurels. Bien que le présent mémoire ne traite que des mécanismes à liaisons de révolution, il peut être étendu à des mécanismes présentant des liaisons prismatiques et avec une prise en compte des limites articulaires. En outre, des espaces de travail plus généraux comme l'espace de travail accessible pourraient être considérés mais avec une plus grande complexité. Il faut toutefois noter que cet algorithme ne tient pas compte des problématiques de collision et d'interférence apparaissant lors de la conception volumique des pièces composant le mécanisme. L'algorithme de synthèse dimensionnelle proposé pour les mécanismes à liaisons de révolution de type série ou parallèle peut être décrit comme suit:

> **Étape** 1: Obtention des formes les plus simples des conditions de singularité série et parallèle à partir d'une analyse géométrique des torseurs par opposition à une approche basée sur le calcul symbolique des jacobiennes $\mathbf{J_X}$ et $\mathbf{J_q}$.
>
> **Étape** 2: Utilisation des paramètres de Denavit-Hartenberg (DH) et résolution des problèmes cinématiques inverses pour obtenir les équations reliant les paramètres opérationnels aux paramètres structurels, pour chaque singularité.
>
> **Étape** 3: Partition des équations de singularité pour identifier les lieux géométriques de singularité distincts correspondant aux vides et ceux correspondant aux frontières extérieures de l'espace de travail.
>
> **Étape** 4: Modification des lieux géométriques de singularité.
> (a) Élimination ou réduction de la formation de vides.
>
> (b) Optimisation ou extension des limites externes de l'espace de travail.
>
> **Étape** 5: Résolution des équations correspondant aux lieux géométriques de singularité incluant les contraintes de conception, afin de trouver l'ensemble des paramètres DH pour le mécanisme.

L'algorithme ci-dessus peut être schématiquement représenté comme sur la figure C.7.

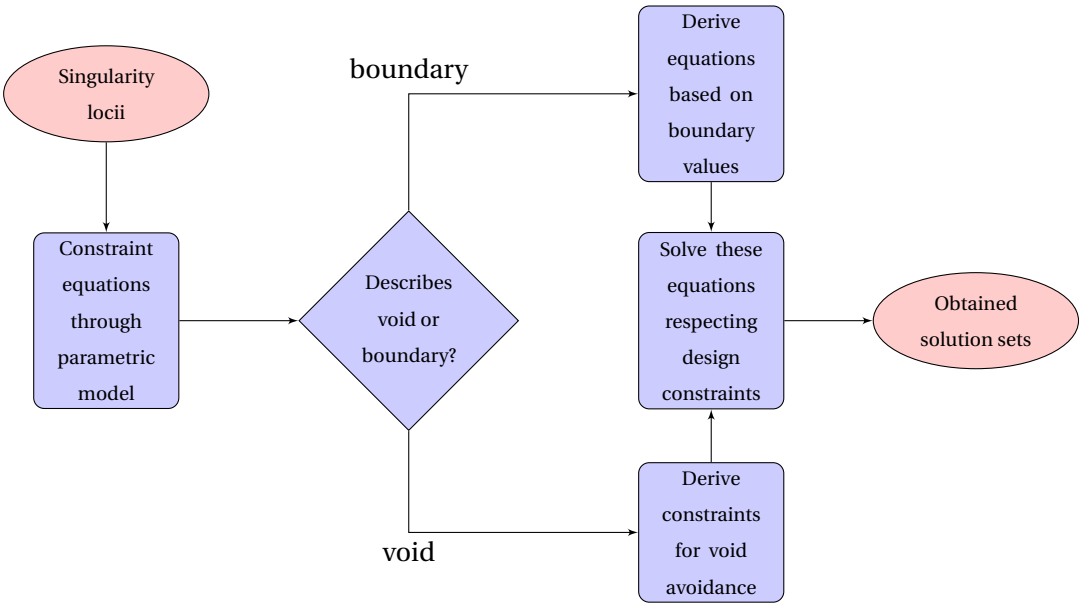

Figure C.7 – Algorithme de synthèse dimensionnelle.

Analyse statique du candidat 2T2R II

Pour l'analyse statique de l'architecture candidate 2T2R II, un effet combiné de la gravité (5N) et des forces d'insertion axiales (15N) est considéré. Le centre de gravité du dispositif est supposé se trouver sur l'axe de l'aiguille à une distance de 130 mm à partir de l'origine du repère de base. Les valeurs maximales des quatre moments d'actionnement $M_{max} = \max(M_1, M_2, M_3, M_4)$ ont été calculées et sont représentées sur la figure C.8 . L'ensemble des points rouges représente l'espace de travail inaccessible. L'ensemble des points bleus

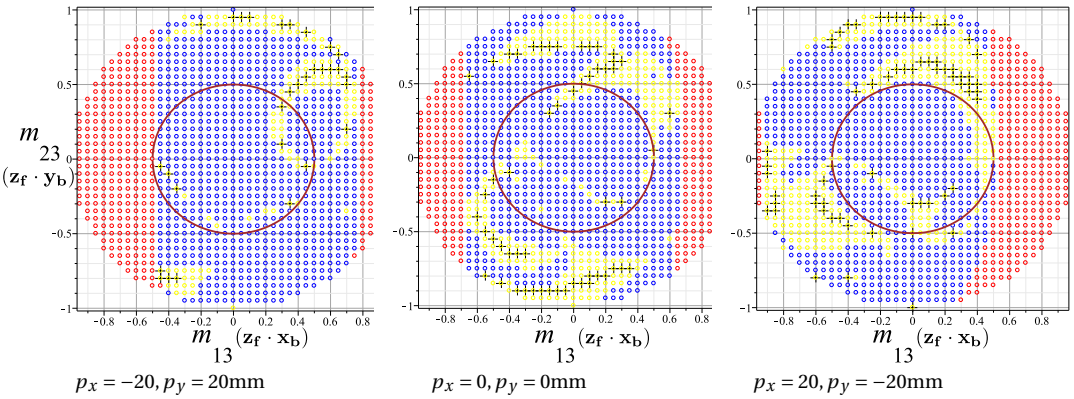

Figure C.8 – Espace de travail possible en couple pour 2T2R

représentent l'espace de travail accessible où les couples d'actionnement $M_{max} < 2$N·m. L'ensemble des points jaunes représentent l'espace de travail accessible où $2 < M_{max} < 10$N·m. L'ensemble des croix noires représentent les points accessibles mais où la matrice jacobienne

est très mal conditionnée et les moments d'actionnement sont très élevés avec $M_{max} > 10$N·m. La zone à l'intérieur du cercle brun est l'espace de travail désiré en orientation. L'existence de ces croix noires isolées et des points jaunes posent des problèmes pour le choix d'une solution technologique pour l'actionnement, en particulier compte tenu du scénario de téléopération du dispositif de positionnement esclave.

Analyse statique du candidat 2R

L'analyse statique du candidat 2R a été réalisée dans les mêmes conditions que le candidat 2T2R. Le couple d'actionnement M_1 est égal à zéro sous l'équilibre statique. Les évolutions du couple d'actionnement M_2 et des forces de réaction aux cinq liaisons pivots peuvent être calculées et sont tracées sur la figure C.9.

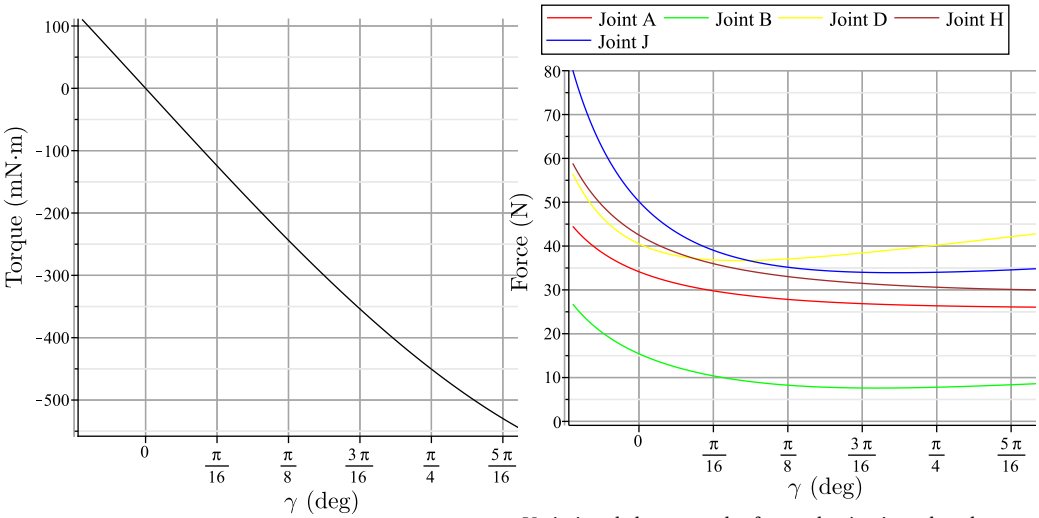

Moment d'actionnement M_2

Variation de la norme des forces de réactions dans les liaisons

Figure C.9 – Évolution des moments d'actionnement et des forces de réaction.

Conclusion

Le niveau élevé des couples d'actionnement en certains points accessibles de l'espace de travail réduit les possibilités de sélection d'une technologie d'actionnement pour le candidat 2T2R, compte tenu des contraintes de taille et de poids du dispositif.Par ailleurs, il s'est avéré difficile d'obtenir une plus grande plage d'orientation (> 30 deg) sans augmenter significativement l'encombrement en hauteur du mécanisme. Les niveaux de couple d'actionnement se sont révélés être beaucoup plus faible pour le mécanisme à architecture 2R ce qui a permis le choix d'une technologie d'actionnement et de transmission adaptée. De plus, un espace de travail en orientation beaucoup plus grand (jusqu'à 60 deg) peut être obtenu avec le mécanisme candidat 2R. Compte tenu des contraintes temporelles du projet ProteCT et des raisons de mise en œuvre pratique, le mécanisme candidat 2R a été retenu pour le projet.

C.3 Outil d'insertion

L'outil d'insertion est peut-être la partie la plus importante et critique de l'ensemble constituant le dispositif d'insertion d'aiguille robotisé. Classiquement, l'aiguille est fixée de façon rigide au dispositif robotisé puis est ensuite insérée via un mécanisme d'insertion adapté. Mais l'observation d'une procédure percutanée manuelle montre que le radiologue insère l'aiguille de manière itérative en une série d'étapes. Entre ces étapes, l'aiguille est relâchée et saisie à nouveau pour d'une part, permettre la manipulation d'aiguilles de grande longueur et d'autre part permettre à l'aiguille partiellement insérée de bouger librement entre deux phases d'insertion. En effet, le maintien extérieur ferme d'une aiguille insérée peut causer des lacérations dans les organes traversés en raison des mouvements physiologiques induits par la respiration du patient. Par conséquent, le dispositif d'insertion doit intégrer cette capacité de lâcher/reprise d'aiguille imitant ainsi le geste manuel du radiologue. Enfin, il est souhaitable que dispositif d'insertion fournisse un retour haptique au praticien pour augmenter l'efficacité et la sécurité de la procédure.

C.3.1 Mécanisme d'insertion

Le degré de liberté correspondant à l'insertion doit être réalisé par un mécanisme permettant un DDL en translation le long de l'axe d'insertion. La réalisation pratique de cette fonction est assurée au moyen d'un mécanisme de Sarrus associé à une liaison cylindrique, comme représenté sur la figure C.10. L'actionnement de ce mécanisme d'insertion est assuré par deux actionneurs piézoélectrique linéaires.

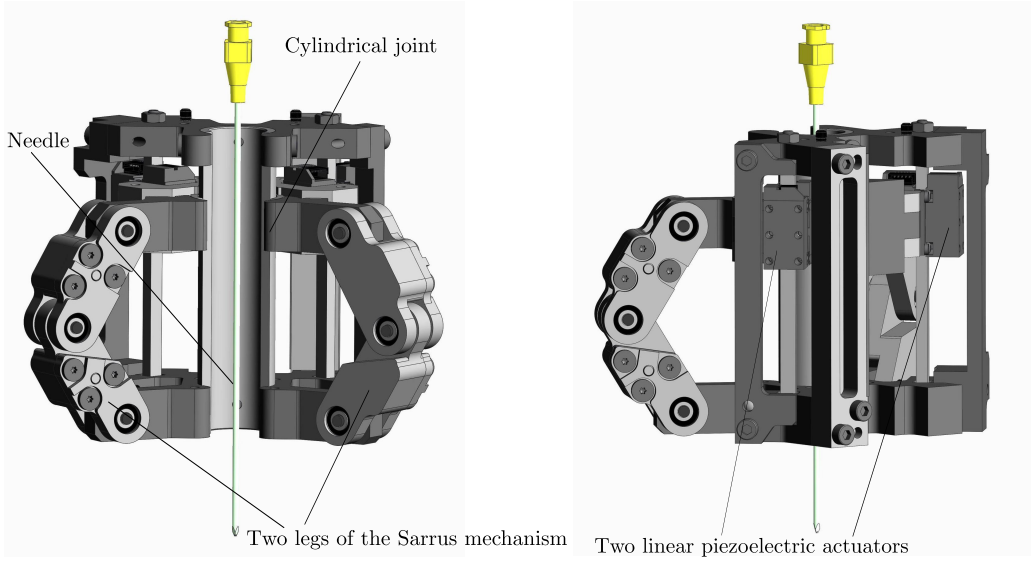

Figure C.10 – Modèle CAO du mécanisme d'insertion équipé de deux moteurs linéaires piézo-électriques (Avec François Schmitt).

C.3.2 Dispositif de préhension de l'aiguille (NGD)

La disponibilité de NGD semble être un facteur limitant pour le développement d'assistants robotiques d'insertion d'aiguille. Pour établir la structure fonctionnelle d'un NGD, principalement quatre sous-fonctions élémentaires sont considérées, à savoir (1) mettre des obstacles autour de l'aiguille, (2) déplacer les obstacles radialement, (3) transmettre le mouvement aux obstacles et (4) actionner les obstacles mobiles. Cette décomposition a permis de formuler les problèmes essentiels à une haut niveau d'abstraction pour laisser solutions ouvertes possibles et de faire une approche systématique plus facile. Le tableau C.1 présente plusieurs principes de solutions pour les sous-fonctions du NGD. Deux types de NGD, le premier utilisant des

			Solution Principles				
			1	2	3	4	5
Subfunctions	1	SF_1	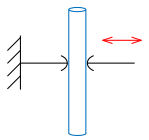	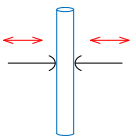	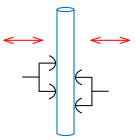	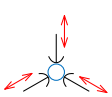	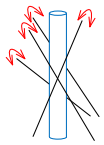
	2	SF_2	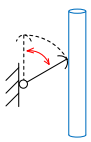	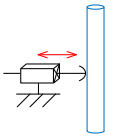	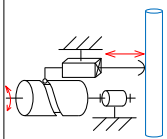	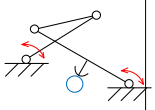	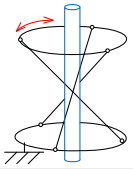
	3	SF_3	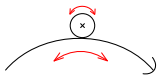	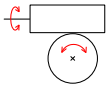	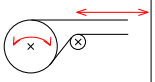		
	4	SF_4		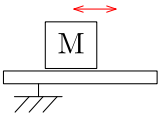	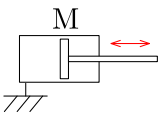		

Table C.1 – Principes de solution pour les sous-fonctions d'un NGD.

pièces rigides (1.3–2.3–3.2–4.1) et le second utilisant des pièces déformables (1.5–2.5–3.2–4.1), ont été conçus dans notre laboratoire.

Dans cette thèse, une comparaison expérimentale de ces deux versions de NGD a été réalisée. Le dispositif expérimental se compose d'une machine de traction Zwick, GmbH (Z005 THN - Allround Line), capable d'appliquer différents efforts et taux de variation d'effort par l'intermédiaire de la traverse de la machine. Une aiguille chirurgicale 18G (diamètre 1.3 mm) en acier inoxydable est maintenue par des mors attachés à la traverse de la machine. Pour un chargement de compression simple, la vitesse de variation de la force est maintenue constante, comme le montre la figure C.12. Les résultats typiques obtenus pour les NGD dans leur version

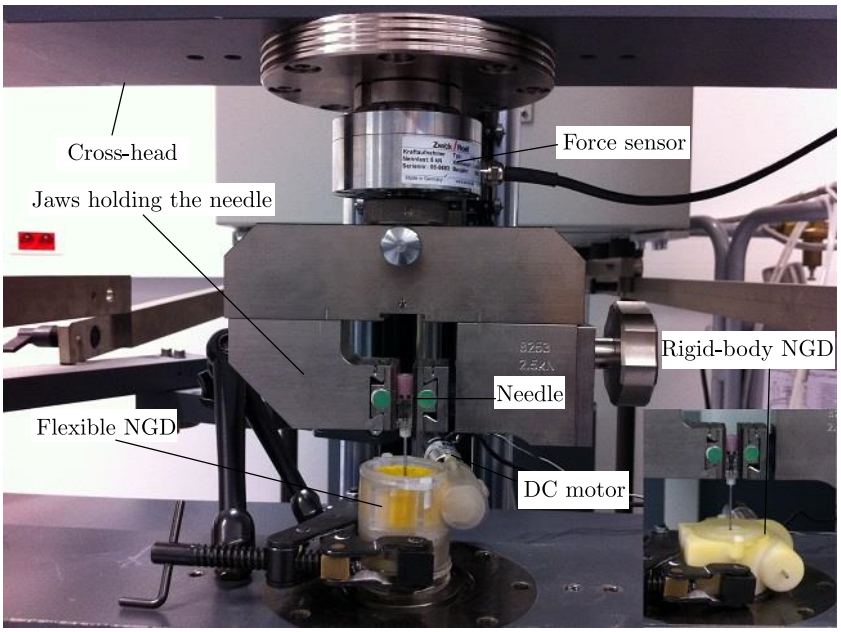

Figure C.11 – Description de l'installation expérimentale.

rigide et flexible sont donnés sur la figure C.12(a). On peut observer que les deux NGD sont capables de suivre la consigne d'effort imposée par la traverse jusqu'à une certaine valeur à partir de laquelle l'aiguille glisse dans le NGD. On peut noter la bien meilleure capacité de serrage du NGD flexible par rapport à la version rigide.

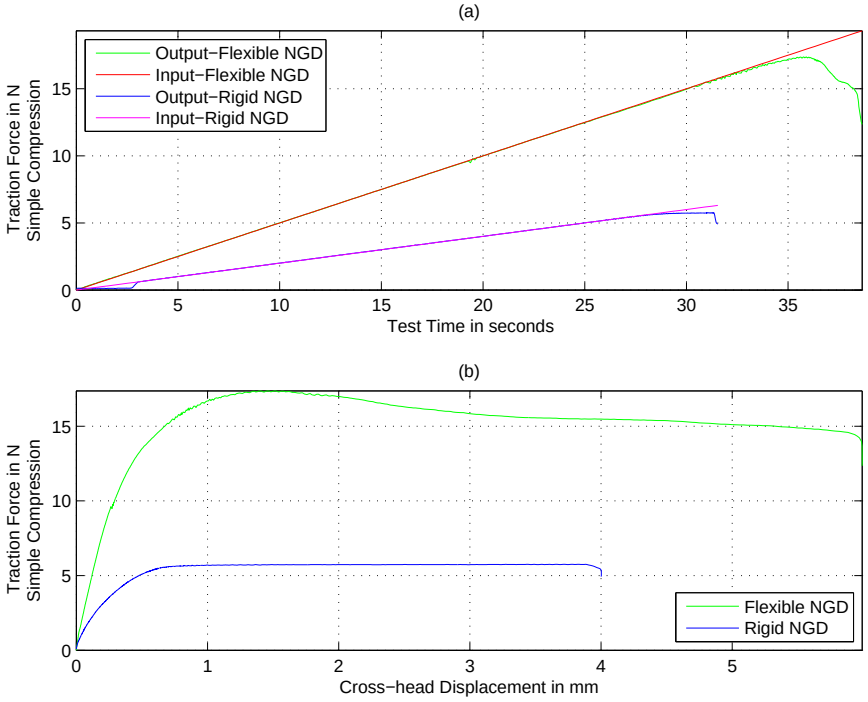

Figure C.12 – Résultats pour un chargement en compression simple.

C.3.3 Capteur de force pour la mesure des efforts d'insertion

Le capteur d'effort proposé présente une structure de mécanisme de Sarrus compliant (compliant Sarrus mechanism: CSM) et met en œuvre des jauges d'extensométrie. Le prototype représenté sur la figure C.13(b) a été fabriqué au moyen d'une machine de prototypage rapide Connex 350 en utilisant un matériau proche du polypropylène. La figure C.14 représente la réponse du capteur de force à un essai de fluage dans lequel un effort d'entrée constant de $f_c = 5N$ est appliqué.

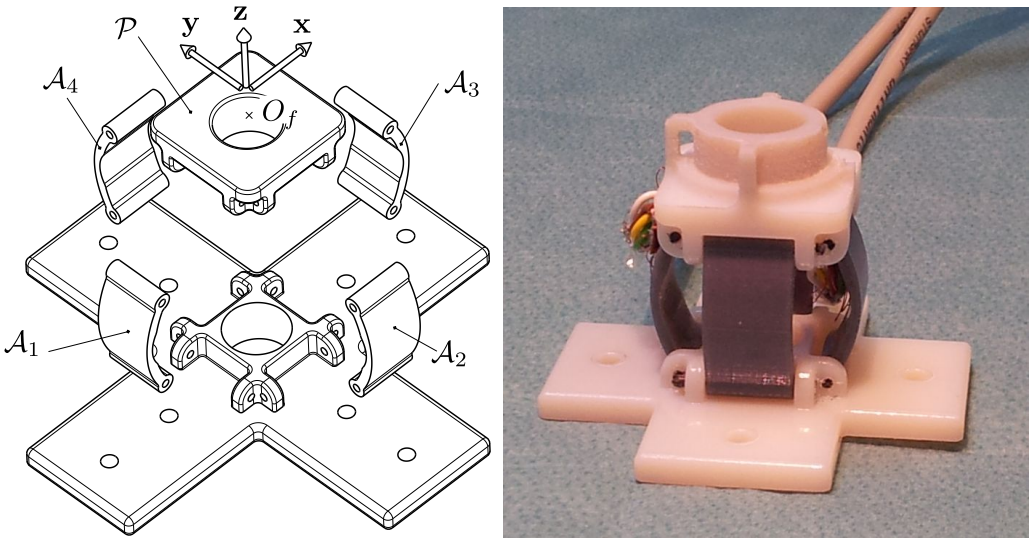

Figure C.13 – Mécanisme de Sarrus compliant (CSM): (a) Vue CAO éclatée (b) Prototype fabriqué.

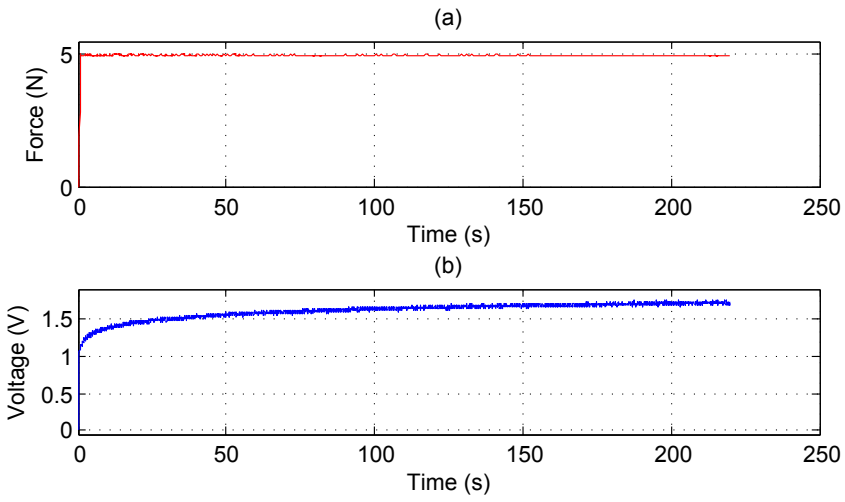

Figure C.14 – Essai de fluage sur le capteur de force CSM: (a) charge appliquée en entrée (b) réponse du capteur.

Une observation attentive de la sortie montre une lente augmentation de la valeur de déformation lorsque le temps augmente. Ainsi, la figure C.14(b) correspond à une réponse de fluage pour un modèle linéaire de Burgers composé de deux ressorts et deux amortisseurs. Sur la base de ce modèle viscoélastique, une loi de correction du signal de mesure a été obtenue pour compenser les effets viscoélastiques du capteur CSM.

C.3.4 Conclusion

Cette section décrit brièvement l'intégration des trois éléments de l'outil d'insertion à savoir le NGD, le mécanisme d'insertion et le capteur de force CSM. Les trois dispositifs sont connectés en série pour donner à l'ensemble un encombrement de forme globalement conique qui est favorable pour limiter les collisions lors des orientations d'aiguille de grande amplitude. Le mécanisme d'insertion est placé en premier, suivi par le capteur de force CSM puis le NGD. L'agencement représentée sur la figure C.15(a) assure que les forces d'insertion d'aiguille axiales sont transmises directement du NGD au capteur de force CSM sans nécessité d'aucun mécanisme intermédiaire. Le mécanisme d'insertion qui se trouve en partie supérieure assure le déplacement en translation de l'ensemble, y compris du capteur et du NGD assurant la préhension de l'aiguille, le long de l'axe d'insertion. La conception du modèle CAO de l'outil d'insertion est représenté sur la figure C.15(b) et a été développé avec François Schmitt, ingénieur du projet ProteCT. La hauteur totale de l'outil d'insertion est de l'ordre de 137 mm.

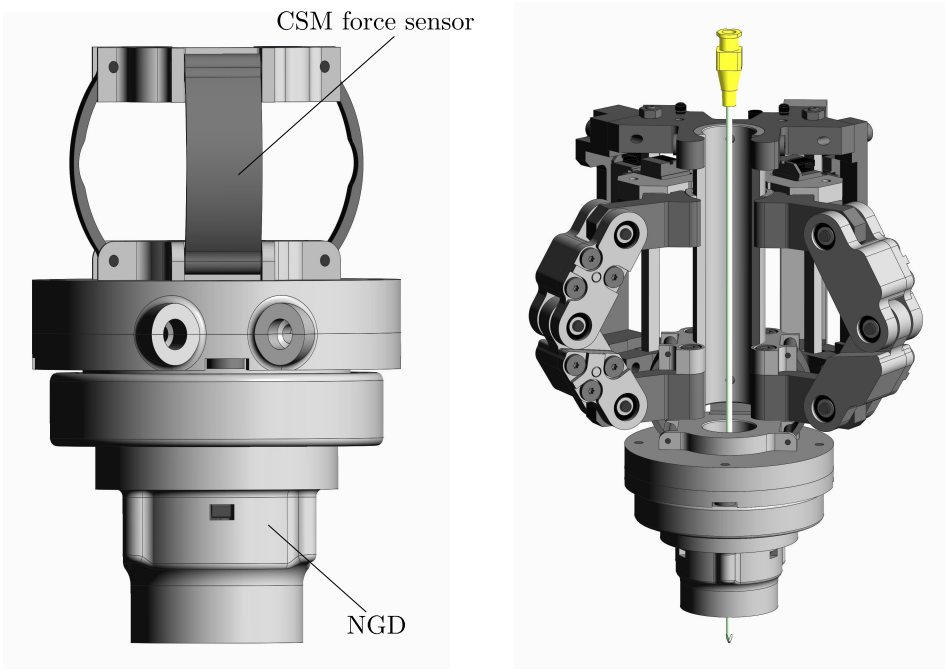

(a) Montage en série du capteur de force CSM et du NGD.

(b) Montage en série du mécanisme d'insertion, du capteur de force CSM et du NGD.

Figure C.15 – Modèle CAO de l'outil d'insertion (avec François Schmitt).

C.4 Conclusion

Le travail de cette thèse a été réalisé dans le cadre général du projet ProteCT qui vise à protéger le radiologue de la surexposition aux rayons X pendant les procédures percutanées sous scanner. Ce projet vise à mettre en place une procédure robotisée téléopéré dans laquelle un dispositif maître est contrôlé à distance par le radiologue et la procédure effectuée par un dispositif robotique esclave monté sur le patient. Au cours de cette thèse, le travail a porté sur la conception et le développement de l'esclave assistant robotique. L'esclave assistant a été conçu pour assurer des fonctionnalités différentes qui imitent les gestes du radiologue dans une procédure manuelle. Ces fonctionnalités sont principalement le positionnement de l'aiguille, sa préhension, son insertion et la mesure des forces d'insertion.

Pour la conception et le développement du dispositif de positionnement de l'aiguille, la tâche a été formulée sur la base de la définition des mobilités désirées pour le mécanisme. Cela a permis d'effectuer une synthèse systématique des architectures mécaniques dédiées à la tâche de positionnement d'aiguille. Une synthèse dimensionnelle des mécanismes a été effectuée pour limiter la taille du dispositif et pour déterminer à la fois le niveau des couples d'actionnement et les forces de réaction aux liaisons pour réaliser le choix des actionneurs et des autres composants standards de guidage et transmission. Un cahier des charges pour la conception de l'outil d'insertion composé d'un mécanisme d'insertion, d'un capteur de force et du NGD été établi. Sur la base de ces spécifications, la conception et l'évaluation expérimentale d'une nouvelle variante de NGD utilisant des pièces flexibles a été réalisée. La conception du capteur de force à l'aide de pièces en matériau polymère, la modélisation de son comportement et son évaluation expérimentale a été effectuée pour améliorer la transparence de l'outil d'insertion sous le scanner CT.

Contributions

Les différents dispositifs proposés dans cette thèse qui constituent l'assistant robotique esclave fournissent diverses contributions à la solution développée pour les procédures percutanées téléopérés dans le cadre du projet ProteCT. Outre les contributions aux besoins dans le contexte médical, le travail dans cette thèse a également contribué à la zone de synthèse et de conception des mécanismes parallèles de mobilité inférieur.

Pour la conception du dispositif de positionnement de l'aiguille, une méthodologie de synthèse d'architecture basée sur une description générique des tâches a été proposée. La nouveauté de ce procédé de synthèse réside dans l'utilisation de la description des contraintes déduites de la définition de tâche en tant que point de départ pour la synthèse du mécanisme. Un ensemble de règles de préférence ont été définies pour caractériser la complexité architecturale du mécanisme. En utilisant cette méthode, une nouvelle famille de mécanismes parallèles 2T2R, dédiée aux procédures d'insertion d'aiguille percutanées robotisées a été synthétisée pour la première fois. Un algorithme de synthèse dimensionnelle original pour des mécanismes parallèles à mobilité réduite a été développé en se basant sur l'étude des

lieux géométriques de singularité par observation des systèmes de torseurs avec une prise en compte des objectifs de taille désirée pour l'espace de travail. Pour limiter le niveau des couples d'actionnement et les forces de réaction, l'analyse des singularités parallèles a également été incluse dans l'algorithme en complément des singularités série.

Une nouvelle variante de NGD utilisant des parties flexibles a été conçue selon les exigences imposées par les procédures percutanées. Cette conception permet de relâcher/reprendre l'aiguille en assurant un recentrage et un passage élargi autour de l'aiguille en dehors des phases d'insertion. Un capteur de force intégré personnalisé basé sur un mécanisme Sarrus compliant a été conçu et validé expérimentalement dans des conditions de chargement quasi-statiques et dynamiques avec une prise en compte de son comportement viscoélastique. Une originalité de cette conception réside dans l'emploi de matériaux polymères prototypés pour améliorer la transparence dans le scanner.

Perspectives

Le travail de cette thèse établit des bases pour la poursuite du développement d'un prototype clinique de l'assistant robotique complet destiné à la réalisation de procédures percutanées dans le contexte de la radiologie interventionnelle.

La méthodologie de synthèse basée sur les tâches avec son ensemble de règles de préférence peut être appliquée pour la synthèse de mécanismes dédiés à d'autres variétés de tâche. Bien que seuls des mécanismes parallèles présentant des jambes à architecture série aient été considérés dans cette étude, la procédure de synthèse proposée pourrait être étendue à des mécanismes comportant des jambes à architecture complexe. L'algorithme de synthèse dimensionnelle peut également être facilement appliquée à des mécanismes parallèles à mobilité inférieure en considérant d'autres types d'espace de travail notamment l'espace de travail accessible. Bien que l'algorithme de synthèse dimensionnelle proposé ne considère que des mécanismes comprenant des liaisons de révolution, son application peut être envisagée sur des mécanismes comportant des liaisons prismatiques avec prise en compte des butées articulaires.

Sur la base du NGD compliant présenté, d'autres variantes de construction pourraient être obtenues en combinant différents principes de solutions proposées dans ce travail. Malgré le fait que le capteur de force CSM ait été conçu pour des procédures de radiologie interventionnelle, l'élément flexible proposé pourrait être utilisé pour de nombreuses applications où seule une mesure d'effort uni-axiale est nécessaire. La modélisation viscoélastique du CSM présenté dans ce travail peut être utilisé pour modéliser des capteurs de force fabriqués à partir d'une grande variété de matériaux polymères. Finalement, des prototypes du NGD et du capteur d'effort compliant ayant été construits et validés expérimentalement d'une manière séparée, il reste à finaliser l'intégration de ces composants pour tester et valider le dispositif d'insertion dans son ensemble.

Bibliography

Agrawal, S. (1991). Workspace boundaries of in-parallel manipulator systems. In , *Fifth International Conference on Advanced Robotics, 1991. 'Robots in Unstructured Environments', 91 ICAR*, pages 1147–1152 vol.2.

Al Janaideh, M. and Krejci, P. (2013). Inverse rate-dependent Prandtl–Ishlinskii model for feedforward compensation of hysteresis in a piezomicropositioning actuator. *IEEE/ASME Transactions on Mechatronics*, 18(5):1498–1507.

Altuzarra, O., Salgado, O., Pinto, C., and Hernández, A. (2013). Analytical determination of the principal screws for general screw systems. *Mechanism and Machine Theory*, 60:28–46.

Angeles, J. (2004). The qualitative synthesis of parallel manipulators. *Journal of Mechanical Design*, 126(4):617.

Arakelian, V., Briot, S., and Glazunov, V. (2008). Increase of singularity-free zones in the workspace of parallel manipulators using mechanisms of variable structure. *Mechanism and Machine Theory*, 43(9):1129–1140.

Badaan, S., Petrisor, D., Kim, C., Mozer, P., Mazilu, D., Gruionu, L., Patriciu, A., Cleary, K., and Stoianovici, D. (2011). Does needle rotation improve lesion targeting? *The International Journal of Medical Robotics and Computer Assisted Surgery*, 7(2):138–147.

Barbé, L. (2007). *Téléopération avec retour d'efforts pour les interventions percutanées*. PhD thesis, Université de Strasbourg, Strasbourg, France.

Barbé, L., Bayle, B., Gangloff, J., de Mathelin, M., and Piccin, O. (2007). Design and evaluation of a linear haptic device. In *2007 IEEE International Conference on Robotics and Automation*, pages 485–490.

Briot, S., Glazunov, V., and Arakelian, V. (2013). Investigation on the effort transmission in planar parallel manipulators. *Journal of Mechanisms and Robotics*, 5(1):011011–011011.

Carovac, A., Smajlovic, F., and Junuzovic, D. (2011). Application of ultrasound in medicine. *Acta Informatica Medica*, 19(3):168–171.

Cole, G., Pilitsis, J., and Fischer, G. (2009). Design of a robotic system for MRI-guided deep brain stimulation electrode placement. In *IEEE International Conference on Robotics and Automation, 2009. ICRA '09*, pages 4450–4456.

Cunha, J. A., Hsu, I.-C., Pouliot, J., Roach Iii, M., Shinohara, K., Kurhanewicz, J., Reed, G., and Stoianovici, D. (2010). Toward adaptive stereotactic robotic brachytherapy for prostate cancer: demonstration of an adaptive workflow incorporating inverse planning and an MR stealth robot. *Minimally invasive therapy & allied technologies: MITAT: official journal of the Society for Minimally Invasive Therapy*, 19(4):189–202.

Dai, J. S. and Jones, J. R. (2003). A linear algebraic procedure in obtaining reciprocal screw systems. *Journal of Robotic Systems*, 20(7):401–412.

De Lorenzo, D., Koseki, Y., De Momi, E., Chinzei, K., and Okamura, A. (2013). Coaxial needle insertion assistant with enhanced force feedback. *IEEE Transactions on Biomedical Engineering*, 60(2):379–389.

Fan, C., Liu, H., Yuan, G., and Zhang, Y. (2011). A novel 2T2R 4-DOF parallel manipulator. In *2011 Fourth International Symposium on Knowledge Acquisition and Modeling (KAM)*, pages 5–8.

Fan, C., Liu, H., and Zhang, Y. (2013). Type synthesis of 2T2R, 1T2R and 2R parallel mechanisms. *Mechanism and Machine Theory*, 61:184–190.

Fang, Y. and Tsai, L.-W. (2002). Structure synthesis of a class of 4-DoF and 5-DoF parallel manipulators with identical limb structures. *The International Journal of Robotics Research*, 21(9):799–810.

Gassert, R., Chapuis, D., Bleuler, H., and Burdet, E. (2008). Sensors for applications in magnetic resonance environments. *IEEE/ASME Transactions on Mechatronics*, 13(3):335–344.

Gassert, R., Moser, R., Burdet, E., and Bleuler, H. (2006). MRI/fMRI-compatible robotic system with force feedback for interaction with human motion. *IEEE/ASME Transactions on Mechatronics*, 11(2):216–224.

Gerovich, O., Marayong, P., and Okamura, A. M. (2004). The effect of visual and haptic feedback on computer-assisted needle insertion. *Computer aided surgery: official journal of the International Society for Computer Aided Surgery*, 9(6):243–249. PMID: 16112974.

Gogu, G. (2005). Mobility of mechanisms: a critical review. *Mechanism and Machine Theory*, 40(9):1068–1097.

Gogu, G. (2006). Fully-isotropic parallel manipulators with five degrees of freedom. In *Proceedings 2006 IEEE International Conference on Robotics and Automation, 2006. ICRA 2006*, pages 1141–1146.

Gogu, G. (2008). *Structural synthesis of parallel robots*. Number v. 149, 159, 173, 183 in Solid mechanics and its applications. Springer, Dordrecht ; London ; New York.

Goh, R. H., Somers, S., Jurriaans, E., and Yu, J. (1999). Magnetic resonance imaging. application to family practice. *Canadian Family Physician*, 45:2118–2132.

Graña, A., Sánchez, A., Zemiti, N., and Poignet, P. (2014). Modelling and control of an ERF-Based needle insertion training platform. In Stoyanov, D., Collins, D. L., Sakuma, I., Abolmaesumi, P., and Jannin, P., editors, *Information Processing in Computer-Assisted Interventions*, number 8498 in Lecture Notes in Computer Science, pages 31–40. Springer International Publishing.

Gwilliam, J., Mahvash, M., Vagvolgyi, B., Vacharat, A., Yuh, D. D., and Okamura, A. (2009). Effects of haptic and graphical force feedback on teleoperated palpation. In *IEEE International Conference on Robotics and Automation, 2009. ICRA '09*, pages 677–682.

Hayes, M. J. D. and Husty, M. L. (2003). On the kinematic constraint surfaces of general three-legged planar robot platforms. *Mechanism and Machine Theory*, 38(5):379–394.

Herder, J. L., Horward, M. J., and Sjoerdsma, W. (1997). A laparoscopic grasper with force perception. *Minimally Invasive Therapy & Allied Technologies*, 6(4):279–286.

Hervé, J. (1999). The lie group of rigid body displacements, a fundamental tool for mechanism design. *Mechanism and Machine Theory*, 34(5):719–730.

Hoffman, J. (2010). Conception et d´eveloppement d'un prototype du ct-bot. Master's thesis, Institut national des sciences appliquées (INSA).

Hong, M. B. and Choi, Y. J. (2010). Formulation of unique form of screw based jacobian for lower mobility parallel manipulators. *Journal of Mechanisms and Robotics*, 3(1):011002–011002.

Hoover, A. and Fearing, R. (2009). Analysis of off-axis performance of compliant mechanisms with applications to mobile millirobot design. In *Intelligent Robots and Systems, 2009. IROS 2009. IEEE/RSJ International Conference on*, pages 2770–2776.

Howell, L. L. (2001). *Compliant mechanisms*. Wiley, New York.

Huang, T., Liu, H., and Chetwynd, D. (2011a). Generalized jacobian analysis of lower mobility manipulators. *Mechanism and Machine Theory*, 46(6):831–844.

Huang, Z., Chen, Z., Liu, J., and Liu, S. (2011b). A 3DOF rotational parallel manipulator without intersecting axes. *Journal of Mechanisms and Robotics*, 3(2):021014–021014.

Huang, Z., Li, Q., and Ding, H. (2013). *Theory of parallel mechanisms*. Springer, Dordrecht; New York.

Hungr, N., Baumann, M., Long, J.-A., and Troccaz, J. (2012). A 3-d ultrasound robotic prostate brachytherapy system with prostate motion tracking. *IEEE Transactions on Robotics*, 28(6):1382–1397.

Hungr, N., Fouard, C., Robert, A., Bricault, I., and Cinquin, P. (2011). Interventional radiology robot for CT and MRI guided percutaneous interventions. In Fichtinger, G., Martel, A. L., and Peters, T. M., editors, *MICCAI (1)*, volume 6891 of *Lecture Notes in Computer Science*, pages 137–144. Springer.

iSYS Medizintechnik (2013). The iSYS 1 positioning unit. http://www.isys.co.at/isys/cms_extract/l29400b29400/isys_1_for_ct.html.

Joinie-Maurin, M., Barbé, L., Piccin, O., Gangloff, J., Bayle, B., and Rump, R. (2010). Design of a linear haptic display based on approximate straight line mechanisms. In *2010 IEEE/RSJ International Conference on Intelligent Robots and Systems (IROS)*, pages 5048–5053.

Khalil, W. and Kleinfinger, J. (1986). A new geometric notation for open and closed-loop robots. In *1986 IEEE International Conference on Robotics and Automation. Proceedings*, volume 3, pages 1174–1179.

Kong, X. and Gosselin, C. (2007). *Type synthesis of parallel mechanisms*. Number v. 33 in Springer tracts in advanced robotics. Springer, Berlin ; New York.

Kong, X. and Gosselin, C. M. (2006). Type synthesis of 4-DOF SP-equivalent parallel manipulators: A virtual chain approach. *Mechanism and Machine Theory*, 41(11):1306–1319.

Krieger, A., Song, S.-E., Cho, N., Iordachita, I., Guion, P., Fichtinger, G., and Whitcomb, L. (2013). Development and evaluation of an actuated MRI-compatible robotic system for MRI-guided prostate intervention. *IEEE/ASME Transactions on Mechatronics*, 18(1):273–284.

Krishnamachari, S. I. (1993). *Applied stress analysis of plastics: a mechanical engineering approach*. Van Nostrand Reinhold, New York.

Kumar, N., Piccin, O., and Bayle, B. (2014a). A task-based type synthesis of novel 2T2R parallel mechanisms. *Mechanism and Machine Theory*, 77:59–72.

Kumar, N., Piccin, O., Meylheuc, L., Barbé, L., and Bayle, B. (2014b). Dimensional synthesis of a novel 2t2r parallel manipulator for medical applications. In *ASME 2014 International Design Engineering Technical Conferences and Computers and Information in Engineering Conference*.

Kumar, N., Piccin, O., Meylheuc, L., Barbe, L., and Bayle, B. (2014c). Design, development and preliminary assessment of a force sensor for robotized medical applications. In *2014 IEEE/ASME International Conference on Advanced Intelligent Mechatronics (AIM)*, pages 1368–1374.

Li, J., Liu, Y., Wang, C., and Sun, L. (2006). Optimal kinematic design of a planar parallel manipulator with high speed and high precision. In *Proceedings of the 2006 IEEE International Conference on Mechatronics and Automation*, pages 1888–1892.

Li, J., Zhang, G., Müller, A., and Wang, S. (2013). A family of remote center of motion mechanisms based on intersecting motion planes. *Journal of Mechanical Design*, 135(9):091009–091009.

Li, Q. and Huang, Z. (2003). Type synthesis of 4-DOF parallel manipulators. In *IEEE International Conference on Robotics and Automation, 2003. Proceedings. ICRA '03*, volume 1, pages 755–760 vol.1.

Li, Q., Huang, Z., and Herve, J. (2004). Type synthesis of 3R2T 5-DOF parallel mechanisms using the lie group of displacements. *IEEE Transactions on Robotics and Automation*, 20(2):173–180.

Maurin, B., Barbé, L., Bayle, B., Zanne, P., Gangloff, J., Mathelin, M., Gangi, A., Soler, L., and Forgione, A. (2004). In vivo study of forces during needle insertions. In *Perspective in Image-guided Surgery: Proceedings of the Scientific Workshop on Medical Robotics, Navigation, and Visualization (MRNV 2004)*, page 415–422.

Maurin, B., Bayle, B., Piccin, O., Gangloff, J., de Mathelin, M., Doignon, C., Zanne, P., and Gangi, A. (2008). A patient-mounted robotic platform for CT-scan guided procedures. *IEEE transactions on bio-medical engineering*, 55(10):2417–2425. PMID: 18838367.

Mazor Robotics (2013). Mazor Robotics Renaissance system for spine surgery. http://mazorrobotics.com/.

Meltsner, M. A., Ferrier, N. J., and Thomadsen, B. R. (2007). Observations on rotating needle insertions using a brachytherapy robot. *Physics in Medicine and Biology*, 52(19):6027–6037.

Melzer, A., Gutmann, B., Remmele, T., Wolf, R., Lukoscheck, A., Bock, M., Bardenheuer, H., and Fischer, H. (2008). INNOMOTION for percutaneous image-guided interventions. *IEEE Engineering in Medicine and Biology Magazine*, 27(3):66–73.

Merlet, J. P. (2006). *Parallel Robots*. Springer.

Okamura, A. (2004). Methods for haptic feedback in teleoperated robot-assisted surgery. *The Industrial robot*, 31(6):499–508. PMID: 16429611 PMCID: PMC1317565.

Ovchinsky, N., Moreira, R. K., Lefkowitch, J. H., and Lavine, J. E. (2012). The liver biopsy in modern clinical practice: A pediatric point-of-view. *Advances in Anatomic Pathology*, 19(4):250–262.

Pahl, G., Beitz, W., Feldhusen, J., and Grote, K.-H. (2007). *Engineering Design – A Systematic Approach*. Springer.

Palli, G., Borghesan, G., and Melchiorri, C. (2012). Modeling, identification, and control of tendon-based actuation systems. *IEEE Transactions on Robotics*, 28(2):277–290.

Passera, K., Selvaggi, S., Scaramuzza, D., Garbagnati, F., Vergnaghi, D., and Mainardi, L. (2013). Radiofrequency ablation of liver tumors: quantitative assessment of tumor coverage through CT image processing. *BMC Medical Imaging*, 13:3.

Piccin, O., Barbé, L., Bayle, B., Mathelin, M. d., and Gangi, A. (2009). A force feedback teleoperated needle insertion device for percutaneous procedures. *The International Journal of Robotics Research*, 28(9):1154–1168.

Piccin, O., Kumar, N., Meylheuc, L., Barbé, L., and Bayle, B. (2012). Design, development and preliminary assessment of grasping devices for robotized medical applications. In *ASME 2012 International Design Engineering Technical Conferences and Computers and Information in Engineering Conference*, volume Volume 4: 36th Mechanisms and Robotics Conference, pages 65–73.

Piccin, O., Renaud, P., Barbé, L., Bayle, B., Maurin, B., and de Mathelin, M. (2005). A robotized needle insertion device for percutaneous procedures. In *Proceedings of the 2005 ASME Design Engineering Technical Conferences*, pages 433–440, Long Beach, CA, USA.

Polygerinos, P., Seneviratne, L., Razavi, R., Schaeffter, T., and Althoefer, K. (2013). Triaxial catheter-tip force sensor for MRI-Guided cardiac procedures. *IEEE/ASME Transactions on Mechatronics*, 18(1):386–396.

Purwar, A. and Gupta, A. (2011). Visual synthesis of RRR-and RPR-legged planar parallel manipulators using constraint manifold geometry. In *ASME 2011 International Design Engineering Technical Conferences and Computers and Information in Engineering Conference*, pages 1081–1092. American Society of Mechanical Engineers.

Ravani, B. and Roth, B. (1983). Motion synthesis using kinematic mappings. *Journal of Mechanical Design*, 105(3):460–467.

Roch, L. (2009). Conception d'un robot d'insertion d'aiguille sous scanner à rayons x. Master's thesis, Institut national des sciences appliquées (INSA).

San Martin, J., Trivino, G., and Bayona, S. (2007). Mechanical design of a minimally invasive surgery trainer using the manipulability as measure of optimization. In *ICM2007 4th IEEE International Conference on Mechatronics*, pages 1–5.

Seifabadi, R., Iordachita, I., and Fichtinger, G. (2012). Design of a teleoperated needle steering system for MRI-guided prostate interventions. In *2012 4th IEEE RAS EMBS International Conference on Biomedical Robotics and Biomechatronics (BioRob)*, pages 793–798.

Shah, S., Kapoor, A., Ding, J., Guion, P., Petrisor, D., Karanian, J., Pritchard, W. F., Stoianovici, D., Wood, B. J., and Cleary, K. (2008). Robotically assisted needle driver: evaluation of safety release, force profiles, and needle spin in a swine abdominal model. *International Journal of Computer Assisted Radiology and Surgery*, 3(1-2):173–179.

Shang, W., Su, H., Li, G., and Fischer, G. (2013). Teleoperation system with hybrid pneumatic-piezoelectric actuation for MRI-guided needle insertion with haptic feedback. In *2013 IEEE/RSJ International Conference on Intelligent Robots and Systems (IROS)*, pages 4092–4098.

Song, H., Hong, I., Cho, M., Lim, H., and Jung, S.-H. (2013a). Development of a needle insertion end-effector for interventional radiology. In *2013 44th International Symposium on Robotics (ISR)*, pages 1–3.

Song, S.-E., Tokuda, J., Tuncali, K., Yamada, A., Torabi, M., and Hata, N. (2013b). Design evaluation of a double ring RCM mechanism for robotic needle guidance in MRI-guided liver interventions. In *2013 IEEE/RSJ International Conference on Intelligent Robots and Systems (IROS)*, pages 4078–4083.

Srivatsan, R. A., Bandyopadhyay, S., and Ghosal, A. (2013). Analysis of the degrees-of-freedom of spatial parallel manipulators in regular and singular configurations. *Mechanism and Machine Theory*, 69:127–141.

Stefanescu, D. M. (2011). *Handbook of Force Transducers: Principles and Components*. Springer.

Stoianovici, D., Cleary, K., Patriciu, A., Mazilu, D., Stanimir, A., Craciunoiu, N., Watson, V., and Kavoussi, L. (2003). AcuBot: a robot for radiological interventions. *IEEE Transactions on Robotics and Automation*, 19(5):927–930.

Su, H. and Fischer, G. (2009). A 3-axis optical force/torque sensor for prostate needle placement in magnetic resonance imaging environments. In *IEEE International Conference on Technologies for Practical Robot Applications, 2009. TePRA 2009*, pages 5–9.

Talasaz, A., Trejos, A., and Patel, R. (2012). Effect of force feedback on performance of robotics-assisted suturing. In *2012 4th IEEE RAS EMBS International Conference on Biomedical Robotics and Biomechatronics (BioRob)*, pages 823–828.

Tan, U.-X., Yang, B., Gullapalli, R., and Desai, J. (2011). Triaxial MRI-Compatible fiber-optic force sensor. *IEEE Transactions on Robotics*, 27(1):65–74.

Tolou, N. and Herder, J. L. (2009). Concept and modeling of a statically balanced compliant laparoscopic grasper. In *ASME 2009 International Design Engineering Technical Conferences and Computers and Information in Engineering Conference*, pages 163–170.

Trantina, G. and Nimmer, R. (1994). *Structural analysis of thermoplastic components*. McGraw-Hill.

Wach, B. (2014). Conception d'un robot d'assistance à l'insertion d'aiguille sous scanner x. Master's thesis, Institut national des sciences appliquées (INSA).

Walsh, C. J., Shepard, J.-A., Gupta, R., Hanumara, N. C., and Slocum, A. H. (2008). A patient-mounted, telerobotic tool for CT-Guided percutaneous interventions. *Journal of Medical Devices*, 2(1):011007–011007.

Wang, S. (2011). The singularity research of a novel 2T2R parallel mechanism. In *2011 Second International Conference on Mechanic Automation and Control Engineering (MACE)*, pages 866–869.

Waspe, A., Cakiroglu, H., Lacefield, J., and Fenster, A. (2006). Design and validation of a robotic needle positioning system for small animal imaging applications. In *28th Annual International Conference of the IEEE Engineering in Medicine and Biology Society, 2006. EMBS '06*, pages 412–415.

Wolf, A. and Shoham, M. (2006). Screw theory tools for the synthesis of the geometry of a parallel robot for a given instantaneous task. *Mechanism and Machine Theory*, 41(6):656–670.

Wu, J., Ge, Q. J., Su, H.-J., and Gao, F. (2012). Kinematic acquisition of geometric constraints for task-oriented design of planar mechanisms. *Journal of Mechanisms and Robotics*, 5(1):011003–011003.

Yip, M., Yuen, S., and Howe, R. (2010). A robust uniaxial force sensor for minimally invasive surgery. *Biomedical Engineering, IEEE Transactions on*, 57(5):1008–1011.

Yu, L., Liu, X., Leng, S., Kofler, J. M., Ramirez-Giraldo, J. C., Qu, M., Christner, J., Fletcher, J. G., and McCollough, C. H. (2009). Radiation dose reduction in computed tomography: techniques and future perspective. *Imaging in medicine*, 1(1):65–84.

Zhang, Y. and Ting, K. (2012). Type synthesis of uncoupled 2T2R parallel manipulators. In *Proceedings of the ASME 2012 International Design Engineering Technical Conferences & Computers and Information in Engineering Conference IDETC/CIE*, Chicago, USA.

Zong, G., Pei, X., Yu, J., and Bi, S. (2008). Classification and type synthesis of 1-DOF remote center of motion mechanisms. *Mechanism and Machine Theory*, 43(12):1585–1595.